Thermodynamics and Heat Transport of doped Spin-Ice Materials

Inaugural-Dissertation

zur

Erlangung des Doktorgrades
der Mathematisch-Naturwissenschaftlichen Fakultät
der Universität zu Köln

vorgelegt von

Simon Scharffe

aus Bergisch Gladbach

Köln, 2016

Berichterstatter: Prof. Dr. T. Lorenz
Prof. Dr. M. Braden

Vorsitzender der Prüfungskommission: Prof. Dr. S. Trebst

Tag der mündlichen Prüfung: 22.04.2016

Contents

1 Introduction

In the field of condensed-matter physics the concept of magnetic frustration leads to fascinating properties which arise from microscopic details of the interplay between different interactions and geometric constraints leading to the existence of complex ground states and exotic excitations [1–3]. Among these exotic excitations are fractionalized electric charges in the quantum Hall effect and fractionalized magnetic dipoles in a class of geometrically frustrated magnets known as spin ice [4]. Prototype spin-ice materials are the pyrochlores $Dy_2Ti_2O_7$ and $Ho_2Ti_2O_7$ where the geometric frustration of magnetic interactions prevents long-range magnetic order down to lowest temperature. The magnetism of both materials can be well described by non-collinear $S = 1/2$ Ising spins with large magnetic moments of about $\mu = 10\mu_\mathrm{B}$ that form a network of corner-sharing tetrahedra. A strong crystal electric field results in an Ising anisotropy with quantization axes pointing along the local $\{111\}$ directions. Antiferromagnetic nearest-neighbor exchange interactions are overcome by strong dipolar interactions leading to an effective ferromagnetic coupling. A sixfold degenerate ground state with two spins pointing into and two out of each tetrahedron originates from the interplay between the geometric constraints and the effective ferromagnetic coupling. This 2in-2out arrangement is equivalent to Pauling's ice rule describing the hydrogen displacement in water ice and results in a residual zero-temperature entropy of $S_\mathrm{P} = R/2 \ln(3/2)$ [5, 6]. The lowest excitation in spin-ice systems is a single spin flip which creates a pair of 1in-3out and 3in-1out configurations on neighboring tetrahedra and due to the ground-state degeneracy such a pair can fractionalize into two individual excitations that can propagate almost independently within the pyrochlore lattice. These unique excitations are described as (anti-)monopoles connected via Dirac strings [4, 7].

The knowledge about the dynamics of these monopoles and their interaction with phonons is still limited [8–10]. A suitable method to investigate the dynamics of the monopoles are measurements of the thermal conductivity. However, a possible monopole contribution to the heat transport is under strong debate [11–15]. Refs. 11–13 assume a phonon-dominated heat transport in zero field and a field-induced suppression of κ_ph by some field-dependent scattering mechanisms of phonons by magnetic excitations. Ref. 13 attributes a low-field decrease of $\kappa(H)$ to a possible magnetic contribution but the description within the Debye-Hückel theory fails which is interpreted to be a lack of evidence for monopole heat transport. In Refs. 14, 15, the interpretation differs and is based on a comparative study of $(Dy_{1-x}Y_x)_2Ti_2O_7$ with $x = 0$, 0.5, and 1. It is found that, in the high-field range above about 1.5 T, a field-induced suppression of $\kappa_{\mathrm{ph}}(H)$ is present for both, the spin ice $Dy_2Ti_2O_7$ and the highly dilute $(Dy_{0.5}Y_{0.5})_2Ti_2O_7$ in which spin-ice behavior is essentially suppressed [16, 17]. In the pure $Dy_2Ti_2O_7$, however, an additional low-field decrease of $\kappa(H)$ is observed. The anisotropic field dependence and the hysteresis behavior clearly correlate with the spin-ice physics. All these findings evidence a sizable κ_{mag} in zero field, which is successively suppressed by an external magnetic field due to the field-induced suppression of the monopole mobility. Experimental indication for a zero-field monopole contribution to the heat transport has also been proposed from an analysis of $\kappa(T)$ of $Ho_2Ti_2O_7$ at different magnetic fields [18]. However, the magnitude of κ_{mag} estimated for $Ho_2Ti_2O_7$ is more than an order of magnitude smaller than κ_{mag} of $Dy_2Ti_2O_7$. To address the question if the monopoles contribute to the thermal conductivity of spin ice, in this thesis a detailed comparative study of the different thermodynamic properties of $Ho_2Ti_2O_7$, $Dy_2Ti_2O_7$ and the corresponding 50% dilute reference materials is performed to clarify the influence of magnetic excitations on the heat transport. The measurements are accomplished at temperatures ranging from 0.3 to 10 K and magnetic fields up to 7 T using custom setups. In addition, the thermal conductivity of the dilution series $(Dy_{1-x}Y_x)_2Ti_2O_7$ for various x is obtained in order to get a more quantitative verification of the monopole contribution to the heat transport. A special emphasis is also put on the low-field hysteresis and relaxation phenomena observed in the thermal conductivity of $Dy_2Ti_2O_7$ at lowest temperature. It is studied in how far equilibration states are realized.

The long-predicted residual entropy for spin ice [5, 6] has been expanded to a generalized Pauling approximation for dilute spin ice [19] where the magnetic Dy^{3+} or Ho^{3+} ions are partly replaced by non-magnetic elements. This generalization has been demonstrated by first studies [19]. But recently, an absence of Pauling's residual entropy S_{P} in $Dy_2Ti_2O_7$ has been reported based on measurements of the specific heat over timescales of 10^4 s [20]. To address this discrepancy, the temperature- and field-dependent change of entropy of the dilution series $(Dy_{1-x}Y_x)_2Ti_2O_7$ with $x = 0$–0.75 is studied by means of the specific heat and the magnetocaloric effect in a temperature range from 0.3 to 30 K. Additional information about the low-temperature thermal equilibration of the systems is gained. Furthermore, Monte Carlo data on the magnetic specific heat and entropy of dilute spin ice have been published [21] which are quantitatively compared to the obtained experimental results.

This thesis is structured as follows. First, a brief overview of the theoretical and experimental work is given in Chap. 2 and 3. In Chap. 4, the spin-ice materials are introduced and the most important findings on these systems are summarized. The sample characterization of the spin-ice compounds is presented in Chap. 5. A comparative study of the spin-ice compounds $Ho_2Ti_2O_7$ and $Dy_2Ti_2O_7$ is performed in Chap. 6 followed by a detailed study on the heat transport and specific heat of dilute spin ice $(Dy_{1-x}Y_x)_2Ti_2O_7$ in Chap. 7 for different directions of the applied magnetic field. A summary of this work is followed by the appendix where the study on the quasi 1D Ising-chain system in transverse magnetic field of the diploma thesis is continued by measurements of the magnetization.

2 Theory

This chapter gives an introduction into the basic concepts and models that are employed in the discussions of the spin-ice systems. A broad overview about conventional mechanisms established in literature is given, and some important basic relations are quoted. More detailed descriptions and further information can be found in literature [16, 22–36].

2.1 Specific heat

The specific heat is one of the fundamental thermodynamic properties. It can provide insights into excitations and phase transitions of solids, gases and fluids. The molar specific heat at a constant volume V or pressure p is given by [24]

$$c_V = N_\mathrm{A}/N \left.\frac{\partial U}{\partial T}\right|_V \qquad c_p = N_\mathrm{A}/N \left.\frac{\partial U}{\partial T}\right|_p \tag{2.1}$$

with the number of particles N, the Avogadro constant N_A and the internal energy U. In a real experiment, it is very difficult to keep the volume of a solid constant and that is why c_p is the experimentally accessible property. However, the relative difference between c_p and c_V is smaller than 1% in solids for $T < 300$ K. Thus, in most cases it is not differentiated between both properties. The total differential of the internal energy $U = U(S, V, N)$ of a system is

$$\mathrm{d}U = T\,\mathrm{d}S - p\,\mathrm{d}V + \mu\,\mathrm{d}N \tag{2.2}$$

with the entropy S, the temperature T, and the electrochemical potential μ. From Eq. (2.2), the relation between c_p and the entropy S is given by

$$c_p = \frac{N_\mathrm{A}}{N} \left.\frac{\partial U}{\partial T}\right|_p = \frac{N_\mathrm{A}}{N} T \left.\frac{\partial S}{\partial T}\right|_p . \tag{2.3}$$

The entropy S is obtained by temperature integration via

$$S = \frac{N_\mathrm{A}}{N} \int\limits_0^T \frac{c_p(T')}{T'} \mathrm{d}T'. \tag{2.4}$$

The specific heat measures the sum of all thermal excitations of a system whereas a separation of the single contributions can be very difficult. However, elementary excitations like phonons or magnons show characteristic temperature dependencies that allow a distinction. The phononic contribution to the specific heat can be either estimated by models, *e.g.* the Debye model, or by measurements of non-magnetic reference materials.

2.1.1 Phonon contribution

The law of Dulong-Petit uses a classical Ansatz and yields a temperature-independent molar specific heat of

$$c_V = \frac{f}{2} N_\mathrm{A} k_\mathrm{B} \tag{2.5}$$

where f are the degrees of freedom. Thus the molar specific heat is obtained via $c_V = 3N_\mathrm{A}k_\mathrm{B} = 3R$ with the general gas constant $R = 8.31$ J/mol K.

Quantum mechanical models are applied to calculate the specific heat in the low-temperature regime. The models invented by A. Einstein and P. Debye are based on the same ansatz. Both models use the Ansatz for the phonons to be harmonic oscillators whose internal energy can be derived via [37]

$$U = \int D(\omega)\langle n(\omega)\rangle \hbar\omega \mathrm{d}\omega \tag{2.6}$$

with density of states $D(\omega)$ and $\langle n(\omega)\rangle$ as the thermal population value of a 1-dimensional oscillator with frequency ω.

Within the Debye model, an averaged isotropic linear dispersion relation $\omega = v_\mathrm{s}k$ is assumed with the average sound velocity v_s. Then, the density of states in 3 dimensions is given by $D(\omega) = V\omega^2/2\pi^2 v_\mathrm{s}^3$ with the volume V of the solid. The molar specific heat is obtained via [24]

$$c_\mathrm{V} = 9R\left(\frac{T}{\Theta_\mathrm{D}}\right)^3 T^3 \int_0^{\Theta_\mathrm{D}/T} \frac{x^4 \mathrm{e}^x}{(\mathrm{e}^x - 1)^2}\,\mathrm{d}x \tag{2.7}$$

with $x = (\hbar\omega)\,/\,(k_\mathrm{B}T)$ and the Debye temperature Θ_D. The integral in Eq. (2.7) can only be solved numerically and for low temperatures ($T \ll \Theta_\mathrm{D}$) the equation converges to the famous T^3-dependence of the lattice contribution to the specific heat

$$c_\mathrm{V} = \frac{12\pi^4}{5} R \left(\frac{T}{\Theta_\mathrm{D}}\right)^3 = \beta T^3. \tag{2.8}$$

For high temperatures ($T \gg \Theta_\mathrm{D}$), Eq. (2.7) yields the classical Dulong-Petit formula $c_\mathrm{V} = 3R$.

In the low-temperature range ($T \ll \Theta_\mathrm{D}$), the Debye model yields a good description of the phononic specific heat of solids. Here, the long-wavelength acoustic phonons are mostly populated which show a nearly linear dispersion. However, systems that reveal flat optical phonon branches are not well described [24, 37, 38]. These flat optical phonon branches (ω is almost constant) are often approximated by the Einstein model in which the phononic contribution is estimated by considering N oscillators with the same frequency ω. Thus, the internal energy from Eq. (2.6) is given by [24]

$$U = 3N\langle n\rangle\hbar\omega = \frac{3N\hbar\omega}{e^{\hbar\omega/k_\mathrm{B}T} - 1}. \tag{2.9}$$

The factor 3 accounts for the three degrees of freedom of every single oscillator. By applying Eq. (2.3), the specific heat is obtained via [24]

$$c_V = \left(\frac{\partial U}{\partial T}\right)_V = 3N_\mathrm{A}k_\mathrm{B}\left(\frac{\hbar\omega}{k_\mathrm{B}T}\right)^2 \frac{e^{\hbar\omega/k_\mathrm{B}T}}{e^{\hbar\omega/k_\mathrm{B}T} - 1}. \tag{2.10}$$

In the high-temperature limit, the Einstein model is also equivalent to the law of Dulong-Petit.

2.1.2 Electronic contribution

The electronic contribution to the specific heat can be obtained from considerations of the free electron gas in a solid. The molar specific heat of the free electron gas is given by

$$c_\mathrm{el} = \frac{R\pi^2}{2}\frac{T}{T_\mathrm{F}} = \gamma T \tag{2.11}$$

where T_F is the Fermi temperature. The total specific heat $c_\mathrm{tot} = c_\mathrm{ph} + c_\mathrm{el}$ in the low-temperature limit $T \ll \Theta_\mathrm{D} \ll T_\mathrm{F}$ is often expressed in terms of

$$\frac{c_\mathrm{tot}}{T} = \gamma + \beta T^2 \tag{2.12}$$

where β follows from Eq. (2.8).

2.1.3 Schottky anomaly

The Schottky anomaly is an effect which results from the thermal population of higher-lying discrete energy levels. The internal energy U of N non-interacting particles with energy levels E_i with degeneracy g_i is given by

$$U = N\frac{\sum\limits_i E_i\ g_i \exp(-E_i/k_\mathrm{B}T)}{Z}. \tag{2.13}$$

with the partition sum $Z = \sum_i g_i \exp(-E_i/k_\mathrm{B}T)$. The molar specific heat of a systems of non-interacting particles with discrete energy levels follows from Eq. (2.13) by $c = N_\mathrm{A}/N \frac{\partial U}{\partial T}$ to be

$$c_\mathrm{sch} = \frac{N_\mathrm{A}}{k_\mathrm{B}T^2}\frac{\sum\limits_i E_i^2\ g_i \exp(-E_i/k_\mathrm{B}T)Z - \left(\sum\limits_i E_i\ g_i \exp(-E_i/k_\mathrm{B}T)\right)^2}{Z^2} \tag{2.14}$$

In the case of a two-level system, where the first g_1-fold degenerate excited state is separated from the g_0-fold degenerate ground state by the energy gap ΔE, Eq. (2.14) simplifies to

$$c_\mathrm{2,sch} = \frac{N_\mathrm{A}\Delta E^2}{k_\mathrm{B}T^2}\frac{g_1}{g_0}\frac{\exp(-\Delta E/k_\mathrm{B}T)}{\left(1 + \frac{g_1}{g_0}\exp(-\Delta E/k_\mathrm{B}T)\right)^2}. \tag{2.15}$$

2.2 Thermal conductivity

The thermal conductivity κ of a solid is given by

$$\vec{j} = -\underline{\underline{\kappa}}\,\vec{\nabla}T \tag{2.16}$$

with the heat current $\vec{j}$ and the temperature gradient $\vec{\nabla}T$ over the solid. The negative sign is related to the fact that the heat flows from the hot end to the cold end of the sample. In general, the thermal conductivity $\underline{\underline{\kappa}}$ is a 2nd-order tensor which reduces to a scalar κ in an isotropic system.

If the kinetic gas theory is applied, the thermal conductivity is determined by heat carrying (quasi-)particles and it can be expressed via [24]

$$\kappa = \frac{1}{d}cv\ell \tag{2.17}$$

where d denotes the dimensionality, c the specific heat, v the group velocity and $\ell = v\tau$ the mean free path of the heat carrying quasi-particles (τ is the relaxation time). In most cases two kinds of excitations are responsible for the heat transport: phonons and electrons. The theoretical description is usually based on the Debye model for phonons, and on electronic gas theory for the electrons.

2.2.1 Phonon contribution

The heat carrying quasiparticles in an insulating crystal lattice are phonons. The phononic specific heat is given by the Debye formula from Eq. (2.7). Using the Debye model, the phononic contribution to the thermal conductivity follows to be

$$\kappa_{\mathrm{ph}} = \frac{k_{\mathrm{B}}}{2\pi^2 v}\left(\frac{k_{\mathrm{B}}}{\hbar}\right)^3 T^3 \int_0^{\Theta_{\mathrm{D}}/T} \frac{x^4 \mathrm{e}^x \tau(\omega, T)}{(\mathrm{e}^x - 1)^2}\,\mathrm{d}x \tag{2.18}$$

with the mean sound velocity v. The temperature and frequency dependent total scattering rate is $\tau^{-1}(\omega, T) = v/\ell$. With assumption that the different scattering processes act independently, one can write τ^{-1} as a sum of the different scattering rates

$$\tau^{-1} = \tau_{\mathrm{um}}^{-1} + \tau_{\mathrm{pt}}^{-1} + \tau_{\mathrm{bd}}^{-1} + \tau_{\mathrm{mag}}^{-1} + \dots \tag{2.19}$$

Many different scattering rates are found in literature. The scattering rates from Eq. (2.19) have the following meanings:

- Umklapp scattering:

  $$\tau_{\mathrm{um}}^{-1} = U\omega^2 T \exp\left(-\frac{\Theta_{\mathrm{D}}}{uT}\right) \tag{2.20}$$

  This term describes the Umklapp scattering where U and u are free parameters. The temperature range where the Umklapp mechanism sets in is defined by the parameter u. With raising temperature, the number of phonons rapidly increases and, thus, this scattering mechanism becomes more and more important.

- Boundary scattering:

  $$\tau_{\mathrm{bd}}^{-1} = v/L \tag{2.21}$$

  This mechanism describes the reflection of phonons at the crystal surface. It is obtained via $\tau_{\mathrm{bd}}^{-1} = v/L$ with the characteristic sample length L. At very low temperatures, this scattering process is dominant in high-quality crystals and hence the mean free path ℓ is only limited by the sample length $\ell \approx L$.

- Point defect scattering:

  $$\tau_{\mathrm{pt}}^{-1} = P\omega^4 \tag{2.22}$$

  In this case τ_{pt}^{-1} is the scattering of phonons on point defects with P as a free fitting parameter and the frequency ω. The frequency dependency of this scattering mechanism can be qualitatively understood. The probability of long wavelength phonons being scattered on point defects is less than of phonons with shorter wavelengths.

- Scattering with magnetic excitations:

  $$\tau_{\mathrm{mag}}^{-1} = M\omega^4 T^2 C_{\mathrm{mag}}(T) \tag{2.23}$$

  This term describes scattering on magnetic excitations around a magnetic transition [39, 40] and results in a suppression of $\kappa(T)$ around the transition temperature. M is a free parameter and $C_{\mathrm{mag}}(T)$ is the temperature-dependent magnetic specific heat, which reveals a peak around the magnetic transition.

2.2.2 Electron contribution

The electronic specific heat is proportional to $k_{\mathrm{B}}T$, see Eq. (2.11). The kinetic gas theory in Eq. (2.17) for the thermal conductivity of quasiparticles is also valid for electronic heat transport. The Fermi velocity v_{F} is applied for the electrons and this yields [25]

$$\kappa_{\mathrm{el}} = \frac{1}{3} c_{\mathrm{el}} v_{\mathrm{F}} \ell = \frac{\pi^2 n k_{\mathrm{B}} T \ell}{3 m v_{\mathrm{F}}} \tag{2.24}$$

where n is the electron density, $c_{\mathrm{el}} = 1/2\, \pi^2 n k_{\mathrm{B}}\, T/T_{\mathrm{F}}$ is the specific heat of the Fermi gas and the Fermi temperature $T_{\mathrm{F}} = \epsilon_{\mathrm{F}}/k_{\mathrm{B}}$. The Fermi energy ϵ_{F} can be obtained via $\epsilon_{\mathrm{F}} = 1/2\, m v_{\mathrm{F}}^2$.

2.2.3 Heat transport by magnetic excitations

In addition to the heat transport by phonons and electrons, which is already well understood, there is a strong interest in finding experimental and theoretical evidence for heat transport by magnetic excitations predicted in 1936 [41]. The analysis of the magnetic heat transport focused on the excitations and the scattering processes by *e.g.* defects, phonons and electrons. Classical spin wave magnetic heat transport was found for ferrimagnetic yttrium-iron-garnet [42], in magnetically ordered systems [43] and later in various low-dimensional (quantum) materials [44–46]. A detailed summary of heat conduction in low-dimensional quantum magnets can be found in Ref. 47. The basic physics which determines the T-dependence of κ is calculated via

$$\kappa = \frac{1}{d} \frac{1}{(2\pi)^d} \int c_k v_k l_k dk \tag{2.25}$$

with the dimensionality d of the system, the specific heat c_k, the velocity v_k and the mean free path l_k of a particle with wave vector k. From Eq. (2.25), a low-temperature result can be derived for the case of 1D and 2D magnetic systems

$$\kappa_{\mathrm{mag}} \propto l_{\mathrm{mag}} f(T), \tag{2.26}$$

with the magnetic mean free path l_{mag} based on the assumption that $l_{\mathrm{mag}} \equiv l_k$ as l_k hardly varies as a function of momentum in the relevant energy range and $f(T)$ reflects the characteristics of the considered spin system as a function of temperature.

Concerning the spin-ice compounds $(\mathrm{Ho}_{1-x}\mathrm{Y}_x)_2\mathrm{Ti}_2\mathrm{O}_7$ and $(\mathrm{Dy}_{1-x}\mathrm{Y}_x)_2\mathrm{Ti}_2\mathrm{O}_7$, the aspect of a possible heat transport by magnetic excitations is under strong debate. It is discussed whether the magnetic monopoles, which are the basic excitations in the spin-ice systems, contribute to the heat transport or not. A detailed study on the magnetic contribution to the heat transport will be presented in Chap. 6 and 7.

2.3 Demagnetization

In the analysis of the spin-ice compounds $\mathrm{Ho}_2\mathrm{Ti}_2\mathrm{O}_7$ and $\mathrm{Dy}_2\mathrm{Ti}_2\mathrm{O}_7$ demagnetization effects have to be taken into account [14, 15, 17, 18, 48, 49]. In many cases demagnetization effects are neglected. The spin-ice materials, however, exhibit large magnetic moments of about $\mu = 10\mu_{\mathrm{B}}$ per magnetic ion and, hence, these effects can become important. The demagnetization effect is strongly anisotropic with respect to the geometry of the sample (shape-anisotropic). Concerning the thermodynamic measurements of the spin-ice compounds, demagnetization effects are taken into account if the magnetic field is applied perpendicular to the longest dimension of the sample. In such a case, the effective magnetic field within the sample can deviate by 10% in maximum from the applied external field for standard sample dimension of about $3 \times 1 \times 1\ \mathrm{mm}^3$. By applying the magnetic field along the longest dimension of the sample, demagnetization effects are neglected because their influence is basically not visible. The demagnetized field within the sample accounts for at least 98-99% of the applied external field. Detailed descriptions of the demagnetization effect can be found in literature [16, 50].

3 Experimental

This chapter introduces the cryogenic setups, the sample holders and the measurement techniques which were applied to obtain the magnetization, specific heat, magnetostriction, thermal conductivity and the magnetocaloric effect data discussed in this thesis. The experimental data were exclusively measured in custom home-built devices.

3.1 Cryogenic environments

The Heliox VL, produced by Oxford Instruments, is a ^{3}He system which can be installed in cryogenic environments with different magnets and allows home-built sample holders to be operated in a high vacuum and in a temperature range from ≈ 0.25 K up to 30 K [51]. Hereby, the ^{3}He is captured in a closed cycle and the base temperature (≈ 0.25 K) is reached by vapor pumping within the closed system.

Fig. 3.1 shows the Heliox VL insert with the features marked by arrows that are required to reach base temperature. The sample holders are attached at the bottom of the insert whereby a distance of 185 mm to the magnetic-field center has to be taken into account for the standard cryostats. The sliding seal allows to slowly insert the system into a cryostat. By pumping the sample chamber (closed with a cone), high vacuum is reached which is essential for specific heat and thermal conductivity measurements. However, a small amount of ^{4}He is used as contact gas

Figure 3.1: ^{3}He refrigerator with sorption pump – Heliox VL

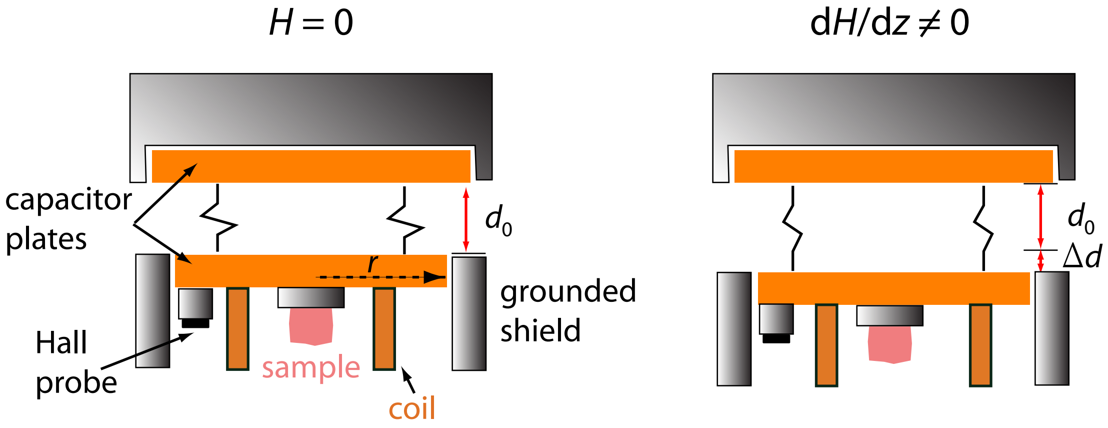

Figure 3.2: Schematic drawing of the Faraday magnetometer. Left: in the absence of a magnetic field, the sample undergoes no force and d_0 remains constant. Right: a gradient $\mathrm{d}H/\mathrm{d}z \neq 0$ leads to a mechanical deflection Δd.

within this chamber in order to quickly cool down the system to 4 K where the gas is pumped by a Carbon sorb. Liquid ^{4}He encloses the HELIOX VL and is evaporated by pumping through the ^{4}He pipe. The main cooling power is located at the λ-plate which reaches a temperature of about 1.8 K. Due to this cooling, the gaseous ^{3}He condenses and is accumulated in the ^{3}He pot. Base temperature is then reached by minimizing the vapor pressure of the liquid ^{3}He in the pot by pumping of the ^{3}He sorb. The cooling power is provided until the ^{3}He is completely evaporated which leads to an operation time of approximately 20 h at base temperature (0.25 K). Temperatures in the range of $0.25\ \mathrm{K} < T \leq 1.7\ \mathrm{K}$ are adjusted by slightly heating the ^{3}He sorb and thereby reducing its pumping performance. The vapor pressure is increased and this results in higher ^{3}He pot temperatures. For $T > 1.7$ K, the ^{3}He pot is directly heated against the cooling power of the λ-plate. Due to the change in the heating mode and the anomalies of ^{4}He at low temperatures and low pressure, the temperature stability of the HELIOX VL strongly varies in the covered temperature range. Around 2 K, the stability has a minimum which can cause problems in the thermal conductivity and specific heat measurements requiring stable conditions. When the ^{3}He is completely evaporated and stored in the sorb, base temperature can be reached again by heating the sorb such that the adsorbed ^{3}He gas is released. This is accompanied with an increase of the ^{3}He-pot temperature to ≈ 2 K and, hence, of the sample holder.

3.2 Magnetization

The magnetization data are obtained in a home-built Faraday magnetometer. The magnetometer can be installed into the ^{3}He system Heliox VL which operates as the temperature controller. Design drawings and details of the functionality can be found in Refs. 52–54. Since the completion of the Faraday magnetometer in 2011, it needed a lot of effort and various measurements techniques were applied to finally obtain high-quality data. By comparing the magnetization data to corresponding data of a commercial Superconducting Quantum Interference Device (SQUID) setup [55], that covers the temperature range from 2 K up to 400 K, the technique could be improved until only minimal deviations were obtained [52, 53].

The functionality of the Faraday magnetometer is shown in a schematic drawing in Fig. 3.2. In zero magnetic field and at constant temperature, the distance d_0 between the two capacitor plates connected via two copper beryllium (CuBe) springs is stabilized and calculated via $d_0 = \epsilon_0 \pi r^2 1/C_0$ with the starting capacity C_0. The capacity is measured with a commercial AC capacitance bridge (AH2550/2500 by Andeen Hagerling) that operates at a fixed frequency of 1 kHz. Here, ϵ_0 is the vacuum permittivity and r is the radius of the smaller capacitor plates which is shielded by a grounded frame to avoid stray fields, see Fig. 3.2. Within a magnetic-field gradient $\mathrm{d}H/\mathrm{d}z \neq 0$, a sample with the magnetic moment m experiences a force $F = m\,\mathrm{d}H/\mathrm{d}z$. This force leads to a deflection Δd that relates to an induced change of the capacitance

$$\Delta d = \epsilon_0 \pi r^2 (\frac{1}{C} - \frac{1}{C_0}). \tag{3.1}$$

As can be seen in Fig. 3.2, the sample is located in the center of an additional coil which can create a magnetic moment $m_\mathrm{c} = nI \cdot A$ with the winding number n, the current I applied by a Keithley 2400/6220 current source and the area A of the coil. The generated m_c compensates or enforces the deflection Δd. Due to the linearity $F = k\Delta d$, an $m_\mathrm{c,ex}$ is extrapolated to fully compensate the magnetic moment of the sample. It turned out that this approach yields the best results [52–54] and it is named "compensation method". In the experiment, the magnetic field gradient is achieved by simply adjusting the Heliox VL to be located above the homogeneous field center. This distance from the center has to be adjusted such that a measurable deflection can be detected in the field gradient, but the maximum accessible field is still large enough. A distance of 2–7 cm was found to be applicable. The magnetization data of this thesis were measured with a distance of 5 cm to the field center which decreases the maximum field by approximately 10% in the operated magnets. The absolute value of the magnetic field within the gradient $\mathrm{d}H/\mathrm{d}z \neq 0$ is measured by a Hall effect probe model LHP-NU [56] which is attached at the same level as the sample, see Fig. 3.2.

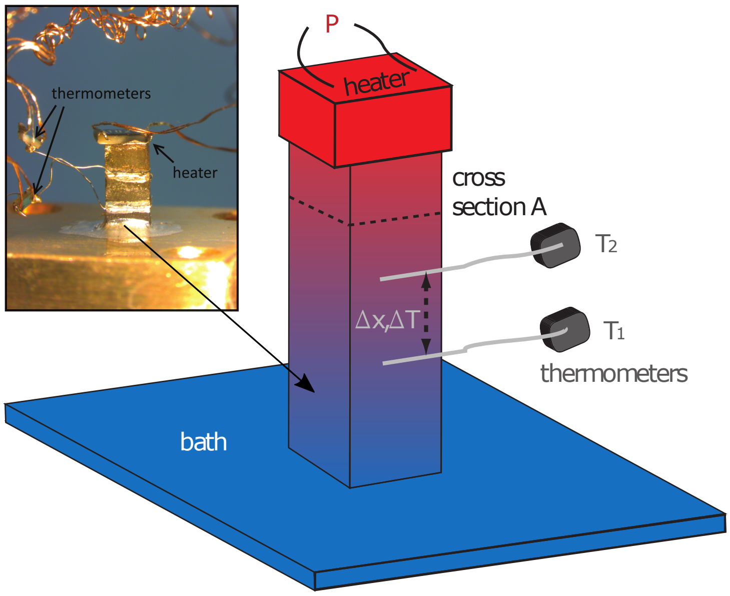

Figure 3.3: Schematic drawing of a sample assembled for a steady-state thermal-conductivity measurement. Inset: real assembled sample.

3.3 Thermal conductivity

The thermal conductivity κ of a sample is a physical transport property which can be measured in an experiment using different methods. The thermal conductivity data shown and discussed in this thesis are produced by applying the steady-state method. Information on different methods can be found in literature [57–61]. Fig. 3.3 shows a schematic drawing of a sample which is prepared for a steady-state thermal-conductivity measurement. A heater is fixed on the top side of the bar-shaped sample which is connected to a thermal bath on the lower side. By applying a power P to the heater, a heat current $\vec{j}$ is produced which flows through the cross section A along the longest dimension of the sample. The resulting temperature difference $\Delta T = T_2 - T_1$ is assumed to be linear within the sample which is an reasonable approximation. It is measured by two thermometers at different levels of the sample. In the experiment, the actual sample temperature is estimated via $T_{\text{sample}} = \frac{1}{2}(T_1 + T_2)$. In order to ensure a measurable variation ΔT and a reliable determination of T_{sample}, the thermometers are attached at approximately one third and two thirds of the sample. Afterwards, Δx is measured under a microscope with an applicable scale.

According to Eq. (2.16), the thermal conductivity of a solid is given by

$$\kappa = \frac{P}{A}\frac{\Delta x}{\Delta T} \tag{3.2}$$

where $P/A = j$ is the heat current. It is assumed that $\mathrm{d}T/\mathrm{d}x$ is constant within the sample. The sample geometry (Δx,A) and the applied power P can directly

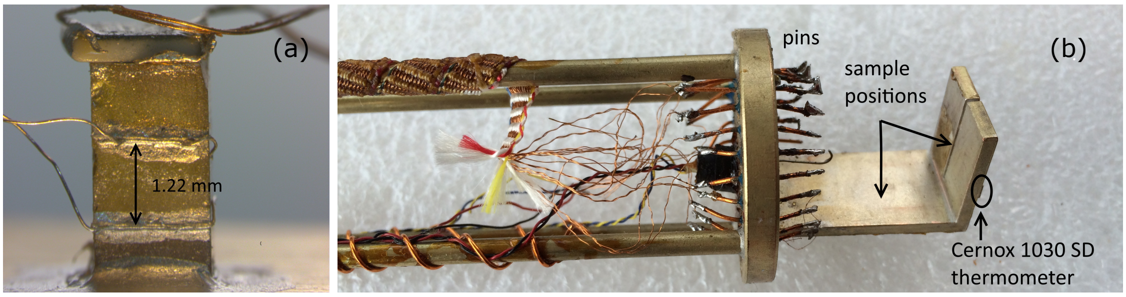

Figure 3.4: Panel (a): expanded view of a $Dy_2Ti_2O_7$ sample with dimension $3 \times 1.7 \times 1.2$ mm^3 prepared for a steady-state thermal-conductivity measurement at low temperatures. The heat gradient ΔT is produced by a SMD heater (1 or 10 kΩ at room temperature) mounted on top of the sample. Panel (b): L-shaped transport holder that allows to orient the sample with respect to the external magnetic field.

be measured, but an exact determination of temperature difference ΔT is quite challenging. Two different approaches are applied to measure ΔT. In the high-temperature regime for 5 K $\leq T \leq$ 300 K, a thermocouple is used which consists of a chromel and a gold-iron alloy (0.07%Fe). Details about this technique can be found in Refs. 16, 32. However, the spin-ice physics only occurs in the low-temperature regime well below 5 K. Hence, the thermal conductivity measurements is obtained by another approach which is introduced in the following.

3.3.1 Low-temperature sample wiring

All measurements were performed on oriented single crystals and most suitable for the steady-state method are bar-shaped samples with dimensions of $\approx 3 \times 1.5 \times 1$ mm^3. Fig. 3.4 (a) shows a detailed view of an oriented single crystal $Dy_2Ti_2O_7$ with dimensions $3 \times 1.7 \times 1.2$ mm^3 that is completely wired for a steady-state thermal-conductivity measurement at lowest temperatures. The typical Δx varies between 0.8 and 1.7 mm. The bottom of the sample is connected to a big copper block that operates as the thermal bath. This block is fixed on the L-shaped transport sample holder shown in Fig. 3.4 (b). Its L-shape allows to mount the sample at different orientations with respect to the external applied magnetic field direction. Fixing the sample on the bottom part leads to an applied magnetic field along the longest dimension of the sample parallel to the heat current, *i.e.*, $\vec{j} \,||\, \vec{H}$. The lateral part of the holder is used to orient a magnetic field perpendicular to the heat current, *i.e.*, $\vec{j} \perp \vec{H}$, along another crystallographic direction. As can be seen in Fig. 3.4 (a), platinum wires with a diameter of 0.05 mm, produced by Heraeus [62], are attached to the sample at approximately one third and two thirds

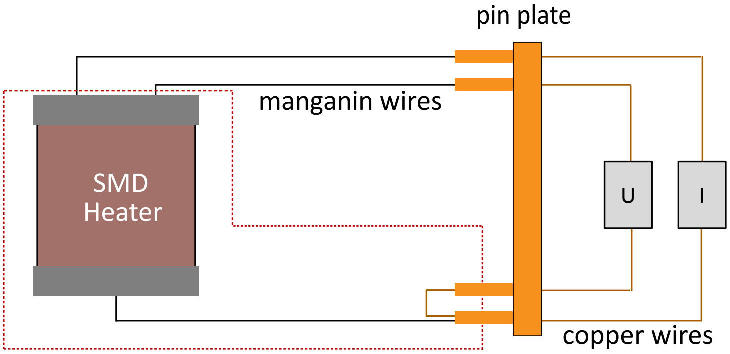

Figure 3.5: Schematic drawing of the pseudo 4-wire technique used to wire the SMD heater in a thermal-conductivity measurement.

of the longest dimension. Platinum is used due to its high thermal conductance (for measuring ΔT) and its considerably high flexibility (even compared to copper wires). This flexibility eases to fix the wires to the backside of the small RuO_2 thermometers ($\simeq 0.2 \times 0.5 \times 1$ mm^3) with silver glue. These RuO_2 thermometers are applied for the low-temperature thermal-conductivity measurements ($0.25\ \mathrm{K} \lesssim T \lesssim 10\ \mathrm{K}$) and exhibit a resistance of 5.3 kΩ at room temperature. Manganin wires electrically connect the RuO_2 thermometers and the SMD heater to the pins of the sample holder, see Fig. 3.4 (a). Here, manganin is utilized due to its sufficient electrical conductivity but very low thermal conductivity. Thus, the majority of the heat provided by the SMD heater flows homogeneously through the sample into the bath instead of dissipating through the attached wires. This effect is even enhanced by spooling comparably long wires to connect the heater and the RuO_2 thermometers. The accuracy of the thermometers is not affected by the growing electrical resistance because the 4-wire technique is applied.

Due to the rather high electric resistance of the manganin wires ($\simeq 60-100\ \Omega$) which electrically connect the heater, it is not possible to prevent them from producing a certain amount of heating power in the experiment. In order to account for this additional amount of heating power, a pseudo 4-wire technique is applied to wire the heater. This wiring technique is depicted in Fig. 3.5. As can be seen, the heater is wired with 3 manganin cables to the pin sheet. Then, the pin of the single connection to the heater is connected to a fourth pin with a short copper wire. This method is equivalent to the standard 4-wire resistivity measurement of the red dashed box. Consequently, the resistance of the heater and of one supply cable is measured. The idea is that half of the heat produced by the wires is transferred to the sample and the other half to the bath. Therefore, the total heating power can be calculated by the sum of the power of the heater and of one manganin cable. The magnitude of the possible error σ can be estimated via $\sigma \leq \frac{R_\mathrm{cable}}{R_\mathrm{heater}} \approx \frac{100\ \Omega}{1-70\ \mathrm{k}\Omega}$.

Adhesives

Due to different requirements for the thermal and electrical properties of the various parts which are assembled in wiring a sample for a heat-transport measurement in the low-temperature regime, it is essential to choose suitable adhesives. The choice depends on whether the sample is an insulator or metallic, on the samples' compatibility with solvents and on the required mechanical stability. The industry offers a large number of products with different properties. This is a list of the adhesives that were used for wiring the crystals:

- **Silver Glue:**
  Leitsilber G3303A Plano GmbH (silver glue) is a solvent-based glue containing silver particles [63]. It is both a good thermal and electrical conductor. In wiring a sample, it is generally applied to mount the 0.05 mm platinum wires at two levels of the crystal, as can be seen in Fig. 3.4 (a). In this process, a da Vinci Maestro Tobolsky-Kolinsky 10/0 brush [64] is utilized to bring a narrow line of silver glue onto the wires which are stretched over the sample. The spin-ice crystals are insulating and, thus, silver glue could also be employed to fix the samples to the thermal bath. Furthermore, it was partly applied to mount the SMD heater on top of the crystals. The silver glue is highly soluble by solvents like acetone which is a clear advantage. In Ref. 16, an arising mechanical instability of the spin-ice crystals mounted with Leitsilber G3303A in an external magnetic field is reported originating from an arising torque for particular field directions. However, it turned out that the stability is sufficient.

- **VGE 7031 Varnish:**
  VGE-7031 Insulating Varnish possesses electrical and bonding properties which make it an applicable adhesive for heat-transport measurements. At cryogenic temperatures, it is electrically insulating and exhibits a sufficiently large thermal conductivity of 0.062 W/mK at 4.2 K and 0.034 W/mK at 1 K [65]. The varnish can be air-dried within 1-2 hours and it can be additionally baked after assembling all parts in order to reach the maximum stability. It is completely solvable in aceton and ethanol. The VGE-7031 Insulating Varnish was partly used to mount the SMD heater on top of the samples. In the case of metallic samples, it is a convenient alternative to mount the crystals on the thermal bath.

3.3.2 Calibration of RuO_2 thermometers

The RuO_2 thermometers are calibrated in advance of every single thermal-conductivity measurement in the low-temperature regime. This is required because

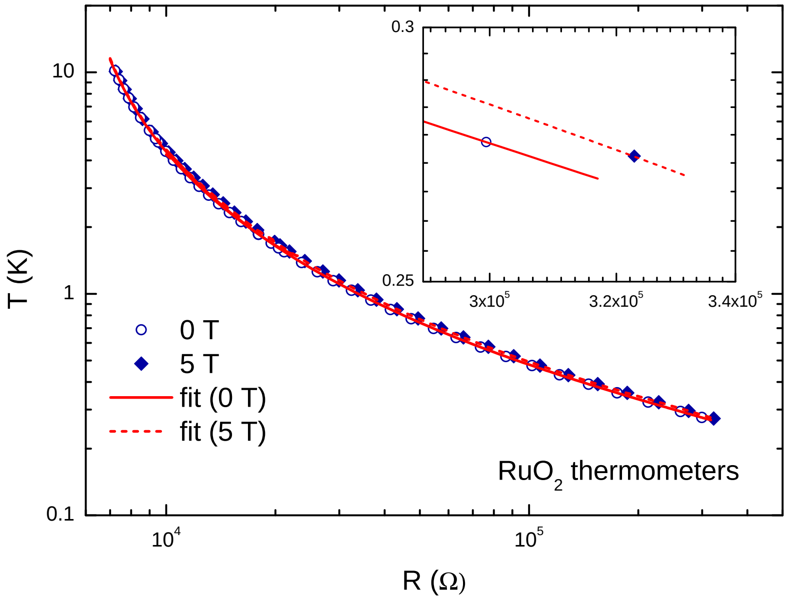

Figure 3.6: Calibration curves of the RuO$_2$ thermometers at 0 T and at 5 T together with polynomial fits. The inset shows an expanded view of the low-temperature field dependence.

their characteristics slightly change by every sample preparation and installation into the cryogenic environment. The calibration is performed in a separate run against the Cernox 1030 SD thermometer of the sample holder, see Fig. 3.4 (c). A characteristic calibration curve of the temperature T as a function of the resistance R of one RuO$_2$ thermometer is shown in Fig. 3.6. It reveals a clear magnetic-field dependence for temperatures below $\simeq 1$ K, see inset. The measured curves are fitted by polynomials of degree 5–7 (solid and dashed red lines). A linear interpolation is used to calculate the field dependence between the measured fields which is found to be a good approximation [16, 32, 66]. In addition, the quality of the calibration can be improved by separately fitting the data in the low-temperature (0.25–2 K) and in the high-temperature regime (1.6 K–10 K). Then, the calibrations have to be switched in the overlapping temperature range.

3.3.3 Measurement instruments

Several instruments are available to measure the resistances R of the thermometers and to apply a power P to the sample heater. Here, a list of the instruments applied for the thermal-conductivity measurements is given:

- **Resistance bridges**
  The Lakeshore 370 [65] is an AC resistance bridge which measures the resistance of the sample-holder thermometer and of the RuO$_2$ thermometers. The Lakeshore 370 is set to auto-range resistance and to voltage excitation mode. It turned out that a voltage excitation of 632 µV is suitable in the

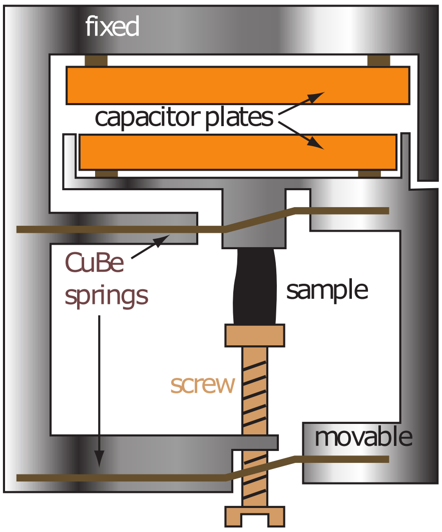

Figure 3.7: Schematic drawing of a thermal expansion/magnetostriction cell with an assembled sample adapted from Ref. 68. The fixed and the movable part are connected via CuBe springs. The length change of the sample is calculated by the measured change in the capacitance.

temperature range from 0.25 K up to about 10 K. This excitation is low enough to prevent self-heating by the thermometers and it is high enough for low-noise data up to 10 K.

- **Keithley instruments**
  A current source and a voltmeter are employed to measure the applied power to the SMD heater. It turned out that a KEITHLEY 2182 nanovoltmeter [67] and a KEITHLEY 6220 current source [67] yield the best accuracy. However, the resolution of the KEITHLEY 182 is still sufficient. The fast operation of a KEITHLEY 6220 is a clear advantage compared to a KEITHLEY 2400.

3.4 Thermal expansion and magnetostriction

The length change ΔL_i along the crystallographic axis i of a crystal can be measured as a function of the temperature (thermal expansion) or the magnetic field (magnetostriction). The most common method to detect small length changes is the capacitance dilatometry. Based on the original design in Ref. 69, different setups have been developed [68, 70, 71]. A schematic drawing of a thermal expansion/magnetostriction cell is shown in Fig. 3.7. Its design is similar to the low-temperature capacitance dilatometer which was applied to obtain the magnetostriction data in this thesis. In general, these setups consist of a fixed and a movable part which are connected via springs. The crystal is clamped with a screw between both parts and the length change ΔL can be calculated by the change in the capacitance ΔC via

$$\Delta L = \epsilon_0 \pi r^2 \left(\frac{1}{C} - \frac{1}{C_0} \right) \tag{3.3}$$

with the starting capacity C_0, the vacuum permittivity ϵ_0 and the radius r of the smaller capacitor plate which is shielded by the grounded movable part to prevent stray fields, see Fig. 3.7. In the experiment, ΔC is measured with a commercial AC capacitance bridge (AH2550/2500 by Andeen Hagerling) that operates at a fixed frequency of 1 kHz. Length changes down to 10^{-10} m can be resolved because ΔC strongly increases for small distances between the plates and due to the high resolution of the capacitance bridges. The thermal expansion coefficient α or magnetostriction coefficient λ can be calculated numerically from the length change ΔL via

$$\alpha = \frac{1}{L_0} \frac{\partial \Delta L(T,H)}{\partial T}, \qquad \lambda = \frac{1}{L_0} \frac{\partial \Delta L(T,H)}{\partial H} \tag{3.4}$$

with the initial length L_0 of the sample.

3.5 Specific heat

In Chap. 7.2, specific heat data of the dilute spin-ice materials $(\mathrm{Dy}_{1-x}\mathrm{Y}_x)_2\mathrm{Ti}_2\mathrm{O}_7$ are presented which were obtained using a custom home-built low-temperature calorimeter. This low-temperature calorimeter was built by O. Breunig during his diploma thesis [72]. The low-temperature physics of the $(\mathrm{Dy}_{1-x}\mathrm{Y}_x)_2\mathrm{Ti}_2\mathrm{O}_7$ crystals strongly vary with its dilution x and, thus, two different methods were acquired to obtain the specific heat data for all systems. The choice of the method depends on the equilibration properties. The relaxation method is a standard technique and it is applicable if the internal equilibration of the phononic and magnetic subsystems in a crystal are much faster than the equilibration to the bath. At very low temperatures $T \lesssim 0.5$ K, the specific heat of pure and weakly dilute spin ice $(\mathrm{Dy}_{1-x}\mathrm{Y}_x)_2\mathrm{Ti}_2\mathrm{O}_7$ with $x \lesssim 0.1$ has to be measured using another approach due to the long-time internal equilibration of the magnetic subsystems [11, 14, 20]. This approach is introduced in Sec. 3.5.2

3.5.1 Relaxation method

One of the standard methods to determine the specific heat of a crystal is the relaxation-time method and a schematic drawing of the experimental setup is shown in Fig. 3.8 (a). The sample is fixed on a sapphire platform by a small amount of

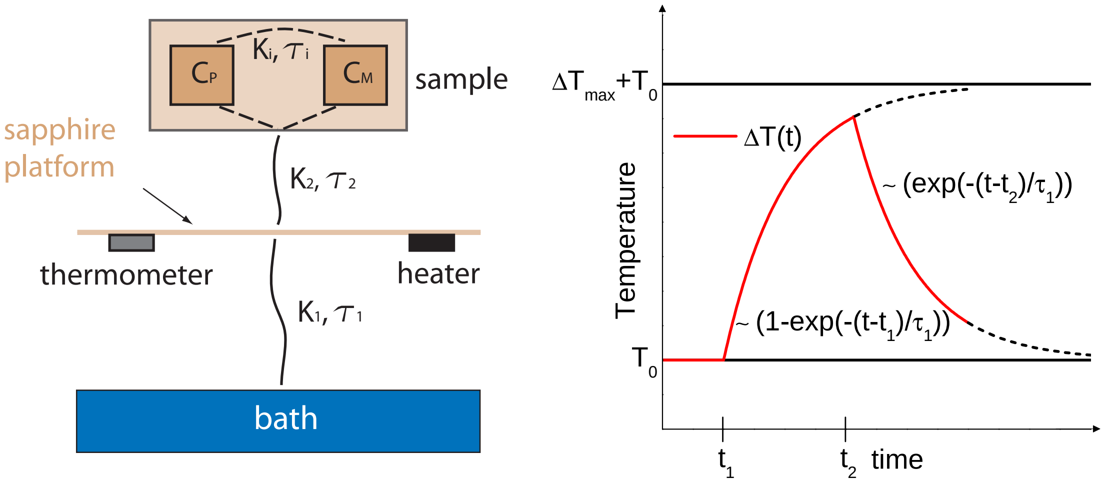

(a) (b)

Figure 3.8: Panel (a): schematic drawing of the specific heat setup adapted from Ref. 14. Panel (b): raw data of the relaxation method. At time t_1, the heater is switched on and $T(t) = \Delta T(t) + T_0$ increases. At t_2, the heater is switched off and $T(t)$ relaxes back towards T_0 with a time constant $\tau = C/K_1$.

grease (Apiezon N) which solidifies upon cooling below room temperature. Sapphire is a suitable material due to its small heat capacity but large thermal conductivity at low temperatures. K_2 denotes the coupling between the platform and the sample via the grease. A thermometer (Cernox 1030 BC) and a SMD heater ($R \simeq 27.3$ kΩ at room temperature) are mounted to the platform by VGE-7031 Insulating Varnish [65]. The whole setup has a defined coupling to the bath via a thin platinum wire with the thermal conductance K_1. Another established method to measure the specific heat is the quasi-adiabatic heat pulse method which, however, was not applied in this thesis. Details can be found in Refs. 72, 73. In contrast to the relaxation method, it requires K_1 to be as small as possible[1].

For the relaxation method, it is assumed that $K_2 = \infty$. The schematic temperature dependence of a single heat pulse as function of time is shown in Fig. 3.8 (b). Within the Heliox VL temperature controller, T_0 does not equal the bath temperature. Instead, T_0 is stabilized by an offset power P_0 of the heater which yields a faster temperature control of the sample temperature and lowers the impact of fluctuations of the Heliox VL. When the stabilization criteria at T_0 are fulfilled, the heating power is increased at t_1 by applying an additional power ΔP to the heater. Hence, $T(t) = \Delta T(t) + T_0$ rises. At time t_2, the additional power ΔP is removed and $T(t)$ relaxes back towards T_0. With $K_2 = \infty$ and $T = T_{\text{sample}} = T_{\text{platform}}$, it

---

[1] Note that a finite K_1 is required to provide a finite cooling power.

follows from the first law of thermodynamics, that

$$\Delta Q = C\,\mathrm{d}T. \tag{3.5}$$

From Eq. (3.5), a differential equation can be extracted and it is given by

$$C\,\mathrm{d}T = \Delta P\mathrm{d}t - K_1(T - T_0)\mathrm{d}t. \tag{3.6}$$

Eq. (3.6) is solved by $\Delta T(t)_{\mathrm{heat}}$ and $\Delta T(t)_{\mathrm{cool}}$ for the heating and relaxation curves, namely [73]

$$\Delta T(t)_{\mathrm{heat}} = \Delta P/K_1(1 - \exp(-(t - t_1)/\tau_1)) \tag{3.7}$$

$$\Delta T(t)_{\mathrm{cool}} = \Delta P/K_1 \exp(-(t - t_2)/\tau_1). \tag{3.8}$$

In the limit of $t \to \infty$, the steady-state equation yields $\Delta P/K_1 = \Delta T(t \to \infty) = \Delta T_{\mathrm{max}}$. The relaxation time τ_1 is related with the heat capacity via $\tau_1 = C/K_1$.

The raw data of the heating and relaxation curves are fitted separately which yields K_1 and τ_1. Note that reliable results are only obtained if τ_1 determined from the heating and from the relaxation curve are identical. The heat capacity of the addenda is measured in a separate run and is subtracted from the data in the same way as the heat capacity of the Apiezon N grease which is known from literature [74, 75]. In the data analysis, so-called τ_2 effects can also be taken into account which arise from an imperfect coupling of the sample to the platform via K_2 [73]. In general, τ_2 is defined by the coupling of the sample to the platform via the low-temperature Apiezon N grease. In order to minimize these effects in the experiment, it has to be ensured that the sample is properly attached with the grease and with a large cross section on the platform.

3.5.2 Heat-flow method

For $T \lesssim 0.5$ K, long-term internal equilibration has been observed in $\mathrm{Dy_2Ti_2O_7}$ [11, 14, 20]. This is related to the fact that the relaxation times τ_i between the different sub-systems C_{P} (phononic) and C_{M} (magnetic) and, especially within C_{M} become very large compared to the equilibration with the platform τ_2 and with the bath τ_1, see Fig. 3.8 (a). In order to account for these long-term equilibration processes, a new approach has been developed which was named "constant heat-flow method" [14]. It analyzes the heating curves over long timescales and is equivalent to the method applied by Pomaranski *et al.* [20, 76] in which the specific heat is derived from the long-time temperature relaxation curves. The constant heat-flow method only differs from the relaxation method by the fact that the raw data $\Delta T(t) = T(t) - T_0$ are recorded for a longer period of time and an exponential

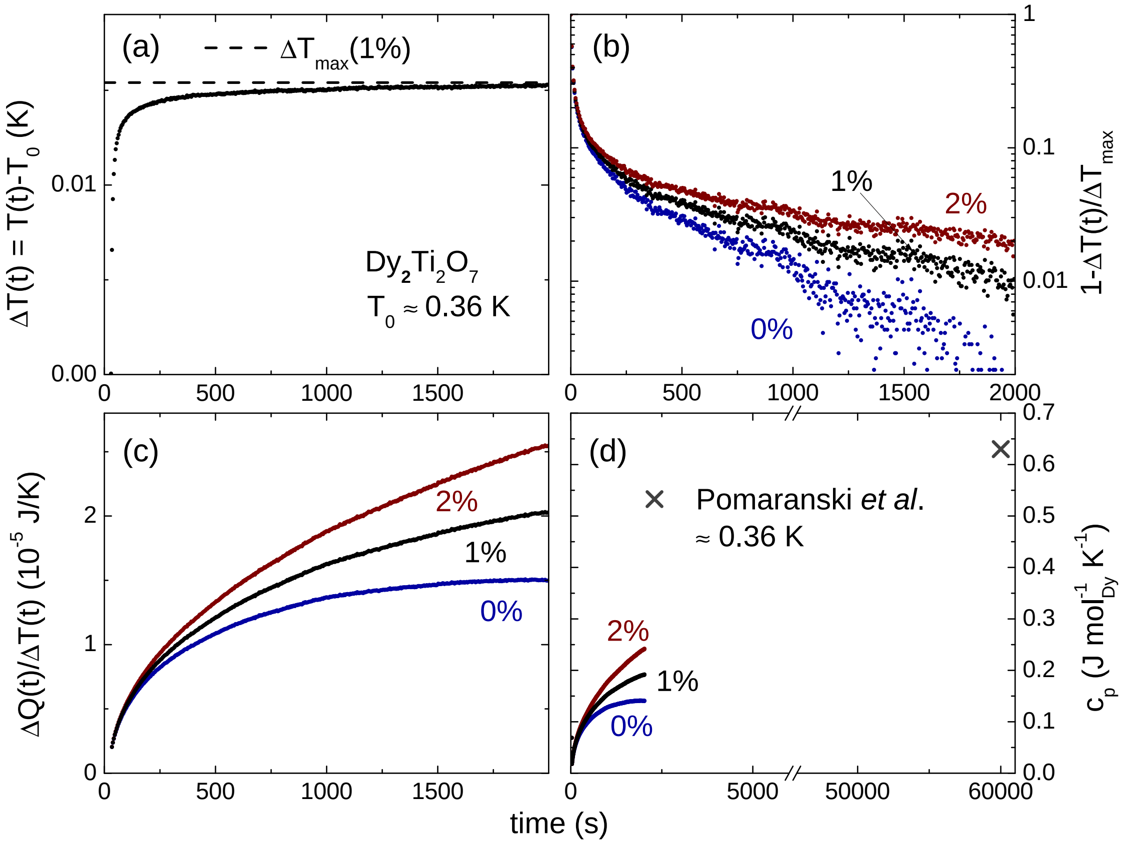

Figure 3.9: Panel (a): heating curve $\Delta T(t) = T(t) - T_0$ of $Dy_2Ti_2O_7$ at $T \approx 0.36$ K. The dashed black line represents $\Delta T_{\mathrm{max}}(1\%)$, see text. Panel (b): $1 - \Delta T(t)/\Delta T_{\mathrm{max}}$ for different ΔT_{max}. Panel (c): constant heat-flow method for different ΔT_{max}. Panel (d): comparison of c_p for different ΔT_{max} and with results from Pomaranski *et al.* [20].

increase of $\Delta T(t)$ is not required. In analogy to the relaxation method, the sample and the platform are raised to a constant temperature T_0 above the thermal reservoir by an offset power. Then, an additional power ΔP is applied to the heater. Exemplary raw data $\Delta T(t) = T(t) - T_0$ of $Dy_2Ti_2O_7$ at $T \approx 0.36$ K are shown in Fig. 3.9 (a). In order to ensure measurable variations in $\Delta T(t)$ over long times, the thermal coupling K_1 to the bath has to be weak. As can be seen, this setup allows for measurements up to about 2000 s whereas the variations in ΔT become too small for $t > 2000$ s. In order to obtain the heat capacity from the raw data, $\Delta T_{\mathrm{max}} = \Delta T(t \to \infty)$ has to be determined which is obtained by an exponential fit to the heating curve in the limit $t \to \infty$ in the relaxation method. Within the constant heat-flow method, ΔT_{max} can either be fixed by $\Delta T(2000$ s$)$ or by an estimation of $\Delta T(t \to \infty)$. Fig. 3.9 (b) presents the time-dependence of $\Delta T(t)$ in the representation $1 - \Delta T(t)/\Delta T_{\mathrm{max}}$ whereas ΔT_{max} is increased by 0%, 1% and 2%

with respect to ΔT(2000 s). With increasing $\Delta T_{\max}$, $1-\Delta T(t)/\Delta T_{\max}$ is enhanced and exhibits a linear decrease in the long-time limit. An exemplary $\Delta T_{\max}$, which is raised by 1% with respect to ΔT(2000 s), is depicted as the black dashed line in panel (a). As can also be seen in panel (b), $1-\Delta T(t)/\Delta T_{\max}$ of $Dy_2Ti_2O_7$ shows a clearly non-linear decrease in the semi-logarithmic representation which makes the standard relaxation method inapplicable. In order to calculate the specific heat via the constant heat-flow method, the heat applied to the sample as a function of time is obtained from the difference

$$\Delta Q(t) = \Delta P t - \int K_1 \Delta T(t)\mathrm{d}t \tag{3.9}$$

between the total amount of heat $\Delta P t$ provided by the heater and the heat flown from the platform to the bath via $\int K_1 \Delta T(t)\mathrm{d}t$ with $K_1 = \Delta P/\Delta T_{\max}$. Thus, the thermal coupling to the bath $K_1 = \Delta P/\Delta T_{\max}$ is related to the estimation of $\Delta T_{\max}$. The heat capacity follows via

$$C(t) = \Delta Q(t)/\Delta T(t) \tag{3.10}$$

which is shown in Fig. 3.9 (c) for different $\Delta T_{\max}$. Naturally, $\Delta Q(t)/\Delta T(t)$ calculated with $\Delta T_{\max}(0\%)$ saturates for $t \to 2000$ s. It turns out that $C(t) = \Delta Q(t)/\Delta T(t)$ is highly sensitive to the estimation of $\Delta T_{\max}$. Thus, a reasonable estimation of $\Delta T_{\max}$ is required. In the analysis of the raw data of this thesis, $\Delta T_{\max} = \Delta T(t \to \infty)$ was obtained by slightly raising ΔT(2000 s) by 0.5-1% such that $1-\Delta T(t)/\Delta T_{\max}$ reveals a linear decrease in the long-time limit but almost vanishes, see panel (b). The constant-heat flow method was applied for $(Dy_{1-x}Y_x)_2Ti_2O_7$ with $x = 0$–0.1 in the low-temperature regime $T \lesssim 0.5$ K. Fig. 3.9 (d) compares the results of the specific heat c_p for different $\Delta T_{\max}$ obtained via the constant heat-flow method to c_p determined by Pomaranski *et al.* [20]. This group applies an equivalent method which analyzes the temperature relaxation curves over $6 \cdot 10^4$ s after the sample temperature is raised by $\approx$ 5–10% above the base temperature T_0. A weak link of $Pt_{91}W_9$ with conductance $K/T \approx 2.8 \cdot 10^{-8}$ W/K^2 was used to connect the sample to a thermal reservoir in order to ensure measurable variations in $\Delta T(t)$ over these long timescales. This approach reduces uncertainties of $\Delta T_{\max}$ but it is extremely sensitive to the stability of the base temperature T_0 which has to be stabilized over the whole time period of a single $\Delta T(t)$ curve ($6 \cdot 10^4$ s). At 0.36 K, c_p of Pomaranski *et al.* exceeds the result obtained via the constant heat-flow method with $\Delta T_{\max}(1\%)$ by a factor of 3. This deviation might stem from a too large coupling to the thermal reservoir which restricted the measurements of $\Delta T(t)$ to 2000 s in the experiment. However, it is systematically shown that the determination of c_p by integrating over these long timescales bares several problems and already small uncertainties in T_0 or $\Delta T_{\max}$ lead to large deviations of c_p in the long-time limit.

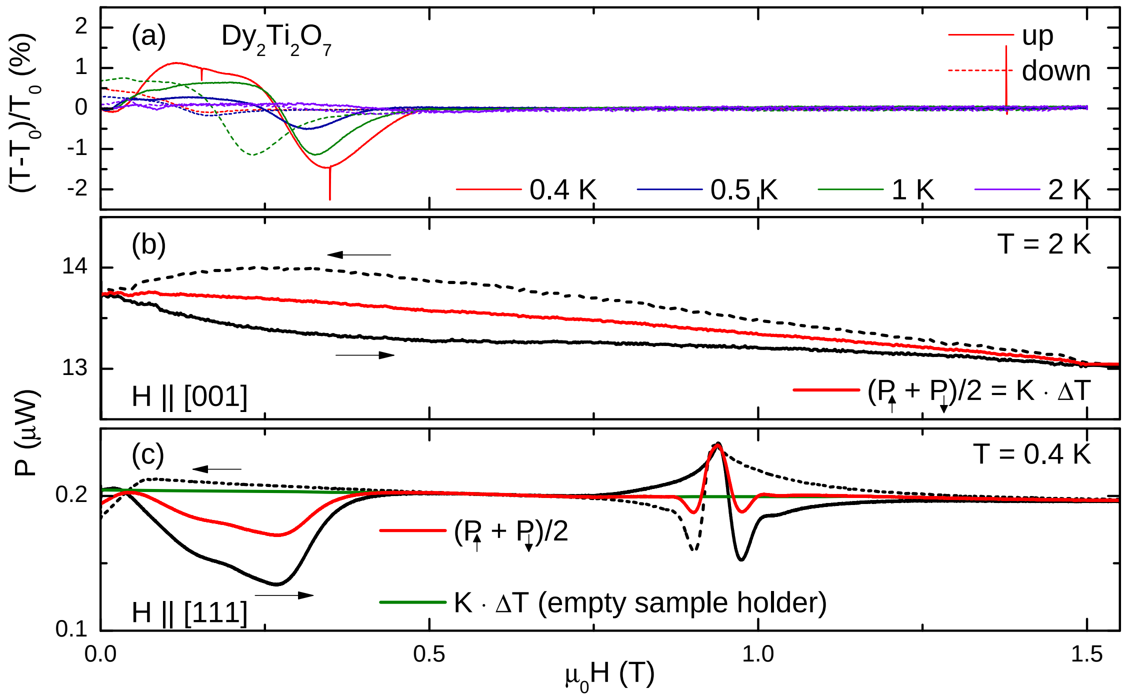

Figure 3.10: Panel (a): relative deviation from the target temperature $(T - T_0)/T_0$ of $Dy_2Ti_2O_7$ at various temperatures. Panel (b): antisymmetric curves of P with increasing and decreasing field at 2 K. The red line represents the symmetric contribution $K\Delta T$ calculated from $(P_\uparrow + P_\downarrow)/2$. Panel (c): non-antisymmetric curves of P at 0.4 K. The background contribution $K\Delta P$ (green line) was determined in a separate run.

3.6 Magnetocaloric effect

This section introduces the magnetocaloric effect which was measured for pure and dilute spin ice $(Dy_{1-x}Y_x)_2Ti_2O_7$ with $x = 0$ and 0.75 at different temperatures. A special analysis of the magnetocaloric effect data allows to determine the change of entropy as a function of the external magnetic field. More information about this field-dependent effect and materials exhibiting magnetocaloric properties can be found in an review article [77]. The experimental data of the magnetocaloric effect were obtained using the low-temperature calorimeter which is also applied for the specific heat measurements, see a schematic drawing in Fig. 3.8 (a). The sample is equally mounted on the sapphire platform by Apiezon N low-temperature grease. Then, the sample temperature T is raised to a target value T_0 above the thermal reservoir of the Heliox VL by an SMD heater in zero magnetic field. When T is stabilized at T_0, the magnetic field is continuously increased and then decreased meanwhile a PID routine steadily controls and stabilizes T to the target temperature. Typical curves of the relative temperature stability $(T - T_0)/T_0$ as a function of the field for $Dy_2Ti_2O_7$ at different target temperatures T_0 are depicted in Fig. 3.10 (a). It turns out that the deviation from the target temperature amounts to about 1.2% in maximum for this material. This is a result of the comparably large heating/cooling of the sample due to the large magnetocaloric effect of the Dy^{3+} ions with $\mu = 10\mu_B$. These deviations are clearly smaller for the dilute system $x = 0.75$ due to the replacement of magnetic ions by non-magnetic yttrium.

The derivation of the change of entropy $\Delta S(H)$ follows Ref. 73. In general, the entropy $S = S(H, T)$ of a system depends on the temperature and the magnetic field. As a consequence, the differential is given by [78]

$$\mathrm{d}S = \left.\frac{\partial S}{\partial T}\right|_H \mathrm{d}T + \left.\frac{\partial S}{\partial H}\right|_T \mathrm{d}H. \tag{3.11}$$

As T is kept constant, the first term in Eq. (3.11) vanishes and the internal energy $U(S, V, N)$ of a magnetic system at constant volume and particle number is determined by

$$\mathrm{d}U = T \cdot \mathrm{d}S = T \left.\frac{\partial S}{\partial H}\right|_T \mathrm{d}H. \tag{3.12}$$

The power P of the heater is adjusted to keep T constant. Furthermore, the heat provided by the heater and the heat flown to the bath via the conductance K equal the differential of the internal energy via

$$\mathrm{d}U = P(H)\mathrm{d}t - K(H)\Delta T\mathrm{d}t. \tag{3.13}$$

Eq. (3.12) and (3.13) can be combined to determine the change of the entropy as a function of the magnetic field

$$\frac{P(H) - K(H)\Delta T}{\gamma} = T \left.\frac{\partial S}{\partial H}\right|_T \tag{3.14}$$

with the sweep rate of the magnetic field $\gamma = \mathrm{d}H/\mathrm{d}t$. The heating power $P(H)$ can be separated into a background contribution and a contribution of the change of entropy whose sign depends on the field sweep direction. In the following, $P_\uparrow$ denotes the heating power with increasing magnetic field and $P_\downarrow$ with decreasing field. Thus, Eq. (3.14) can be rewritten to

$$P_{\uparrow,\downarrow}(H) = K(H)\Delta T \pm |\gamma| T \left.\frac{\partial S_{\uparrow,\downarrow}}{\partial H}\right|_T. \tag{3.15}$$

The first term in Eq. (3.15) represents the background contribution $K(H)\Delta T$ and accounts for the heating power to reach the temperature difference ΔT between the sample and the thermal reservoir. $K(H)\Delta T$ is independent of the field-sweep

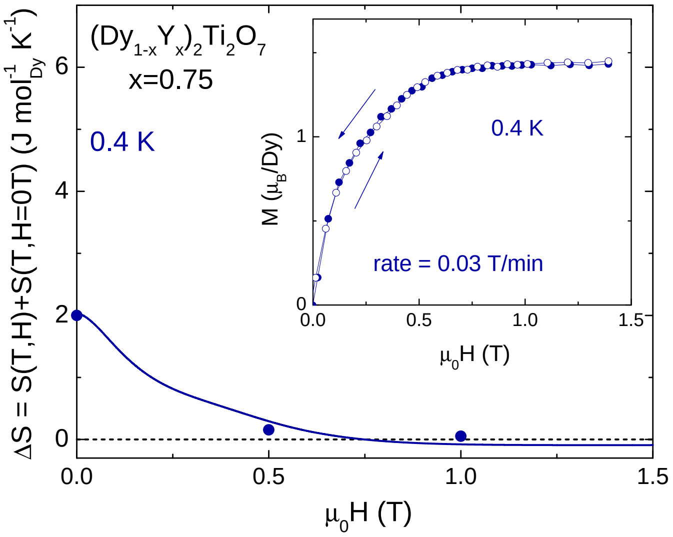

Figure 3.11: $\Delta S(H)$ of $(\mathrm{Dy}_{1-x}\mathrm{Y}_x)_2\mathrm{Ti}_2\mathrm{O}_7$ with $x = 0.75$ for $\vec{H}\,||\,[001]$ at 0.4 K. The inset shows $M(H)$ at 0.4 K obtained by applying the same field-sweep rate.

direction. In thermodynamics, a process can be reversible ($\Delta S = 0$) or irreversible ($\Delta S > 0$). Thus, $\partial S_{\uparrow,\downarrow}/\partial H$ can also be reversible or irreversible as a function of the magnetic field at constant T. Note that a reversible $\partial S_{\uparrow,\downarrow}/\partial H$ is related to a non-hysteretic magnetization $M(H)$ and vice versa. Additionally, a reversible $\partial S_{\uparrow,\downarrow}/\partial H$ results in antisymmetric $P_\uparrow(H)$ and $P_\downarrow(H)$ with respect to the background contribution $K(H)\Delta T$ which is shown exemplarily in Fig. 3.10 (b) for $\mathrm{Dy}_2\mathrm{Ti}_2\mathrm{O}_7$ at 2 K. Here, spin-ice physics is mainly suppressed and $M(H)$ exhibits no hysteresis (reversible). In this case, the addenda $K(H)\Delta T$ cancels out for $P_\uparrow - P_\downarrow$ and the change of the molar entropy ΔS is obtained via integration

$$\Delta S = S(H) - S(H') = \frac{m_{\mathrm{mol}}}{2m|\gamma|T} \int_{H'}^{H} \left[P_\uparrow(H') - P_\downarrow(H')\right] \mathrm{d}H' \tag{3.16}$$

with the mass of the sample m and its molar mass m_{mol}. This result is independent of geometric details and a calibration of the empty sample holder is not required. The background contribution can be determined via $(P_\uparrow(H) + P_\downarrow(H))/2 = K\Delta T$ (red solid line). Fig. 3.11 shows an exemplary curve of a reversible $\Delta S(H)$ determined via Eq. (3.16) for $(\mathrm{Dy}_{1-x}\mathrm{Y}_x)_2\mathrm{Ti}_2\mathrm{O}_7$ with $x = 0.75$ at 0.4 K. The curve is shifted to match $\Delta S(T, 0\ \mathrm{T})$ obtained from temperature-dependent measurements in zero field. The results of $\Delta S(T, H = \mathrm{const.})$ at fixed magnetic fields are represented by the closed blue circles. The inset depicts the non-hysteretic $M(H)$ in the case of a reversible $\Delta S(H)$. The agreement between $\Delta S(H)$ and $\Delta S(T, H = \mathrm{const.})$ at fixed magnetic fields is considerably well. Slight deviation result from the large slope in $\Delta S(T, 0\ \mathrm{T})$ in zero field which exhibits uncertainties in estimating the absolute value.

If the change of entropy $\Delta S(H)$ is, however, irreversible in a magnetic-field loop, its determination becomes more difficult. Because in this case, the energy of the mag-

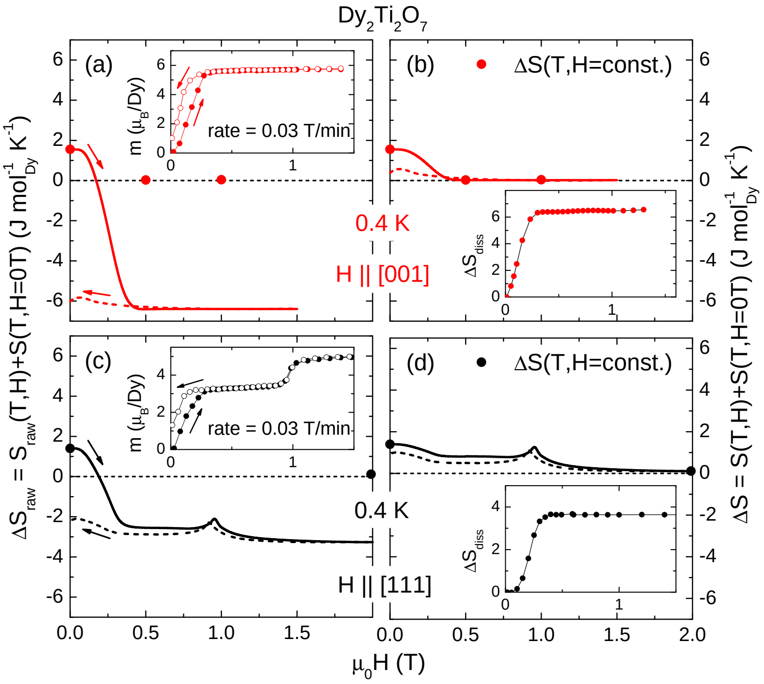

Figure 3.12: Panel (a) and (c): $\Delta S_{\text{raw}}(H)$ at 0.4 K for $\vec{H}\,||\,[001]$ and $\vec{H}\,||\,[111]$. The insets show $M(H)$ determined with the same field-sweep rate. Panel (b) and (c): $\Delta S(H)$ at 0.4 K determined from $\Delta S_{\text{raw}}(H)$, see text. The insets show ΔS_{diss}, see text.

netic system is dissipated to the phononic system (sample heats up) with increasing field. But with decreasing field, this amount of heat is not fully released back to the magnetic system. Thus, $P_{\uparrow}(H)$ and $P_{\downarrow}(H)$ are non-antisymmetric with respect to the background $K\Delta T$. This is shown exemplarily in Fig. 3.10 (c) for $Dy_2Ti_2O_7$ at 0.4 K. The background contribution $K(H)\Delta T$ (green solid line) cannot simply calculated by $(P_{\uparrow}(H) + P_{\downarrow}(H))/2$ (red solid line). First, the background $K(H)\Delta T$ has to be determined in a separate run with an empty sample holder. Then, it is separately subtracted from $P_{\uparrow}$ and $P_{\downarrow}$ which leads to a raw $\Delta S_{\uparrow,\downarrow\text{raw}}$ obtained via

$$S_{\uparrow,\downarrow\text{raw}}(H) - S_{\uparrow,\downarrow\text{raw}}(H') = \pm\frac{m_{\text{mol}}}{m|\gamma|T}\int_{H'}^{H}\left[P_{\uparrow,\downarrow}(H') - K(H')\Delta T\right]\mathrm{d}H'. \tag{3.17}$$

Typical curves for $\Delta S_{\uparrow,\downarrow\text{raw}}(H)$ are presented in Fig. 3.12 (a) and (c) for $Dy_2Ti_2O_7$ with $\vec{H}\,||\,[001]$ and [111] at 0.4 K. Both curves $\Delta S_{\uparrow\text{raw}}$ are again shifted to match $\Delta S(T, 0\text{ T})$ and the results of $\Delta S(T, H = \text{const.})$ are represented by the closed circles. $\Delta S_{\downarrow\text{raw}}$ is shifted to match $\Delta S_{\uparrow\text{raw}}$ at high magnetic fields (2 T) where the magnetization is saturated. An irreversible process of the magnetic system as a function of the magnetic field is correlated with a hysteresis in $M(H)$, see insets of panel (a) and (c). Note that $\Delta S_{\uparrow\text{raw}}(H)$ does absolutely not reproduce $\Delta S(T, H = \text{const.})$. As discussed above, this large discrepancy originates from the dissipation of energy from the magnetic to the phononic system with increasing field which is not completely released within a closed field loop. Thermodynamics

T (K)	P	I	D	$I_{\max}$ (A)
0.4	50	0.06	0.002	$3 \cdot 10^{-5}$
0.7	40	0.05	0.003	$3 \cdot 10^{-5}$
1	30	0.04	0.009	$3 \cdot 10^{-5}$
2	25	0.03	0.01	$5 \cdot 10^{-5}$
5	20	0.02	0.012	$9 \cdot 10^{-5}$

Table 3.1: PID parameters of the experimental setup with coupling to the bath via three platinum wires and four copper screws. The first column indicates the temperature up to which the parameters are applied. The PID controller output expends a number between 0 and 1 which is multiplied with the maximum current $I_{\max}$ in the fifth column.

tell that the amount of this heat per mole is given by

$$\Delta U_{\text{diss}}(H) = \Delta S_{\text{diss}}(H) \cdot T = N_{\text{A}} \cdot \mu_{\text{B}} \int_{H'}^{H} (M_{\downarrow}(H') - M_{\uparrow}(H'))\, \mathrm{d}H' \tag{3.18}$$

with the Bohr magneton μ_{B}. $M(H)$ has to be measured applying the same field sweep rate $|\gamma|$ as used for the magnetocaloric effect data to determine the exact $\Delta U_{\text{diss}}(H)$. Curves of $\Delta S_{\text{diss}}(H) = \Delta U_{\text{diss}}(H)/T$, calculated from corresponding $M(H)$ via Eq. (3.18), are shown in the insets of Fig. 3.12 (b) and (d). The final step is to obtain the real change of entropy $\Delta S_{\uparrow,\downarrow}(H)$ from $\Delta S_{\uparrow,\downarrow_{\text{raw}}}(H)$ which bares several uncertainties because $\Delta S_{\text{diss}}(H)$ is determined as a sum for increasing and decreasing field. Thus, it has to be split into a contribution to $\Delta S_{\uparrow_{\text{raw}}}(H)$ and to $\Delta S_{\downarrow_{\text{raw}}}(H)$. As can be seen in the insets of Fig. 3.12 (a) and (c), the hysteresis in $M(H)$ only occurs in the low-field regime below 0.5 T for both field directions. Thus, the low-field decrease of $\Delta S_{\uparrow_{\text{raw}}}(H < 0.5\text{ T})$ is scaled such that the whole corrected curve $\Delta S_{\uparrow}(H)$ matches $\Delta S(T, H = \text{const.})$. This reduces the decrease by $\Delta S_{\uparrow_{\text{raw}}}(0.5\text{ T}) - \Delta S_{\uparrow}(0.5\text{ T}) = \Delta S_{\uparrow,\text{cor}}$. Note that $\Delta S_{\text{diss}}(0.5\text{ T}) > \Delta S_{\uparrow,\text{cor}}$ is required to obtain reliable results. Then, $\Delta S_{\text{diss}}(0.5\text{ T}) - \Delta S_{\uparrow,\text{cor}} = \Delta S_{\downarrow,\text{cor}}$ yields the correction to $\Delta S_{\downarrow_{\text{raw}}}(H < 0.5\text{ T})$. Afterwards, the low-field increase of $\Delta S_{\downarrow}(H < 0.5\text{ T})$ is scaled such that its magnitude is given by $\Delta S_{\downarrow}(0\text{ T}) - \Delta S_{\downarrow}(0.5\text{ T}) = \Delta S_{\downarrow_{\text{raw}}}(0\text{ T}) - \Delta S_{\downarrow_{\text{raw}}}(0.5\text{ T}) + \Delta S_{\downarrow,\text{cor}}$. The resulting curves $\Delta S_{\uparrow}(H)$ and $\Delta S_{\downarrow}(H)$ for $Dy_2Ti_2O_7$ at 0.4 K are shown in Fig. 3.12 (b) and (d).

In general, it turned out that the change of entropy $\Delta S(H)$ of crystals, which reveal reversible magnetic properties, can be measured applying the magnetocaloric effect in an efficient way and with a high accuracy, as discussed for $(Dy_{1-x}Y_x)_2Ti_2O_7$ with $x = 0.75$. However if the magnetic properties are irreversible (*e.g.* $Dy_2Ti_2O_7$ below about 0.6 K), this method bares several uncertainties concerning the background contribution $K\Delta T$ and the splitting of $\Delta S_{\text{diss}}(H)$ to $P_{\uparrow}(H)$ and $P_{\downarrow}(H)$. Thus, the applicability and accuracy is clearly reduced for these systems.

During initial experiments, it was observed that the standard coupling of the sapphire platform to the bath via one platinum wire, which is applied for the relaxation measurements of the specific heat, is not sufficient for $(\mathrm{Dy}_{1-x}\mathrm{Y}_x)_2\mathrm{Ti}_2\mathrm{O}_7$ with $x \leq 0.75$. Due to the large magnetic moment of $\mu = 10\ \mu_\mathrm{B}$ of the Dy^{3+} ions, a considerable large heating of the samples arises while raising the magnetic field. As a consequence, the power P of the heater is partly switched off by the PID routine to compensate this large heating. Then, Eq. (3.16) and (3.17) are not applicable. In order to account for this effect, the coupling of the platform to the bath was accomplished by three platinum wires and 4 copper screws in the experiment presented within this thesis. Hence, the cooling power of the bath is strongly enhanced which leads to an increased $K(H)\Delta T$ for both field directions. Therefore, the change of the temperature can be compensated by the PID controller without switching off the heater. The PID parameters for the applied setup are given in Tab. 3.1.

4 Introduction to spin ice

This chapter introduces spin-ice systems and gives an overview about magnetic frustration, the history of spin ice, the analogy to water ice and theoretical models. Furthermore, recent literature results on spin ice are summarized.

4.1 Magnetic frustration

In general, frustration is defined as the competition between nearest neighbor interactions or between nearest neighbors and next-nearest neighbors in a many-body system such that not every atom can minimize its energy due to local constraints. It usually arises in systems that comprise spins which reside on the sites of a lattice built of elementary triangular or tetrahedral units and which are coupled antiferromagnetically to each other. However, geometric frustration can also occur in systems with strong single-ion easy-axis anisotropy with non-collinear spins which are coupled ferromagnetically. This is realized in some pyrochlore oxide materials in which the Ising-like magnetic rare earth moments are located on the edges of corner-sharing tetrahedra and are coupled via effective ferromagnetic interactions [79, 80].

In order to illustrate the principle of frustration, Fig. 4.1 (a) shows the textbook example of magnetic frustration. The Ising spins reside on the edges of a triangle interacting via nearest-neighbor antiferromagnetic exchange. If the first two spins align antiparallel the third one is frustrated because its two possible orientations, up and down, possess the same energy. The third spin cannot simultaneously minimize its interactions with both others. G. Wannier showed in 1950 that this system remains disordered down to zero temperature and reveals a degeneracy of the ground state [81]. The ground-state degeneracy is a defining characteristic of frustration from the theoretical perspective. In the discussed scenario, the number of ground states grows exponentially with the number of spins possessing a residual ($T = 0$) entropy. This is in contrast to the third law of thermodynamics claiming $S \to 0$ for $T \to 0$. Fig. 4.1 (b) shows that frustration can also arise if ferromagnetic spins reside on a triangle. The spins are arranged along an easy axis which points towards the center and the first two spins have a parallel component. Then, the

Figure 4.1: Illustration of magnetic frustration with ferromagnetic and antiferromagnetic exchange interaction. Panel (a): textbook example of magnetic frustration with antiferromagnetic coupling. The ferromagnetic coupling of panel (b) in 2D is extended to 3D in panel (c) where the system minimizes its energy by a 2in-2out configuration. Panel (d): mapping of (c) to 2D according to Ref. 79.

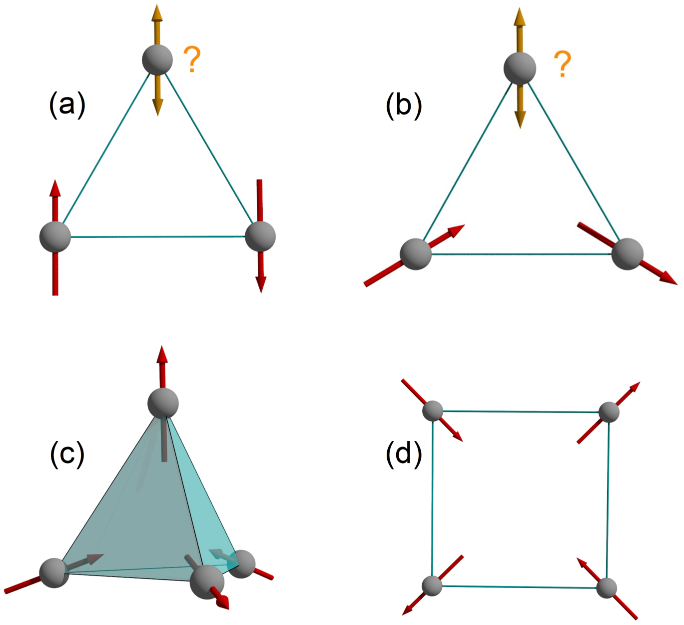

third spin remains frustrated and cannot order ferromagnetically to both others. The 2D scenario of panel (b) is extended to 3D in panel (c). The spins reside on the edges of a tetrahedron and point along a local easy axis towards the center of the tetrahedron. Geometric frustration arises if the coupling is ferromagnetic. The system minimizes its energy by a configuration where two spins point into the tetrahedron and two out. This ground state is 6-fold degenerate and it is discussed to occur in spin-ice materials. The configuration of panel (c) can be mapped to 2D which is shown in panel (d) [79].

4.2 History

In principle, the history of spin ice began in the 1930s when W. Giauque *et al.* measured the heat capacity of common water ice from 15 K up to 273 K and found an unaccounted residual entropy [82, 83]. L. Pauling explained this result in terms of a macroscopic number of proton configurations of the H^+ ions that are located around the oxygen ions [5]. A mismatch is present between the crystalline symmetry of ice and the local hydrogen bonding requirements of the water molecules. Pauling's argument to estimate the proton entropy considered one mole of water ice which consists of N O^{2-} ions and therefore $2N$ O-O bonds. By taking into account that all bonds obey the first Bernal-Fowler ice rule, each O-O bond has two possible

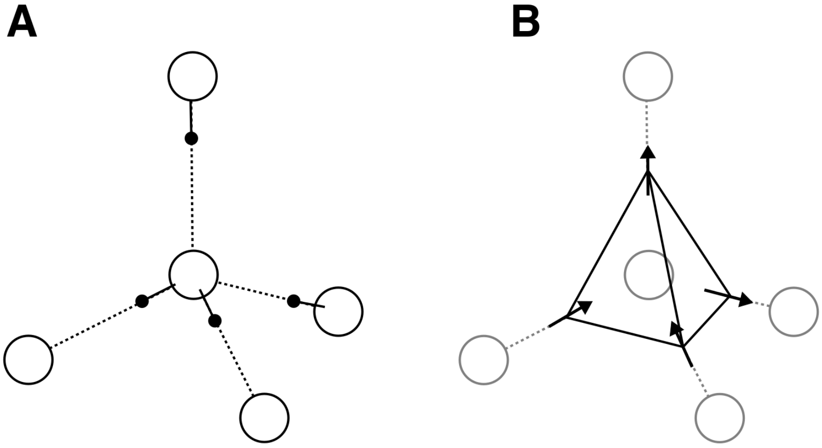

Figure 4.2: Analogy of water ice and spin ice taken from Ref. 79. Panel (a) shows the structure of water-ice where the oxygen ions are surrounded by four protons. Two of these protons are located close to the central oxygen and two sit close to neighboring oxygen atoms. Panel (b) emphasizes the analogy to spin ice. Two spins of a single tetrahedron point towards its center while two point out of the tetrahedron to the center of neighboring tetrahedra.

proton positions. Thus, there are $2^{(2N)}$ possible proton positions in the considered system and 16 possible proton configurations for each oxygen ion. 10 out of these 16 configurations are energetically unfavorable, namely the OH_4^{2+} configuration, the $4OH_3^+$ configurations, the $4OH^-$ configurations and the O^{2-} configuration. As a consequence, there are six configurations according to the Bernal-Fowler rules which are energetically favorable around each oxygen ion. This leads to an upper bound on the number of ground states, Ω, by simply reducing the $2^{(2N)}$ possible states by a weight factor of 6/16 for each oxygen ion. Hence, Ω is estimated by

$$\Omega \leq 2^{2N}(6/16)^N = (3/2)^N. \tag{4.1}$$

As a result, the residual entropy per H^+ ion (which introduces an additional factor of 1/2) can be obtained via

$$S = \frac{R}{2}\ln(\Omega) = \frac{N_\mathrm{A}k_\mathrm{B}}{2}\ln(3/2) = 1.69\ \mathrm{J\ mol^{-1}K^{-1}}. \tag{4.2}$$

This model reproduced the results of W. Giauque *et al.* published in Ref. 83 within 1-2%.

A class of insulating magnetic materials in which the configurational disorder of the magnetic moments is analogous to the disorder in water ice was intensively studied during the last two decades. Due to this analogy, these materials were named

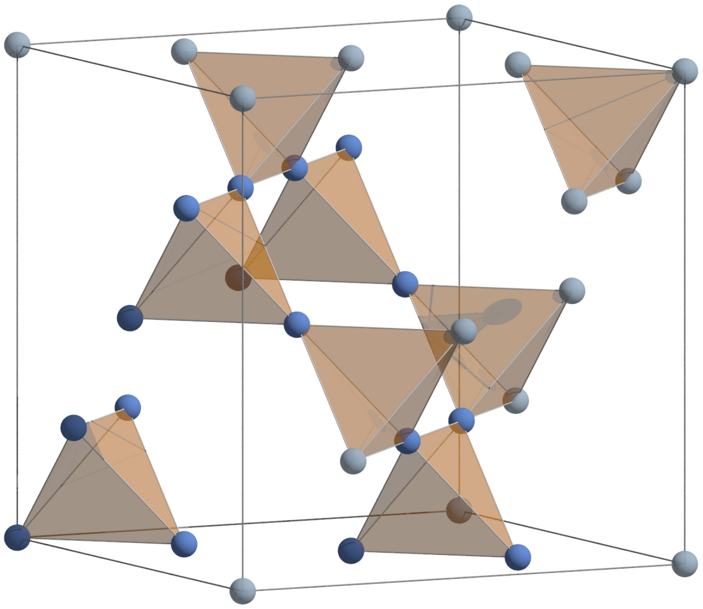

Figure 4.3: Cubic unit cell of the pyrochlore lattice which contains 16 lattice sites (dark blue spheres). The gray spheres represent sites which arise from the periodicity of the lattice. As a guide-to-the-eye, the tetrahedra are highlighted in brown.

spin ice. Fig. 4.2 (a) shows the structure of water ice where the oxygen ions are surrounded by four protons. Two of these protons are located closer to the central oxygen and two reside close to neighboring oxygen atoms. This ground state is 6-fold degenerate. Panel (b) depicts the situation in spin ice which is built of corner-sharing tetrahedra that form a pyrochlore structure which will be discussed in the following. One single tetrahedron consists of four spins where two point towards its center while two point out of the tetrahedron to the center of a neighboring one in order to minimize its energy. The most prominent representatives of spin-ice materials are $Dy_2Ti_2O_7$ and $Ho_2Ti_2O_7$ whose thermodynamic properties will be investigated in Chaps. 5-7.

The name pyrochlore originates from the mineral $NaCaNb_2O_6F$ whose structure was first reported by von Gaertner in 1930 [84]. The name, literally 'green fire', originates from the fact that the mineral shows green color upon ignition. The spin-ice materials such as $Dy_2Ti_2O_7$ and $Ho_2Ti_2O_7$ crystallize in this cubic pyrochlore structure with space group $Fd\bar{3}m$ [79, 85, 86] which is shown in Fig. 4.3. The magnetic Dy^{3+} (Ho^{3+}) ions and the non-magnetic Ti^{4+} ions reside on two interpenetrating pyrochlore lattices, respectively. Here, it will be focused on the magnetic system whose unit cell contains 16 sites which are represented by the dark blue spheres. The corner-sharing tetrahedra are highlighted in brown. The gray circles represent the sites which arise from the periodicity of the lattice and are shown for a better illustration of the 3D structure. The lattice constant is found to be $a = 10.124$ Å for $Dy_2Ti_2O_7$ and $a = 10.1041$ Å for $Ho_2Ti_2O_7$ [87].

In Refs. 85, 88, it was found that an effective ferromagnetic nearest-neighbor coupling is present in $Ho_2Ti_2O_7$, characterized by a positive Curie-Weiss temperature $\theta_W \approx 1.9$ K which indicates a coupling between the Ho^{3+} ions with $J \approx 1$ K[1]. Furthermore, no magnetic transition was found down to 0.05 K. The surprising result was explained by a strong crystal electric field of trigonal symmetry that forces the magnetic Ho^{3+} moments to point strictly along the local $\{111\}$ direction to the center of a tetrahedron. This anisotropy allows to describe the Ho^{3+} moments as effective classical Ising spins $S_i^{z_i}$ with local quantization axis $\{111\}$ at the site i. For a single tetrahedron with such $\{111\}$ Ising spins sitting on each corner and interacting with a nearest-neighbor ferromagnetic coupling, the minimum energy is found to be one of six states with two spins pointing into and two spins pointing out, see Fig. 4.2 (b).

In 1999, Ramirez *et al.* found an analogy between the frustrated pyrochlore $Ho_2Ti_2O_7$ and the compound $Dy_2Ti_2O_7$ by determining its residual zero-point entropy which is similar to the residual entropy of water ice [90]. It was the first experimental evidence for the existence of the spin-ice state. During the following years, several groups measured the specific heat of $Dy_2Ti_2O_7$ and partially confirmed these results [19, 91, 92]. Recent specific-heat data support an absence of Pauling's residual entropy in $Dy_2Ti_2O_7$ which will be discussed in Sec. 4.5.

However, it turned out that the simple ferromagnetic model with strong anisotropy along local $\{111\}$ directions is not sufficient to explain all characteristics of the spin-ice materials $Dy_2Ti_2O_7$ and $Ho_2Ti_2O_7$. Due to the large magnetic moment $\mu \approx 10\mu_B$ of the Dy^{3+} and Ho^{3+} ions [93], it is found that the scale for the magnetostatic dipolar interactions between nearest neighbors, which refers to the direct interaction between two magnetic dipoles, can be calculated to be $D \approx 1.4$ K [80, 93]. Thus, D and J are of comparable magnitude. Hence, the dipolar interactions must be taken into account. Furthermore, the nearest neighbor exchange interactions in $Dy_2Ti_2O_7$ and $Ho_2Ti_2O_7$ were actually found to be antiferromagnetic [79, 80], which would by itself cause a phase transition to a long range ordered state with $T_N \sim |\Theta_W|$ distinguished by Monte Carlo simulations [85, 88]. As a consequence, a model of $\{111\}$ Ising pyrochlore magnets with antiferromagnetic nearest-neighbor exchange and long-range magnetic dipole interactions was successfully introduced and led to a convenient description of the experimental results [79, 94–96]. The corresponding

---

[1] The Curie-Weiss temperature of $Dy_2Ti_2O_7$ is obtained from dc susceptibility to be $\theta_W \approx$ 1.1 K [89].

Hamiltonian is given by [96]

$$\begin{aligned}\mathcal{H} &= -J \sum_{\langle (i,a),(j,b)\rangle} \vec{S}_i^a \cdot \vec{S}_j^b \\ &\quad + D r_{\mathrm{nn}}^3 \sum_{\substack{i>j \\ a,b}} \frac{\vec{S}_i^a \cdot \vec{S}_j^b}{|\vec{R}_{ij}^{ab}|^3} - \frac{3(\vec{S}_i^a \cdot \vec{R}_{ij}^{ab})(\vec{S}_i^b \cdot \vec{R}_{ij}^{ab})}{|\vec{R}_{ij}^{ab}|^5}. \end{aligned} \tag{4.3}$$

The vectors $\vec{S}_i^a = \theta_i^a \hat{z}^a$ represent the Ising spins of the Dy^{3+} or Ho^{3+} ions at site $\vec{R}_i$ which point along the local easy axis $\hat{z}^a$ in one of the $\{111\}$ directions. The Ising variable is $\theta_i^a = \pm 1$ and the $\hat{z}^a$ are normalized to $|\hat{z}^a| = 1$. The vector $\vec{R}_{ij}^{ab} = \vec{R}_{ij} + \vec{r}^{ab}$ connects the spins $\vec{S}_i^a$ and $\vec{S}_j^b$. The exchange energy J is antiferromagnetic and D is the dipolar energy scale. Due to the local $\{111\}$ easy axes, it follows that $\hat{z}^a \cdot \hat{z}^b = -1/3$ and therefore $J_{\mathrm{nn}} = J/3$ if the exchange interaction is restricted to nearest neighbors. The dipolar interaction energy can be obtained via

$$D = \frac{\mu_0}{4\pi} \frac{\mu^2}{r_{\mathrm{nn}^3}}. \tag{4.4}$$

The magnetic moments of the Dy^{3+} and Ho^{3+} ions in the pyrochlore lattice were experimentally determined to be $\mu \approx 10\mu_{\mathrm{B}}$ by magnetization [97] and neutron scattering [98]. The typical nearest-neighbor distance of the systems is given by $r_{\mathrm{nn}} \approx 3.54$ Å. The dipole-dipole interaction at nearest neighbor distances can be calculated to be $D_{\mathrm{nn}} = 5D/3$, since $\hat{z}^a \cdot \hat{z}^b = 1/3$ and $(\hat{z}^a \cdot \vec{R}_{ij}^{ab})(\hat{z}^b \cdot \vec{R}_{ij}^{ab}) = 2/3$ following from Eq. (4.3). Thus for both systems $\mathrm{Ho_2Ti_2O_7}$ and $\mathrm{Dy_2Ti_2O_7}$, the dipole-dipole interaction is given by $D_{\mathrm{nn}} \approx 2.35$ K. From these results, an effective nearest-neighbor energy scale can be introduced

$$J_{\mathrm{eff}} = J_{\mathrm{nn}} + D_{\mathrm{nn}}. \tag{4.5}$$

In literature the exchange couplings are found to be $J_{\mathrm{nn}} \approx -1.24$ K for $\mathrm{Dy_2Ti_2O_7}$ [80] and $J_{\mathrm{nn}} \approx -0.52$ K for $\mathrm{Ho_2Ti_2O_7}$ [99]. Hence, $J_{\mathrm{eff}} > 0$ and, thus, ferromagnetic for both $\mathrm{Dy_2Ti_2O_7}$ with $J_{\mathrm{eff}} = 1.1$ K and $\mathrm{Ho_2Ti_2O_7}$ with $J_{\mathrm{eff}} = 1.8$ K. The effective Hamiltonian is given by

$$\mathcal{H} = -3\, J_{\mathrm{eff}} \sum_{\langle (i,a),(j,b)\rangle} \vec{S}_i^a \cdot \vec{S}_j^b. \tag{4.6}$$

In the presence of an external magnetic field Eq. (4.6) expands to

$$\mathcal{H} = -3\, J_{\mathrm{eff}} \sum_{\langle (i,a),(j,b)\rangle} \vec{S}_i^a \cdot \vec{S}_j^b - \mu \sum_i \vec{S}_i \cdot \vec{H}_{\mathrm{ext}}. \tag{4.7}$$

Concerning the crystal electric field level scheme of the Dy^{3+} ions ($4f^9$) in $Dy_2Ti_2O_7$, which is created by the surrounding O^{2+} ions, an Ising-type $|J = \pm 15/2\rangle$ Kramers doublet is found to almost completely form the ground state [89]. In Ref. 100, the exact level scheme is obtained by fitting of nuclear quadrupole resonance (NQR) experiments and the ground state wave function $|\Psi_{\mathrm{gs,Dy}}\rangle$ consists of the following contributions

$$\begin{aligned} |\Psi_{\mathrm{gs,Dy}}\rangle \;=\; & +0.9861\,|\pm 15/2\rangle - 0.1561\,|\pm 9/2\rangle - 0.041\,|\pm 3/2\rangle \\ & +0.035\,|\mp 3/2\rangle + 0.007\,|\mp 9/2\rangle\,. \end{aligned} \tag{4.8}$$

Obtained results for the gap to the first excited doublet state vary between 140 K and 380 K in literature [100–104]. Due to the strong Ising character of the ground state, the total angular momentum of the Dy^{3+} ions can be calculated via

$$m_z = g_s\mu_{\mathrm{B}}S_z + g_L\mu_{\mathrm{B}}L_z \approx 2\mu_{\mathrm{B}}\frac{5}{2} + 1\mu_{\mathrm{B}}5 = 10\mu_{\mathrm{B}} \tag{4.9}$$

with $g_S \approx 2$ and $g_L = 1$ as the Landé factors of the spin and the orbital momentum.

The crystal electric field scheme of $Ho_2Ti_2O_7$ is very similar to that of $Dy_2Ti_2O_7$. The electric field acting on the magnetic ions also gives rise to an almost ideal classical Ising spin. The $J = 8$ multiplet of the Ho^{3+} ($4f^{10}$) ion splits into ten levels due to the D_{3d} local symmetry [98, 105]. The ground state almost purely consists of the $|J = \pm 8\rangle$ doublet. In Ref. 106, the exact level scheme is determined by fitting neutron scattering experiments and the ground state wave function $|\Psi_{\mathrm{gs,Ho}}\rangle$ is given by

$$\begin{aligned} |\Psi_{\mathrm{gs,Ho}}\rangle \;=\; & -0.979\,|\mp 8\rangle \pm 0.189\,|\pm 5\rangle - 0.014\,|\pm 2\rangle - 0.070\,|\mp 1\rangle \\ & -0.031\,|\mp 4\rangle \pm 0.005\,|\mp 7\rangle\,. \end{aligned} \tag{4.10}$$

Slightly different results of the ground-state wave function, which also almost purely consists of the $|J = \pm 8\rangle$ doublet, can be found in Ref. 107. The first excited state of the crystal-electric field multiplet is well separated from the ground state by a gap of $\Delta E = 240$ K determined by magnetic susceptibility measurements [101]. This yields the same value for the total angular momentum like in $Dy_2Ti_2O_7$, namely

$$m_z = g_s\mu_{\mathrm{B}}S_z + g_L\mu_{\mathrm{B}}L_z \approx 2\mu_{\mathrm{B}}2 + 1\mu_{\mathrm{B}}6 = 10\mu_{\mathrm{B}}. \tag{4.11}$$

In summary, $Ho_2Ti_2O_7$ and $Dy_2Ti_2O_7$ are 3D realizations of a spin ice. The influence of quantum mechanics on the classical Ising spins in $Dy_2Ti_2O_7$ and $Ho_2Ti_2O_7$ is studied in literature [108, 109]. An estimate of quantum effects in the systems is found to be well below experimentally relevant temperatures.

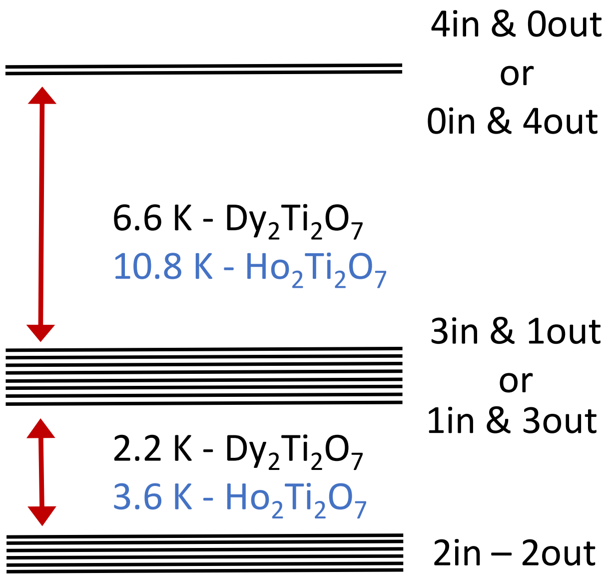

Figure 4.4: Energy levels of the single-tetrahedron approximation with effective coupling $J_{\mathrm{eff}} = 1.1$ K for $Dy_2Ti_2O_7$ [80] and $J_{\mathrm{eff}} = 1.8$ K for $Ho_2Ti_2O_7$ [99] at zero magnetic field.

4.3 Single-tetrahedron approximation in external magnetic field

The single-tetrahedron approximation is often applied to describe the phenomena of spin-ice materials [10]. Here, only the four spins of one tetrahedron are considered. The splitting of the possible states can easily be calculated which is depicted in Fig. 4.4 at zero magnetic field. The ground state is sixfold degenerate, represented by the 6 black lines at the bottom. Above this ground state, the 8-fold degenerate first excited state 3in-1out or 1in-3out is found. The highest-lying spin configuration is 4in-0out or 0in-4out which is located 6.6 K (10.8 K) in $Dy_2Ti_2O_7$ ($Ho_2Ti_2O_7$) above the first excited state. Spin-ice physics occurs around 1 K and, thus, the 4in-0out and 0in-4out configurations will not be taken into account.

For spin-ice materials, the field-dependence of the physical properties is of high interest. Therefore, the competition between the external field and the magnetic moments with easy axes along the local [111] directions has to be discussed. Fig. 4.5 shows the spin-ice pyrochlore structure with a magnetic field applied along the main crystallographic axes. The red arrows indicate the spins which are in the 2in-2out ground-state configuration. The external magnetic field is represented by black arrows.

The Zeeman splitting of the single-tetrahedron configurations for the different field directions is shown in Fig. 4.6 (a)-(h). For $\vec{H} \,||\, [001]$, one out of the six degenerate ground states is energetically favorable having components of all four spins along the field direction, see panel (c). The ground-state degeneracy is lifted for finite fields along [001].

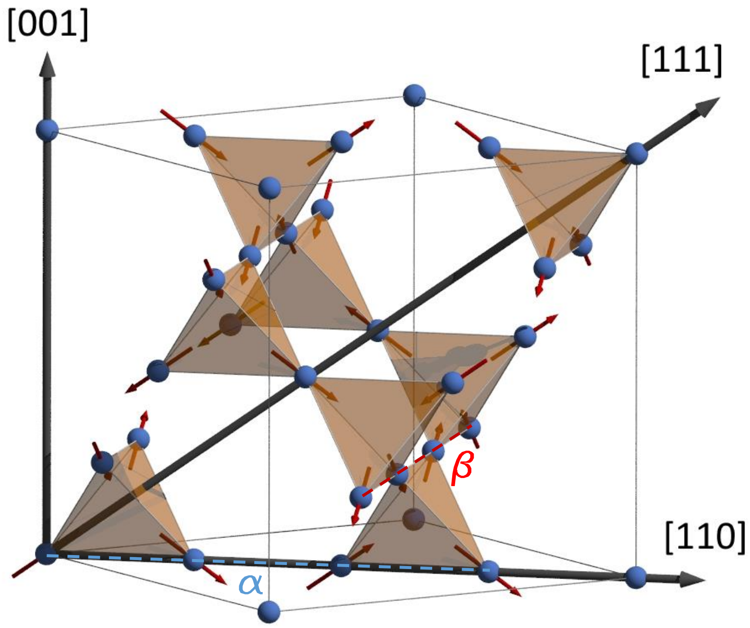

Figure 4.5: Pyrochlore structure with the corner-sharing tetrahedra of magnetic Dy^{3+} or Ho^{3+} ions in external magnetic field. The red arrows represent the spins. The α and β chains are highlighted as dashed lines.

For $\vec{H}\,||\,[111]$ however, the field-dependence of the energy levels is more complex. For this particular field direction, the spin-ice structure can be best visualized by alternating triangular planes (green) and Kagomé-ice planes (blue), see Fig. 4.7. At finite fields, the spins within the triangular planes point parallel to the field in [111] direction. Within the Kagomé-ice planes, the spins only have a component parallel or antiparallel to the applied field. Starting in zero field with the 6-fold degenerate 2in-2out configuration as the ground state, a 3-fold degenerate state with 2in-2out configuration is entered for $0 < H < 1$ T in $Dy_2Ti_2O_7$ and $0 < H < 1.5$ T in $Ho_2Ti_2O_7$. Here, the triangular planes are fully polarized whereas one out of the three spins within the Kagomé plane still exhibits a component antiparallel to the field. The ice-rule is still fulfilled. At 1 T for $Dy_2Ti_2O_7$ and at 1.5 T for $Ho_2Ti_2O_7$, a level crossing occurs. Here, the ground state changes from the 3-fold degenerate 2in-2out state into a non-degenerate 3in-1out (1in-3out) state where the last spin with component antiparallel to the field is flipped, see Fig. 4.6 (d) and (e).

If the magnetic field is applied along [110], the 6-fold degenerate 2in-2out ground-state configuration splits into three 2-fold degenerate 2in-2out states, see Fig. 4.6 (i). The ground state is given by a 2in-2out configuration where two spins have a component parallel to the field and the other two point perpendicular to the field. Considering the pyrochlore structure for $\vec{H}\,||\,[110]$, so-called α and β chains are formed. Within the α chains, the spins have a component parallel to the applied field whereas the spins in the β chains are arranged in a plane perpendicular to the field, see Fig. 4.5.

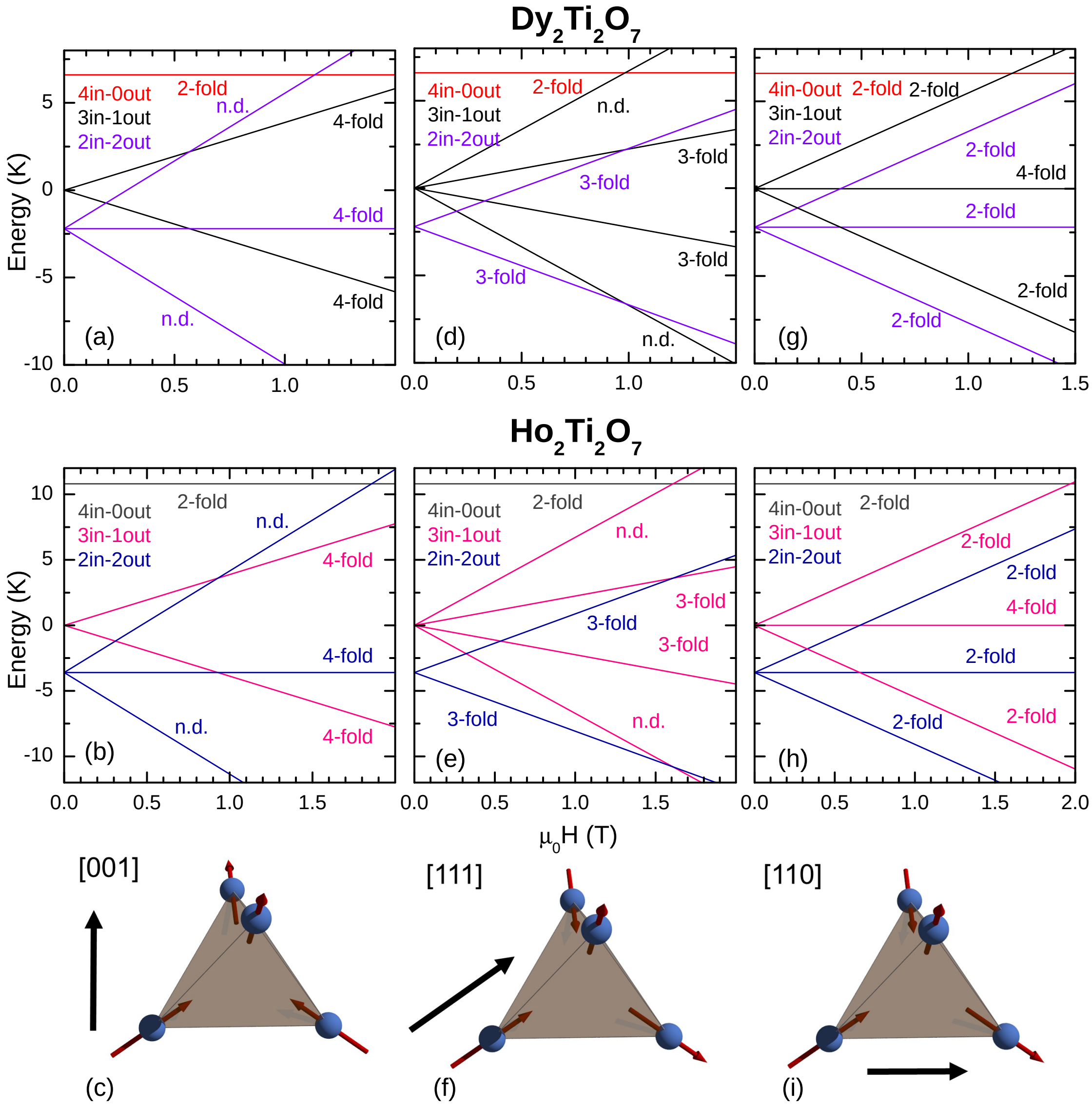

Figure 4.6: Energy of the single-tetrahedron approximation in applied magnetic field along [001], [111] and [110] for $Dy_2Ti_2O_7$ and $Ho_2Ti_2O_7$ adapted from Ref. 16.

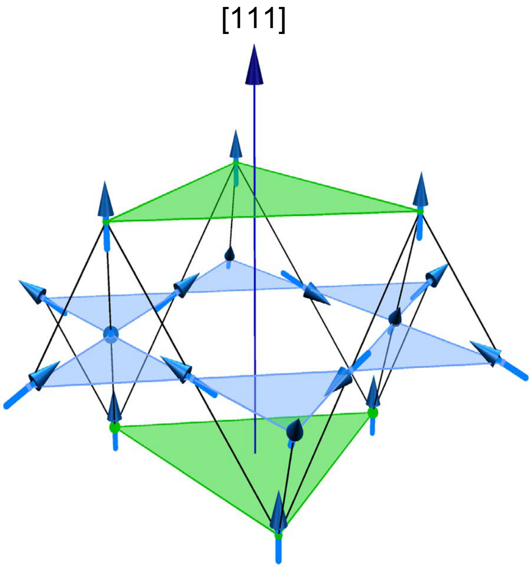

Figure 4.7: Visualization of the spin-ice structure for $\vec{H}\,||\,[111]$. For this field direction, the structure consists of alternating triangular planes (green) and Kagomé-ice planes (blue). Taken from Ref. 110.

4.4 Internal thermal equilibration

It has been discovered that the spin-ice systems $Dy_2Ti_2O_7$ and $Ho_2Ti_2O_7$ reveal long-time thermal-relaxation phenomena in different physical properties at lowest temperatures. Below about 0.6 K, these phenomena set in and signal strongly increasing timescales for the internal thermal equilibration. This section will give an overview about the most important results concerning this topic in literature.

Matsuhira *et al.* observe relaxation processes in the ac susceptibility and dc magnetic relaxation measurements in $Dy_2Ti_2O_7$ [111]. They find that the spin dynamics is well described by using two relaxation times [τ_s (short time) and τ_l (long time)]. Both parameters increase on cooling. In order to get an insight in the energy involved in these relaxation processes, $\tau(T)$ is described by an Arrhenius law in the temperature range 0.5 K-1 K. From the temperature dependence of τ_s and τ_l, an energy barrier of $E \approx 9.2$ K (8-9J_{eff}) is obtained. The system shows relaxation on time scales of $\tau_l = 10^2 - 10^5$ s between 0.25 K and 0.5 K.

Revell *et al.* discuss the time-dependent magnetic relaxation in $Dy_2Ti_2O_7$ and show that it decays with a stretched exponential followed by a very slow long-time tail [112]. They give experimental evidence that the rapidly diverging timescale originates from a temperature-dependent attempt rate proportional to the monopole density. They measure relaxations of about 10^2 s at $T \approx 0.5$ K. The data are in good agreement with Ref. 111.

Yaraskavitch *et al.* performed low-temperature magnetic ac susceptibility measurements of single-crystal $Dy_2Ti_2O_7$ [113]. The relaxation is found to exhibit thermally activated Arrhenius behavior with an activation energy of 9.79 K ($\approx 9J_{\text{eff}}$). For $Ho_2Ti_2O_7$, the description by an Arrhenius law yields an activation energy close to $6J_{\text{eff}}$ [114]. Distinct quantifiable differences between $Ho_2Ti_2O_7$ and $Dy_2Ti_2O_7$ are found in the absorption spectra. Clear deviations between these iso-structural spin ices are also found in the field dependence of the heat transport, see Chap. 6, and in ultrasonic investigations [115, 116].

Long-time relaxations were also observed in the thermal transport κ of $Dy_2Ti_2O_7$. Li *et al.* observe relaxations of $\kappa(t)$ in $Dy_2Ti_2O_7$ in zero field and at finite magnetic field after successive field sweeps for $\vec{H} \,||\, [001]$ and [110] [13]. The time dependence is fitted by a single exponential function and is obtained to be $\tau_{[100]} = 1100 - 1600$ min and $\tau_{[110]} = 900$ min. Relaxations for $\vec{H} \,||\, [111]$ are not not observed which is in clear contrast to the results on $\kappa(t)$ presented in Sec. 7.1. Klemke *et al.* focused on the anomalous relaxation times in the low temperature regime ($T < 1.1$ K) by analyzing the temperature-dependent specific heat and thermal conductivity measurements [11]. The time-dependent temperature relaxation curves are found to be non-exponential concerning one single relaxation time. The data were fitted with a thermodynamic field theory model including multiple relaxation times. It is discussed that the magnetic system of $Dy_2Ti_2O_7$ consists of different subsystems which reveal different relaxation times. Kolland *et al.* also measured the specific heat and the thermal conductivity of $Dy_2Ti_2O_7$ [14–16]. The time-dependent heat transport $\kappa(t)$ after successive field sweeps for $\vec{H} \,||\, [001]$ was measured in the low-temperature regime at 0.4 K and it can be described by two relaxation times $\tau_1 \approx$ 8 min and $\tau_2 \approx 100$ min. Furthermore, they introduced a new method to measure the specific heat for $T \lesssim 0.6$ K in order to account for the slow equilibration processes. The constant heat-flow method, which has already been introduced in Sec. 3.5.2, was applied and the specific heat was measured up to 1000 s to reach thermal equilibrium. This method yields enhanced values of the specific heat compared to the standard relaxation method [90, 117]. In Ref. 20 a similar method is used by measuring the thermal equilibration of $Dy_2Ti_2O_7$ up to 60,000 s. The consequences of this long-term measurements compared to previous results will be discussed the following.

4.5 Pauling's residual entropy

In 1935, a residual entropy was found to be present in water ice [82, 83]. Due to the analogy between water ice and spin ice, Ramirez *et al.* determined the residual entropy of $Dy_2Ti_2O_7$ by measurements of the specific heat [90]. The $c(T)/T$ data in zero field and at 0.5 T are shown in Fig. 4.8 (a). The entropy $S(T)$ is

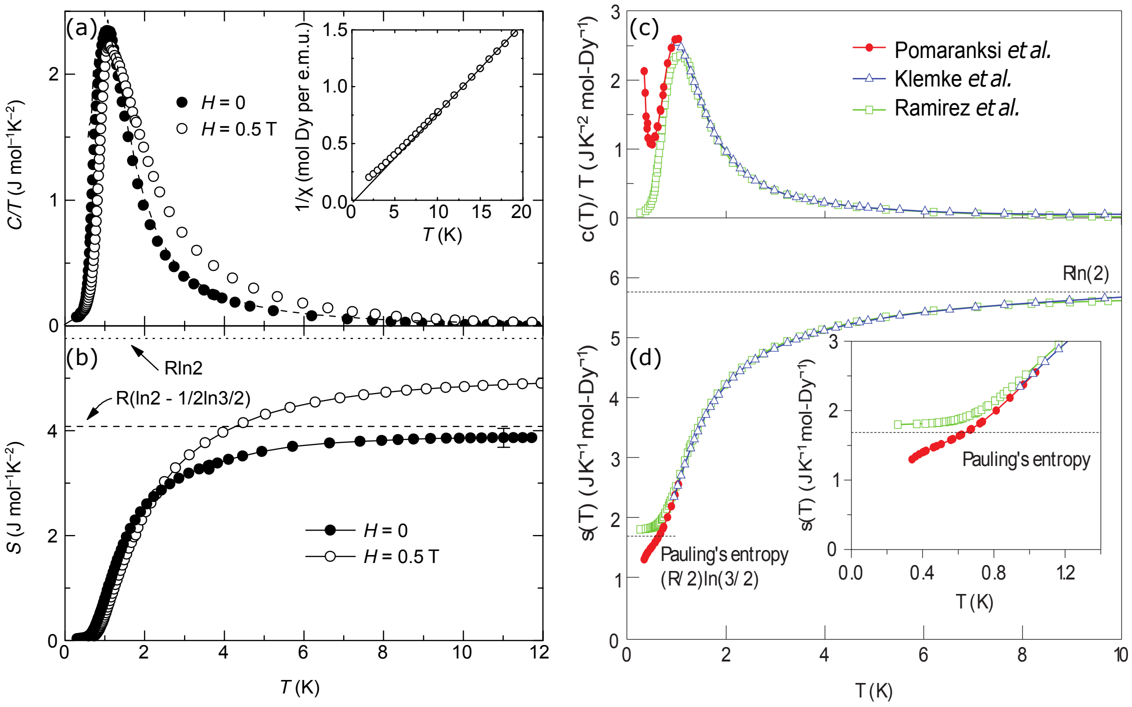

Figure 4.8: Panels (a) and (b) show $C(T)/T$ data and the entropy $S(T)$ of $Dy_2Ti_2O_7$ determined in 1999 [90]. Panel (c): Pomaranski *et al.* published new specific heat data of $Dy_2Ti_2O_7$ in 2013 [20]. Panel (d): The entropy $S(T)$ clearly falls below $R/2\ln(3/2)$.

obtained via integration of $c(T)/T$, see panel (b). $S(T)$ exhibits no temperature-dependence for $T \lesssim 0.7$ K and differs from the value for a two-level system $R\ \ln(2)$ by $1/2\,R\ \ln(3/2)$. This difference corresponds to the predicted value for the residual entropy of water ice [5]. The residual entropy of $1/2\,R\ \ln(3/2)$ in $Dy_2Ti_2O_7$ seemed to be confirmed by various specific heat measurements [19, 91, 92, 117, 118]. In 2013, Pomaranski *et al.* published specific heat data c/T of $Dy_2Ti_2O_7$ [20] which are shown in Fig. 4.8 (c). In contrast to previous approaches, they measured the thermal equilibration of $Dy_2Ti_2O_7$ in order to determine the specific heat. In the experiment, the sample temperature was raised by $\Delta T \approx 5\%$ to 10% above the temperature of the thermal reservoir. By measuring $\Delta T(t)$ up to 60,000 s, non-exponential long-time thermal relaxation was observed below about 0.5 K. Then, the specific heat was obtained via integration over the entire relaxation curve [76]. Due to the non-exponential long-term relaxations, they gain enhanced values of the specific heat and c/T even increases for $T \leq 0.5$ K which is in complete contrast to the previous results [19, 91, 92, 117, 118]. Thus, the entropy of $Dy_2Ti_2O_7$ falls below Pauling's residual entropy. The question whether the entropy completely vanishes in the long-time limit or converges towards a finite but smaller residual entropy

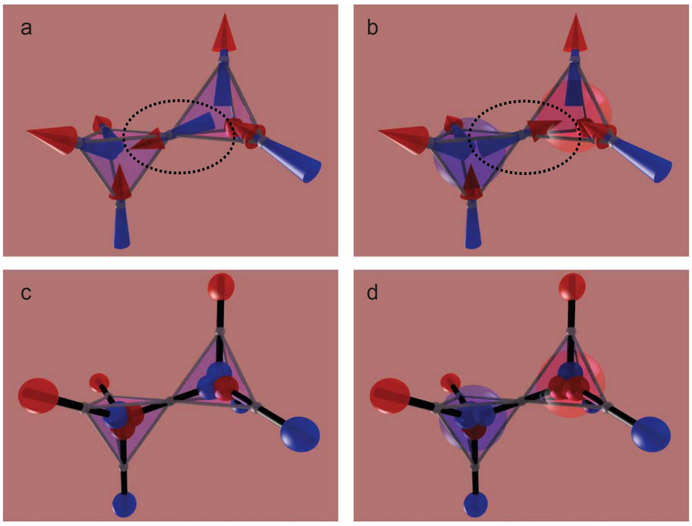

Figure 4.9: (a) The ground state with the 2in-2out configuration. (b) Flipping a single spin creates a pair of a magnetic monopole and anti monopole. (c) The spin-ice ground state can be transformed into an energy "dumbbell" model with different charges. (d) Monopole excitation in the "dumbbell" model. Taken from Ref. 4.

cannot be clearly answered and is still under debate. A discussion of the specific heat and entropy of the dilution series $(Dy_{1-x}Y_x)_2Ti_2O_7$ in magnetic field will follow in Sec. 7.2. The results will also be compared to the data of Refs. 20, 90.

The study on the residual entropy of $Ho_2Ti_2O_7$ is more difficult due to an additional nuclear spin contribution, known to also exist in other Ho^{3+} salts[2]. This nuclear spin contribution is well described by a Schottky anomaly with a theoretical maximum of 0.9 R in the specific heat for Ho($I = 7/2$). The effect originates from a splitting of the eight nuclear levels [99, 120]. The subtraction of the nuclear contribution leads to a considerably large uncertainty in the temperature range of 0.6–0.9 K where the nuclear specific heat rises sharply [99]. Thus, a reliable study on the residual entropy is very complicated. Both, the nuclear contribution and a possible residual entropy would appear at similar temperatures.

4.6 Magnetic monopoles & dumbbell model

In spin-ice materials, the first excited state from the ground state is created by a single spin flip of a spin between two tetrahedra which results in a violation of the ice rule by a transition from a 2in-2out state (see Fig. 4.9 (a)) to 3in-1out and 1in-3out states of neighboring tetrahedra depicted in Fig. 4.9 (b). A pair of a monopole and an antimonopole is established. These lattice excitations are topological defects with properties which are similar to Dirac's magnetic monopoles and are introduced

---

[2] Recently, a nuclear contribution in $Dy_2Ti_2O_7$ is also discussed [119] which however does not account for the increase of c/T found by Pomaranski *et al.* [20].

by Castelnovo *et al.* [4]. Within the model, the dipole interactions of Eq. (4.3) are be replaced by energy "dumbbells" that consist of equal and opposite magnetic charges. These charges are located on the ends of the diamond bonds and are shown in Fig. 4.9 (c). The charges on each diamond bond can be adjusted in two ways and reproduce the two orientations of the original dipole. This constraint fixes the value of the charge at $Q = \pm\mu/a_\mathrm{d}$, with the diamond lattice bond length as $a_\mathrm{d} = \sqrt{3/2}\, r_\mathrm{nn}$.

The Hamiltonian of the energy of a configuration of dipoles which is a result of the pairwise interaction energy of magnetic charges is then given by [4]

$$\mathcal{H} = \frac{\mu_0}{4\pi}\sum_{\alpha<\beta}\frac{Q_\alpha Q_\beta}{r_{\alpha\beta}} + \frac{1}{2}\upsilon_0\sum_\alpha Q_\alpha^2 \tag{4.12}$$

with Q_α as the total magnetic charge at site α and $r_{\alpha\beta}$ as the distance between two sites. The finite self-energy $\upsilon_0/2$ is introduced in order to reproduce the net nearest-neighbor interaction. In Ref. 4, it is shown that Eq. (4.12) is equivalent to the dipolar energy Hamiltonian in Eq. (4.3) up to very small corrections that vanish at least with $1/r^5$. In the model, the system minimizes its energy if each diamond lattice site is net neutral, *i.e.*, $Q_\alpha = 0$. This restriction is only accomplished if the ice rule 2in-2out is respected and leads to the ground state of the system, see Fig. 4.9 (c). Within the dumbbell model, the residual entropy in the low-temperature range directly follows and agrees with the Pauling entropy. Excited states are introduced via flipping a single dipole/dumbbell which generates a local net dipole moment of 2μ. In this case, two adjacent sites with net magnetic charge of $Q_\alpha = \pm q_\mathrm{m} = \pm 2\mu/a_d$ are created. This configuration is equivalent to a pair of a monopole and an antimonopole, see Fig. 4.9 (b) and (d).

This monopole and antimonopole pair can be separated from each other without further violations of the ice rule 2in-2out. Within this separation, the neutrality of the tetrahedra is kept, see Fig. 4.10. However, there is a small energy cost to separate such a pair due to Coulomb interaction which is given by

$$F = -\frac{\mu_0}{4\pi}\frac{q_\mathrm{m}^2}{r}. \tag{4.13}$$

As a consequence of the finite energy cost to bring the monopoles to infinity, the local dipolar excitation of a single spin flip fractionalizes. The so-called Dirac string which connects the separated monopoles in Fig. 4.10 is highlighted in white. The energy of such a Dirac string does not diverge with its length as there are no domain walls along the string. This leads to the deconfinement of the monopoles. The magnetic field lines turn from red to blue by connecting the monopole and antimonopole. The elementary excitations of spin ice with properties similar to Dirac's monopoles were introduced according to Castelnovo *et al.* [4]. However,

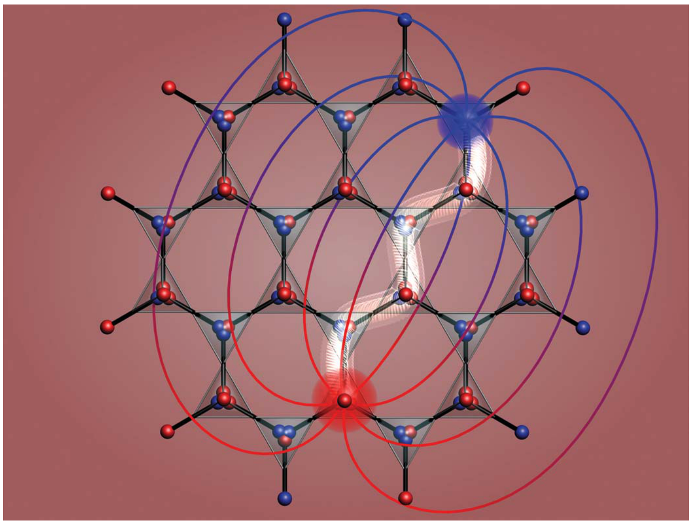

Figure 4.10: A pair of separated monopole and antimonopole (large red and blue balls). The Dirac string is highlighted in white and the lines represent the magnetic field [4].

there are differences between the Dirac condition [7] and the dumbbell model. In Dirac's theorem, it is stated that the electric charge e and any magnetic charge q_{m} must fulfill the following equation

$$e \cdot q_{\mathrm{m}} = \frac{nh}{\mu_0} \tag{4.14}$$

with an integer n. As a consequence, any monopole must be quantized in units of $q_{\mathrm{m}} = h/\mu_0 e \cdot n$. Within the dumbbell model [4], no reference to Dirac's quantization condition Eq. (4.14) is given. The magnitude of a spin ice monopole is given by

$$q_{\mathrm{m}} = \frac{2\mu}{a_{\mathrm{d}}} = \frac{2\mu}{\mu_{\mathrm{B}}} \frac{\alpha \lambda_{\mathrm{C}}}{2\pi a_{\mathrm{d}}} q_{\mathrm{D}} \approx \frac{q_{\mathrm{D}}}{8,000} \tag{4.15}$$

with λ_{C} as the Compton wavelength for an electron and α as the fine-structure constant. The quantized magnetic charge is q_{D}. The charge of a monopole in spin ice can be continuously tuned by applying pressure, because this changes the value μ/a_{d} [4]. In standard electromagnetic theory, the source of a magnetic field can either be a moving charge or a static dipole, but never a static magnetic charge. This is expressed by the Gauss' theorem

$$\nabla \cdot \vec{B} = \nabla \cdot (\vec{M} + \vec{H}) = 0 \tag{4.16}$$

which, however, allows for excitations like in spin ice that correspond to divergences in the magnetic field $\vec{H}$ or in the magnetic moment $\vec{M}$. Thus, the monopoles can be considered as sources and sinks of $\vec{H}$.

4.7 Monopole dynamics

The physics of spin ice are governed by the dipolar model Hamiltonian in Eq. (4.3). Within this model, the magnetic moments of the Dy^{3+} and Ho^{3+} ions are considered to be classical Ising spins pointing along their local easy axis in [111] direction with a nearest-neighbor exchange J and a dipolar energy scale D. Both are considered to be purely Ising type. The model is found to be applicable to describe the thermodynamic properties on a quantitative level [4, 80, 94, 99]. Due to the rise in the specific heat below 0.5 K observed by Pomaranski *et al.* [20], a discussion about possible influences of quantum effects arose [121, 122]. However, Rau *et al.* formulate an estimate of the scale of quantum effects in $Ho_2Ti_2O_7$ and $Dy_2Ti_2O_7$, finding it will below experimentally relevant temperatures [108]. Thus, quantum effects are neglected and the strong Ising character of the spin-ice systems results in a dispersionless excitation spectra, as can be seen schematically in Fig. 4.4. As a consequence, the monopole excitations do not possess a group velocity [108, 123]

$$v_k = \partial\epsilon/\partial k = 0 \tag{4.17}$$

with the dispersion relation $\epsilon(k)$. Due to the absence of v_k, the dynamics of the deconfined quasiparticles (monopoles) in spin ice are diffusive [10, 103]. These quasiparticles are localized in real space rather than in reciprocal space. Thus, the kinetic gas theory can be applied to describe the dynamics of the magnetic monopoles and antimonopoles. The diffusion coefficient is related via

$$D_{\mathrm{mag}} = \frac{\kappa_{\mathrm{mag}}}{c_{\mathrm{mag}}} = \frac{v_{\mathrm{mag}}\ell}{3} = \mu k_{\mathrm{B}} T \tag{4.18}$$

with the magnetic contribution to the heat transport κ_{mag}, to the specific heat c_{mag}, the velocity v_{mag}, the mean-free path ℓ and the mobility of the monopoles μ. The dynamics of the anomalous monopole excitations is subject of intense research [4, 8–10, 14, 49, 92, 103, 111, 113, 124–129] and will also be intensively studied in the following.

In contrast to the above discussed spin-ice materials with strong Ising character like $Dy_2Ti_2O_7$ and $Ho_2Ti_2O_7$, several studies also focus on so-called quantum spin ices which exhibit enhanced quantum effects. Within these systems, the Hamiltonian consists of a matrix of exchange couplings with $J_{ij}^{\mu\nu} = J_{ji}^{\nu\mu}$ and a dispersion relation $\epsilon(k)$ with $v_k \neq 0$ is observed [130]. Among the magnetic pyrochlore materials, $Yb_2Ti_2O_7$, $Er_2Ti_2O_7$, $Pr_2Ti_2O_7$ and possibly $Tb_2Ti_2O_7$ are quantum spin-ice candidates [130–133].

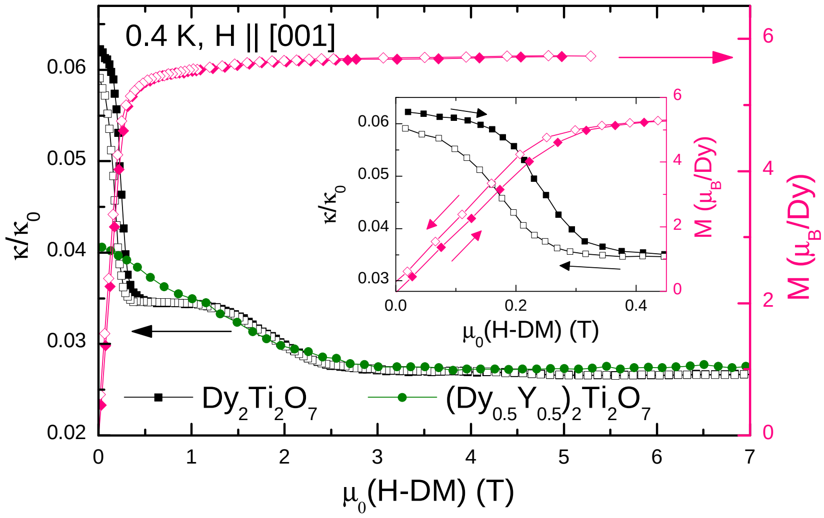

Figure 4.11: Thermal conductivity κ of $Dy_2Ti_2O_7$ and $(Dy_{0.5}Y_{0.5})_2Ti_2O_7$ in comparison with the magnetization $M(H)$. Inset: expanded view of the low-field regime. Adapted from Ref. 16.

4.8 Literature heat transport

In literature some results about the heat transport of $Dy_2Ti_2O_7$ and $Ho_2Ti_2O_7$ are found whereas the dilute spin ice is hardly studied. Klemke *et al.* measured the thermal conductivity of $Dy_2Ti_2O_7$ using the steady-state method and a heat pulse technique in a temperature range from 0.3 K to 30 K in magnetic fields applied along the [110] direction [11]. The heat transport below 10 K is interpreted to be phononic. The temperature dependence of $\kappa(T)$ is attributed to scattering of phonons on magnetic excitations (monopoles) due to a quadratically varying $\kappa(T)$ instead of a cubic temperature dependence expected for boundary scattering in a pure single crystal. Note that even the non-magnetic iso-structural reference compound $Y_2Ti_2O_7$ exhibits a power-law behavior of $T^{2.4}$ below about 4 K [14]. The interpretations of Klemke *et al.* are also not supported by the thermal conductivity data shown in Chaps. 6 and 7.

Sun *et al.* investigate the magnetic-field dependence of low-temperature heat transport of $Dy_2Ti_2O_7$ for different magnetic field directions [12, 13]. In Ref. 12, it is observed that $\kappa(H)$ displays an irreversibility in the Kagomé-ice phase for $\vec{H} \,||\, [111]$ which has no direct correspondence in the magnetization hysteresis. Possible origins of this irreversibility are discussed including a field misalignment effect and a pinning effect of the magnetic monopoles by the weak disorders. In addition, an estimation of the mean free path of phonons at low temperatures suggests that the magnetic excitations (magnetic monopoles) do not make a sizable contribution to heat transport because the experimentally obtained κ is smaller than the phonon term in a boundary scattering limit. In Ref. 13, $\kappa(H)$ of $Dy_2Ti_2O_7$ is studied in magnetic fields up to 14 T along [001], [111] and [110]. Experimentally, it is found that the low-T $\kappa(H)$ isotherms do not only exhibit a steplike decrease at the low-field (< 2 T) magnetic transitions but also a field dependence in the high-field regime (> 7 T). A monopole thermal conductivity is extracted from the $\kappa(H)$ curves for all three magnetic field directions from the suppression of $\kappa(H)$ up to 0.5 T at 0.36 K. These results are compared to Debye-Hückel theory [10] which yields unreasonably too large values for the monopole velocity. This finding is interpreted to be a lack of a descriptions in terms of monopole heat transport. However, the Debye-Hückel theory fails to describe the specific heat of $Dy_2Ti_2O_7$ below ≈ 0.5 K [20, 92] and, thus, is not applicable in this temperature range. As will be discussed below, the thermal conductivity data within this thesis contradict this interpretation and support the existence of a sizable monopole contribution to the heat transport.

Kolland *et al.* also studied the heat transport of spin ice $Dy_2Ti_2O_7$ [14–16] for a magnetic field along the crystallographic axes [001], [110] and [111]. The main findings are a strongly anisotropic thermal conductivity and an experimental evidence for monopole heat transport [14]. Fig. 4.11 shows the corresponding $\kappa(H)$ data for $\vec{H} \,||\, [001]$ together with the dilute reference compound $(Dy_{0.5}Y_{0.5})_2Ti_2O_7$ and the magnetization $M(H)$ of $Dy_2Ti_2O_7$. The $\kappa(H)$ curve of $Dy_2Ti_2O_7$ on raising field (closed black symbols) strongly decreases to ≈40% of the initial value by raising the field from 0 T up to 0.5 T. Then, $\kappa(H)$ reveals a plateau-like feature until it further decreases at about 1.5 T. In the high-field regime, $\kappa(H)$ remains essentially constant up to 7 T. The curve measured with decreasing magnetic field (open black symbols) reveals a low-field hysteresis. The inset shows an expanded view of the low-field hysteresis together with $M(H)$ and it turns out that both properties systematically correlate here and, thus, with the lifting of the ground-state degeneracy for $\vec{H} \,||\, [001]$. As $M(H)$ is essentially saturated for magnetic fields larger than ≈ 0.5 T (except van Vleck susceptibility), it is concluded that the complete suppression of $\kappa(H)$ in a magnetic field of about 0.5 T arises from the loss of monopole mobility or, in other words, the large $\kappa_{\mathrm{mag}}(0\ \mathrm{T})$ is a consequence of the zero-field ground-state degeneracy. The kink around 1.5 T is discussed to be a phononic feature that arises from lattice distortions [15]. This interpretation is also supported by the $\kappa(H)$ data of $(Dy_{0.5}Y_{0.5})_2Ti_2O_7$ in the main panel of Fig. 4.11 (open green symbols). The corresponding data do not show a strong low-field drop, but $\kappa(H)$ slightly decreases up to ≈ 2 T and match the curves of $Dy_2Ti_2O_7$ in the high-field range. In addition, no low-field hysteresis is present. It can be concluded from $\kappa(H)$ and $M(H)$ data that spin-ice physics is essentially suppressed in $(Dy_{0.5}Y_{0.5})_2Ti_2O_7$ [15, 16, 129].

A microscopic model to qualitatively explain this zero-field heat transport of magnetic monopoles in $Dy_2Ti_2O_7$, which is based on the correlation between the field-dependent thermal conductivity $\kappa(H)$ and the magnetization $M(H)$ for $\vec{H} \,||\, [001]$, is introduced by Kolland *et al.* [14, 16]. Fig. 4.12 (a) shows the mapping of the 3D pyrochlore structure containing the corner-sharing tetrahedra to 2D represented by

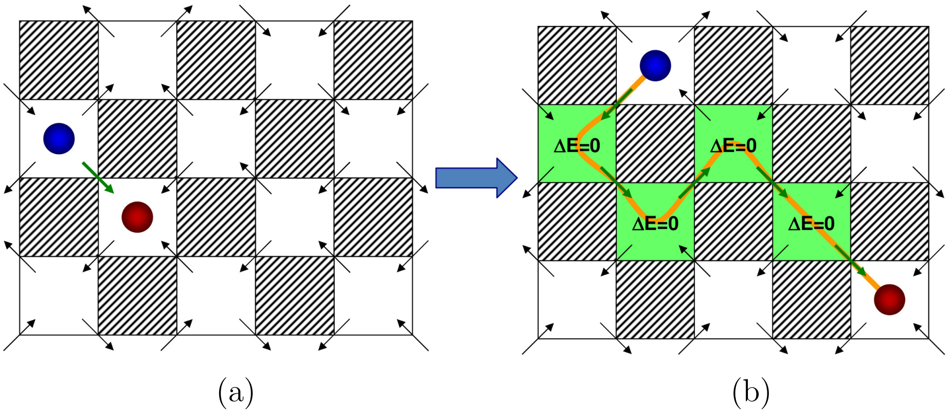

(a) (b)

Figure 4.12: 2D mapping of the 3D pyrochlore structure. The white squares represent the corner-sharing tetrahedra. The arrows indicate the spins which can either point into or out of one tetrahedron. Panel (a): creation of a pair of monopole and antimonopole via a single spin flip. Panel (b): monopole (antimonopole) propagation through the crystal via spin flips. The yellow line symbols the Dirac string of the excitation. Taken from Ref. 16.

the white squares. The arrows indicate the spins. This is not an exact mapping of the 3D structure, however it is a suitable representation to explain the spin-flips in $Dy_2Ti_2O_7$ [79]. Note that the orientation of the spins is randomly distributed with respect to the majority of the tetrahedra being in the 2in-2out spin-ice ground state. One single spin flip (green arrow) creates a pair of monopole and antimonopole (blue & red ball). Once this excitation is created and in zero magnetic field, it can fractionalize and propagate independently through the crystal via additional spin flips without further violating the ice rule, see Fig. 4.12 (b). A finite Coulomb attraction is present $-\mu_0 q_\mathrm{m}^2/(4\pi r)$ with the distance r between a monopole/antimonopole and the magnetic charge q_m according to the dumbbell model [4]. This attraction is obtained from Monte Carlo simulations of a dipolar spin ice [4, 134]. Thus, the monopoles cannot be regarded as completely independently propagating excitations but as weakly confined particles which does, however, not influence the qualitative model. The spins flipped in order to separate the monopole and antimonopole are highlighted in green and form the Dirac string of this excitation [4]. This high mobility in zero magnetic field in spin ice for one excitation originates from the sixfold degenerate ground state, *i.e.* all the 2in-2out configurations are energetically equivalent. Hence, the configuration in panel (a) has the same energy like the configuration shown in panel (b). Note that the estimation is based on the single-tetrahedron approximation introduced in Sec. 4.3 which only includes nearest-neighbor interactions.

Fig. 4.13 (a) shows an equivalent mapping of the 3D pyrochlore lattice to 2D in

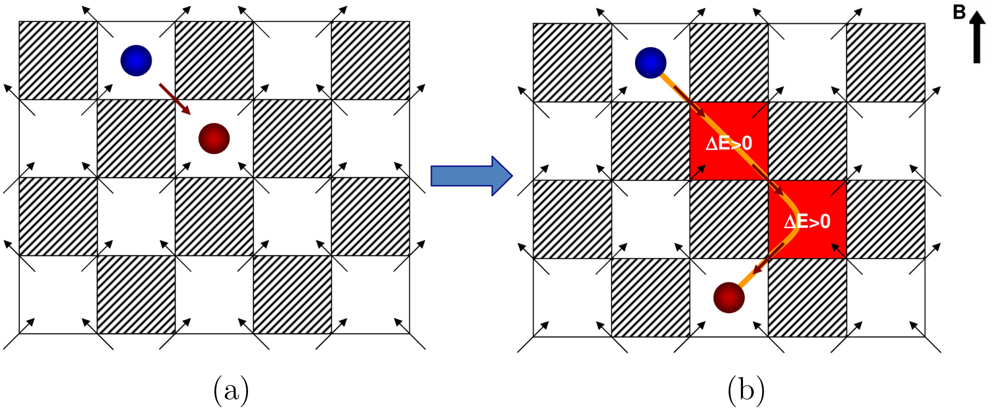

(a) (b)

Figure 4.13: 2D mapping of the 3D pyrochlore structure in finite magnetic field $\vec{H}\,||\,[001]$. Panel (a): creation of a pair of monopole and antimonopole upon a field-induced non-degenerate ground state which consists of one single type of 2in-2out configuration for all tetrahedra. Panel (b): suppressed monopole mobility in a finite field along [001]. Taken from Ref. 16.

a magnetic field $\vec{H}\,||\,[001]$. Note that in a finite field along [001], a field-induced non-degenerate ground state is entered, *i.e.*, the system consists of one single type of 2in-2out configuration for all tetrahedra. This is realized by a configuration in which all the spins have a component parallel to the applied field along [001] represented by the black arrow in the right upper corner. Then, the energy to create an excitation by a single spin flip is increased due to the Zeeman splitting. Hence, the energy cost for the creation of a pair of monopole and antimonopole is increased compared to the same scenario in zero field in Fig. 4.12 (a). This increase of energy is indicated by the red arrow in Fig. 4.13 (a). Fig. 4.13 (b) highlights that the mobility of this excitation is suppressed for this particular field direction because every additional spin flip costs Zeeman energy. Thus, the monopoles and antimonopoles are confined which would result in a suppressed κ_{mag} for $\vec{H}\,||\,[001]$. Hence, the model qualitatively explains the results shown in Fig. 4.11.

The heat transport of the iso-structural spin ice $Ho_2Ti_2O_7$ is less investigated. Toews *et al.* measured the temperature-dependent thermal conductivity for $\vec{H}\,||\,[111]$ down to 0.1 K [18]. A magnetic contribution is obtained via $\kappa(0\text{ T}) - \kappa(8\text{ T})$ which is discussed to both transfer heat and scatter phonons. These magnetic excitations are interpreted as monopole-like excitations whose behavior is described via the Debye-Hückel theory [10]. But the Debye-Hückel theory fails to describe the specific heat below about 0.5 K and, thus, it is not applicable to describe the monopole dynamics there. The field-dependent $\kappa(H)$ data of $Ho_2Ti_2O_7$ in Chap. 6 systematically show that the method applied by Toews *et al.* is not reasonable to extract the monopole contribution to the thermal conductivity.

5 Sample characterization

5.1 Crystal growth

In order to investigate the thermodynamic properties of the spin-ice compounds $Dy_2Ti_2O_7$ and $Ho_2Ti_2O_7$, single crystals of the two mother systems are required. Large single crystals of $Dy_2Ti_2O_7$ were grown by M. Valldor [135] using the floating-zone technique in a mirror furnace and during the diploma thesis of V. Cho [136]. Doping is a powerful tool to separate the different contributions to the specific heat and thermal conductivity. Therefore, single crystals of $(Dy_{1-x}Y_x)_2Ti_2O_7$ with $x = 0.05$–0.4 were grown by P. Laschitzky [137], with $x = 0.5$ by M. Valldor [135] and with $x = 0.75$ by J. F. Welter [138]. The same approach can be applied for $Ho_2Ti_2O_7$. V. Cho synthesized $Ho_2Ti_2O_7$ and the dilute reference systems $(Ho_{1-x}Y_x)_2Ti_2O_7$ with $x = 0.2$–0.5. Within these systems, the magnetic Dy^{3+} or Ho^{3+} are replaced by non-magnetic yttrium ions which exhibit similar ionic radii. Hence, the magnetic contributions are dilute whereas the phononic properties are essentially conserved. Similarly, the phonon contribution can be disturbed by partly replacing the non-magnetic Ti^{4+} (titanium) by non-magnetic Zr^{4+} (zirconium). Thus, single crystals of $Dy_2(Ti_{1-x}Zr_x)_2O_7$ with $x = 0.1$ were grown and analyzed by M. Valldor [135]. $Dy_2(Ti_{1-x}Zr_x)_2O_7$ with $x = 0.05$–0.1 and $Ho_2(Ti_{1\text{-x}}Zr_{\text{x}})_2O_7$ with $x = 0.05$ were synthesized by J. F. Welter [138]. The quality of all crystals was analyzed using X-ray powder diffraction and X-ray Laue diffraction. Another efficient tool in characterizing the samples' quality are magnetization measurements. The corresponding results will be shown in the following.

For the sample growth, the floating-zone method was applied in a mirror furnace. Hereby, the floating zone was run twice through the bars to obtain crystals without cracks. Subsequently, these bars were tempered for approximately 70 hours within an oxygen atmosphere [136–138]. This technique was utilized in order to account for an oxygen deficiency known to occur in spin ice materials [139]. The influence of this oxygen deficiency is investigated in Ref. 139 by comparing magnetization and neutron scattering measurements of as-grown and oxygen-tempered $Dy_2Ti_2O_7$ crystals. It is found that oxygen-vacancy defects suppress magnetic moments on neighboring rare-earth sites and, thus, the saturation magnetization is slightly reduced. Furthermore, these magnetic distortions slow down the long-time monopole

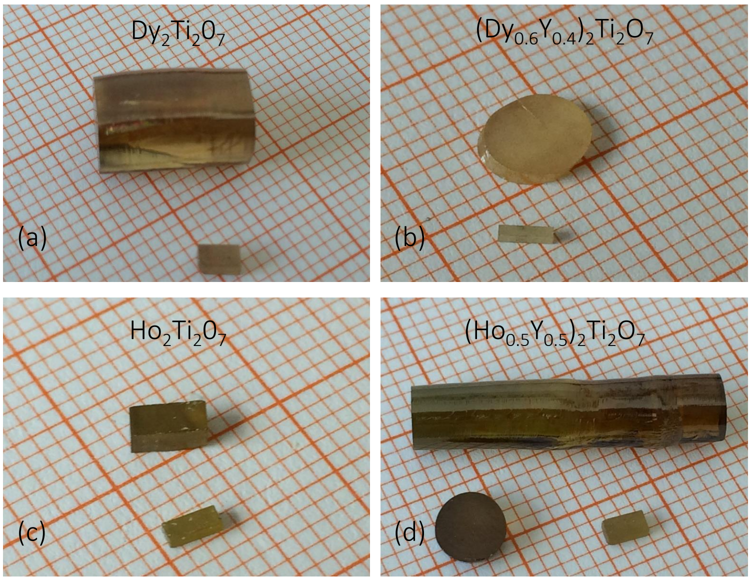

Figure 5.1: Panels (a)-(d): samples of pure spin-ice materials and of yttrium-doped compounds.

dynamics at sub-Kelvin temperatures. After being tempered in oxygen atmosphere, the single crystals were oriented in the X-ray Laue camera and cut into samples with dimensions of approximately $3 \times 1 \times 1\ \mathrm{mm}^3$. Fig. 5.1 (a)-(d) shows single crystals of the pure spin ice materials $Dy_2Ti_2O_7$ and $Ho_2Ti_2O_7$ in comparison with yttrium-doped crystals. Slight variations in the samples' color are observed after applying the floating-zone method twice and tempering in oxygen atmosphere.

5.2 Dilute spin ice: $(Dy_{1\text{-}x}Y_x)_2Ti_2O_7$

5.2.1 Literature

In order to characterize the samples of the different spin-ice compounds and the dilute systems, magnetization measurements are a powerful method to determine the single-crystal quality. The magnetization data can be checked concerning its saturation value and the magnetic anisotropy. Fig. 5.2 (a) shows literature magnetization data of $Dy_2Ti_2O_7$ for a magnetic field applied along the three high-symmetry directions [100], [110] and [111] at 1.8 K [89]. The single-tetrahedron approximation including the Kagomé-ice value are denoted and plotted as solid and dashed lines. The data reveal the strong magnetic anisotropy of $Dy_2Ti_2O_7$ because of the different high-field values of $M(H)$. For all three field directions, the high-field data roughly agree with the model of the single-tetrahedron approximation but all curves reveal a finite slope there. The finite slope originates from the non-collinear local quantization axes of the magnetic ions at the different corners of each tetrahedron.

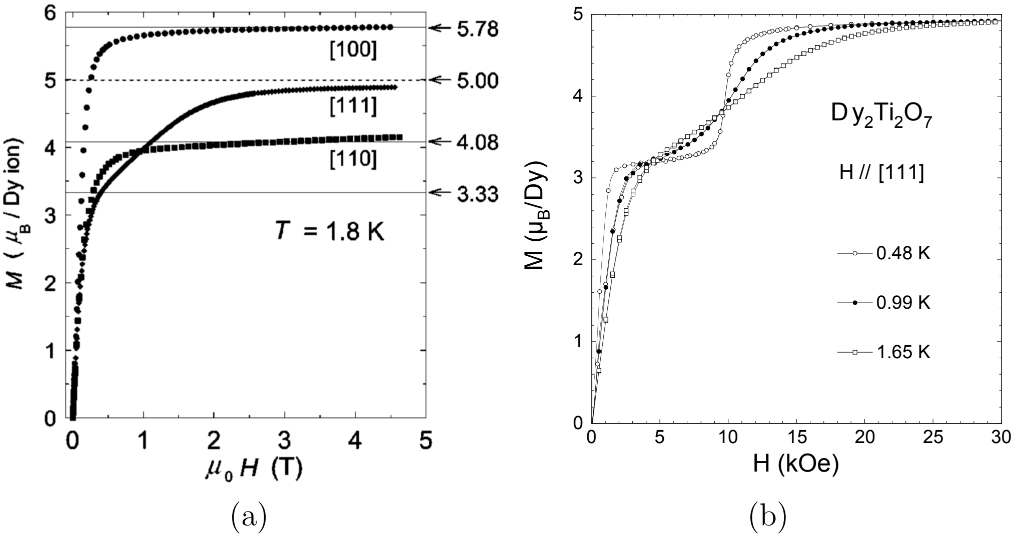

Figure 5.2: Panel (a): comparison of the magnetization of $Dy_2Ti_2O_7$ for a magnetic field applied along the three high-symmetry directions [100], [110] and [111] at 1.8 K, taken from Ref. 89. The theoretical saturation values and the Kagomé-ice plateau value of the single-tetrahedron approximation are denoted and plotted as lines. Panel (b): magnetization of $Dy_2Ti_2O_7$ along [111] in a temperature range from 0.48 K up to 1.65 K, taken from Ref. 117.

Thus, for any direction of the external field the magnetic ions feel a symmetry-breaking transverse field component, which mixes the higher-lying levels into the ground state doublet, that in zero field almost completely consists of $|\pm 15/2\rangle$ for $Dy_2Ti_2O_7$. This effect causes a van Vleck susceptibility which is seen as the finite slope in the high-field magnetization data. In literature, this slope varies between about 0.3 to 1%/T with respect to the absolute value of $M(H)$ [15, 89, 140, 141].

Fig. 5.2 (b) presents the field-dependent $M(H)$ data of $Dy_2Ti_2O_7$ for $\vec{H} \,||\, [111]$ in a temperature range from 0.48 K up to 1.65 K [117]. These curves are measured down into the low-temperature regime where the spin-ice physics occurs in $Dy_2Ti_2O_7$. At 0.48 K, $M(H)$ strongly increases on raising the magnetic field and at about 0.2 T the systems enters the 3-fold degenerate Kagomé-ice phase which is observed as a plateau-like feature. The Kagomé-ice phase has already been discussed in Sec. 4.3 and a visualization of the pyrochlore lattice for a field along [111] is shown in Fig. 4.7 on page 43. A finite slope is observed within the Kagomé-ice phase which arises from a mixing of 3in-1out and 1in-3out configurations to the 2in-2out ground state at finite temperatures. The slope decreases on lowering the temperature. At 1 T, the curve exhibits a sharp jump in $M(H)$ which can be attributed to the transition into the fully-polarized non-degenerate phase. With increasing temperature, the

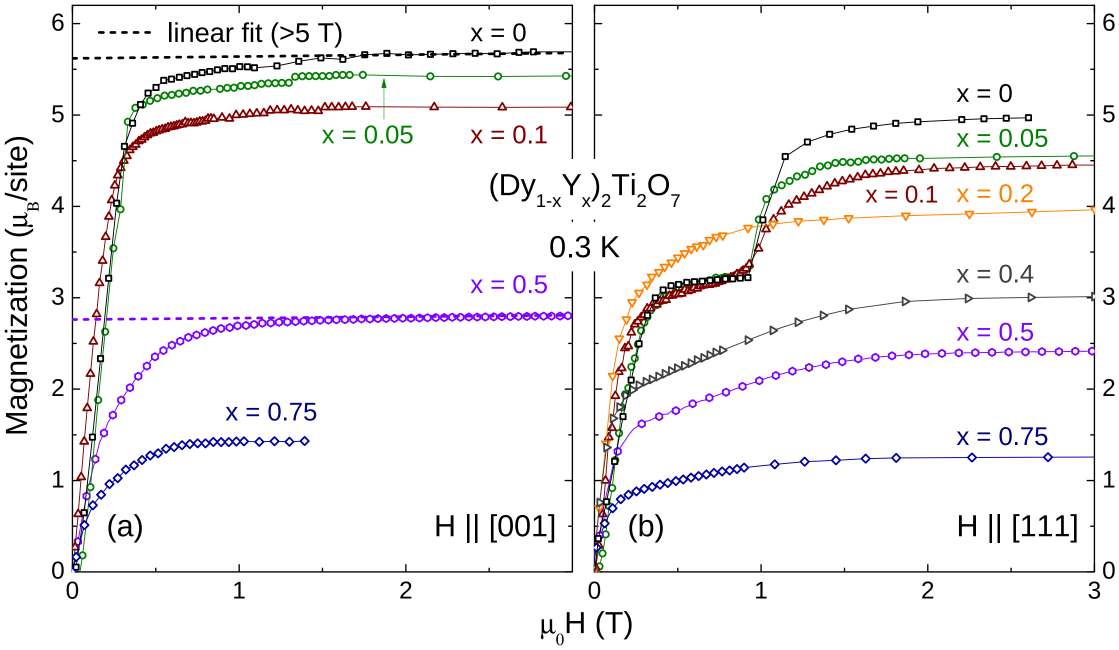

Figure 5.3: Magnetization of $(Dy_{1-x}Y_x)_2Ti_2O_7$ with $x = 0$—0.75 at 0.3 K with $\vec{H}\,||\,[001]$ in panel (a) and with $\vec{H}\,||\,[111]$ in panel (b). Linear fits to the high-field regime to obtain the yttrium content are represented by the dashed lines in panel (a).

Kagomé-ice plateau smears out and is hardly visible at 1.65 K which is consistent with the data in panel (a). Above about 1 K, spin-ice physics is essentially suppressed. Furthermore, the van Vleck susceptibility is also observed in the high-field regime of Fig. 5.2 (b).

5.2.2 Magnetization

All the presented $M(H)$ measurements were performed after zero-field cooling. As can be seen in Fig. 5.3 (a), the $M(H)$ curves of the dilute materials $(Dy_{1-x}Y_x)_2Ti_2O_7$ with $x = 0.05$–0.75 reveal a similar field-dependence like the mother compound $Dy_2Ti_2O_7$ for $\vec{H}\,||\,[001]$. The absolute values of $M(H)$ correlate with the degree of dilution x in the high-field regime above 1 T because the $M(H)$ data are shown in units of μ_B/site (equivalent to μ_B/Dy for $Dy_2Ti_2O_7$). Hence, the saturation value can be used to check the degree of dilution and, thus, the sample quality which will be discussed in the following. For $x = 0$, it turns out that the literature data shown in Fig. 5.2 (a) are reproduced. For high magnetic fields ($H > 2$ T), a finite slope is observed where higher-lying levels are mixed into the ground state doublet $|\pm15/2\rangle$. This van Vleck susceptibility is also observed for the dilute systems.

Magnetization data $M(H)$ are shown in Fig. 5.3 (b) with $\vec{H}\,||\,[111]$ at 0.3 K. Again, the literature data of Fig. 5.2 (b) are well reproduced. At 0.3 K, the Kagomé-ice plateau is even more pronounced. The data also reveal the van Vleck contribution in the high-field regime. Due to this van Vleck susceptibility, which is found in all $M(H)$ curves of the spin ice materials, the yttrium content cannot be simply determined by comparing the saturation value of the $M(H)$ curves to the prediction from the single-tetrahedron approximation. Thus, the yttrium content was checked the following way. In the high-field regime ($5\text{ T} < H < 7\text{ T}$), a linear fit was applied to all $M(H)$ curves. Thus, an y-intercept is obtained for all x. If the y-intercept value for $x = 0$ is considered to be correct, then its relative change for $x > 0$ can be compared to the nominal yttrium content. This method is applied exemplarily to the curves for $x = 0$ and 0.5 represented by the dashed lines in panel (a). It is found that $y_{x=0} = 5.62$ and $y_{x=0.5} = 2.76$ which yields an experimentally obtained content of $x = 0.0509$. Thus, the deviation to the nominal content accounts for about 1.7%. The nominal and the experimentally obtained content agree within 1-2% for all dilutions x [136–138]. Furthermore, the data in Fig. 5.3 (b) show that the Kagomé-state plateau appears in the $M(H)$ data for $x \leq 0.1$. At a dilution level of $x = 0.2$, it is already smeared out and hardly visible. For $x > 0.2$, the Kagomé-ice phase has vanished. This originates from the statistical replacement of the magnetic Dy ions by non-magnetic Y ions according to the dilution x which systematically suppresses spin-ice physics.

5.3 Zirconium doping: $Dy_2(Ti_{1\text{-}x}Zr_x)_2O_7$

Another approach to influence the properties of $Dy_2Ti_2O_7$ is to replace the titanium Ti^{4+} ions by zirconium Zr^{4+}. This is supposed to manipulate the phononic properties of the crystals. Due to similar ionic radii, the Zr^{4+} ions (89.904 g/mol) will be located on the sites of the Ti^{4+} ions (47.949 g/mol) [142]. Fig. 5.4 depicts $M(H)$ data of $Dy_2(Ti_{1-x}Zr_x)_2O_7$ with $x = 0$–0.1 for $\vec{H}\,||\,[111]$ at 0.3 K. The field dependencies are similar for all x but it is observed that the Zr doping systematically shifts the transition temperature into the fully-polarized phase to higher magnetic fields. It is shifted from approximately 0.96 T ($x = 0$) to 1.05 T ($x = 0.1$). Hence, the effective nearest-neighbor coupling $J_{\text{eff}} = J_{\text{nn}} + D_{\text{nn}}$ seems to be increased, see Eq. (4.5) and (4.6). This can be explained by the increased ionic radii of the Zr ions $r = 0.72$ Å compared to the Ti ions $r = 0.61$ Å [142]. In Ref. 53, the magnetic Grüneisen ratio of $Dy_2Ti_2O_7$ is determined and under considerations of J_{eff} being

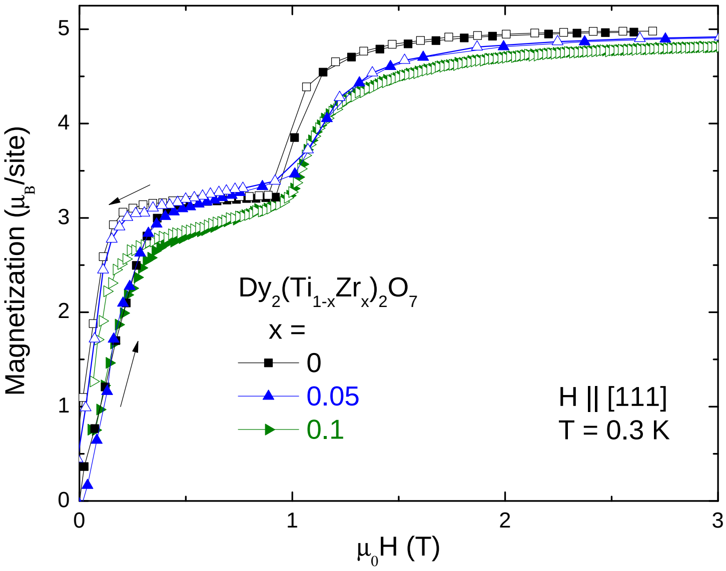

Figure 5.4: Magnetization of $Dy_2(Ti_{1-x}Zr_x)_2O_7$ with $x = 0$–0.1 for $\vec{H} \,||\, [111]$ at 0.3 K.

the dominant energy scale it follows

$$\frac{\partial \ln J_{\text{eff}}}{\partial p_i} = -0.29\%\text{GPa}^{-1}. \tag{5.1}$$

In Eq. (5.1), the negative sign symbols that J_{eff} decreases by applying pressure on the crystal. Note that $D_{\text{nn}} > 0$ whereas the nearest-neighbor coupling is antiferromagnetic $J_{\text{nn}} < 0$. By applying pressure on the system, D_{nn} increases because $D_{\text{nn}} \propto 1/r^3$, see Eq. (4.3). Thus, the increase of J_{nn} must be comparably larger as J_{eff} increases in total. Because $r_{\text{Zr}} > r_{\text{Ti}}$, local lattice distortions arise for $x > 0$ and, thus, a negative chemical pressure is created. According to Eq. (5.1), a negative chemical pressure leads to an increased J_{eff} and as a consequence the transitions into the fully-polarized phase shift to higher magnetic fields with increasing x, see Fig. 5.4. This finding is also consistent with literature where J_{eff} is found to be sensitive to the lattice constant [143, 144]. For example, a reduction of the lattice constant by approximately 1.68% from $Dy_2Ti_2O_7$ to $Dy_2Ge_2O_7$ results in a decrease of J_{eff} from about 1.3 K to 0.67 K [143]. It will be discussed in the following that the Zr doping also influences the magnetic contribution to the thermal conductivity. For $x = 0.05$ and 0.1, a slope is observed within the Kagomé-ice phase whose origin is unclear. It is most likely related to the fact that the magnetic field was increased too fast. Hence, the systems could not equilibrate. As will be discussed for $Ho_2(Ti_{0.95}Zr_{0.05})_2O_7$, the $M(H)$ data reproduce the data of $Ho_2Ti_2O_7$ concerning the slope within the Kagomé-ice phase. All curves reveal a low-field hysteresis. This remnant magnetization originates from the Kagomé-ice phase which is entered by increasing the magnetic field. Within this phase the triangular planes are fully polarized whereas the ice rule is not violated. Thus with decreasing field, the system remains in this configuration which exhibits a net-magnetization along [111]

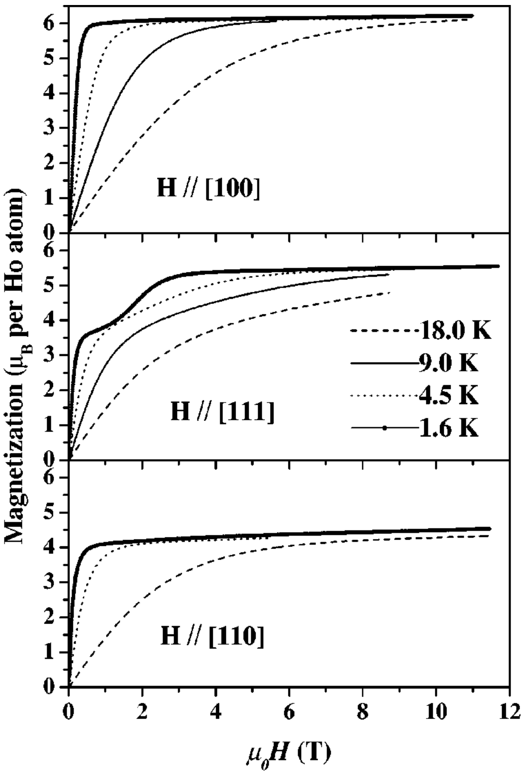

Figure 5.5: Field dependence of the magnetization of $Ho_2Ti_2O_7$ for magnetic fields applied along the three high symmetry directions [100], [110] and [111] in a temperature range from 1.6 K up to 18 K. Taken from Ref. 145.

and results in the low-field hysteresis.

5.4 Dilute spin ice: $(Ho_{1-x}Y_x)_2Ti_2O_7$

5.4.1 Literature

The magnetization of $Ho_2Ti_2O_7$ is already known from literature [145–147]. Fig. 5.5 shows the magnetization data as a function of the external magnetic field along the three high-symmetry directions [100], [111] and [110] taken from Ref. 145. All the curves reveal the finite slope originating from the van Vleck susceptibility in the high-field regime above about 3 T where higher-lying levels are mixed to the almost purely $|\pm 8\rangle$ ground state of the Ho^{3+} ions. For $\vec{H} \,||\, [100]$ and at 1.6 K, $M(H)$ exhibits a strong increase in the low-field range and almost saturates at $\approx 6\ \mu_B$/Ho. With increasing temperature, the low-field slope decreases and the curves approach a Brillouin-like shape. For a magnetic field along [111], $M(H)$ strongly increases towards the Kagomé-ice plateau which reveals a finite slope at 1.6 K. This plateau has vanished at higher temperatures ($T \geq 4.5$ K). Due to the larger effective nearest-neighbor coupling $J_{\text{eff}} = 1.8$ K of $Ho_2Ti_2O_7$ compared to $J_{\text{eff}} = 1.1$ K in

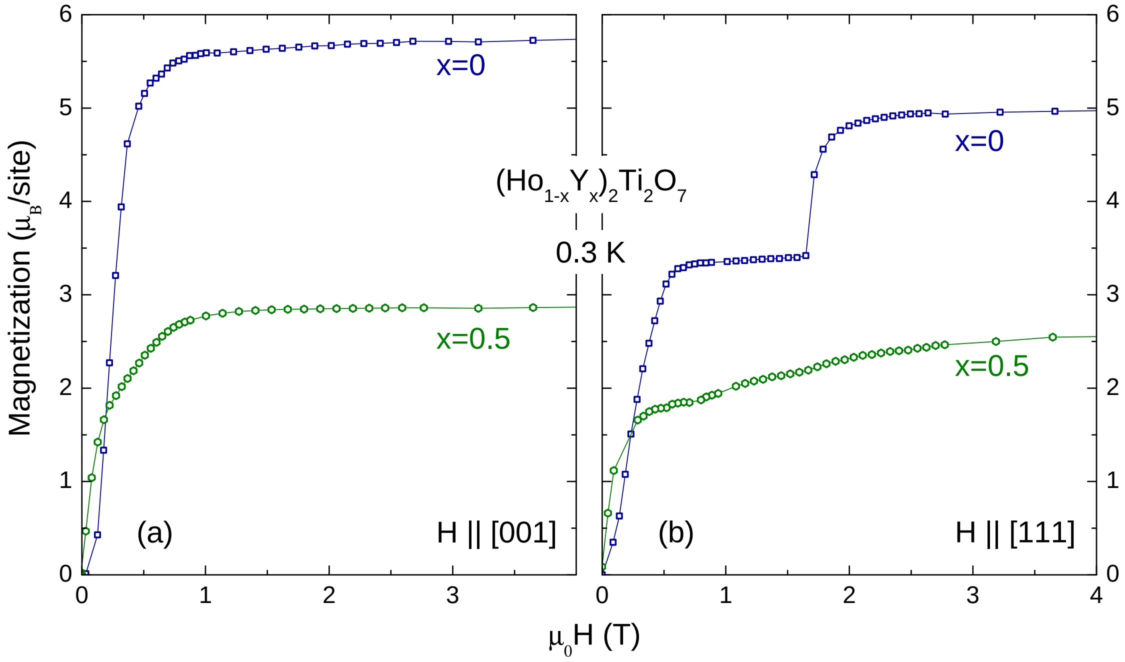

Figure 5.6: Magnetization of $(Ho_{1-x}Y_x)_2Ti_2O_7$ with $x = 0$–0.75 at 0.3 K with $\vec{H}\,||\,[001]$ in panel (a) and with $\vec{H}\,||\,[111]$ in panel (b).

$Dy_2Ti_2O_7$, the transition into the fully-saturated phase shifts to higher magnetic fields and occurs at about 1.5 T. The absolute values of the $M(H)$ curves in Fig. 5.5 clearly exceed the predictions of the single-tetrahedron approximation 5.78 μ_B/Ho for $\vec{H}\,||\,[100]$, 5 μ_B/Ho for $\vec{H}\,||\,[111]$ and 4.08 μ_B/Ho for $\vec{H}\,||\,[110]$, respectively. On the one hand, this is related to the van Vleck susceptibility. But on the other hand, it can be seen that this deviation is too large to originate purely from this contribution. The magnetization data of Ref. 145 were obtained using an Oxford Instruments vibrating sample magnetometer (VSM). The absolute accuracy is indicated to be $\approx 3\%$ whereas the deviation accounts for $\approx 7\%$. Literature high quality magnetization data for all three field directions would be desirable[1].

5.4.2 Magnetization

The magnetization of $(Ho_{1-x}Y_x)_2Ti_2O_7$ was obtained after cooling in zero magnetic field. As can be seen in Fig. 5.6 (a) and (b), all the curves reveal the finite slope in the high-field regime originating from the van Vleck susceptibility. For $Ho_2Ti_2O_7$, the field dependence is consistent with the literature data but the absolute values

---

[1] In Ref. 147, the magnetization is only measured for $\vec{H}\,||\,[111]$.

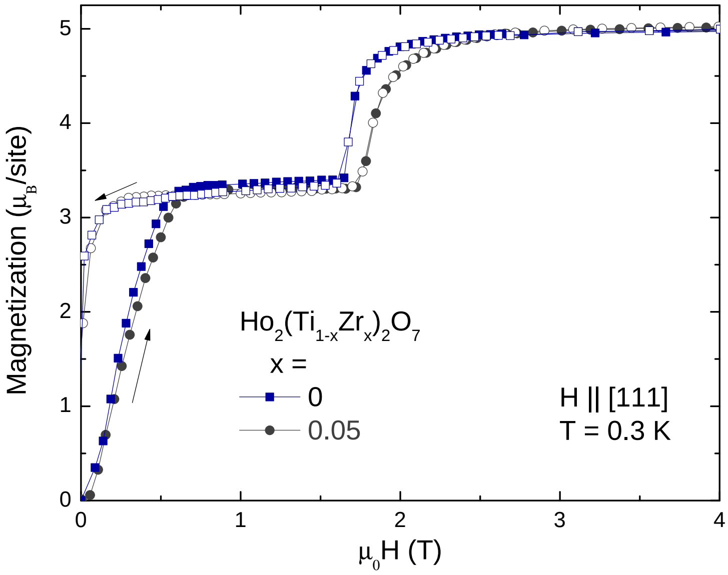

Figure 5.7: Magnetization of $Ho_2(Ti_{1\text{-}x}Zr_x)_2O_7$ with $x = 0$ and 0.05 for $\vec{H} \,||\, [111]$ at 0.3 K.

of $M(H)$ are slightly reduced which is however consistent with the $M(H)$ data of $Dy_2Ti_2O_7$, compare to Fig. 5.3. For $\vec{H} \,||\, [111]$ and $x = 0$, $M(H)$ is almost constant within the Kagomé-ice phase and the transition into the fully-polarized phase occurs in form of a sharp kink at about 1.6 T which is in good agreement with literature and the enhanced effective nearest-neighbor coupling $J_{\text{eff}} = 1.8$ K. For $x = 0.5$, similar field dependencies are observed compared to the pure system but the absolute values are clearly reduced due to the statistical replacement of Dy^{3+} ions by Y^{3+}. Furthermore, the characteristics of the Kagomé-ice phase have essentially vanished with $\vec{H} \,||\, [111]$ and no transition feature is observed. As discussed in Sec. 5.2.2, the nominal yttrium content was checked by applying a linear fit to the high-field ($5\text{ T} < H < 7\text{ T}$) magnetization data for all x. Then, the relative decrease of the y-intercept with increasing x is compared to the value of the pure compound $Ho_2Ti_2O_7$ which is considered to be correct. This yields a relative yttrium content which can be compared to the nominal content. They agree within 1-2% for all dilutions [136, 138].

5.5 Zirconium doping: $Ho_2(Ti_{1\text{-}x}Zr_x)_2O_7$

Fig. 5.7 compares the magnetization of $Ho_2Ti_2O_7$ with the zirconium-doped compound $Ho_2(Ti_{1\text{-}x}Zr_x)_2O_7$ with $x = 0.05$ at 0.3 K for $\vec{H} \,||\, [111]$. The $M(H)$ curves with increasing and decreasing field of both compounds nearly exactly match each other below about 1.6 T where the data show an almost constant Kagomé-ice plateau and a low-field hysteresis with a remnant magnetization. As discussed above, the remnant magnetization originates from the fully-polarized

Kagomé-ice planes which results in a net magnetization along [111]. Similarly to $Dy_2(Ti_{1-x}Zr_x)_2O_7$ in Sec. 5.3, the transition into the fully-polarized phase shifts to a distinct higher field from 1.6 T for $x = 0$ to 1.8 T for $x = 0.05$ by partly replacing Ti^{4+} by Zr^{4+}. The origin of this effect can be explained straightforwardly by the Grüneisen ratio which was determined for $Dy_2Ti_2O_7$, see Eq. (5.1), and is also applicable for the iso-structural $Ho_2Ti_2O_7$. A rising negative chemical pressure is created by an increasing x due to the enhanced ionic radii of the Zr ions which locally distort the lattice. This results in an enhanced J_{eff}. In Ref. 138, it is reported that a single crystal with $x = 0.1$ could not be synthesized for the Ho-based materials due to an arising instability of the growth process within the mirror furnace. The grown crystals were extremely fragile and Laue X-ray diffraction proved the absence of single crystallinity. Up to now, it is unclear why the Dy-based compounds $Dy_2(Ti_{1-x}Zr_x)_2O_7$ allow for higher doping with Zr.

6 $Ho_2Ti_2O_7$ vs. $Dy_2Ti_2O_7$

As already discussed, a finite magnetic contribution in zero field was extracted for $Dy_2Ti_2O_7$ by consideration of the field-dependence of the heat transport κ and a comparative study with $(Dy_{0.5}Y_{0.5})_2Ti_2O_7$ by Kolland *et al.* [14, 16]. Toews *et al.* extracted a κ_{mag} for $Ho_2Ti_2O_7$ by measurements of $\kappa(T)/T$ at different fixed magnetic fields [18]. On the basis of these results, a comparison of the heat transport between the two spin-ice compounds $Ho_2Ti_2O_7$ and $Dy_2Ti_2O_7$ is of great interest. A comparative study with the dilute compounds $(Ho_{0.5}Y_{0.5})_2Ti_2O_7$ and $(Dy_{0.5}Y_{0.5})_2Ti_2O_7$ is performed in order to fully understand the dominant mechanisms in κ of both compounds. The interpretations are additionally supported by magnetization $M(H)$ and magnetostriction $\Delta L/L$ data. Furthermore, the thermal conductivity of the pure spin-ice systems is compared to the corresponding data of the zirconium-doped compounds $Ho_2(Ti_{1\text{-x}}Zr_{\text{x}})_2O_7$ and $Dy_2(Ti_{1-x}Zr_x)_2O_7$.

6.1 Literature results

The comparative study between the heat transport of $Ho_2Ti_2O_7$ and $Dy_2Ti_2O_7$ can be motivated by the presentation of previous results on $Ho_2Ti_2O_7$, namely temperature dependent $\kappa(T)/T$ data of Toews *et al.* [18] which are shown in Fig. 6.1 (a). The corresponding data for $Dy_2Ti_2O_7$ are depicted in panel (b). Comparable scales are applied. Note that $\vec{H} \,||\, \vec{j} \,||\, [111]$ is applied for $Ho_2Ti_2O_7$ and $\vec{H} \,||\, \vec{j} \,||\, [001]$ for $Dy_2Ti_2O_7$. Toews *et al.* observed that $\kappa(8\ \mathrm{T})/T$ is suppressed compared to $\kappa(0\ \mathrm{T})/T$ in the low-temperature regime $T \lesssim 0.65$ K and a magnetic contribution to κ is extracted via $\kappa(0\ \mathrm{T}) - \kappa(8\ \mathrm{T})$. This magnetic contribution is interpreted to originate from monopole-like excitations and their behavior is described via existing Debye-Hückel theory [10]. As can be seen in Fig. 6.1 (b), the field dependence of the corresponding $\kappa(T)/T$ data of $Dy_2Ti_2O_7$ is much more pronounced and persists up to higher temperatures $T > 1.1$ K. Note that the $\kappa(T)/T$ data of $Dy_2Ti_2O_7$ are consistent with the data of Kolland *et al.* [14, 16] where the magnetic contribution to the heat transport is extracted by consideration of the temperature- and field-dependent thermal conductivity and additional measurements on the dilute reference material $(Dy_{0.5}Y_{0.5})_2Ti_2O_7$. Kolland *et al.* finally extract κ_{mag} by

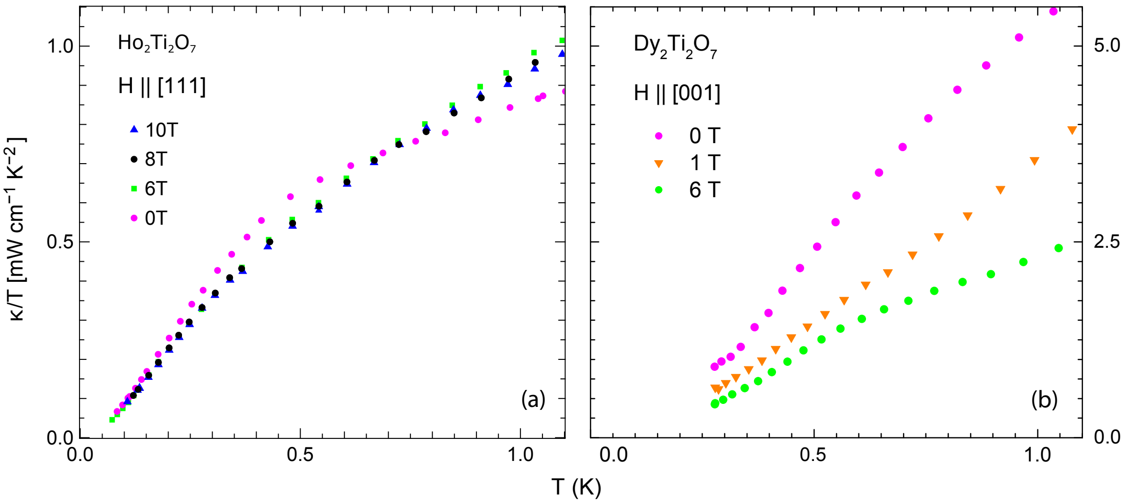

Figure 6.1: Panel (a): thermal conductivity $\kappa(T)/T$ of $Ho_2Ti_2O_7$ at different fixed magnetic fields obtained by Toews *et al.* [18]. Panel (b): thermal conductivity $\kappa(T)/T$ of $Dy_2Ti_2O_7$. Comparable scales are applied.

obtaining $\kappa(0\ \text{T}) - \kappa(0.5\ \text{T})$ for $Dy_2Ti_2O_7$ with $\vec{H}\,||\,[001]$ due to a significant low-field suppression of $\kappa(H)$ which systematically correlates with $M(H)$ data and the spin-ice physics [14]. Because of these discrepancies, a comparative study of the field-dependence of $Ho_2Ti_2O_7$ and $Dy_2Ti_2O_7$ is performed.

6.2 Experimental results

6.2.1 Magnetic field || [001]

Fig. 6.2 compares representative measurements of $\kappa(H)$ for both materials $Ho_2Ti_2O_7$ (blue) and $Dy_2Ti_2O_7$ (black) in the temperature range from 0.4 to 4 K. The curves reveal that the overall field dependencies of $\kappa(H)$ in the higher field range are very different. $Dy_2Ti_2O_7$ shows a continuous decrease of $\kappa(H)$ above about 1.5 T, whereas $\kappa(H)$ of $Ho_2Ti_2O_7$ increases with magnetic field. As can be seen in Fig. 6.3, the magnetization of both materials for $\vec{H}\,||\,[001]$ is essentially saturated above about 1 T in this low-temperature range. The opposite field dependencies of $\kappa(H)$ are not related to the spin-ice physics, which mainly takes place below 1 T. In the field range below about 0.5 T, $\kappa(H)$ of both materials are essentially similar. Both show a rapid drop, which can be attributed to a field-induced suppression of $\kappa_{\text{mag}}(H)$. In particular towards higher temperature, this effect is significantly less pronounced in $Ho_2Ti_2O_7$ than it is in $Dy_2Ti_2O_7$. On this qualitative level, the

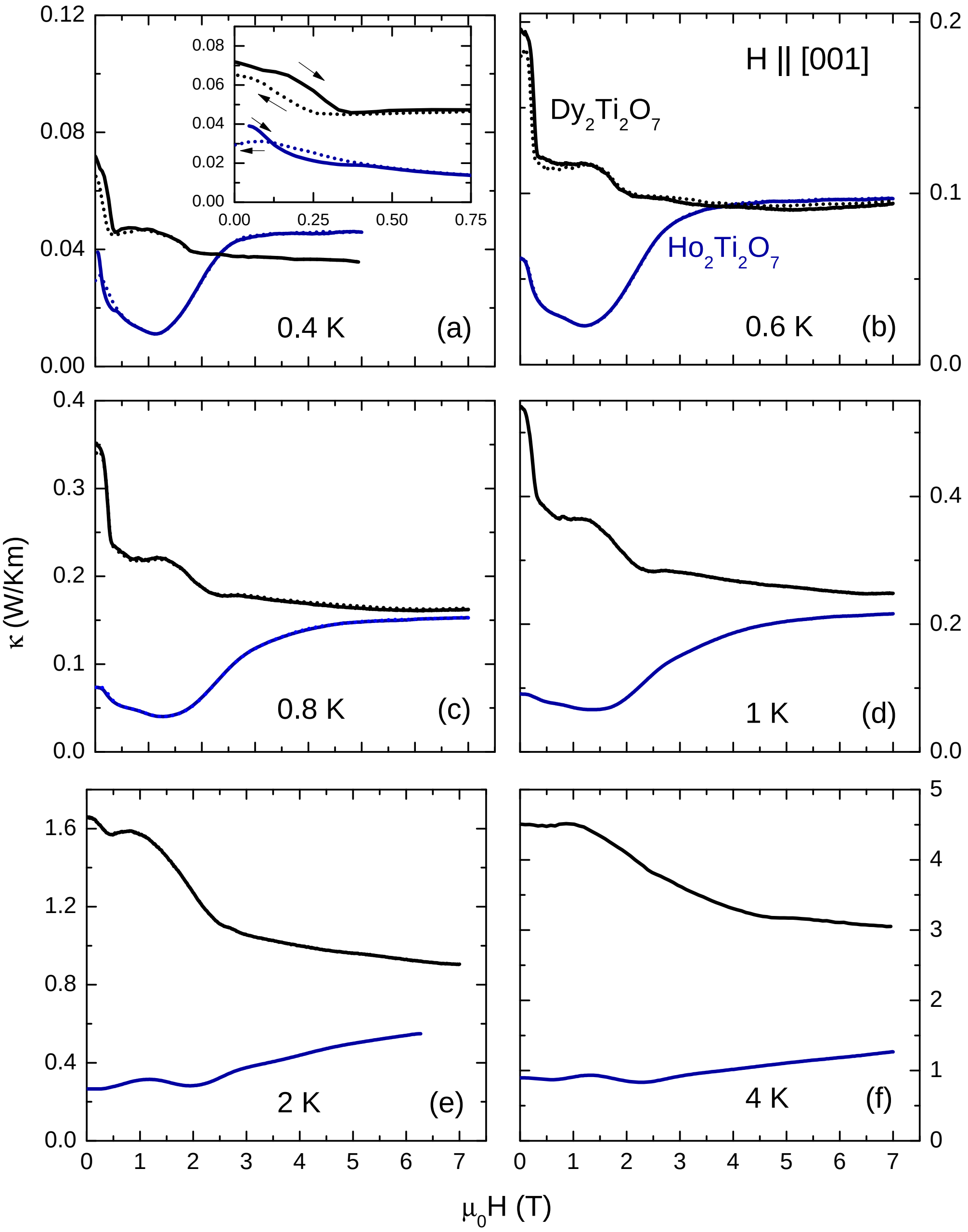

Figure 6.2: Thermal conductivity $\kappa(H)$ of $Dy_2Ti_2O_7$ (black) and $Ho_2Ti_2O_7$ (blue) as a function of the magnetic field $\vec{H} \,||\, [001]$ in the temperature range $0.4\ \mathrm{K} \leq T \leq 4\ \mathrm{K}$. The inset of panel (a) shows an expanded view of the low-field range at 0.4 K. The arrows indicate the field-sweep direction.

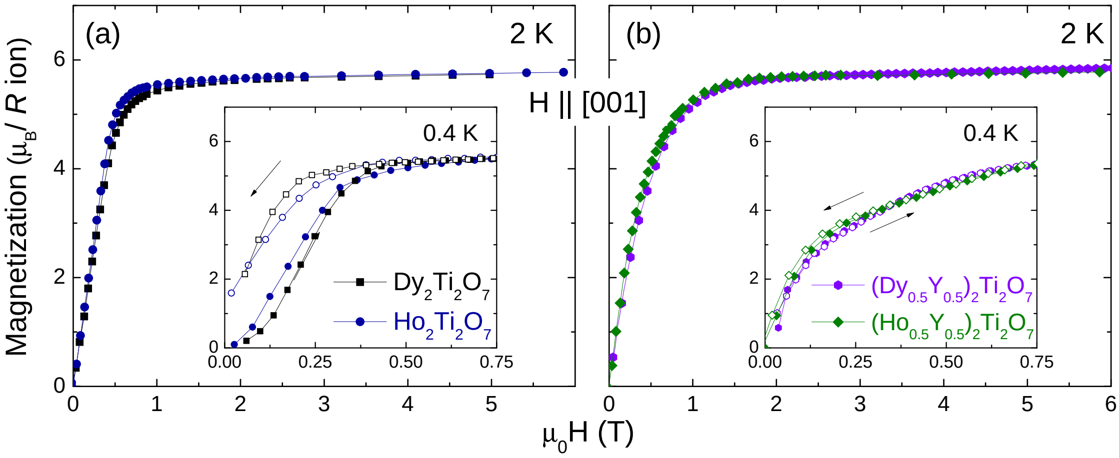

Figure 6.3: Panel (a): Magnetization $M(H)$ with $R = $ Ho or Dy. All the data were measured with increasing and decreasing magnetic field, but hysteresis effects only occur below about 0.6 K, as can be exemplary seen in the inset for 0.4 K. Panel (b): $M(H)$ of the half-doped compounds $(Ho_{0.5}Y_{0.5})_2Ti_2O_7$ and $(Dy_{0.5}Y_{0.5})_2Ti_2O_7$. Even at 0.4 K no sizable hysteresis is present (see inset).

data of Fig. 6.2 seem to confirm the previous result of Toews *et al.* [18] shown in Fig. 6.1 (a).

In order to get a more quantitative estimate of $\kappa_{\text{mag}}(H)$ of $Ho_2Ti_2O_7$ from the thermal conductivity data, the field dependence of the underlying phonon contribution $\kappa_{\text{ph}}(H)$ is required. Therefore, heat transport measurements on the highly dilute compounds $(Dy_{0.5}Y_{0.5})_2Ti_2O_7$ and $(Ho_{0.5}Y_{0.5})_2Ti_2O_7$ were performed. Within these materials, half of the magnetic ions are replaced by non-magnetic Y^{3+}. It is expected that the spin-ice physics is essentially suppressed in the half-doped crystals [14, 16]. This is confirmed by the magnetization data for $\vec{H} \,||\, [001]$. The $M(H)$ data of the spin-ice materials in Fig. 6.3 (a) are very similar and reveal a hysteresis in the low-field regime below 0.5 T at 0.4 K, see inset. The corresponding $M(H)$ curves of the dilute systems in Fig. 6.3 (b) do not show any hysteresis even at low temperatures of $T = 0.4$ K (inset). Furthermore, the characteristic Kagomé-ice plateau in the $M(H)$ curves for $\vec{H} \,||\, [111]$ has vanished in the dilute material, see Fig. 5.3 (b) on page 58.

In Fig. 6.4, characteristic $\kappa(H)$ curves of $(Dy_{0.5}Y_{0.5})_2Ti_2O_7$ and $(Ho_{0.5}Y_{0.5})_2Ti_2O_7$ are compared in the temperature range of $0.4\text{ K} \leq T \leq 4$ K. It is found that $\kappa(H)$ of $(Dy_{0.5}Y_{0.5})_2Ti_2O_7$ monotonically decreases in the whole field range up to 7 T. In contrast, all $(Ho_{0.5}Y_{0.5})_2Ti_2O_7$ data reveal a monotonic increase in the high-field range whereas $\kappa(H)$ exhibits a small low-field drop at 0.4 and 0.6 K which has completely vanished at 1 K. At 4 K, $\kappa(H)$ decreases up to ≈ 2 T and then

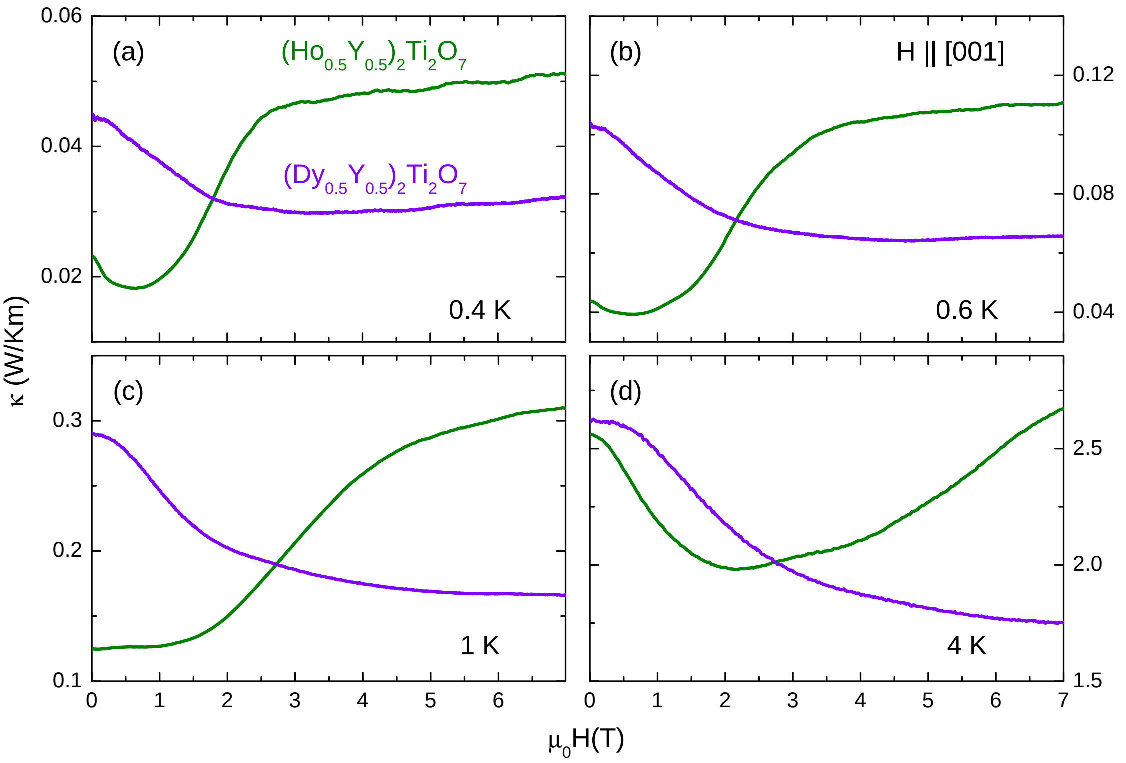

Figure 6.4: Thermal conductivity along the [001] direction of $R\mathrm{YTi_2O_7}$ with $R = \mathrm{Dy}$ (violet) and $R = \mathrm{Ho}$ (green) as a function of the magnetic field $\vec{H} \parallel [001]$ for different temperatures.

also shows the high-field increase. As the spin-ice physics in these materials is almost completely suppressed, these data yield clear evidence that the opposite field dependencies of $\kappa(H)$ of the Dy- and the Ho-based materials arise from different field dependencies of the phononic background. This raises the question why $\kappa_{\mathrm{ph}}(H)$ decreases with increasing field in $(\mathrm{Dy_{0.5}Y_{0.5}})_2\mathrm{Ti_2O_7}$ and increases in $(\mathrm{Ho_{0.5}Y_{0.5}})_2\mathrm{Ti_2O_7}$. As localized magnetic moments may serve as scattering centers for the phonons and because spin flips are suppressed in large magnetic fields, this mechanism can explain an increase of $\kappa_{\mathrm{ph}}(H)$ as it is observed in $(\mathrm{Ho_{0.5}Y_{0.5}})_2\mathrm{Ti_2O_7}$, but it cannot explain the decreasing $\kappa_{\mathrm{ph}}(H)$ of $(\mathrm{Dy_{0.5}Y_{0.5}})_2\mathrm{Ti_2O_7}$. As it has already been discussed by Kolland *et al.* [15], the decrease of $\kappa_{\mathrm{ph}}(H)$ is probably related to magnetic-field induced lattice distortions. These distortions arise from the fact that the local quantization axes of the magnetic ions at the different corners of each tetrahedron are not collinear. Consequently, for any direction of the external magnetic field at least 3/4 of the magnetic ions feel a symmetry-breaking transverse field component, which mixes the higher-lying levels into the ground state doublet, which in zero field almost completely consists of the $\pm J_z^{\mathrm{max}}$ state [100–102]. This

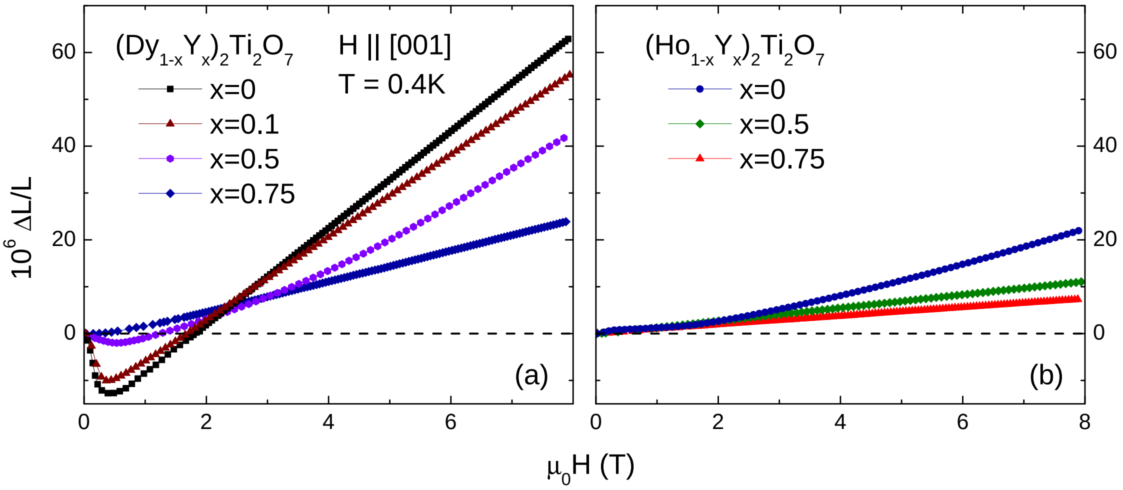

Figure 6.5: Field dependent measurements of the magnetostriction $\Delta L(H)/L$ of $(Dy_{1-x}Y_x)_2Ti_2O_7$ and $(Ho_{1-x}Y_x)_2Ti_2O_7$ for $\vec{H} \,||\, [001]$ at 0.4 K.

effect causes a van Vleck susceptibility, which is seen as a finite positive slope in the high-field magnetization data, see Chap. 5. A further consequence is a pronounced anisotropic magnetostriction, *i.e.* field-induced length changes $\Delta L_i(H)$.

A significant elongation of $\Delta L_i || H$ and weak contractions of $\Delta L_i \perp H$ were found for $Dy_2Ti_2O_7$ in Ref. 15. Within a simplified classical picture, such field-induced lattice distortions may be visualized as resulting from the finite torques $\vec{\mu} \times \vec{H}$, which tend to align the non-collinear localized magnetic moments towards the field direction. With respect to the phononic heat transport, $\kappa_{\rm ph}(H)$ may decrease with increasing field due to the reduced lattice symmetry. In addition, the spin-flip rate may also increase due to the stronger mixing of the $\pm J_z^{\rm max}$ states with other J_z levels, but this effect should vanish towards larger fields when spin flips are suppressed by the enhanced Zeeman splitting. Summarizing the discussion so far, there are different mechanisms which may either increase or decrease $\kappa_{\rm ph}(H)$ and it is difficult to predict which of them dominates. Experimentally, it is found that the Dy- and the Ho-based materials are very different in this respect and this difference is not restricted to $\kappa_{\rm ph}(H)$. As is shown in Fig. 6.5 for $\vec{H} \,||\, [001]$ at 0.4 K, the magnetostriction for the Dy-based materials $(Dy_{1-x}Y_x)_2Ti_2O_7$ is about ≈ 4 times larger than that of the corresponding Ho-based ones. Moreover, $\Delta L/L$ correlates for both compounds with the degree of the dilution x, *i.e.* with the content of the magnetic Dy^{3+} (Ho^{3+}) ions, respectively. The low-field contraction of $(Dy_{1-x}Y_x)_2Ti_2O_7$ for $0 \leq x \leq 0.5$, which results in a minimum at about 0.75 T, also correlates with the dilution and probably originates from the fact that the systems enter a non-degenerate ground state for finite fields along [001] and are magnetized up to ≈ 0.75 T. This rearrangement of all the spins pointing along their local {111} direction in order to have a component parallel to the external field results in this low-field minimum. In general the magnetostriction in the Dy-based materials is much stronger and seems to make the distortion-induced decrease of $\kappa_{\mathrm{ph}}(H)$ the dominant process, whereas in the Ho-based materials the decreasing phonon scattering by spin flips is dominant.

Because the electronic configurations of Dy^{3+} and Ho^{3+} just differ by one electron ($4f^9$ *vs.* $4f^{10}$) in the inner $4f$ shell, it may appear surprising that the magnetostriction $\Delta L(H)$ and the magnetic-field dependent phonon heat transport $\kappa_{\mathrm{ph}}(H)$ of the Dy- and the Ho-based materials are so different. However, both quantities depend on various material parameters and, in particular, the differences in the crystal-field level schemes of both ions may become important [100–102, 148], *e.g.* the fact that there is a Kramers protection of the zero-field doublet states of Dy^{3+} but not for those of Ho^{3+}. In Ref. 115, the ultrasound properties of $\mathrm{Ho_2Ti_2O_7}$ and $\mathrm{Dy_2Ti_2O_7}$ are investigated and it is found that the overall temperature dependence is similar at high temperatures, however pronounced differences appear at low temperatures and low magnetic fields, *i.e.* close to and in the spin-ice state. It is claimed that magnetoelastic interactions are relevant for the physics of these spin-ice materials, but no detailed explanation for the differences is given.

With respect to the question of a possible heat transport via magnetic monopoles, the different $\kappa_{\mathrm{ph}}(H)$ in the high-field range are of minor importance because the spin-ice behavior is restricted to low fields. Therefore, the main question in this context is, whether it is possible to obtain a reliable estimate of the phononic background. In Fig. 6.6, $\kappa(H)$ measurements at different temperatures of the spin-ice materials $\mathrm{Ho_2Ti_2O_7}$ and $\mathrm{Dy_2Ti_2O_7}$ are compared with $\kappa(H)$ of $\mathrm{(Ho_{0.5}Y_{0.5})_2Ti_2O_7}$ and $\mathrm{(Dy_{0.5}Y_{0.5})_2Ti_2O_7}$. Unfortunately, it is not possible to simply subtract the $\kappa(H,T)$ curves of the reference material from the respective pure spin-ice curves. The main reason is that the absolute values of κ of different samples differ, which is partly due to experimental errors as, *e.g.*, the exact determination of the sample's geometry. This uncertainty should however not exceed 20% and could be treated by a temperature- and field-independent scaling factor. More important for a transport property is, however, its dependence on defect and impurity scattering. Because κ usually increases with increasing sample quality, one may expect somewhat lower values of κ for the dilute reference compound than for the pure spin-ice. This is more or less fulfilled for the Dy-based materials, see Fig. 7.20, but not for the Ho-based ones. If, however, the above-described spin-flip scattering is a dominant scattering mechanism for κ_{ph} in a certain temperature and field range, its decrease due to the lower Ho content may overcompensate an increasing Ho/Y-disorder scattering in the dilute material. In addition, κ_{ph} can be reduced by scattering via crystal-field excitations of the partially filled $4f$ shells of Ho and Dy, but due to the rather large energy splitting this effect should become relevant towards higher temperatures and, indeed, $\kappa(T)$ of $\mathrm{Y_2Ti_2O_7}$ significantly exceeds that of $\mathrm{Dy_2Ti_2O_7}$

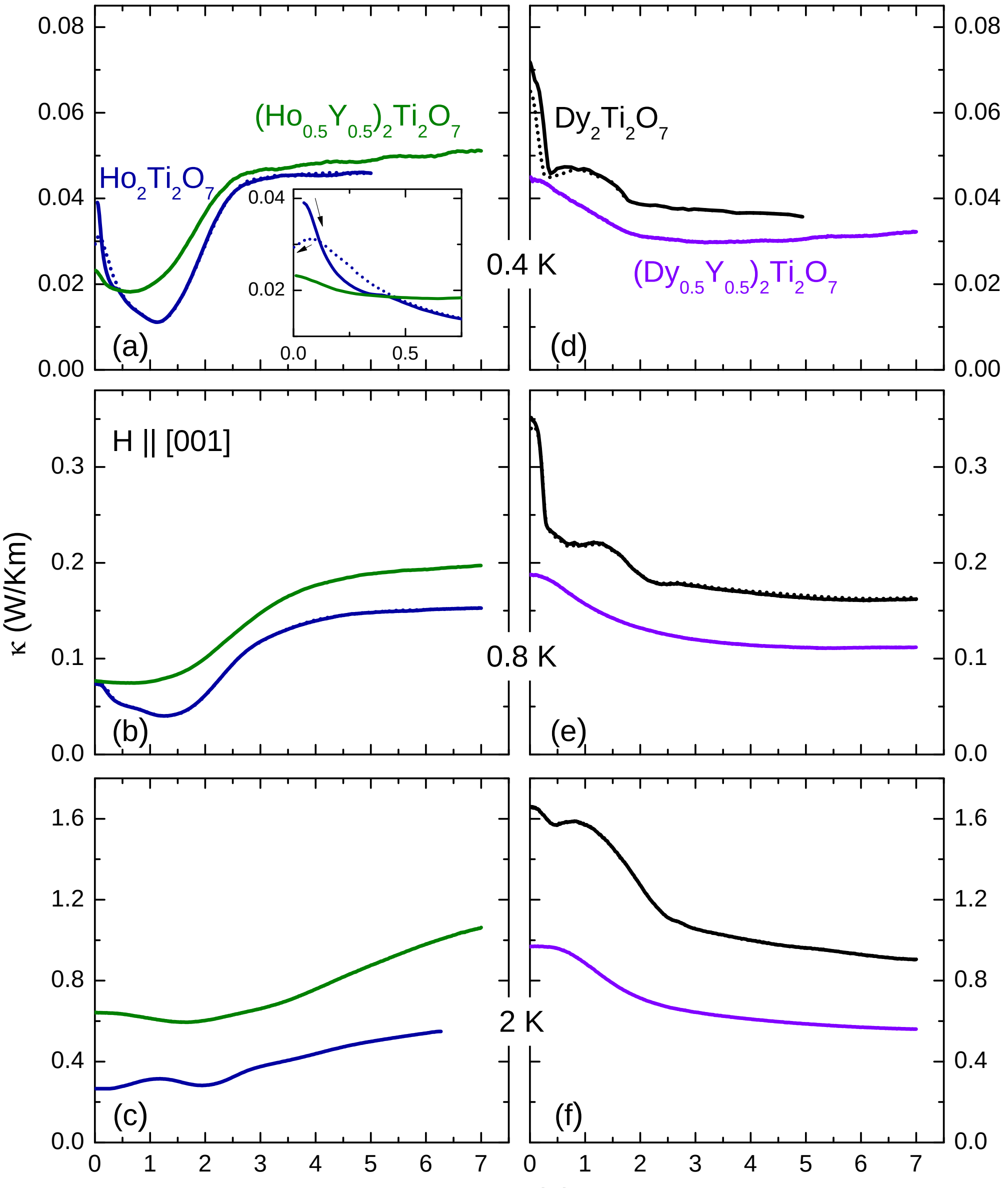

Figure 6.6: Comparison of the thermal conductivity $\kappa(H)$ of the Ho-based (left) and the Dy-based (right) spin-ice materials R_2Ti$_2$O$_7$ with the corresponding $\kappa(H)$ of the respective non-spin-ice reference materials RYTi$_2$O$_7$. The inset of panel (a) shows the low-field range of the Ho-based materials at 0.4 K .

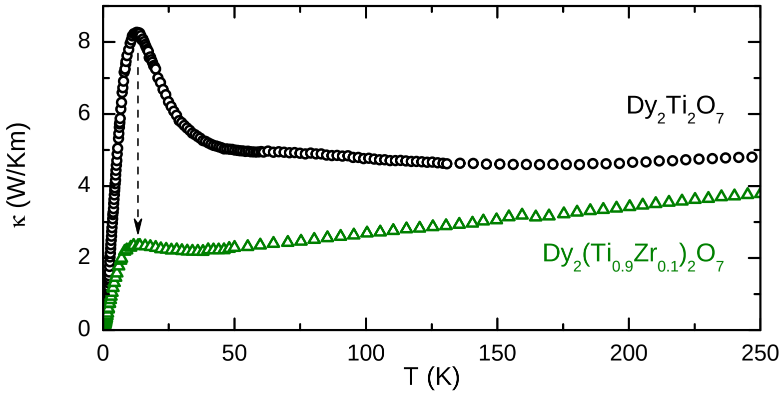

Figure 6.7: Thermal conductivity $\kappa(T)$ of $Dy_2Ti_2O_7$ and $Dy_2(Ti_{0.9}Zr_{0.1})_2O_7$ from 2 K up to 250 K in zero field for $\vec{j}\,||\,[1\bar{1}0]$. Taken from Ref. 16.

in the range of about 2 to 100 K [14]. Due to all these reasons and the possibility that even the half-doped materials may still show some remnant spin-ice behavior it has to be concluded that an unambiguous quantitative determination of the phonon background $\kappa_{\text{ph}}(H)$ is not possible.

The influence of 50% dilution with non-magnetic yttrium on the heat transport of $Ho_2Ti_2O_7$ and $Dy_2Ti_2O_7$ is studied. In order to further investigate κ_{mag} and κ_{ph}, thermal conductivity measurements on zirconium-based compounds $R_2(Ti_{1-x}Zr_x)_2O_7$ with R= Dy,Ho were performed. The zirconium ions (Zr^{4+},89.904 g/mol) will reside on the sites of the titanium ions (Ti^{4+},47.949 g/mol) in the pyrochlore lattice due to the similar ionic radii of $r_{\text{Zr}} = 0.72$ Å and $r_{\text{Ti}} = 0.61$ Å. In Fig. 6.7, $\kappa(T)$ of $Dy_2(Ti_{0.9}Zr_{0.1})_2O_7$ is compared to $Dy_2Ti_2O_7$ in the temperature range from about 2 K up to 250 K taken from Ref. 16. It is indeed found that the $\kappa(T)$ data of $Dy_2(Ti_{0.9}Zr_{0.1})_2O_7$ is suppressed in comparison with $Dy_2Ti_2O_7$ in the whole temperature range. It shows a glassy behavior originating from defect scattering due to the Zr doping into the phononic system. The maximum in $\kappa(T)$ of $Dy_2Ti_2O_7$ located at about 25 K with $\kappa(25\text{ K}) \simeq 8.2$ W/Km is suppressed down to $\kappa(25\text{ K}) \simeq 2.4$ W/Km in $Dy_2(Ti_{0.9}Zr_{0.1})_2O_7$.

Fig. 6.8 (a)-(f) compares the field dependence $\kappa(H)$ of $Dy_2Ti_2O_7$ (black squares) with $Dy_2(Ti_{0.95}Zr_{0.05})_2O_7$ (blue triangles) and $Dy_2(Ti_{0.9}Zr_{0.1})_2O_7$ (green triangles) in a temperature range from 0.4 K up to 4 K. The magnetic field is applied along $\vec{H}\,||\,[001]$ for all crystals. The heat current is sent along [001] for $x = 0$ and 0.05 whereas $\vec{j}\,||\,[1\bar{1}0]$ for $x = 0.1$. As mentioned above, the $\kappa(H)$ curves of $Dy_2Ti_2O_7$ reveal a low-field drop up to ≈ 0.5 T for $T \leq 2$ K before entering a plateau-like feature in the intermediate field range. At ≈ 1.5 T, $\kappa(H)$ shows an additional shoulder-like feature and slightly decreases in the high-field range (not shown here, see Fig. 6.2). The low-field drop, which has vanished at 4 K, is attributed to the reduced mobility of the magnetic excitations, *i.e.* the (anti-)monopoles. For finite $\vec{H}\,||\,[001]$, a non-degenerate ground-state is entered. As can be seen in Fig. 6.8 (a)-(f), it is found that the absolute value of κ decreases with an increase of Zr

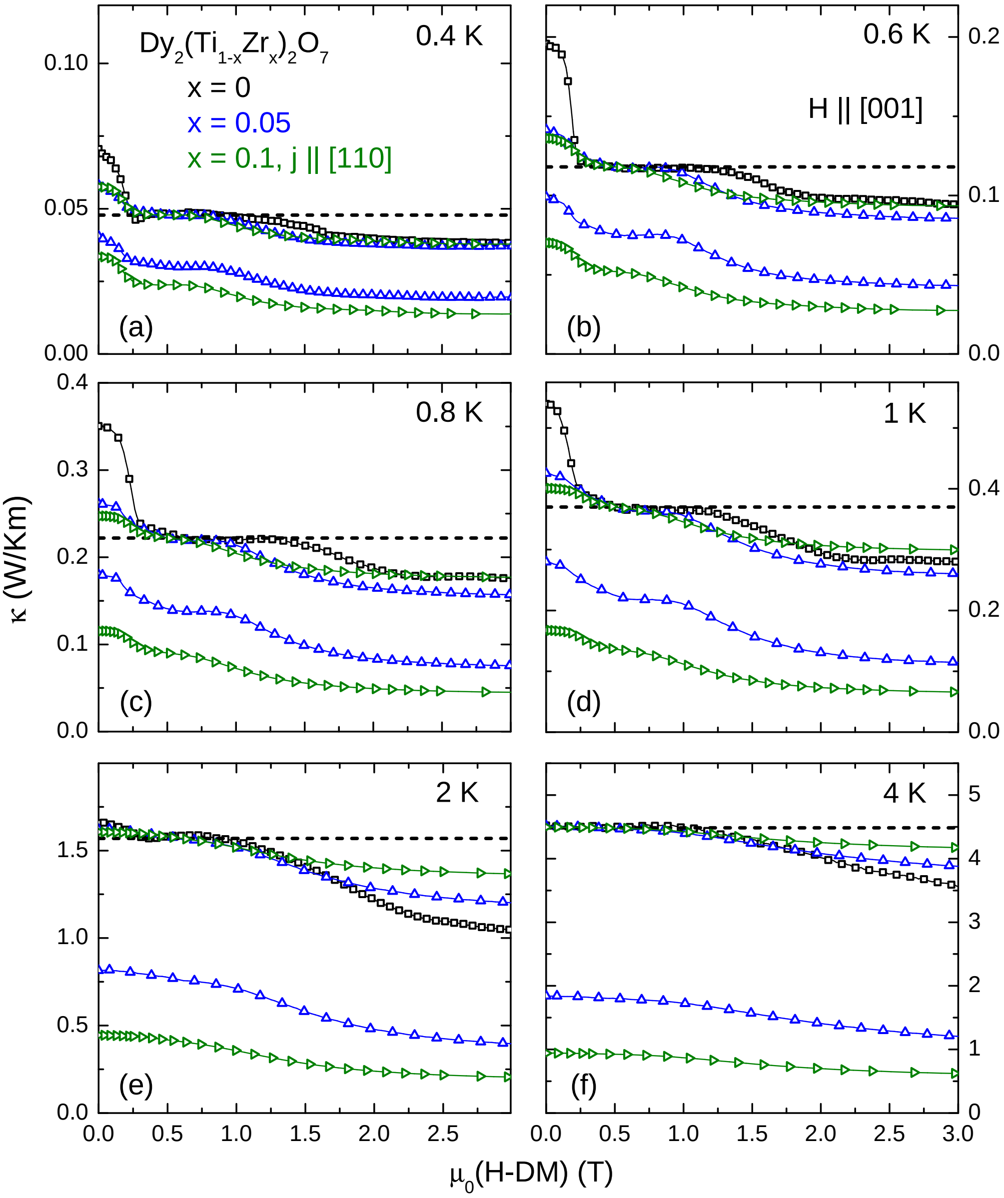

Figure 6.8: Heat transport of $Dy_2(Ti_{1-x}Zr_x)_2O_7$ with $x = 0$ and 0.05 for $\vec{H} \,||\, \vec{j} \,||\, [001]$ and with $x = 0.1$ for $\vec{H} \,||\, [001]$ and $\vec{j} \,||\, [110]$. The curves for $x = 0.05$ and 0.1 are shifted to the match the zero-field phononic backgrounds at 0.5 T (black dashed lines) of the $Dy_2Ti_2O_7$ curves.

doping because defect scattering is enhanced. Furthermore, the $\kappa(H)$ curves also show a low-field drop up to ≈ 0.5 T for $T \leq 2$ K and a second shoulder-like decrease in the intermediate field range. In the high-field range, $\kappa(H)$ only slightly decreases with field as observed for $Dy_2Ti_2O_7$. The black dashed lines in panels (a)–(f) represent the estimated zero-field phononic backgrounds at ≈ 0.5 T in the pure $Dy_2Ti_2O_7$. The $Dy_2(Ti_{1-x}Zr_x)_2O_7$ curves with $x = 0.05$ and 0.1 are shifted such that they match these backgrounds at 0.5 T. As a consequence, it turns out that the shoulder-like decrease in the intermediate field range clearly shifts towards smaller fields from ≈ 1.5 T in $Dy_2Ti_2O_7$ towards ≈ 1 T in the Zr-doped compounds and it is almost smeared out for $x = 0.1$. Furthermore, the suppression of $\kappa(H)$ in the low-field range is clearly less pronounced than in the pure spin ice $Dy_2Ti_2O_7$. The low-field decrease in $Dy_2Ti_2O_7$ is more pronounced for $\vec{H} \,||\, [001]$ and $\vec{j} \,||\, [1\bar{1}0]$, see Fig. 4.11 on page 50, than for $\vec{H} \,||\, \vec{j} \,||\, [001]$ in Fig. 6.2. As a consequence, the low-field decreases for $x = 0.05$ and 0.1 reveal comparable magnitudes which is most likely a result of the different directions of the heat current.

A similar study to investigate the influence of Zr doping was performed for the Ho-based materials. The corresponding field-dependent $\kappa(H)$ data of $Ho_2(Ti_{1\text{-x}}Zr_\text{x})_2O_7$ with $x = 0$ and 0.05 are shown in Fig. 6.9 (a)-(f) in a temperature range from 0.4 K up to 4 K. As observed for the Dy-based materials, the absolute values of κ are suppressed for $x = 0.05$ compared to the pure system $Ho_2Ti_2O_7$ which is consistent with the enhanced defect scattering. In addition, the $x = 0.05$ curves are shifted in the same manner like the Dy-based compounds such that they match the $x = 0$ curves at 0.5 T. It is observed that the low-field drop and especially the high-field increase are both systematically reduced for $x = 0.05$ compared to $x = 0$.

Summarizing the $\kappa(H)$ data of the Zr-doped compounds shown in Figs. 6.8 and 6.9, it is found that the Zr doping manipulates κ_ph due to enhanced scattering on defects. But as already discussed in Sec. 5.3, the replacement of Ti by Zr applies a negative pressure on the system and according to the Grüneisen ratio from Ref. 53, this results in an increase of the effective nearest neighbor energy scale J_eff between the magnetic moments, see Eq. (4.5). The increase of J_eff is confirmed by the magnetization data $M(H)$. Hence, it is not surprising that the Zr doping also suppresses the magnetic contribution κ_mag to the thermal conductivity, namely the low-field decrease up to 0.5 T of $\kappa(H)$ for the Ho- and Dy-based materials.

6.2.2 Magnetic contribution

Based on the results for the thermal conductivity derived in the previous section, an extraction of κ_mag for $Dy_2Ti_2O_7$ and $Ho_2Ti_2O_7$ can be accomplished. It

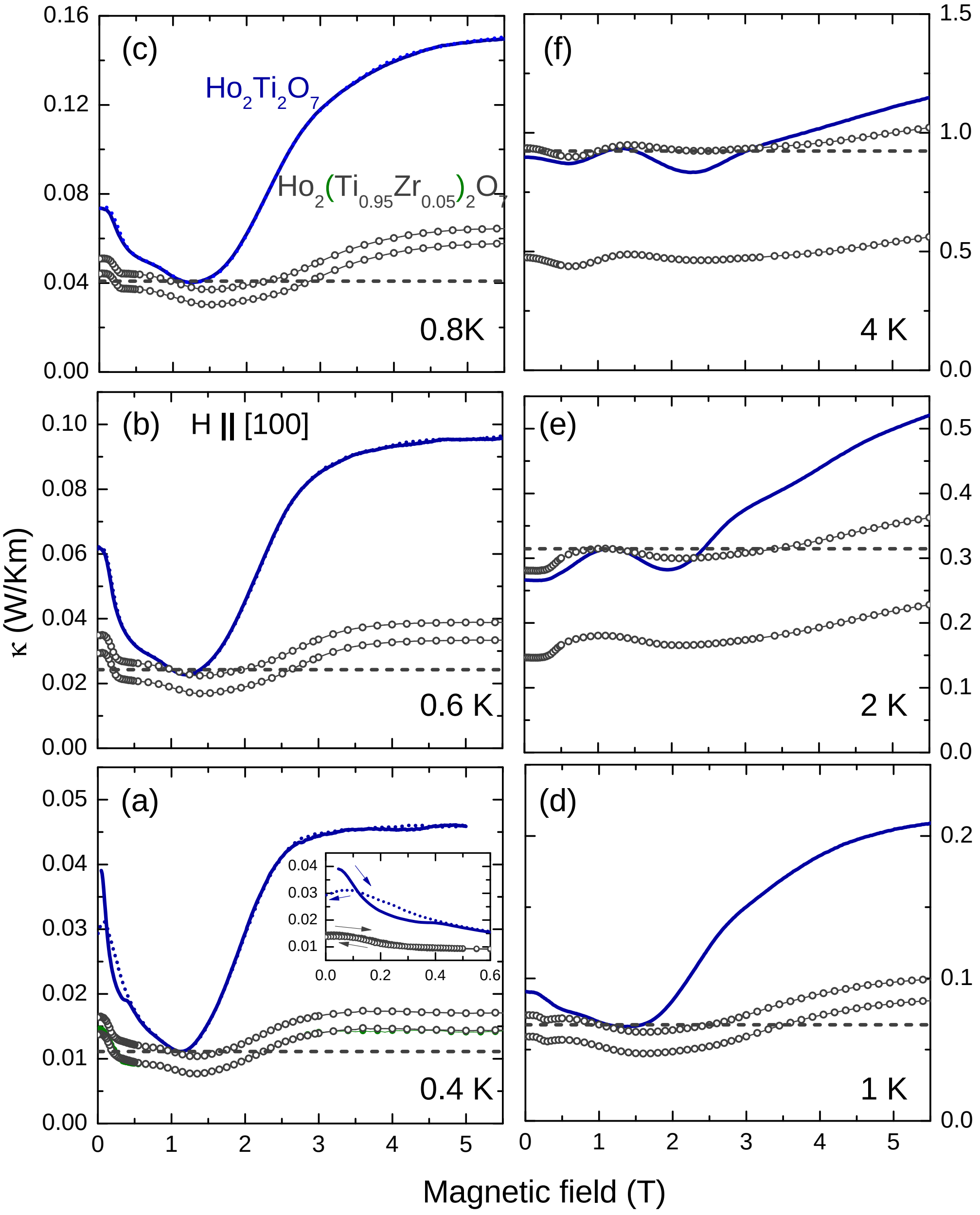

Figure 6.9: Heat transport of $Ho_2(Ti_{1\text{-}x}Zr_x)_2O_7$ with $x = 0$ and 0.05 for $\vec{H}\,||\,[001]$ and $\vec{j}\,||\,[001]$. The curves for $x = 0.05$ are shifted to the match the zero-field phononic backgrounds at 0.5 T (gray dashed lines) of the $Ho_2Ti_2O_7$ curves.

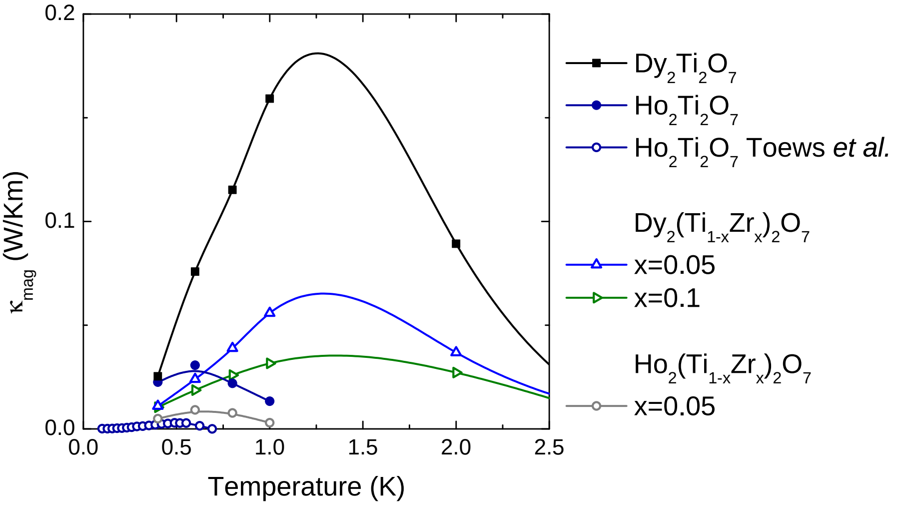

Figure 6.10: Magnetic contribution κ_{mag} in zero field of $Dy_2Ti_2O_7$ and $Ho_2Ti_2O_7$ together with κ_{mag} data from Toews *et al.* [18] for $Ho_2Ti_2O_7$. The κ_{mag} for $Dy_2(Ti_{1-x}Zr_x)_2O_7$ with $x = 0.05$–0.1 and for $Ho_2(Ti_{1\text{-x}}Zr_{\text{x}})_2O_7$ with $x = 0.05$ are also shown. The lines are guides to the eye.

appears reasonable to assume an essentially field-independent $\kappa_{\mathrm{ph}}^{H\to 0}$ in the low-field range for $Dy_2Ti_2O_7$. Because $\kappa(\vec{H}\,||\,[100])$ of $Dy_2Ti_2O_7$ shows a step-like decrease to a pronounced plateau starting around 0.5 T, which anticorrelates with the rapid saturation of the magnetization for this field direction, $\kappa_{\mathrm{ph}}^{H\to 0}$ was estimated by these plateau values. Then, the magnetic heat transport can be derived via $\kappa_{\mathrm{mag}}(H) \simeq \kappa(H) - \kappa_{\mathrm{ph}}^{H\to 0}$ which is also applied for the Zr-doped materials $Dy_2(Ti_{1-x}Zr_x)_2O_7$ with $x = 0.05$ and 0.1. An analogous analysis is more difficult for $Ho_2Ti_2O_7$ with $\vec{H}\,||\,[001]$, because the $\kappa(H)$ curves do not show plateau-like features around ≈ 0.5 T (see Fig. 6.2). Concerning the comparison with the data of $(Ho_{0.5}Y_{0.5})_2Ti_2O_7$, it can be seen that again considering just the difference of both data sets does not yield reliable results for κ_{mag}. Nevertheless, this comparison reveals that the low-temperature $\kappa(H)$ curves of $Ho_2Ti_2O_7$ show a sharp low-field decrease suggesting the presence of a sizable κ_{mag} in zero-field, whereas the corresponding $\kappa(H)$ curves of $(Ho_{0.5}Y_{0.5})_2Ti_2O_7$ only weakly change with field below 1 T (see Figs. 6.4 and 6.6). Thus, it appears again reasonable to assume an essentially field-independent $\kappa_{\mathrm{ph}}^{H\to 0}$ for $Ho_2Ti_2O_7$ and in order to get at least a rough estimate of $\kappa_{\mathrm{mag}}(H) \approx \kappa(H) - \kappa_{\mathrm{ph}}^{H\to 0}$, it is assumed that $\kappa_{\mathrm{ph}}^{H\to 0} \approx \kappa(0.5\ \mathrm{T})$. The same equation is applied for $Ho_2(Ti_{1\text{-x}}Zr_{\text{x}})_2O_7$ with $x = 0.05$. These differences at various fixed temperatures then yield an estimate of the temperature-dependent zero-field $\kappa_{\mathrm{mag}}(T)$, which is compared to the corresponding $\kappa_{\mathrm{mag}}(T)$ of the Dy-based materials in Fig. 6.10. In addition, the estimated $\kappa_{\mathrm{mag}}(T)$ of $Ho_2Ti_2O_7$ from Toews *et al.* [18] is displayed, which, as already mentioned above, is much smaller. Note that all three estimates of $\kappa_{\mathrm{mag}}(T)$ refer to zero magnetic field, but the result from Ref. 18 was determined with $\vec{H} \,||\, \vec{j} \,||\, [111]$ whereas the results for $\kappa_{\mathrm{mag}}(T)$ within this thesis were extracted for $\vec{H} \,||\, \vec{j} \,||\, [001]$ due to the lifting of the ground-state degeneracy for this particular field direction. With respect to a possible monopole heat transport, the direction of the heat flow should be of minor importance, because an isotropic monopole mobility can be expected in zero field. Moreover, it may also be naively expected that a possible monopole contribution $\kappa_{\mathrm{mag}}(T)$ should be of comparable order of magnitude for the two spin-ice materials $\mathrm{Ho_2Ti_2O_7}$ and $\mathrm{Dy_2Ti_2O_7}$ as they are iso-structural and because of the very similar energy scales characterizing their spin-ice behavior. In view of the above-described experimental uncertainties, the comparison of the $\kappa_{\mathrm{mag}}(T)$ data of both materials essentially confirms these expectations, which is a basic result. Moreover, the data indicate that $\kappa_{\mathrm{mag}}(T)$ of $\mathrm{Ho_2Ti_2O_7}$ is significantly smaller than $\kappa_{\mathrm{mag}}(T)$ of $\mathrm{Dy_2Ti_2O_7}$. This difference can be naturally explained by an enhanced spin-flip/phonon scattering in $\mathrm{Ho_2Ti_2O_7}$, which would simultaneously explain the reduced κ_{mag} and κ_{ph} in zero field and the observed increase of $\kappa_{\mathrm{ph}}(H)$ with increasing magnetic field $\vec{H}$. Concerning the $\kappa_{\mathrm{mag}}(T)$ of $\mathrm{Ho_2Ti_2O_7}$ an important question is why the estimate from Ref. 18 is so much smaller than the corresponding results in Fig. 6.10. In Ref. 18, temperature-dependent measurements of $\kappa(T)$ at constant fields $H = 0$, 6, 8, and 10 T were performed, see Fig. 6.1 (a), and because the $\kappa(T)$ data in the field range between 6 and 10 T are identical, these high-field data were assumed to represent a field-independent background κ_{ph}. The measurements of $\kappa(H)$ shown in Figs. 6.2 and 6.4 of the Ho-based materials confirm such a field-independent $\kappa_{\mathrm{ph}}(H > 5\ \mathrm{T})$, but there is a pronounced field dependence in the intermediate field range between 0.5 T and 2 T. Concerning the magnetic contributions of the Zr-doped materials, it is found $\kappa_{\mathrm{mag}}(T)$ is already strongly suppressed for a doping of $x = 0.05$ both for the Ho- and Dy-based systems. For $\mathrm{Dy_2(Ti_{1-x}Zr_x)_2O_7}$ with $x = 0.1$, $\kappa_{\mathrm{mag}}(T)$ is even further reduced. The magnitude of this suppression is most likely related to an enhanced monopole scattering on defects.

6.2.3 Magnetic field || [111]

A pronounced field dependence of $\kappa(H)$ is not only observed for the configuration $\vec{H} \,||\, \vec{j} \,||\, [100]$ discussed in the previous section, but also for the configuration $\vec{H} \,||\, \vec{j} \,||\, [111]$ studied by Toews *et al.* [18]. The corresponding data are shown in Fig. 6.11. For $\vec{H} \,||\, [111]$, the $\kappa(H)$ measurements of the Ho(Dy)-based spin ice show additional features up to about 1.5(1) T, which are related to the occurrence of the Kagomé-ice phase for this field direction and are absent in the respective $\kappa(H)$ data of the reference materials. The data in Fig. 6.11 (a)-(f) clearly show that applying the high-field data $\kappa(T, H > 6\ \mathrm{T})$ as an estimate of $\kappa_{\mathrm{ph}}^{H\rightarrow 0}$ overestimates this

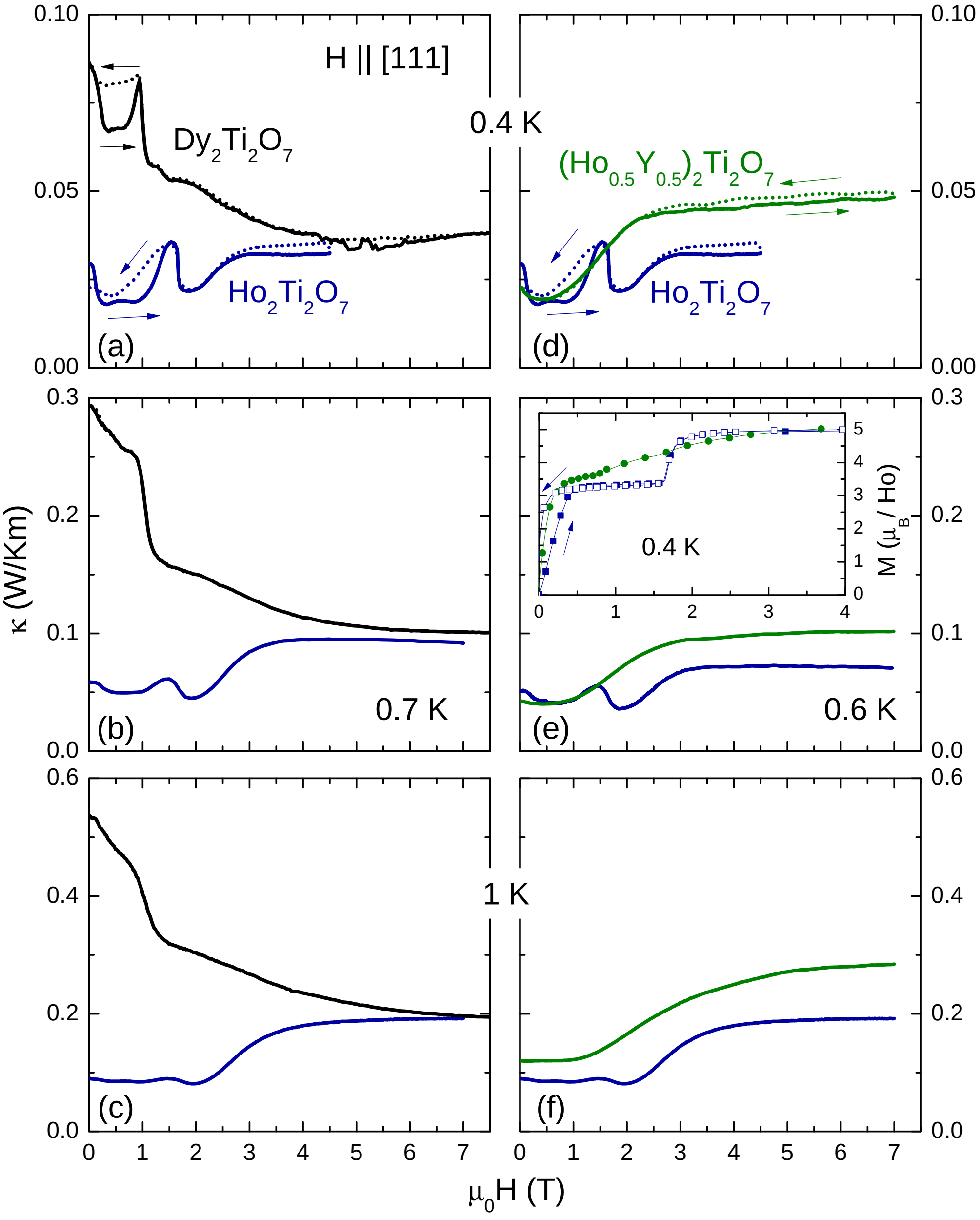

Figure 6.11: Comparison of the thermal conductivity $\kappa(H)$ of the spin-ice materials $Ho_2Ti_2O_7$, $Dy_2Ti_2O_7$ and the reference material $(Ho_{0.5}Y_{0.5})_2Ti_2O_7$ for $\vec{H} \,||\, [111]$. Inset of panel (e): Magnetization of $Ho_2Ti_2O_7$ and $(Ho_{0.5}Y_{0.5})_2Ti_2O_7$ at 0.4 K. The $Dy_2Ti_2O_7$ data are taken from Ref. 16

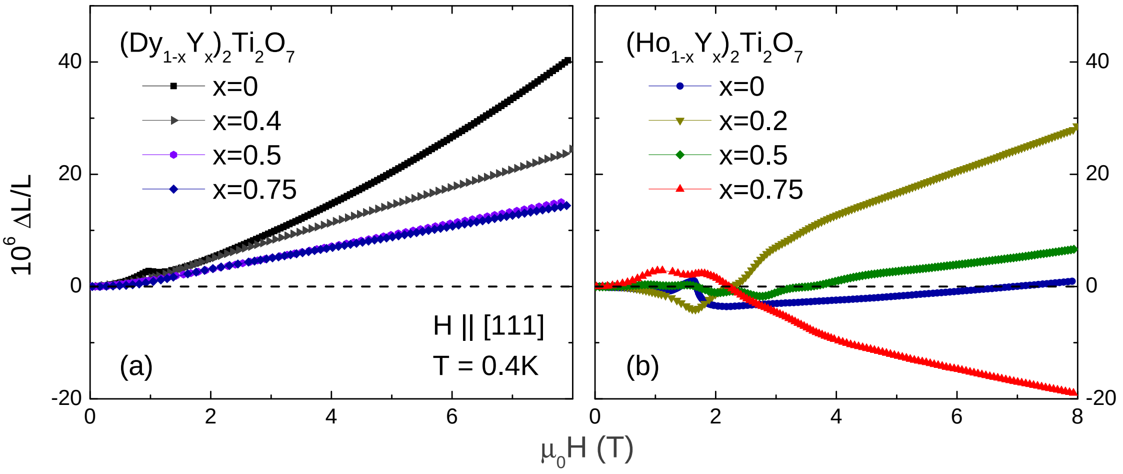

Figure 6.12: Field dependend measurements of the magnetostriction $\Delta L(H)/L$ of $(Dy_{1-x}Y_x)_2Ti_2O_7$ and $(Ho_{1-x}Y_x)_2Ti_2O_7$ for $\vec{H}\,||\,[111]$ at 0.4 K.

background considerably and causes a drastic underestimate of the corresponding zero-field $\kappa_{\mathrm{mag}}(T, H = 0)$. In Ref. 18, a finite $\kappa_{\mathrm{mag}}(T, H = 0) > 0$ is only found for $T < 0.65$ K, because for higher temperature the high-field data of $\kappa(T)$ exceed those in zero field. As can be seen from Figs. 6.2 and 6.11, the high-field data of κ for both configurations of $\vec{H}$ and $\vec{j}$ are larger than the corresponding zero-field data down to our lowest temperature of 0.4 K. Nevertheless, the shown data agree to those of Ref. 18 concerning the difference $\kappa(T, H > 6\text{ T}) - \kappa(T, H = 0)$ is systematically decreasing with falling temperature and a sign change may be suspected at somewhat lower temperature.

As already discussed above, there are at least two mechanisms that either increase or decrease $\kappa_{\mathrm{ph}}(H)$. Experimentally, it has been found that there are huge deviations between the Dy- and the Ho-based materials and this difference is not restricted to $\kappa_{\mathrm{ph}}(H)$. Fig. 6.12 compares the magnetostriction $\Delta L/L$ for $\vec{H}\,||\,[111]$ at 0.4 K of $(Dy_{1-x}Y_x)_2Ti_2O_7$ with $(Ho_{1-x}Y_x)_2Ti_2O_7$ for different dilution x. It is observed that $\Delta L/L$ is also larger for the Dy-based materials than for the corresponding Ho-based ones with $\vec{H}\,||\,[111]$ but the difference is much smaller than for $\vec{H}\,||\,[001]$, compare Fig. 6.5. In the dilute systems $(Dy_{1-x}Y_x)_2Ti_2O_7$ with $x \geq 0.5$ in panel (a), $\Delta L/L$ scales with the degree of the dilution, whereas the curve for $x = 0.5$ and 0.75 match. The curve with $x = 0$ reveals a kink at about 1 T which signals the transition into the fully polarized phase. This transition is smeared out for the higher dilute systems with $x \geq 0.4$ which is in good agreement with the magnetization data $M(H)$ in Fig. 5.3 (b) on page 58. The magnetostriction of the Ho-based compounds in panel (b) is, however, more difficult to study. For $x = 0$ and 0.5, $\Delta L/L$ is much smaller than for the Dy-based materials and supports the interpretation of the

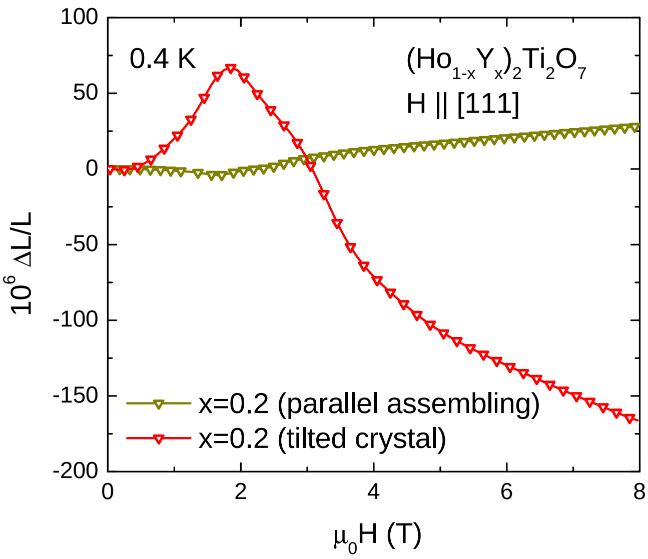

Figure 6.13: Comparison of $\Delta L/L$ of $(\mathrm{Ho}_{1-x}\mathrm{Y}_x)_2\mathrm{Ti}_2\mathrm{O}_7$ with $x = 0.2$ for $\vec{H}$ applied along the crystallographic [111] direction and for a crystal tilted by roughly $3-5°$ with respect to the external field. The data are taken from Ref. 138.

reduced lattice distortion in the Ho-based systems. A kink occurs at ≈ 1.5 T for $x = 0$ also signaling the transition into the fully polarized phase similar to the data in panel (a). However, the curves with $x = 0.5$ and 0.75 show a comparably large $\Delta L/L$ compared to the Dy-based crystals and additionally differ in the sign.

This comparable large $\Delta L/L$ for $(\mathrm{Ho}_{1-x}\mathrm{Y}_x)_2\mathrm{Ti}_2\mathrm{O}_7$ with $x = 0.5$ and 0.75 and the sign change most likely originate from a highly sensitive magnetostriction with respect to the orientation of the sample to the applied field. This sensitivity seems to be much more pronounced for $\vec{H}\,||\,[111]$. The interpretation is confirmed by the data shown in Fig. 6.13 which are taken from Ref. 138. It depicts $\Delta L/L$ data of a $(\mathrm{Ho}_{1-x}\mathrm{Y}_x)_2\mathrm{Ti}_2\mathrm{O}_7$ crystal with $x = 0.2$ whose crystallographic axis was aligned parallel to the applied magnetic field in [111] direction within the magnetostriction cell by eye in comparison with a crystal whose crystallographic axis was tilted by roughly $3-5°$ with respect to the field at 0.4 K. It turns out that the deviation of the field from the crystallographic axis has a huge effect on the magnitude of $\Delta L/L$ which is about 6.8 times larger in maximum for the tilted crystal. Furthermore, the sign of $\Delta L/L$ has changed. Hence, it has to be stated that the magnetostriction data of the spin-ice materials bare experimental uncertainties. This uncertainty includes a possible misorientation of the samples within the X-ray Laue diffractometer. As a consequence an exact quantitative analysis of the data is difficult, especially for $\vec{H}\,||\,[111]$. But nevertheless, it is observed that $\Delta L/L$ is essentially larger for the Dy-based compounds than for the Ho-based compounds which yields an explanation for the different field dependencies of $\kappa_{\mathrm{ph}}(H)$.

6.3 Conclusion

In conclusion, a clear experimental evidence for a sizable magnetic contribution κ_{mag} to the low-temperature, zero-field heat transport of both spin-ice materials $Ho_2Ti_2O_7$ and $Dy_2Ti_2O_7$ was observed. This κ_{mag} is attributed to the magnetic monopole excitations, which are highly mobile in zero field and this mobility is effectively suppressed in external magnetic fields causing a drop of $\kappa_{\mathrm{mag}}(H)$ in the low-field range for $\vec{H} \,||\, [001]$. The results for κ_{mag} of Toews *et al.* [18] could be systematically disproved. Towards higher magnetic fields, a significant field dependence of the phononic heat conductivities $\kappa_{\mathrm{ph}}(H)$ of $Ho_2Ti_2O_7$ and $Dy_2Ti_2O_7$ is found, which are, however, of opposite signs. This field dependence was also observed in the highly dilute reference materials $(Ho_{0.5}Y_{0.5})_2Ti_2O_7$ and $(Dy_{0.5}Y_{0.5})_2Ti_2O_7$. It is found that the decreasing $\kappa_{\mathrm{ph}}(H)$ in the Dy-based materials probably arise from field-induced lattice distortions, which are seen in magnetostriction data. This effect seems to be less important in the Ho-based materials, which show a significantly smaller magnetostriction while at the same time the scattering of phonons by spin flips appears to be significantly stronger than in the Dy-based materials. Consequently, both κ_{mag} and κ_{ph} in zero field are smaller in $Ho_2Ti_2O_7$ than they are in $Dy_2Ti_2O_7$ and the field dependences of κ_{ph} are of opposite signs. A comparative study of the heat transport of $Dy_2Ti_2O_7$ and $Ho_2Ti_2O_7$ with the doped compounds $Dy_2(Ti_{1-x}Zr_x)_2O_7$ and $Ho_2(Ti_{\text{1-x}}Zr_{\text{x}})_2O_7$ ($x \leq 0.1$) reveals that the Zr doping systematically reduces κ due to an enhanced defect scattering. A glassy behavior is observed. Furthermore, both κ_{mag} and the κ_{ph} are clearly suppressed compared to the pure compounds $Dy_2Ti_2O_7$ and $Ho_2Ti_2O_7$. The Zr doping increases defect scattering in the phononic system but it also results in a reduced κ_{mag}.

7 Dilute spin ice $(Dy_{1-x}Y_x)_2Ti_2O_7$

This chapter concerns the thermal conductivity, specific heat, and magnetocaloric effect of spin ice $Dy_2Ti_2O_7$ and the influence of increasing yttrium dilution on these quantities. The low-temperature relaxation effects are studied in the heat transport as well as the specific heat. In literature, a non-monotonical residual entropy $S_P(x)$ is predicted to be present within the dilute materials $(Dy_{1-x}Y_x)_2Ti_2O_7$ which is highly questionable and will be investigated in detail. In Chap. 6, clear evidence for a magnetic contribution to the heat transport of $Ho_2Ti_2O_7$ and $Dy_2Ti_2O_7$ is observed. Its magnitude is estimated from the low-field behavior of $\kappa(H)$ and an investigation of the corresponding 50% dilute systems $(Dy_{0.5}Y_{0.5})_2Ti_2O_7$ and $(Ho_{0.5}Y_{0.5})_2Ti_2O_7$. Additionally, it turned out that the phononic contributions κ_{ph} of both systems are of opposite sign. According to the field dependence of $\kappa(H)$, a quantitative extraction of κ_{mag} with a high degree of accuracy is more promising for $Dy_2Ti_2O_7$ than for $Ho_2Ti_2O_7$. Thus, the heat transport of the whole dilution series $(Dy_{1-x}Y_x)_2Ti_2O_7$ with $x = 0$–0.75 is studied. The extraction of κ_{mag} along with results of c_{mag} enable to determine the diffusion coefficient D_{mag} for the dilute spin-ice systems.

7.1 Hysteresis and relaxation effects

The exotic magnetic excitations discussed as (anti-)monopoles in spin ice $Dy_2Ti_2O_7$ have already been investigated by thermal conductivity measurements and experimental evidence for zero-field monopole heat transport in $Dy_2Ti_2O_7$ and $Ho_2Ti_2O_7$ was found. For finite magnetic fields with $\vec{H} \,||\, [001]$, κ_{mag} decreases and is essentially suppressed at a field around ≈ 0.5 T which is associated with a suppression of the monopole mobility. Furthermore, pronounced hysteresis effects are observed between the $\kappa(H)$ curves measured with increasing or decreasing magnetic field for all three field directions $\vec{H} \,||\, [001]$, [110] and [111] [12–16, 48, 129]. Within the low-temperature regime below about 0.6 K, it is found that the initial zero-field cooled value $\kappa_0 = \kappa(H = 0)$ is basically not recovered by $\kappa(H \to 0)$ measured with decreasing magnetic field. These reduced $\kappa(H \to 0)$ values then slowly relax back towards the corresponding initial κ_0 as a function of time [14]. As introduced in Sec. 4.4, slow relaxation phenomena are also present in the specific heat at low

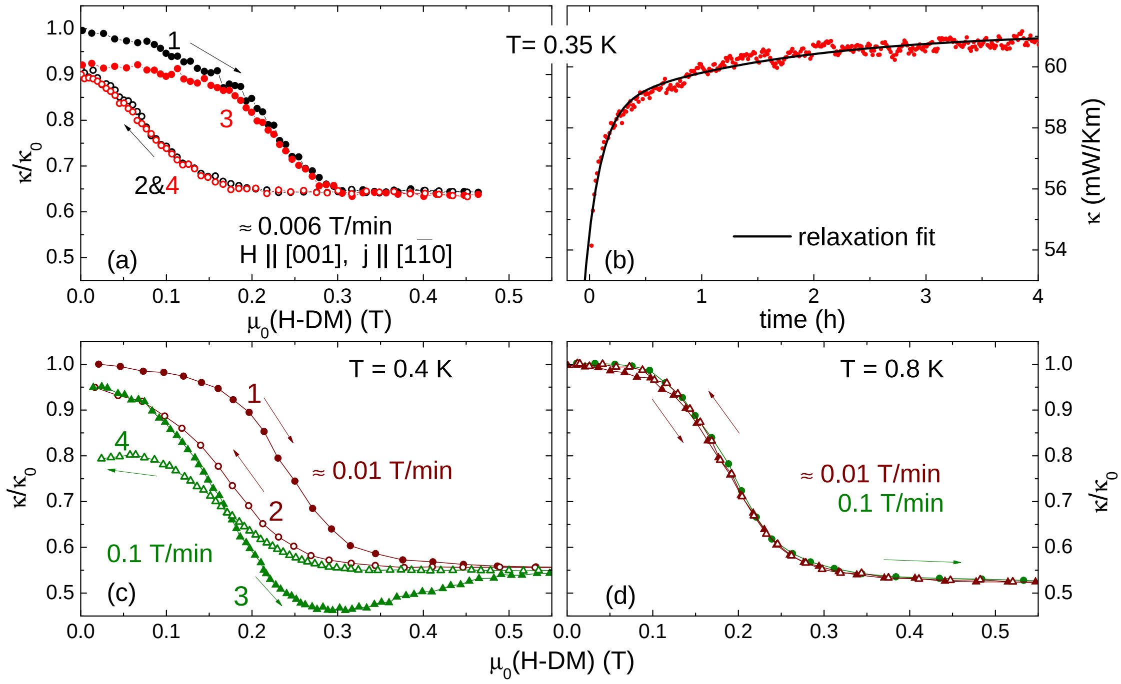

Figure 7.1: $\kappa(H)/\kappa_0$ curves for $\vec{H}\,||\,[001]$ and $\vec{j}\,||\,[1\bar{1}0]$ measured with different field-sweep rates. The order of the successive field sweeps is marked by the numbers 1-4, where the initial sweep was started after cooling in zero field. Panel (b) shows the relaxation of the reduced zero-field value towards the initial κ_0. The data are taken from Ref. 16.

temperatures [11, 14, 20, 149], and additionally in other physical properties of $Dy_2Ti_2O_7$, like the magnetization [111] and the ac susceptibility [113, 150].

In this section, the unusual hysteresis effects of $\kappa(H)$ for the magnetic field directions along [001] and [111] are studied. Thus, the main question is in how far the different κ values obtained by thermal conductivity measurements represent equilibrium values. Therefore, $\kappa(H)$ for different magnetic-field sweep rates and the influence of different cooling procedures are investigated. In addition, relaxation measurements of κ as a function of time were performed after different field-sweep cycles and the influence of the direction of the heat current on the hysteresis effects for $\vec{H}\,||\,[111]$ is examined.

7.1.1 $\vec{\mathbf{H}}\,||\,[001]$ and $\vec{\mathbf{j}}\,||\,[1\bar{1}0]$

In Fig. 7.1 (a)-(d), $\kappa(H)$ curves as a function of the external field are presented for varying magnetic field-sweep rates. Note that the curves are normalized to κ_0 and the heat current $\vec{j}$ is applied along $[1\bar{1}0]$. The initial κ_0 is obtained after zero-field cooling. Fig. 7.1 (a) shows that after sweeping the magnetic field up and down at 0.35 K the final $\kappa(H \to 0)$ only recovers about 90% of its initial zero-field κ_0, see curves (1) and (2). A subsequent field cycle results in $\kappa(H)$ curves (3) and (4) with equal endpoints, where curves (2) and (4) perfectly match each other. As can be seen in Fig. 7.1 (b), the reduced zero-field $\kappa(H \to 0)$ slowly relaxes back towards the zero-field-cooled κ_0. The data are fitted with two relaxation times and this yields large relaxation of $\tau_1 \simeq 8$ min and $\tau_2 \simeq 100$ min. In the complete high-field range above 0.3 T, however, no such slow relaxation effects are observed. Here, $\kappa(H)$ is non-hysteretic. These low-field relaxation processes raise the question how the measured $\kappa(H)$ values also depend on the magnetic field sweep rate. The corresponding results are shown in Fig. 7.1 (c)-(d) at different temperatures. At 0.4 K in panel (c), the initial field cycle curves (1) and (2) were measured with a sweep rate of about 0.01 T/min and the $\kappa(H \to 0)$ curve (2) recovers about 95% of the initial κ_0. Then, for the subsequent cycle the field-sweep rate was increased up to 0.1 T/min. This increase causes additional features in $\kappa(H)$. Curve (3) measured with increasing field reveals a clear minimum around 0.3 T, but nevertheless approaches the initial $\kappa(H)$ curve (1) around 0.55 T. Decreasing the field again results in the $\kappa(H)$ curve (4), which matches curve (2) down to ≈ 0.3 T. For smaller magnetic fields however, an even larger hysteresis opens and $\kappa(H \to 0)$ only recovers about 80% of the initial κ_0. Thus, the $\kappa(H \to 0)$ values highly depend on the magnetic field-sweep rate.

The data of Fig. 7.1 (a) and (c) suggest that even comparable small field-sweep rates of ≈ 0.01 T/min may be too large to reach equilibrium states in the low-temperature range of spin ice. At higher temperatures, these slow equilibration vanishes, as is expected and shown in Fig. 7.1 (d) for 0.8 K. Here, the subsequent cycles with curves (1)-(4) match each other in the whole field regime up to ≈ 0.55 T and $\kappa(H)$ is non-hysteretic. However, the hysteresis effects can also disappear in the low-temperature range by increasing the magnetic field above about 0.5 T. This conclusion can be drawn from the data of Fig. 7.1 (a) and (c) and it is consistent with the high-field thermal conductivity and magnetization data presented in Chap. 6. The magnetization $M(H)$ unveils a hysteresis below about 0.5 T for $\vec{H} \,||\, [001]$ and it is essentially saturated for higher magnetic fields. As a consequence, it appears natural that the relaxation/hysteresis effects rather rapidly vanish for $H > 0.5$ T. One might suspect that the slow equilibration in the low-temperature/low-field region is a single-ion property of the large Ising spins of the Dy^{3+} ions, which only slowly equilibrate because of the rather large splitting to the higher-lying crystal-field states. This can be ruled out, however, from measurements of the thermal conductivity and magnetization on the related half-doped material $(\mathrm{Dy}_{0.5}\mathrm{Y}_{0.5})_2\mathrm{Ti}_2\mathrm{O}_7$, which does not show such hysteresis effects [15, 16, 53, 129]. Hence, it can be concluded that the slow equilibration is a particular spin-ice feature which is at least vanished in $(\mathrm{Dy}_{0.5}\mathrm{Y}_{0.5})_2\mathrm{Ti}_2\mathrm{O}_7$. A detailed study on the influence of yttrium

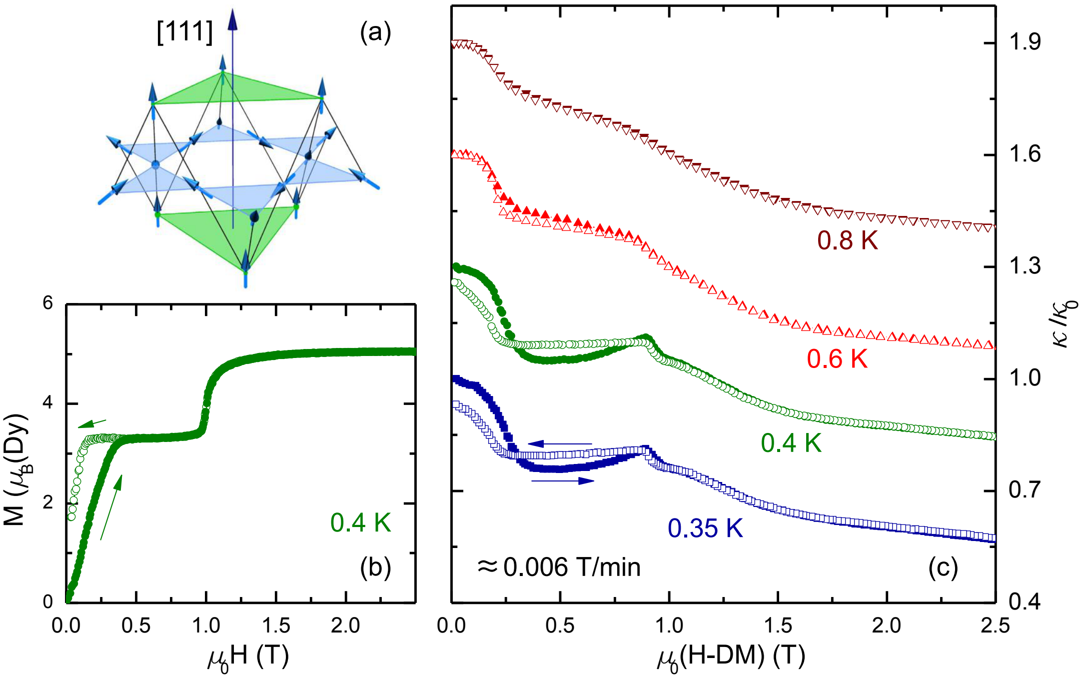

Figure 7.2: Panel (a): alternating triangular and Kagomé-ice planes for $\vec{H} \,||\, [111]$ taken from Ref. 110. Panel (b): corresponding magnetization curves. Panel (c): field dependence $\kappa(H)$ for $\vec{H} \,||\, [111]$ and $\vec{j} \,||\, [1\bar{1}0]$. The $\kappa(H)/\kappa_0$ curves for different temperatures are shifted with respect to each other. The data are taken from Ref. 16.

dilution on the slow equilibration in $(Dy_{1-x}Y_x)_2Ti_2O_7$ will be performed in Sec. 7.2 by specific heat measurements.

7.1.2 $\vec{H} \,||\, [111]$ and $\vec{j} \,||\, [1\bar{1}0]$

The interpretations of the low-temperature slow relaxation in spin ice for $\vec{H} \,||\, [001]$ were in principle straightforward. By applying an external field along [111], the situation gets more complex. For this field direction, $\kappa(H)$ exhibits a hysteresis in the so-called Kagomé-ice state, which is realized at low temperature below ≈ 1 T. As can be seen in Fig. 7.2 (a), the pyrochlore structure for $\vec{H} \,||\, [111]$ can be best visualized as alternating triangular (highlighted in green) and Kagomé planes (highlighted in blue) of Dy^{3+} spins, which point along their local {111} directions. The spins of the triangular planes are fully aligned already by small fields $\vec{H} \,||\, [111]$, but within the Kagomé planes a competition between the 2in-2out ice rule and the

Zeeman energy occurs. This results in a threefold degenerate Kagomé-ice state, where in every tetrahedron 1 out of the 3 Dy moments of the Kagomé plane has a finite component opposite to the magnetic-field direction. At low temperatures, the Kagomé-ice phase is characterized by a plateau in the magnetization $M(H)$ up to about 1 T, where a transition to the fully polarized state occurs, see Fig. 7.2 (b). In contrast to the $M(H)$ data that do not reveal a hysteresis within the Kagomé-ice state, $\kappa(H)$ is strongly hysteretic according to Kolland *et al.* [15] and Sun *et al.* [12]. In Ref. 12, the heat current $\vec{j}$ was applied along and perpendicular to the magnetic field, *i.e.* with $\vec{j}$ perpendicular and within the Kagomé planes, respectively. In Ref. 15, $\vec{j}$ was applied along $[1\bar{1}0]$. However, there are also deviations between the results of Ref. 12 and Ref. 15. According to Ref. 12 no hysteresis of the zero-field values $\kappa(H = 0)$ seems to be present. This means that the initial value κ_0 is fully recovered by $\kappa(H \to 0)$ measured with decreasing field for both directions of $\vec{j}$. In contrast, it is found in Ref. 15 that the zero-field values $\kappa(H = 0)$ reveal a hysteresis for $\vec{j} \,||\, [1\bar{1}0]$.

Fig. 7.2 (c) displays $\kappa(H)/\kappa_0$ for $\vec{H} \,||\, [111]$ with a heat current $\vec{j}$ along $[1\bar{1}0]$ at various temperatures from Ref. 15. The data were measured with a field-sweep rate of ≈ 0.006 T/min. The plateau-like feature of $\kappa(H)$ below ≈ 1 T clearly signals the Kagomé-ice phase. As already mentioned above, below ≈ 0.6 K the $\kappa(H)$ data show a clear hysteresis in the Kagomé-ice phase, whereas no such hysteresis is present in the plateau region of the corresponding magnetization curve at 0.4 K shown in Fig. 7.2 (b). Moreover, the initial κ_0 obtained after zero-field cooling is clearly not recovered within the low-temperature field cycles. Here, $\kappa(H \to 0)$ results in reduced zero-field values, which as a function of time slowly relax towards κ_0 [16]. This zero-field relaxation is present for all three field directions $\vec{H} \,||\, [001]$, $\vec{H} \,||\, [110]$, and $\vec{H} \,||\, [111]$, where in all cases the heat current is driven along $[1\bar{1}0]$ [15, 16, 48]. In the high-field region $H > 1$ T, where the magnetization is essentially saturated, no slow relaxation or hysteresis occur in analogy to $\vec{H} \,||\, [001]$.

The origin of the relaxation processes and hysteresis within the Kagomé-ice phase is still unclear. That is why, complete low-field hysteresis loops of $\kappa(H)$ for positive and negative magnetic field were performed at 0.4 K which are shown in Fig. 7.3 (a). Concerning the reduced zero-field values, the observed systematics of $\kappa(H)$ in panel (a) are analogous to that already discussed above for $\vec{H} \,||\, [001]$. Again $\approx 90\%$ of the initial value are recovered. In addition, it turns out that the hysteresis in the Kagomé-ice phase in the initial field cycle, curves (1) and (2), is smaller than in the subsequent cycles. In particular, the minima in the $\kappa(H)$ curves (3) and (5) are more pronounced than the minimum in the initial curve (1). In order to further investigate these phenomena, relaxation studies within this field region were carried out and are depicted in Fig. 7.3 (b)-(c). First, the time dependence $\kappa(t)$ was measured at constant field and temperature starting from the $\kappa(H)$ curve

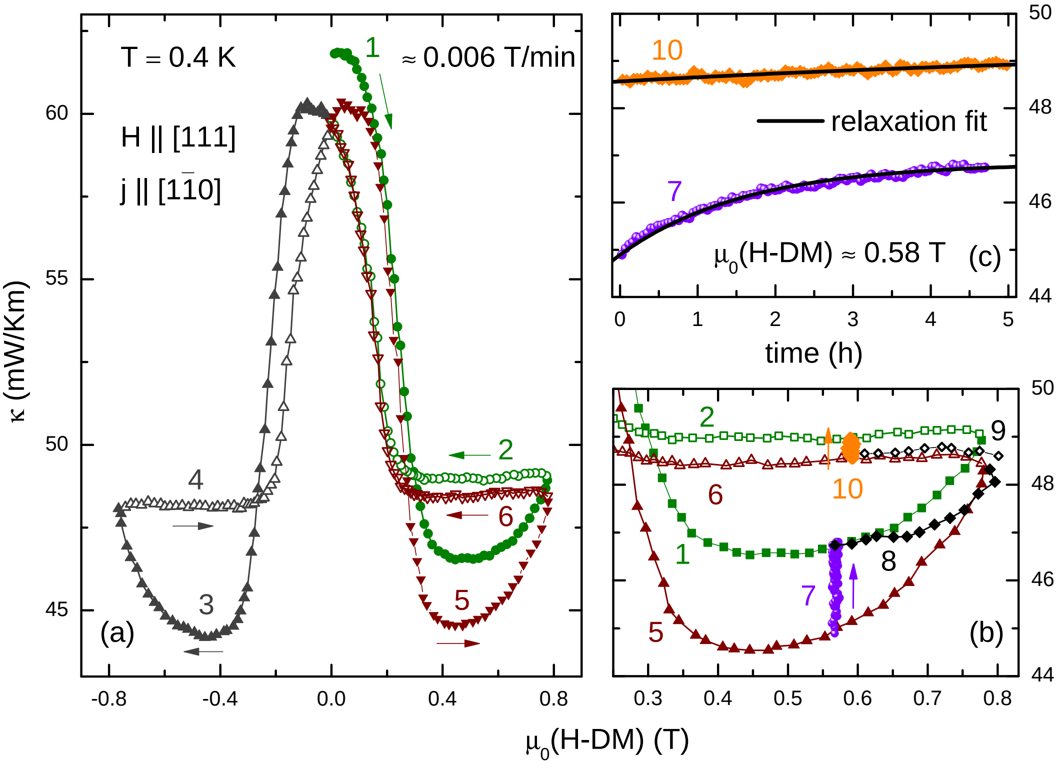

Figure 7.3: Low-field hysteresis loops of $\kappa(H)$ are displayed in (a), where the order of the successive field sweeps is marked by the numbers 1-6. An expanded view of $\kappa(H)$ in the Kagomé-ice region is displayed in (b), which also shows the $\kappa(t)$ curves (7) and (10) and the additional field sweeps (8) and (9); see text. The relaxation curves $\kappa(t)$ with corresponding fits as a function of time are displayed in (c). The data are taken from Ref. 16

(5). Similar to the zero-field case, slow relaxation occurs with a time constant $\tau \approx 100$ min and the $\kappa(t)$ curve seems to relax towards the initial $\kappa(H)$ curve (1). Thus, the relaxation measurement was stopped after 4.5 hours and the field was cycled up to 0.8 T and back to ≈ 0.58 T. The corresponding $\kappa(H)$ curves (8) and (9) do, however, not follow the initial field dependent $\kappa(H)$ curves (1) and (2). Instead, the $\kappa(H)$ curve (8) approaches curve (5) and the field-decreasing $\kappa(H)$ curve (9) essentially follows curve (6). At ≈ 0.58 T, $\kappa(t)$ was again measured and a weak, almost linear increase of $\kappa(t)$ yielding a very large relaxation rate of $\tau \approx 520$ min. These data suggest that the relaxation within the Kagomé-ice phase is not directly related to the zero-field relaxation and also reveal that, depending on the field and temperature region, a true thermal equilibrium can be hardly reached under typical experimental conditions. This seems exclusively possible in regions where the magnetization $M(H)$ is also saturated. No relaxation or hysteresis have been

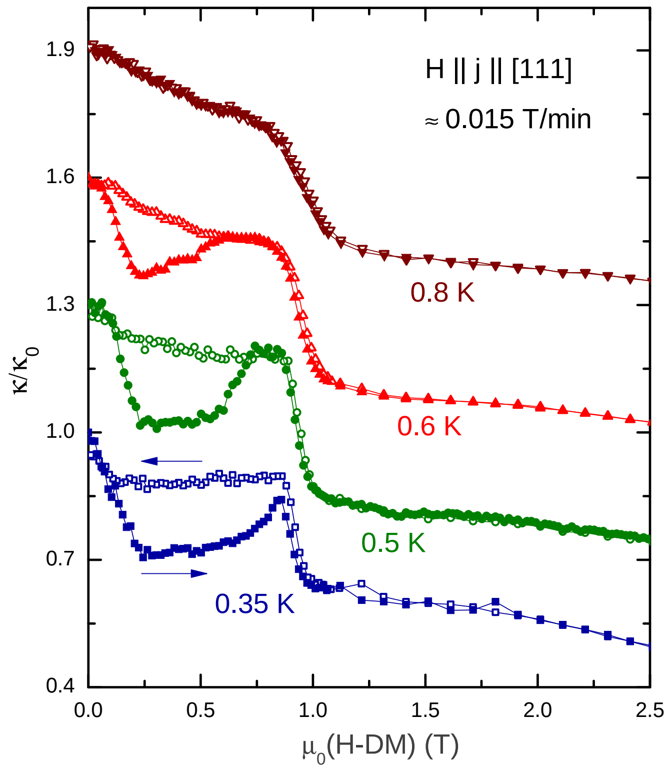

Figure 7.4: Field dependence $\kappa(H)/\kappa_0$ for $\vec{H}\,||\,[111]$ and $\vec{j}\,||\,[111]$ with different field-sweep directions (marked by arrows). The curves for different temperatures are shifted with respect to each other.

found within these regimes so far.

7.1.3 $\vec{\mathbf{H}}\,||\,[111]$ and $\vec{\mathbf{j}}\,||\,[111]$

Fig. 7.4 displays the field-dependence $\kappa(H)/\kappa_0$ for the same magnetic-field direction [111] as in the previous section, but in this case with the heat current $\vec{j}\,||\,[111]$. Again, within the Kagomé-ice phase the data reveal a hysteresis of $\kappa(H)$ which has no analogue in the magnetization curves for $\vec{H}\,||\,[111]$, see Fig. 7.2 (b). However, there are also systematic differences between $\kappa(H)/\kappa_0$ curves for the same field but different heat current directions. First of all comparing the data of Fig. 7.2 (c) and Fig. 7.4, the hysteresis width with respect to the different absolute values of $\kappa(H)$ in the Kagomé-ice phase is significantly larger for $\vec{j}\,||\,[111]$ than for $\vec{j}\,||\,[1\bar{1}0]$. Secondly, the upper critical field, where the hysteresis closes, strongly decreases with increasing temperature for $\vec{j}\,||\,[111]$, while it is essentially temperature-independent for $\vec{j}\,||\,[1\bar{1}0]$. Finally, for $\vec{j}\,||\,[111]$ the initial zero-field κ_0 is recovered in the field-decreasing runs despite the fact that there is a finite remnant magnetization, when $M(H)$ is measured with a comparable sweep rate, see Fig. 7.2 (b). This fact is very surprising as the $\kappa(H)$ with $\vec{H}\,||\,[111]$ and $\vec{j}\,||\,[111]$ is the only combination were the initial κ_0 is recovered.

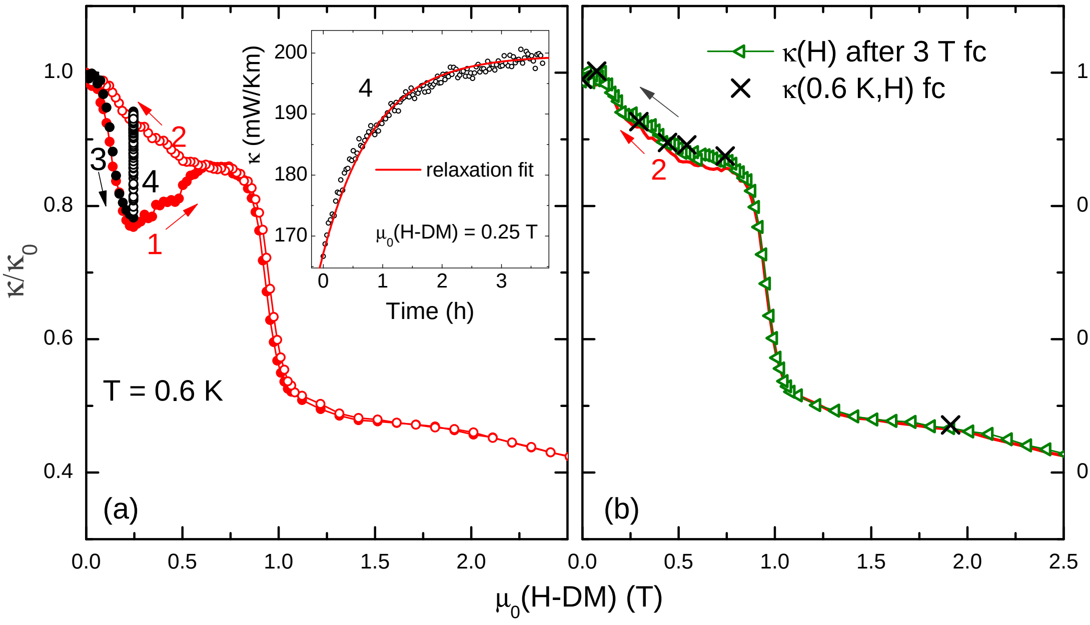

Figure 7.5: Successive field sweeps (1)-(3) at 0.6 K together with a relaxation curve (4) are shown in panel (a). The inset displays the $\kappa(t)$ curve (4) as a function of time, while in panel (b) the $\kappa(H)/\kappa_0$ curve (2) is compared to different $\kappa(H)/\kappa_0$ values obtained by field cooling and to a field-decreasing run measured after field cooling in 3 T.

Relaxation and zero-field-cooled measurements of $\kappa(H)/\kappa_0$ for $\vec{H}\,||\,\vec{j}\,||\,[111]$ reveal that in the hysteresis region of $\kappa(H)/\kappa_0$ the curves measured with decreasing field, are closer to thermal equilibrium than the curves with increasing field. This is confirmed by the data shown in Fig. 7.5 (a) where $\kappa(t)$ relaxes from the lower $\kappa(H)$ curve (1) to the upper curve (2) at $T = 0.6$ K. A single exponential fit to the $\kappa(t)$ data yield a relaxation time $\tau \approx 52$ min, see inset. Moreover, the $\kappa(H)$ values obtained either by field-cooling in various fixed fields or by field-cooling in 3 T and decreasing the field to 0 T well agree with the initial field decreasing $\kappa(H)$ curve (2), as shown in Fig. 7.5 (b). Qualitatively, this hysteresis and relaxation of $\kappa(H)$ can be understood by assuming that disorder within the Kagomé-ice phase causes an additional suppression of κ, because starting from the fully polarized high-field state will cause less disorder in the Kagomé-ice phase than entering this phase from the entropic zero-field spin-ice ground state. In addition, it was found that the presence or absence of a zero-field hysteresis of $\kappa(H \to 0)$ for $\vec{H}\,||\,[111]$ depends on the direction of $\vec{j}$ and this indicates that the strength and the direction of a heat current through spin ice is most likely an additional parameter to influence its thermal equilibration.

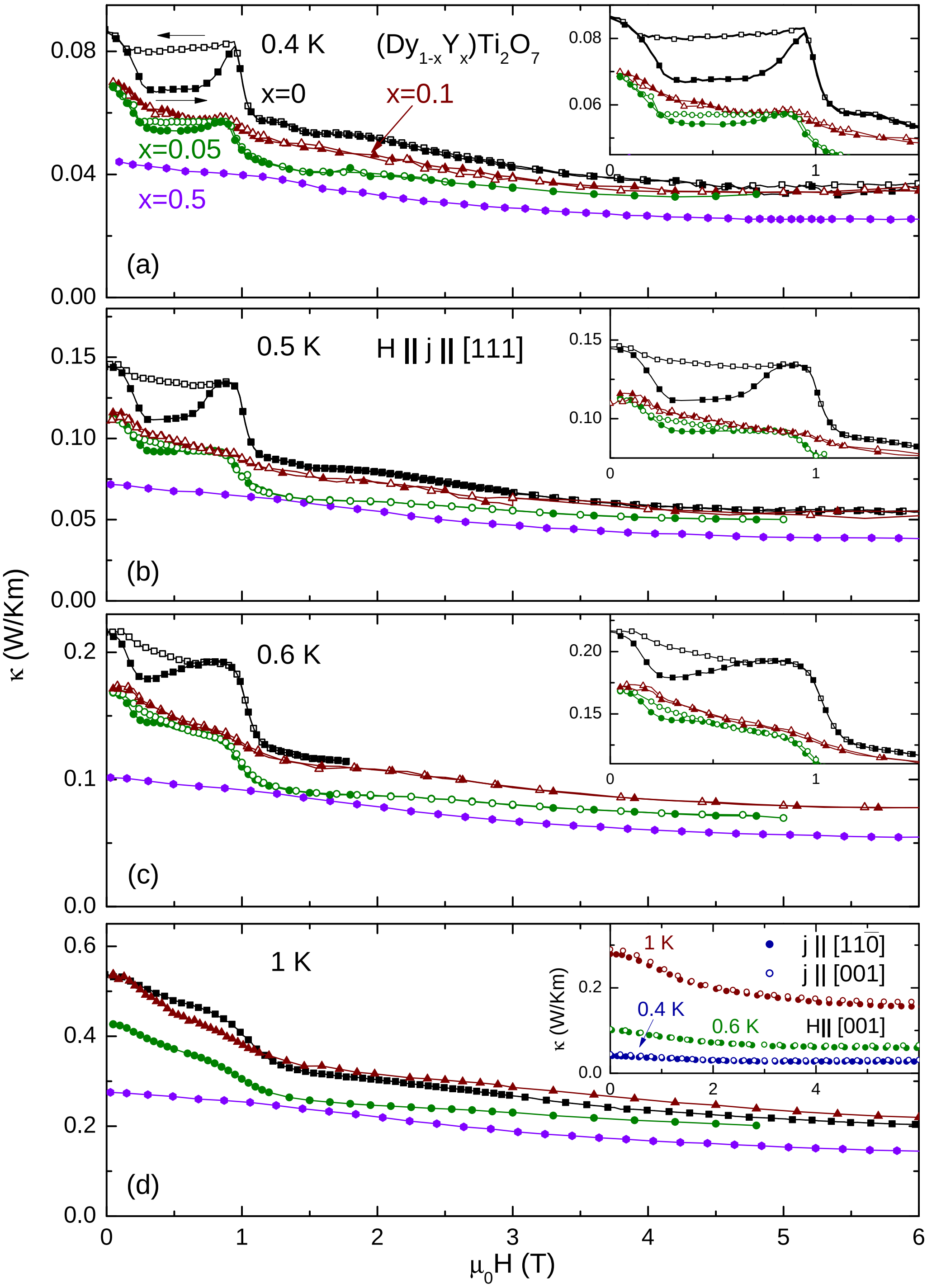

Figure 7.6: Thermal conductivity of $(Dy_{1-x}Y_x)_2Ti_2O_7$ with $x = 0$–0.5 for $\vec{H} \,||\, [111]$. The heat current is applied along [111] ($\vec{j} \,||\, [1\bar{1}0]$ for $x = 0.5$). Insets panels (a)-(c): expanded view of the low-field regime. Inset of panel (d): comparison of κ for $\vec{H} \,||\, [001]$ with $\vec{j}$ along [001] and along [1$\bar{1}$0].

In order to further study the hysteresis within the Kagomé-ice phase in the thermal conductivity of $Dy_2Ti_2O_7$ for $\vec{H}\,||\,[111]$, $\kappa(H)$ was also measured for the dilute spin-ice compounds $(Dy_{1-x}Y_x)_2Ti_2O_7$ with $x = 0.05$–0.5. The corresponding data of the pure crystal and the dilute systems are shown in Fig. 7.6 (a)-(d) in the temperature range from 0.4 K up to 1 K. The insets of panel (a)-(c) show an expanded view of the low-field range. The heat current was basically applied along [111], whereas for $x = 0.5$ the data were obtained with $\vec{j}\,||\,[1\bar{1}0]$. It was checked for $\vec{H}\,||\,[001]$ with $\vec{j}\,||\,[001]$ and $\vec{j}\,||\,[1\bar{1}0]$, that the direction of the heat current can be neglected at a dilution level of $x = 0.5$ which is shown in the inset of Fig. 7.6 (d) for different temperatures. The data represented by the open symbols were measured with $\vec{j}\,||\,[001]$ and the closed symbols depict data with $\vec{j}\,||\,[1\bar{1}0]$. Both data sets well agree in the whole temperature range. As can be seen in the inset of panel (a), the huge hysteresis within the Kagomé-ice phase in $\kappa(H)$ of the pure $Dy_2Ti_2O_7$ is already strongly reduced by a dilution of $x = 0.05$ at 0.4 K. For $x = 0.1$, no hysteresis is present and $\kappa(H)$ decreases in the low-field regime up to about 1 T. The curve for $x = 0.5$ does not show a strong field dependence as $\kappa(H)$ weakly decreases up to 6 T. As naturally expected, the hysteresis in the $x = 0$ and 0.05 curves reduces with increasing temperatures and has vanished in both compounds at 1 K, see panel (d). In addition, the transition into the fully-polarized phase, which occurs around 1 T in $Dy_2Ti_2O_7$, broadens with increasing temperature and is hardly visible at 1 K. These data reveal that the Kagomé-ice phase hysteresis in $\kappa(H)$ is highly sensitive to dilution with non-magnetic yttrium and has already vanished for $x = 0.1$ at 0.4 K.

The above findings support the interpretation that disorder of the magnetic moments within the Kagomé-ice planes strongly suppresses the thermal conductivity in this region. In contrast to the curves of $Dy_2Ti_2O_7$ measured with decreasing field, which show enhanced values of $\kappa(H)$ in the Kagomé-ice phase, the curves for $x = 0.05$ and 0.1 do not reveal this tendency but nearly follow the reduced values measured with increasing field which most likely originates from an increasing disorder with increasing dilution x. Furthermore, it is a surprise finding that $\kappa(H \to 0)$ recovers the initial value κ_0 for $\vec{H}\,||\,\vec{j}\,||\,[111]$ which is confirmed for all x. Here, the heat current is applied perpendicular to the Kagomé-ice planes which would naively lead to reduced κ values due to the polarized triangular planes in-between for finite fields along [111]. In contrast the initial value κ_0 is not recovered by $\kappa(H \to 0)$ for the configuration $\vec{H}\,||\,[111]$ and $\vec{j}\,||\,[1\bar{1}0]$ in which the heat is sent through the Kagomé planes. The origin of this effect is unclear and it could be speculated that the coupling between the polarized triangular planes and the Kagomé is larger than expected. Hence, the monopole heat transport is not reduced along this direction compared to the transport in the Kagomé planes.

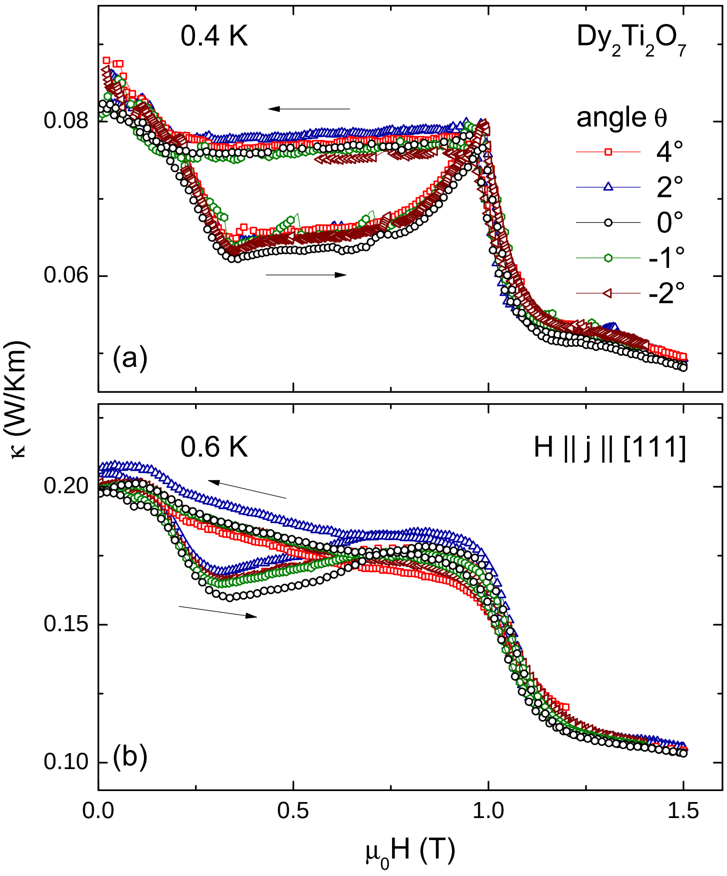

Figure 7.7: Angle dependent thermal conductivity κ as a function of the magnetic field of $Dy_2Ti_2O_7$ for $\vec{j} \,||\, [111]$ at 0.4 and 0.6 K. The angle θ indicates the deviation of $\vec{H}$ from the [111] direction within the [111]-[$1\bar{1}0$] plane.

Angle-dependent heat transport

This section concerns $\kappa(H)$ of $Dy_2Ti_2O_7$ for $\vec{j} \,||\, [111]$ whereas the magnetic field can be applied along any direction within the [111]-[$1\bar{1}0$] plane. This was accomplished by a solenoid magnet which was operated in a custom cryostat. In this setup, it is possible to change the direction of the magnetic field within the [111]-[$1\bar{1}0$] plane by simply turning the insert from outside the cryostat.

This experiment is motivated by the occurrence of this low-field hysteresis in κ within the Kagomé-ice phase for $\vec{H} \,||\, [111]$ which has also been observed in Refs. 12, 15, 48, 129 and has no analogue in the magnetization $M(H)$. Relaxation processes and the influence of non-magnetic dilution by yttrium on the hysteresis were already investigated. The Kagomé-ice phase, which is realized at low temperatures for $\vec{H} \,||\, [111]$ below about 1 T, is only threefold degenerate if the magnetic field is exactly applied along [111]. Fig. 7.2 (a) shows an illustration of the alternating triangular and Kagomé planes with respect to the [111] direction. The threefold degeneracy is a result of the triangular planes which are fully polarized already by small fields $\vec{H} \,||\, [111]$ and the competition between the 2in-2out ground state and the Zeeman energy in the Kagomé planes where in every tetrahedron 1 out of the 3 Dy moments has a finite component opposite to the field. However, a small misalignment of the applied field from this [111] direction would lift the degeneracy because in this case one out of the three configurations for every tetrahedron within the Kagomé planes would be energetically favorable. Hence, the target of this angle-dependent study is to find out whether the presence or absence of the threefold degeneracy is related to the hysteresis of κ in the Kagomé-ice phase.

In the experiment, it was possible to measure $\kappa(H)$ with different directions of the applied magnetic field within the [111]-[1$\bar{1}$0] plane whereas the heat current j is always sent along [111] which is the longest dimension of the sample. The corresponding data are displayed in Fig. 7.7 (a)-(b). The angle θ determines the deviation of the applied field from the [111] direction in the [111]-[1$\bar{1}$0] plane. Panel (a) shows $\kappa(H)$ at 0.4 K. For $\theta = 0°$, $\kappa(H)$ reveals the expected behavior for $\vec{H} \,||\, \vec{j} \,||\, [111]$. A hysteresis is observed within the Kagomé-ice phase and close to 1 T the transition into the fully polarized phase occurs. Furthermore, $\kappa(H)$ measured with decreasing field recovers the initial values κ_0 obtained after zero-field cooling which is observed for $\vec{j} \,||\, [111]$ in contrast to $\vec{j} \,||\, [1\bar{1}0]$, compare Fig. 7.2 (c). But as can be seen in Fig. 7.7 (a)-(b), the hysteresis of $\kappa(H)$ within the Kagomé plane is not influenced for different angles θ. The size and shape of the hysteresis stay constant and the zero-field value is recovered for all shown θ. Furthermore, $\kappa(H)$ was also measured for additional angles between $-2° \leq \theta \leq 4°$ in steps of 0.2° (not shown). No visible change was observed within the additional measurements. Thus, it can be concluded that a the lifting of the ground state degeneracy for $\vec{H} \,||\, [111]$ due to a small misalignment of the applied field is not related to the hysteresis in $\kappa(H)$. As a consequence, another mechanism has to be the origin. As discussed above, it is most likely that the disorder in the Kagomé-ice phase results in an additional suppression of κ, as less disorder will be present coming from the fully-polarized phase with $\kappa(H \to 0)$ than entering the Kagomé-ice phase from the entropic 6-fold degenerate spin-ice ground state in zero magnetic field.

7.1.4 Conclusion

The thermal conductivity κ of the spin-ice compound $Dy_2Ti_2O_7$ shows strong hysteresis and slow relaxation processes towards equilibrium states in the low-temperature and low-field regime. In general, the thermal conductivity in the hysteretic regions slowly relaxes towards larger values suggesting that there is an additional suppression of the heat transport by disorder in the non-equilibrium states. The degree of hysteresis does not only depend on temperature and the magnetic-field direction, but also on the rate of the magnetic-field change and, for $\vec{H} \,||\, [111]$ even on the direction of the heat current. The observation that the rate of thermal equilibration in spin ice can be influenced by a finite heat current along certain directions may yield important information about the dynamics of monopole excitations and their interaction with phonons. In addition, the hysteresis within the Kagomé-ice phase in κ was studied for the dilute spin-ice materials $(\mathrm{Dy}_{1-x}\mathrm{Y}_x)_2\mathrm{Ti}_2\mathrm{O}_7$ with $x \leq 0.5$ and for the pure compound $\mathrm{Dy}_2\mathrm{Ti}_2\mathrm{O}_7$ at different angles of the applied field within the [111]-[1$\bar{1}$0] plane. An increasing dilution x leads to a rapid suppression of the hysteresis whereas the initial $\kappa(0\ \mathrm{T})$ is recovered for all x for the configuration $\vec{H} \,||\, \vec{j} \,||\, [111]$. The magnitude and shape of the hysteresis did not reveal an angle-dependence for small θ. The above findings support the interpretation that the hysteresis within the Kagomé-ice phase in κ most likely originates from disorder instead of a misalignment of the applied magnetic field which would lift the 3-fold ground-state degeneracy there.

7.2 Specific heat and entropy

7.2.1 Literature results

One of the hot topics concerning spin ice $\mathrm{Dy}_2\mathrm{Ti}_2\mathrm{O}_7$ is a possible residual entropy of $1/2\,R\,\ln(3/2)$ for $T \to 0$ K in analogy to water ice. A residual entropy for water ice was predicted by L. Pauling in 1935 [5]. Later, the water-ice lattice was mapped onto the pyrochlore structure and, thus, the question arose whether this residual entropy can also be observed for spin ice $\mathrm{Dy}_2\mathrm{Ti}_2\mathrm{O}_7$.

Refs. 90–92, 118 report a practically temperature-independent low-temperature entropy $S_{\mathrm{ex}}(T < 0.4\ \mathrm{K}) \simeq S_{\mathrm{P}}$ where S_{ex} is the experimentally obtained entropy and $S_{\mathrm{P}} = 1/2\,R\,\ln(3/2)$ denotes Pauling's entropy. As discussed in Sec. 4.4, very slow-relaxation effects were observed for $\mathrm{Dy}_2\mathrm{Ti}_2\mathrm{O}_7$ at lowest temperatures in different physical properties [11, 14, 14, 20, 48, 111–113, 151]. The observation of the low-temperature slow equilibration processes led to an experiment by Pomeranski *et al.* which confirmed the absence of Pauling's residual entropy in $\mathrm{Dy}_2\mathrm{Ti}_2\mathrm{O}_7$ [20], see also Sec. 4.5. These relaxation processes typically set in below ≈ 0.6 K and are related to strongly increasing timescales for the internal thermal equilibration. Another open issue is the influence of non-magnetic dilution on the spin-ice ground state. Sen *et al.* introduced a microscopic Hamiltonian that predicts a topological spin glass for spin-ice materials with small non-magnetic dilution [152]. Features such as the simultaneous appearance of topological spin liquidity and glassiness appear along with the presence of small frozen moments alongside a sizable fluctuating component within this model. They predict that weakly-dilute spin ice undergoes a crossover into a topological Coulomb phase below Θ_{W} coming from a paramagnetic state. By further decreasing the temperature, the free monopoles

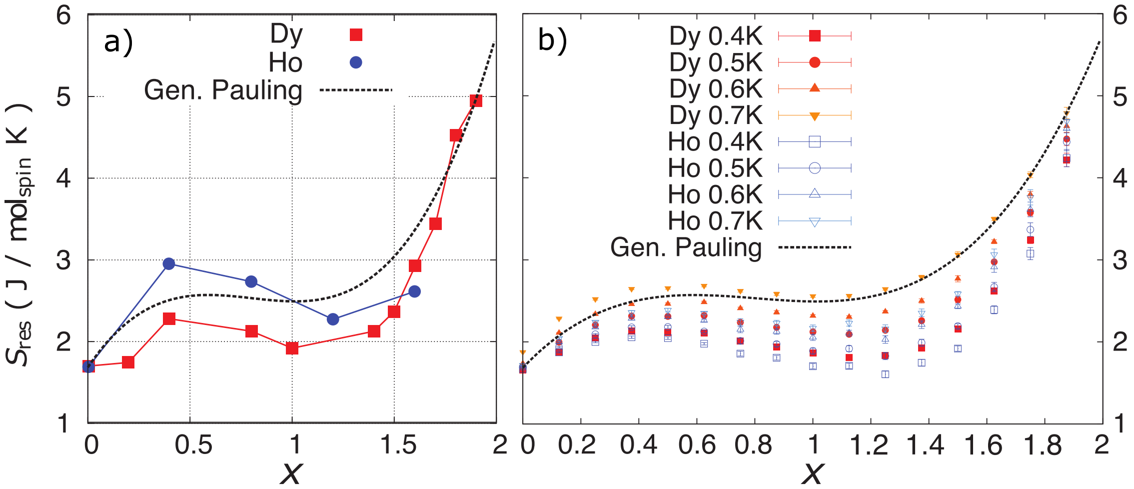

Figure 7.8: Panel (a): Generalized Pauling approximation of the residual entropy $S_\mathrm{p}(x)$ in comparison with experimental results of $Dy_2Ti_2O_7$ and $Ho_2Ti_2O_7$ taken from Ref. 19. Panel (b): $S_\mathrm{p}(x)$ together with Monte Carlo results for $0.4\ \mathrm{K} \leq T \leq 0.7\ \mathrm{K}$ from Ref. 21.

freeze and become impurity monopoles before the topological spin glass phase appears at T_C. In Ref. 152, it is claimed that $(Dy_{1-x}Y_x)_2Ti_2O_7$ and $(Ho_{1-x}Y_x)_2Ti_2O_7$ are possible candidates to confirm this topological spin glass phase. However, the specific heat results on $(Dy_{1-x}Y_x)_2Ti_2O_7$ within this thesis can neither confirm nor negate the existence of this phase as the transition temperatures are well below the experimental accessible regime. The model would be applicable for $x \lesssim 0.1$ with a transition temperature $T_\mathrm{C} \leq 0.087$ K.

The influence of non-magnetic dilution in spin ice has also been investigated by Ke *et al.* in 2007 where Pauling's model was generalized and a non-monotonic residual entropy $S_\mathrm{P}(x)$ as a function of the dilution content x was predicted [19]. This generalized Pauling model is depicted in Fig. 7.8 (a) together with the experimental results $S_\mathrm{ex}(x, T = 0.4\ \mathrm{K})$ of $Dy_2Ti_2O_7$ and $Ho_2Ti_2O_7$ obtained from specific heat data. The experimental data more or less confirm the model. But there are several reasons why this result is highly questionable. Firstly, they do not take the slow-thermal equilibration in the low-temperature regime into account. Secondly, the data reveal huge uncertainties in estimating the phononic specific heat to high-enough temperature. Thirdly, a strong slope of c/T for the highly-dilute systems at lowest temperatures (≈ 0.4 K) is neglected which can be clearly observed in the data. In 2014, Monte Carlo (MC) simulations of dilute spin ice were published by Lin *et al.* which are interpreted to confirm the non-monotonic dependence $S_\mathrm{P}(x)$ [21]. The corresponding data are shown in Fig. 7.8 (b). However for $x > 0.2$, the numerically obtained entropy $S_\mathrm{MC}(x, T < 0.7\ \mathrm{K})$ (colored symbols) falls below the predicted $S_\mathrm{P}(x)$ (dashed black line) and decreases further towards lower temperature. The MC data is not quantitatively compared to experimental data $S_\mathrm{ex}(x,T)$ because of uncertainties in estimating the phononic background [21]. The notation of Refs. 19, 21 differs from this thesis ($\mathrm{Dy_{2\text{-}x}Y_xTi_2O_7}$ *vs.* $(\mathrm{Dy}_{1-x}\mathrm{Y}_x)_2\mathrm{Ti_2O_7}$). Because the results of Ke *et al.* [19] and Lin *et al.* [21] are questionable and the influence of yttrium dilution on the low-temperature slow equilibration is not investigated, a detailed specific-heat study of the dilution series $(\mathrm{Dy}_{1-x}\mathrm{Y}_x)_2\mathrm{Ti_2O_7}$ with $x = 0$–0.75 is presented.

7.2.2 Experimental results

The measurements have been performed on oriented $(\mathrm{Dy}_{1-x}\mathrm{Y}_x)_2\mathrm{Ti_2O_7}$ single crystals of ≈ 20 mg using the home-built calorimeter presented in Sec. 3.5. In the high-temperature regime, the standard relaxation-time method is applied for the specific heat which was introduced in Sec. 3.5.1. However, this method only yields reliable results if the internal equilibration within the crystal is much faster than the equilibration to the bath. That is why, the relaxation method is only applicable in the high-temperature regime for the pure and weakly dilute systems $(\mathrm{Dy}_{1-x}\mathrm{Y}_x)_2\mathrm{Ti_2O_7}$ with $x < 0.2$. It fails if the internal thermal equilibration becomes too slow. In this regime, the constant heat-flow method is used, see Sec. 3.5.2. This method analyzes the heating curve over a longer timescale [14] and is equivalent to the method applied by Pomaranski *et al.* [20] where the specific heat is derived from temperature-relaxation curves.

Thermal equilibration

Fig. 7.9 compares typical heating curves of the normalized temperature difference $1-\Delta T(t)/\Delta T_\mathrm{max}$ where $\Delta T = T - T_0$ and T_0 is the stabilized base temperature. At $T_0 \simeq 0.8$ K, the heating curves over the entire dilution range in $(\mathrm{Dy}_{1-x}\mathrm{Y}_x)_2\mathrm{Ti_2O_7}$ are straight lines in a semi-logarithmic representation. This is expected if the internal thermal equilibration, where internal means inside the sample as well as between the sample and the platform, is much faster than the thermal relaxation to the external heat bath. Then, the heat capacity is obtained via $C = \tau K$ from the standard relaxation method with the relaxation time τ and the thermal conductance $K = \Delta P/\Delta T_\mathrm{max}$ between the sample platform and the thermal bath. For lower base temperatures $T_0 \simeq 0.5$ K and 0.36 K, however, the relaxation curves of pure $\mathrm{Dy_2Ti_2O_7}$ become non-exponential as a consequence of the slow internal thermal equilibration. Here, the heat capacity is obtained via the constant heat-flow method. A weak thermal coupling K to the bath is necessary to resolve variations of $\Delta T(t)$ using the constant heat-flow method over long time. The K of the

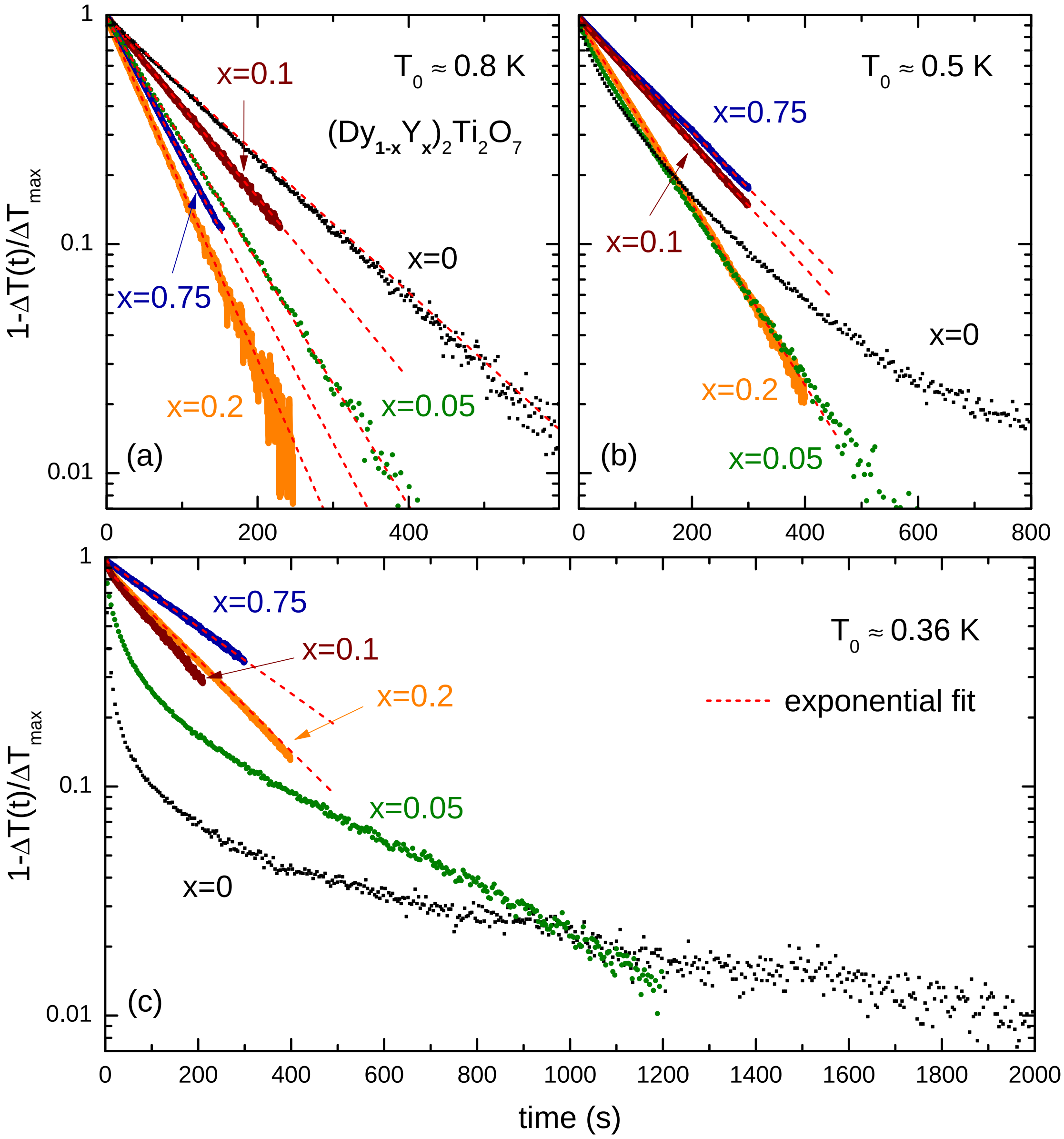

Figure 7.9: Heating curves $1-\Delta T(t)/\Delta T_{\max}$ of $(\mathrm{Dy}_{1-x}\mathrm{Y}_x)_2\mathrm{Ti}_2\mathrm{O}_7$ with $x = 0$–0.75. Here, $\Delta T(t) = T(t) - T_0$ is measured relative to the base temperature T_0 and $\Delta T_{\max}$ is its limiting value. The dashed red lines are fits to those data showing an exponential decay with a single relaxation time.

actual setup is however relatively large and therefore restricts the measurements up to ≈ 2000 s. Concerning the dilute $(\mathrm{Dy}_{1-x}\mathrm{Y}_x)_2\mathrm{Ti}_2\mathrm{O}_7$ systems in Fig. 7.9, the low-temperature heating curves for $x = 0.05$ and 0.1 also show non-exponential behavior. Thus, the constant heat-flow method had also been applied below 0.6 K. These relaxation effects are, however, much less pronounced than in pure $\mathrm{Dy}_2\mathrm{Ti}_2\mathrm{O}_7$, and for $x \geq 0.2$ the heating curves remain exponential down to the lowest temperature. Thus, it can be stated that the data reveal that the ultra-slow thermal equilibration in $\mathrm{Dy}_2\mathrm{Ti}_2\mathrm{O}_7$ is drastically suppressed by comparatively weak dilution with non-magnetic Y.

Specific heat

Fig. 7.10 (a) shows the specific heat c of $(\mathrm{Dy}_{1-x}\mathrm{Y}_x)_2\mathrm{Ti}_2\mathrm{O}_7$ measured in zero magnetic field as a function of the temperature for different degrees of dilutions x. Above ≈ 1 K, $c(x, T)$ continuously decreases with increasing x. For $1\ \mathrm{K} < T < 10\ \mathrm{K}$, $c(T)$ is dominated by its magnetic contribution c_{mag}. The corresponding decrease in c is essentially reflecting the decreasing amount of magnetic Dy ions with increasing x. The phonon contribution to the specific heat c_{ph} starts to dominate in the high-temperature regime above 10 K. Here, the data show a systematic decrease with increasing x which can be explained by the fact that yttrium is much lighter than dysprosium. The molar mass per formula unit (fu) of $(\mathrm{Dy}_{1-x}\mathrm{Y}_x)_2\mathrm{Ti}_2\mathrm{O}_7$ decreases from 533 to 386 $\mathrm{g/mol_{fu}}$ between $x = 0$ and 1, respectively. That is why, a larger x enhances the eigenfrequencies of the acoustic phonon branches. Therefore, the low-temperature increase of c_{ph} sets in at higher temperature. The phonon contribution c_{ph} to the specific heat of the Dy-containing compounds is determined by rescaling the temperature axis of the measured $c(T)$ of the non-magnetic $\mathrm{Y}_2\mathrm{Ti}_2\mathrm{O}_7$. The measured $c(T)$ curve of $\mathrm{Y}_2\mathrm{Ti}_2\mathrm{O}_7$ is shown in Fig. 7.10 (a) represented by the red balls. It confirms the trend that c_{ph} decreases with increasing x. The rescaling of $\mathrm{Y}_2\mathrm{Ti}_2\mathrm{O}_7$ enables to match the specific heat of $(\mathrm{Dy}_{1-x}\mathrm{Y}_x)_2\mathrm{Ti}_2\mathrm{O}_7$ in the temperature range around 25 K, *i.e.* via

$$c(x = 1, r_x \cdot T) = c(x < 1, T \simeq 25\ \mathrm{K}) \tag{7.1}$$

with x-dependent scaling factors ranging from $r_x = 0.8$ to 0.95 for $0 \leq x \leq 0.75$, respectively. As an example, the resulting c_{ph} of the pure $\mathrm{Dy}_2\mathrm{Ti}_2\mathrm{O}_7$ is shown as a dashed red line in Fig. 7.10 (a) and the magnetic contributions are derived via

$$c_{\mathrm{mag}}(x, T) = c(x, T) - c(x = 1, r_x \cdot T). \tag{7.2}$$

The curves of c_{mag} for all $x \leq 0.75$ are shown in Fig. 7.10 (b). Here, the data are normalized to the amount of the magnetic Dy ions and are presented as c_{mag}/T as a function of the temperature T. In this representation, the data for all x almost

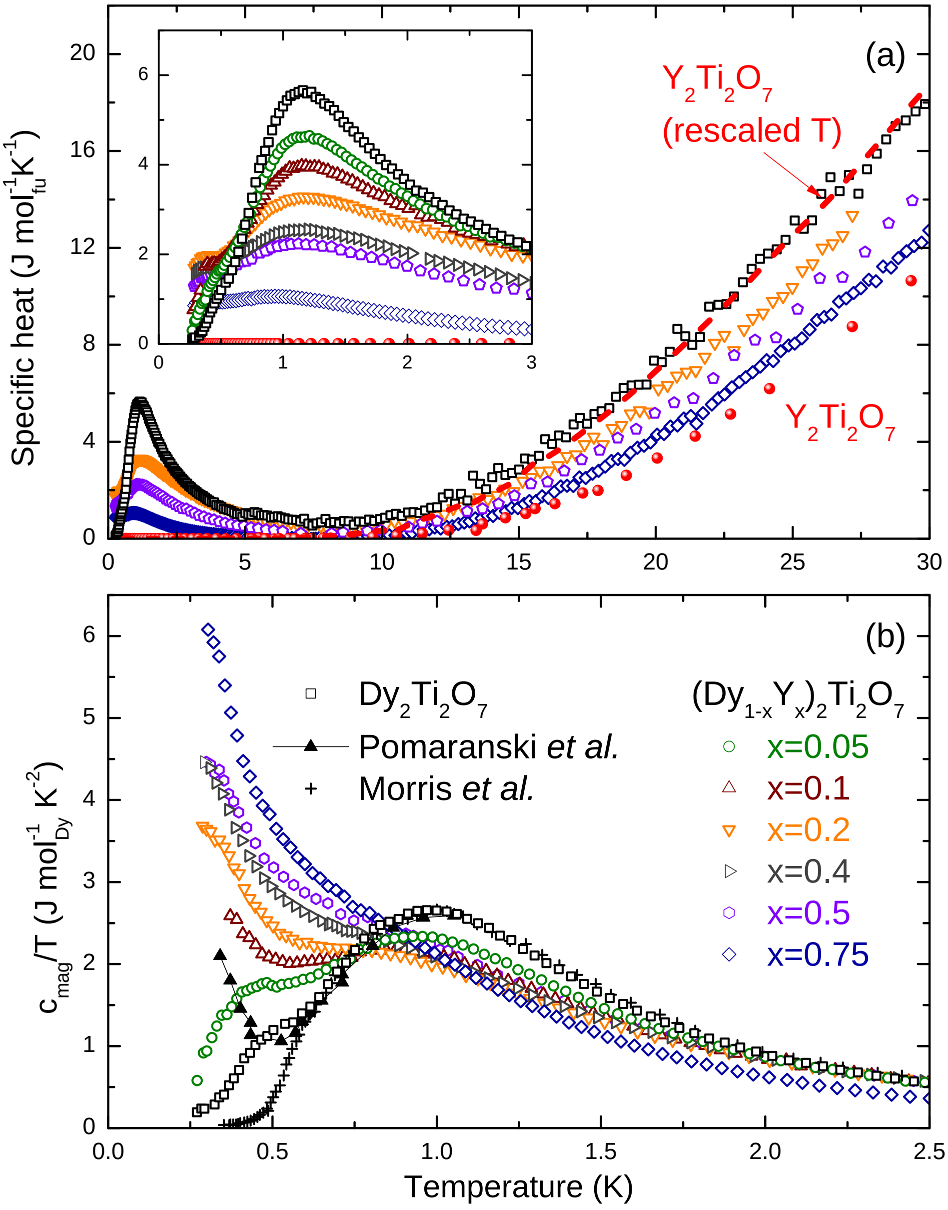

Figure 7.10: (a) Specific heat $c(T)$ per formula unit (fu) of $(\mathrm{Dy}_{1-x}\mathrm{Y}_x)_2\mathrm{Ti}_2\mathrm{O}_7$ for selected x with an expanded view of the low-temperature range for all x in the inset. The phononic contributions $c_{\mathrm{ph}}(x,T)$ were estimated by the specific heat of non-magnetic $\mathrm{Y}_2\mathrm{Ti}_2\mathrm{O}_7$ after rescaling the temperature axis such that the data sets match around $T \simeq 25$ K, as is shown for $x = 0$ by the dashed line. In (b), the resulting magnetic contribution $c_{\mathrm{mag}}(x,T) = c(x,T) - c_{\mathrm{ph}}(x,T)$ normalized by the Dy content is displayed in the representation c_{mag}/T versus T for $T \leq 2.5$ K. For $\mathrm{Dy}_2\mathrm{Ti}_2\mathrm{O}_7$, c_{mag}/T obtained either by a standard relaxation measurement (+,[92]) or after extremely long-time equilibration (▲,[20]) are included.

coincide above 2 K whereas below ≈ 0.7 K a drastic increase of c_{mag}/T with increasing x is found. Thus, the temperature dependence of the entropy $\partial S/\partial T = c_{\mathrm{mag}}/T$ strongly increases with x for $T < 0.7$ K. This finding is independent from the uncertainty in estimating the phononic background. In the entire temperature range of Fig. 7.10 (b) any realistic c_{ph} is negligibly small compared to c_{mag}. Furthermore, the strong increase of $\partial S/\partial T = c_{\mathrm{mag}}/T$ for $T < 0.7$ K is also essentially independent from the slow thermal equilibration effects, which are only present in the weakly dilute samples at very low temperatures, see Fig. 7.9. The obtained specific heat data of $Dy_2Ti_2O_7$ agree well with the low-temperature ($T \lesssim 0.6$ K) data of Kolland *et al.* [14] and those of Klemke *et al.* [11, 153] (not shown) which have in common that they were all measured over comparable timescales of about 10^3 s. These data are significantly larger than the data measured with the standard-relaxation method by Morris *et al.* [90, 92] represented by the black crosses. Pomaranski *et al.* report that the timescales to reach thermal equilibrium in $Dy_2Ti_2O_7$ drastically increase below ≈ 0.4 K up to 10^4 s [20]. As a consequence, the specific heat data of Fig. 7.10 (b) (as well as those of Refs. 11, 14, 153) lie below the data of Ref. 20 for $T < 0.6$ K who considered the thermal equilibration over these longer timescales. Above 0.6 K, all the shown datasets merge up to the highest temperature shown. The thermally equilibrated c_{mag}/T data of $Dy_2Ti_2O_7$ from Ref. 20 show a strong increase below 0.4 K and exceeds c_{mag}/T of $x = 0$ and 0.05 of this thesis. However, the data clearly remain below the corresponding data for $x \geq 0.2$. Even the curve of $x = 0.1$ reveals a similar tendency and yields higher values than the data of Ref. 20.

Fig. 7.11 compares the specific heat divided by temperature c/T of the whole dilution series $x = 0$–0.75 in zero magnetic field with the corresponding curves in a magnetic field of 0.5 T and 1 T applied along [001]. This direction was chosen as the ground-state degeneracy can already be lifted by small fields. It is symmetry equivalent to all four local {111} quantization axes and field strengths between 0.5 and 1 T are already sufficient to reach a fully saturated magnetization at $T \simeq 0.5$ K, see Fig. 5.3 on page 58. In addition, such fields enable that around 25 K the full entropy S_∞ of a two-level system should approximately be reached and the thermal population of higher-lying crystal field levels is still negligible. The experimental curves in panels (a)-(g) reveal that the low-temperature maximum in c, which essentially reflects the amount of magnetic Dy^{3+}, systematically shifts to higher temperatures for all x. This is also consistent with the calculations from the single-tetrahdron approximation in magnetic field, see Fig. 4.6 on page 42. In the high-temperature regime for $T \gtrsim 25$ K, the obtained c/T data exhibit no field dependence for all x and, thus, field-independent phonon contributions $c_{\mathrm{ph}}(x, T)/T$ are estimated by the specific heat of non-magnetic $Y_2Ti_2O_7$ after rescaling the temperature axis such that the data sets match around $T \simeq 25$ K, represented by the red dashed line. The insets of Fig. 7.11 (a)-(g) show an expanded view of the low-temperature regime

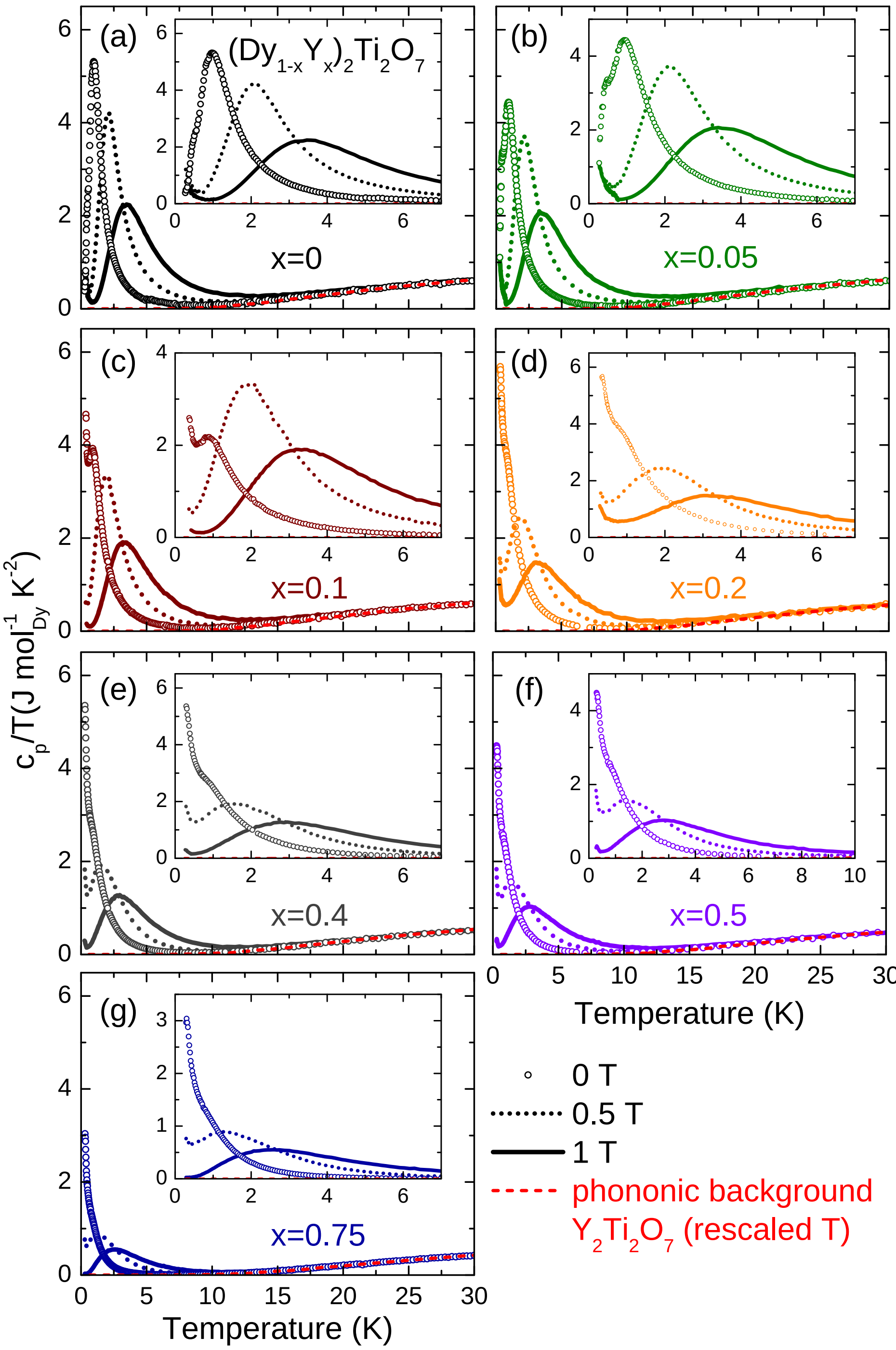

Figure 7.11: Specific heat over temperature $c(T)/T$ in magnetic field along [001] of the dilution series $(\mathrm{Dy}_{1-x}\mathrm{Y}_x)_2\mathrm{Ti}_2\mathrm{O}_7$. The field-independent phonon contributions $c_{\mathrm{ph}}(x,T)/T$ were estimated by the specific heat of non-magnetic $\mathrm{Y}_2\mathrm{Ti}_2\mathrm{O}_7$ after rescaling the temperature axis such that the data sets match around $T \simeq 25$ K, represented by the red dashed line. The insets show an expanded view of the low-temperature regime.

where c is suppressed with increasing magnetic field.

In literature, c_{ph} is often estimated by the Debye model or a simple power-law, e.g. $\beta T^3 + \beta' T^5$, which match the measured total $c(T)$ around 15 K [19, 21, 90, 91]. However, these models systematically overestimate the phononic background. As a consequence, the obtained entropy changes for finite magnetic fields do not reach the full entropy $S_\infty = R\ln(2) \simeq 5.76$ J/mol K of a two-level system [19, 21, 90, 91], even though the fields are large enough to fully lift the ground-state degeneracy. This latter problem can be avoided when c_{ph} is estimated by the measured c of a suitable non-magnetic reference material such as $Y_2Ti_2O_7$ in this thesis and $Eu_2Ti_2O_7$ in literature [118, 154, 155].

Entropy

The magnetic entropy $S(T)$ in zero field is obtained by temperature integration of c_{mag}/T in Fig. 7.10 (b). The zero-field magnetic entropy S_{mag} of the series $(Dy_{1-x}Y_x)_2Ti_2O_7$ with $x = 0$–0.75 together with S_{mag} obtained from the $c(T)/T$ curves in magnetic field from Fig. 7.11 are depicted in Fig. 7.12. The red dashed lines highlight the generalized Pauling approximation $S_{\text{P}}(x)$ [19]. As described above, the temperature-rescaled c_{ph} of the non-magnetic $Y_2Ti_2O_7$ was used to check the reliability of the procedure by measuring the specific heat of all $(Dy_{1-x}Y_x)_2Ti_2O_7$ samples at 0.5 T and 1 T applied along the [001] direction. For all the curves in Fig. 7.12, S_{mag} was shifted to match the full entropy $S(25\text{ K}) = S_\infty = R\ln(2)$ and for each x a magnetic-field independent c_{ph} was used. As shown in Fig. 7.12, the corresponding low-temperature extrapolations $S(T \to 0, H \geq 0.5\text{ T}) \to 0$ confirm the expected vanishing residual entropy in finite magnetic fields for all x.

The main question that should be answered in this section is whether there is experimental evidence for a degenerate zero-field ground state in the dilute spin ice $(Dy_{1-x}Y_x)_2Ti_2O_7$ or not. This means, is it justified to extrapolate the derived low-temperature entropy to a finite zero-temperature residual entropy? As the slow thermal equilibration processes complicate the interpretation of the data in the low-temperature regime, the following discussion is restricted to $T \geq 0.4$ K for the weakly dilute samples with $x \leq 0.1$. As is shown in the inset of Fig. 7.12 (a), the low-temperature entropy of pure $Dy_2Ti_2O_7$ is close to the expected S_{P} and has a weak, but finite temperature dependence. This approximate plateau-like feature of the entropy may be interpreted as one justification for the description of $Dy_2Ti_2O_7$ in terms of a spin ice down to these temperatures. It remains, however, an open issue, whether or not the remaining entropy would finally vanish towards lower temperature in a fully thermally equilibrated $Dy_2Ti_2O_7$. According to Ref. 20, the slope of S_{mag} further increases below 0.4 K, thus indicating that some kind

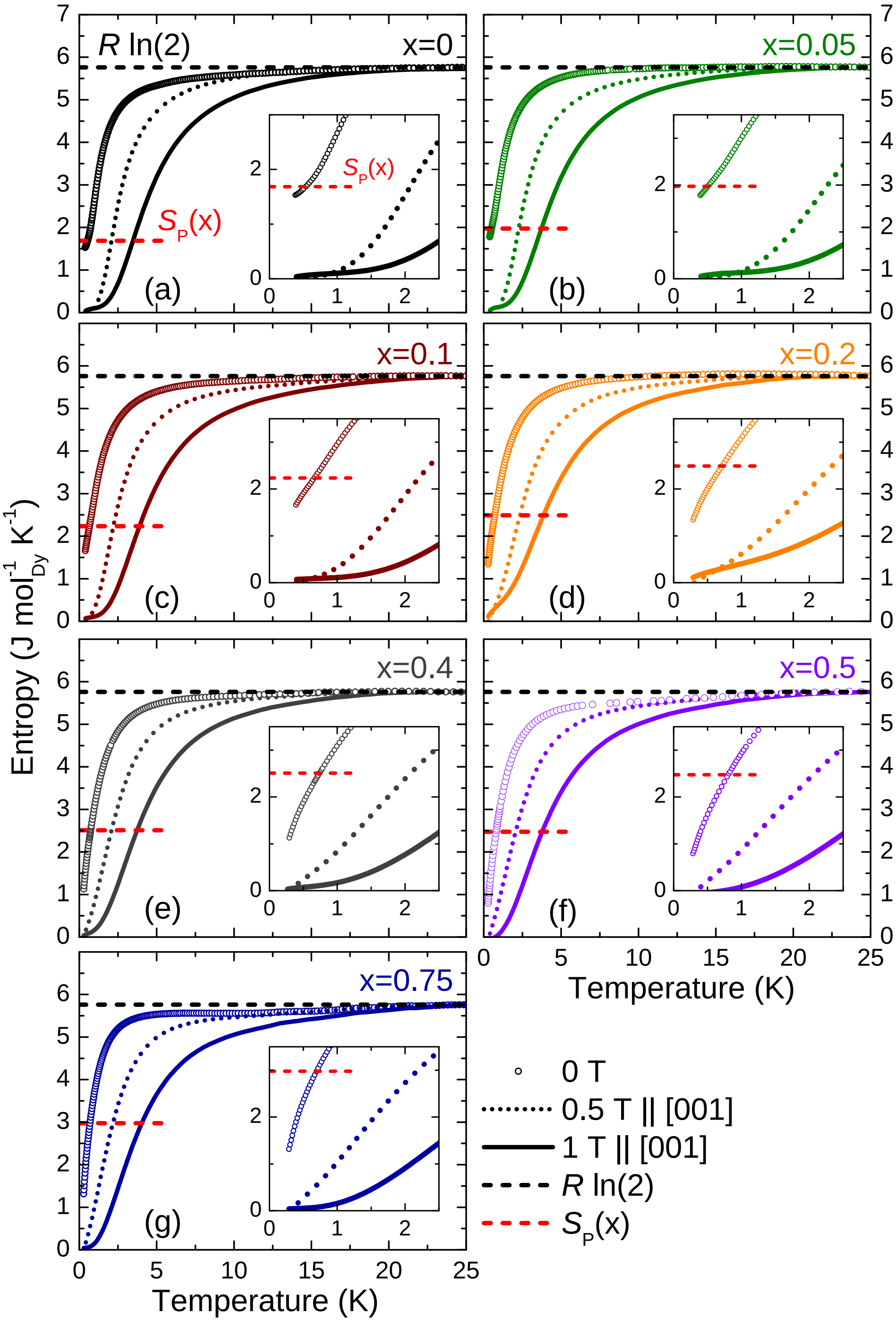

Figure 7.12: Entropy $S_{\mathrm{ex}}(T)$ of $(\mathrm{Dy}_{1-x}\mathrm{Y}_x)_2\mathrm{Ti}_2\mathrm{O}_7$ obtained by integration of c_{mag}/T measured in $H = 0$, 0.5, and 1 T $\parallel$[100]. All curves are shifted to match the full entropy $S_\infty = R\ln(2)$ of a two-level system at $T = 25$ K. The red dashed lines mark the zero-field residual entropy $S_{\mathrm{P}}(x)$ predicted by a generalized Pauling approximation [19].

of ordered ground state ultimately evolves in $Dy_2Ti_2O_7$. It is expected that this low-temperature increase of S_{mag} arises from quantum effects, additional weaker interactions and/or magnetoelastic coupling. The real ground state of $Dy_2Ti_2O_7$ and other (quantum) spin ice materials of the rare-earth pyrochlores are in most cases not known [108, 109, 119, 156, 157]. In Ref. 122, quantum and classical Monte Carlo simulations are applied to establish a phase diagram of the ground state as a function of quantum tunneling. As discussed above, a small amount of non-magnetic dilution may induce a so-called topological spin glass phase [152].

With increasing dilution level x in $(\mathrm{Dy}_{1-x}\mathrm{Y}_x)_2\mathrm{Ti}_2\mathrm{O}_7$, the experimental entropy at lowest temperatures clearly falls below $S_{\mathrm{P}}(x)$ and its temperature dependence systematically increases. For weaker dilution like $x \leq 0.1$, a linear extrapolation $S_{\mathrm{ex}}(x, T \to 0)$ would still lead to a finite zero-temperature residual entropy. This finding may be interpreted as some reminiscence of spin-ice behavior in this temperature regime. But for higher dilutions $x \geq 0.2$, the deviation between $S_{\mathrm{P}}(x)$ and the experimental $S_{\mathrm{ex}}(x, T)$ as well as the slope $\partial S_{\mathrm{ex}}/\partial T = c_{\mathrm{mag}}/T$ become so large that a consideration with a finite residual entropy is absolutely not justified. This conclusion is in strong contrast to the early interpretation of Ke *et al.* [19] introducing the generalized Pauling approximation $S_{\mathrm{P}}(x)$. Within this discussion, it has to be emphasized that $S_{\mathrm{P}}(x)$ is a zero-temperature result and it is significantly larger than $S_{\mathrm{ex}}(x, T)$ especially for $x \geq 0.2$. Furthermore, it has to be noticed that a detailed analysis of the data from Refs. 19, 21 yields similar results. The c_{mag}/T data exhibit a comparable low-temperature increase like the data within this section for $x \geq 0.2$ and, thus, the strong slope of the low-temperature entropy already rules out an interpretation in terms of a finite residual entropy.

Pauling's approximation and Monte Carlo data

In addition, Ref. 21 compares the model of the generalized Pauling residual entropy $S_{\mathrm{P}}(x)$ to the low-temperature entropy $S_{\mathrm{MC}}(x, T)$ obtained by Monte Carlo simulations. In Fig. 7.13, the experimental low-temperature entropy $S_{\mathrm{ex}}(x, T)$ of $(\mathrm{Dy}_{1-x}\mathrm{Y}_x)_2\mathrm{Ti}_2\mathrm{O}_7$ is compared to the corresponding MC simulation [21] and $S_{\mathrm{P}}(x)$ [19]. For $x \geq 0.2$, it is found that the lowest-temperature values of both, $S_{\mathrm{MC}}(x, T)$ and $S_{\mathrm{ex}}(x, T)$ significantly fall below $S_{\mathrm{P}}(x)$. Note again that $S_{\mathrm{P}}(x)$ is a zero-temperature result. The data show a good quantitative agreement between the MC simulation and the experimental results at $T = 0.7$ K. $S_{\mathrm{ex}}(x, T)$ is nicely reproduced by $S_{\mathrm{MC}}(x, T)$ in the entire dilution range $0 \leq x \leq 0.75$ of the $(\mathrm{Dy}_{1-x}\mathrm{Y}_x)_2\mathrm{Ti}_2\mathrm{O}_7$ compounds. This result confirms the quality of the specific heat data and of the crystals, because the values are obtained via subtracting c_{ph} from the raw data c and integrating c_{mag}/T over the whole temperature regime. In the low-temperature range, the Monte Carlo data $S_{\mathrm{MC}}(x, T = 0.4\ \mathrm{K})$ overestimate the

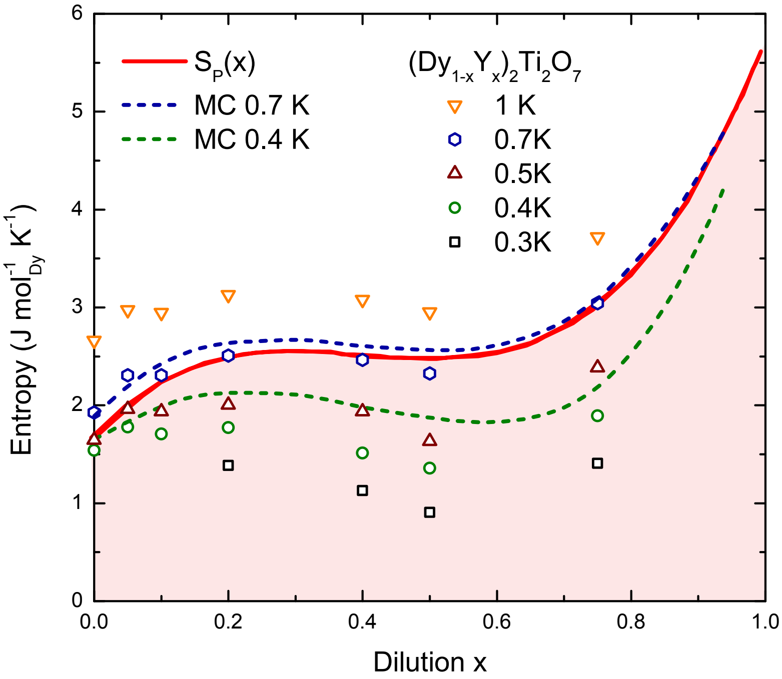

Figure 7.13: Comparison of the low-temperature entropy $S_{\mathrm{ex}}(x, T)$ of $(\mathrm{Dy}_{1-x}\mathrm{Y}_x)_2\mathrm{Ti}_2\mathrm{O}_7$ (symbols) with the corresponding $S_{\mathrm{MC}}(x, T)$ from Monte Carlo simulations (dashed lines,[21]) and the zero-temperature residual entropy $S_{\mathrm{P}}(x)$ (solid line) expected from a generalized Pauling approximation [19].

experimental results and essentially reproduce the experimental $S_{\mathrm{ex}}(x, T = 0.5\text{ K})$. Thus, an extension of the Monte Carlo simulations down to lower temperatures and including quantum effects would be of high interest. Refs. 19, 21 predict the non-monotonic x dependence of $S_{\mathrm{P}}(x)$ and a shallow maximum of the entropy around $x \approx 0.2$. This can be seen in the data shown in Fig. 7.13 for $S_{\mathrm{ex}}(x, T \geq 0.4\text{ K})$, while below that temperature the slow thermal equilibration for $x \leq 0.1$ prevents a definite conclusion. In the high-dilution regime for $x = 0.5$ to 0.75, the entropy increases again and this might reflect that with increasing x the average dipole-dipole interaction decreases. Hence, the temperature-dependent drop of the entropy continuously shifts towards lower temperature and consequently the entropy at constant temperature continuously increases with x.

Magnetocaloric effect

Within the previous section, the temperature-dependent entropy of the dilute spin-ice materials $(\mathrm{Dy}_{1-x}\mathrm{Y}_x)_2\mathrm{Ti}_2\mathrm{O}_7$ was determined via integration of the magnetic contribution to the specific heat data c_{mag}/T. But measurements of the specific heat are comparable time consuming and a reliable estimation of the phononic background is required. Another approach to investigate the change of entropy is a special analysis of the magnetiocaloric effect data according to Ref. 73. This approach is less time consuming as the magnetic field is continuously changed and requires no estimation of a phononic contribution. Hence, the magnetocaloric effect

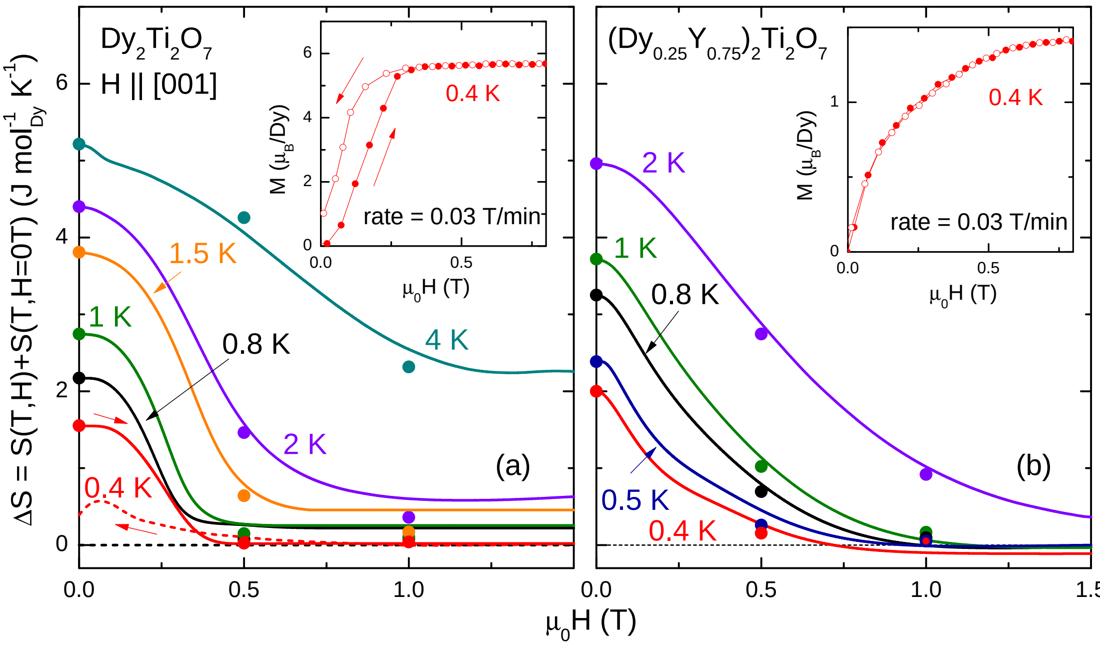

Figure 7.14: Entropy change ΔS of $(\mathrm{Dy}_{1-x}\mathrm{Y}_x)_2\mathrm{Ti}_2\mathrm{O}_7$ with $x = 0$ and 0.75 as a function of the magnetic field applied along [001]. The closed symbols represent results from $\Delta S(T)$, see text. The insets show the magnetization $M(H)$ at 0.4 K.

of the dilute spin ice $(\mathrm{Dy}_{1-x}\mathrm{Y}_x)_2\mathrm{Ti}_2\mathrm{O}_7$ with $x = 0$ and 0.75 for an external magnetic field applied along the [001] and [111] direction was measured by stabilizing the temperature while sweeping the magnetic field. The suitable setup for these measurements is the low-temperature calorimeter which was operated in a custom cryostat with magnetic fields up to 9 T. The experimental details and the analysis of the raw data are introduced in Sec. 3.6. According to Eq. (3.16) and (3.17), the change of entropy $\Delta S(H)$ can be obtained from the change in the heating power P while sweeping the external field whereas the temperature T of the sample is kept constant.

The field-dependent entropy change $\Delta S(H)$ of $\mathrm{Dy}_2\mathrm{Ti}_2\mathrm{O}_7$ with $\vec{H}$ || [001] for 0.4 K $\leq T \leq$ 4 K is shown in Fig. 7.14 (a). The curves are shifted such that they match $\Delta S(T, 0\ \mathrm{T})$ of the temperature-dependent measurements from Sec. 7.2.2. The results of $\Delta S(T, H = \mathrm{const.})$ at fixed magnetic fields (0,0.5 T and 1 T) are represented by the closed symbols. As can be seen, the field-dependent $\Delta S(H)$ curves show a strong low-field decrease for $T \leq 2$ K which correlates with the increase in the magnetization $M(H)$ in this field regime, see inset of panel (a). For finite fields $\vec{H}$ || [001], the system enters a non-degenerate ground state which results in a suppression of the entropy. Above about 0.5 K, the magnetization $M(H)$ of $\mathrm{Dy}_2\mathrm{Ti}_2\mathrm{O}_7$ is non-hysteretic which is also observed in $\Delta S(H)$. At 0.4 K, $M(H)$ exhibits a

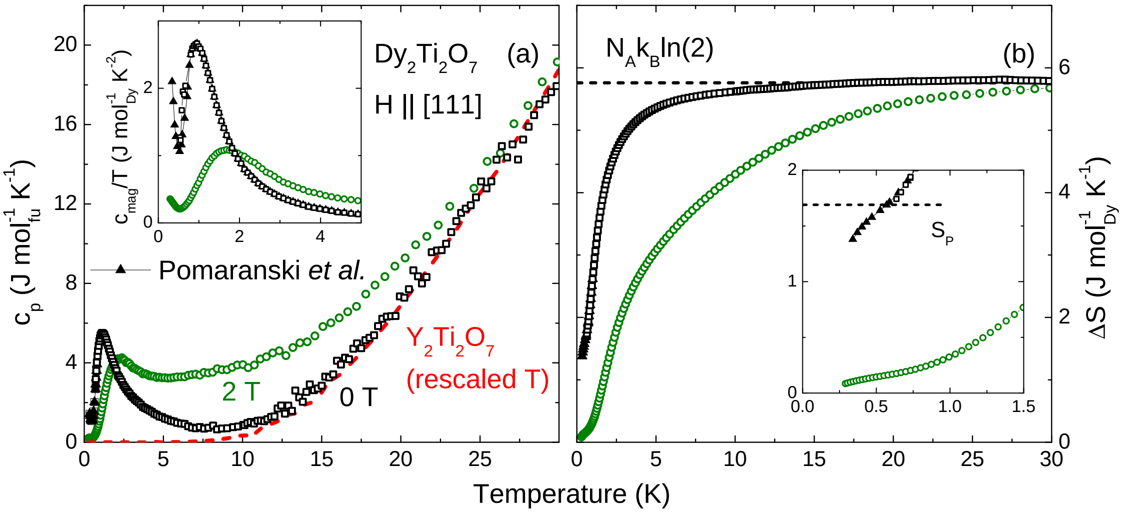

Figure 7.15: Panel (a): specific heat $c(T)$ of $Dy_2Ti_2O_7$ as a function of the temperature with a magnetic field of 2 T applied along [111]. Below about 0.6 K, specific heat data are applied from Pomaranski *et al.* [20] depicted by the black triangles in all panels. The phonon contribution c_{ph} is taken from Sec. 7.2.2 and is represented by the red dashed line. The inset depicts c_{mag}/T where the phononic background is subtracted. Panel (b): entropy $S(T)$ calculated by integration of c_{mag}/T. The data is shifted such that it matches $R\ln(2)$ at 30 K. The inset shows an expanded view of the low-temperature regime.

hysteresis in the low-field regime, see inset of panel (a). The size of the hysteresis is related to the amount of heat U_{diss} which is dissipated from the magnetic system to the phononic system with increasing field and which is not fully released back with decreasing field. Thus, the change of entropy had to be corrected by $S_{\mathrm{diss}} = U_{\mathrm{diss}}/T$ which is discussed in detail in Sec. 3.6. In Fig. 7.14 (a), the hysteresis in $M(H)$ coincides with the hysteresis in $\Delta S(H)$ and reflects that the full entropy of the zero-field ground state is not fully released with decreasing field at 0.4 K. In general, it can be concluded that the field-dependent $\Delta S(H)$ and the temperature-dependent $\Delta S(T, H = \text{const.})$ are in good agreement. The agreement between $\Delta S(H)$ and $\Delta S(T, H = \text{const.})$ is even enhanced for the highly-dilute crystal $(Dy_{1-x}Y_x)_2Ti_2O_7$ with $x = 0.75$ as can be seen in Fig. 7.14 (b). Again, the curves of $\Delta S(H)$ are shifted such that they match the values of specific-heat-based $\Delta S(T, 0\text{ T})$ in zero magnetic field for each temperature. For $0.4\text{ K} \leq T \leq 2\text{ K}$, both data sets nearly perfectly match. For all temperatures, $\Delta S(H)$ decreases with increasing magnetic field and is completely suppressed at 1.5 T for $T \leq 1$ K which reflects the suppression of the ground-state degeneracy. At 0.4 K, $\Delta S(H)$ and $\Delta S(T, H = \text{const.})$ slightly deviate. This deviation originates from the large slope of $\Delta S(T, 0\text{ T})$ for $T \lesssim 1$ K, see Fig. 7.12.

In order to compare the change of entropy $\Delta S(H)$ as a function of the magnetic field along [111] with the temperature-dependent $\Delta S(T)$, the specific heat $c(T)$ in zero field and at 2 T with $\vec{H}\,||\,[111]$ is obtained which is shown in Fig. 7.15 (a). Note that these curves (0 T and 2 T) are measured on a different sample cut out of the same single crystal like the curves shown in Fig. 7.10. Below about 0.6 K, the specific heat data of Pomaranski *et al.* [20] are applied which are depicted by the black triangles and lead to the increase in c and especially c_{mag}/T in the low-temperature regime. The red dashed line is the estimation of the phonon contribution c_{ph} which has already discussed in the previous section. It was distinguished by rescaling the temperature axis of the non-magnetic $\mathrm{Y_2Ti_2O_7}$ such that the data match those of $\mathrm{Dy_2Ti_2O_7}$ in zero magnetic field around $T \simeq 25$ K. It turns out that $c(T)$ at 2 T slightly exceeds c_{ph} in the temperature range of 25 K $\leq T \leq$ 30 K. A comparably large magnetic field of 2 T induces a non-degenerate ground state in $\mathrm{Dy_2Ti_2O_7}$ for $\vec{H}\,||\,[111]$ but it also shifts the magnetic contribution to higher temperatures and, hence, the full entropy $R\ln(2)$ is not reached at 25 K. For $\vec{H}\,||\,[001]$, the magnetic fields of 0.5 T and 1 T are already sufficient to reach a non-degenerate ground state and, thus, the full entropy $S_\infty = R\ln(2)$ of a two-level system is obtained at 25 K. The inset of Fig. 7.15 (a) depicts c_{mag}/T which is determined via $c_{\mathrm{mag}}/T = c(T)/T - c_{\mathrm{ph}}(T)/T$. The temperature integration of c_{mag}/T yields the change of entropy which is shown in Fig. 7.15 (b) whereas the inset shows an expanded view of the low-temperature regime. The data $\Delta S(T, 0\ \mathrm{T})$ is shifted such that it matches $R\ln(2)$ at 30 K. The curve $\Delta S(T, 2\ \mathrm{T})$ does not completely saturate up to 30 K. The shift is estimated such that a linear extrapolation yields $\Delta S(T \to 0, 2\ \mathrm{T}) \to 0$.

The entropy change $\Delta S(H)$ data of $\mathrm{Dy_2Ti_2O_7}$ as a function of the magnetic field with $\vec{H}\,||\,[111]$ are shown in Fig. 7.16 for 0.4 K $\leq T \leq$ 4 K. The curves are again shifted such that they match $\Delta S(T, 0\ \mathrm{T})$. The closed symbols represent the values of $\Delta S(T, H = \mathrm{const.})$ at 0 T and 2 T. It turns out that there are slight differences between the temperature- and field-dependent ΔS above 1 K. Note that both quantities are obtained by integration over the whole temperature- or field-range. Thus, already slight experimental uncertainties lead to comparably large deviations in $\Delta S(T, H)$. The transition into the fully-polarized phase is found as a maximum in $\Delta S(H)$ at about 1 T which is consistent with $M(H)$, see inset. At 0.4 K, $M(H)$ reveals a low-field hysteresis. Here, the magnetocaloric effect data are corrected as discussed above, see also Sec. 3.6 for details about the data analysis. It turns out that $\Delta S_\uparrow(H)$ and $\Delta S_\downarrow(H)$ are hysteretic below about 1.5 T. The origin of this hysteresis, which has no analogue in the magnetization, is unclear. It most probably stems from the fact that the magnetic field is changed too fast (rate of 0.03 T/min) which leads to possible delays in the reaction of the magnetic system in $\mathrm{Dy_2Ti_2O_7}$. The Kagomé-ice phase is seen as a plateau in $\Delta S_\uparrow(H)$ and $\Delta S_\downarrow(H)$ between 0.3 T $< H <$ 0.9 T at 0.4 K. In this plateau

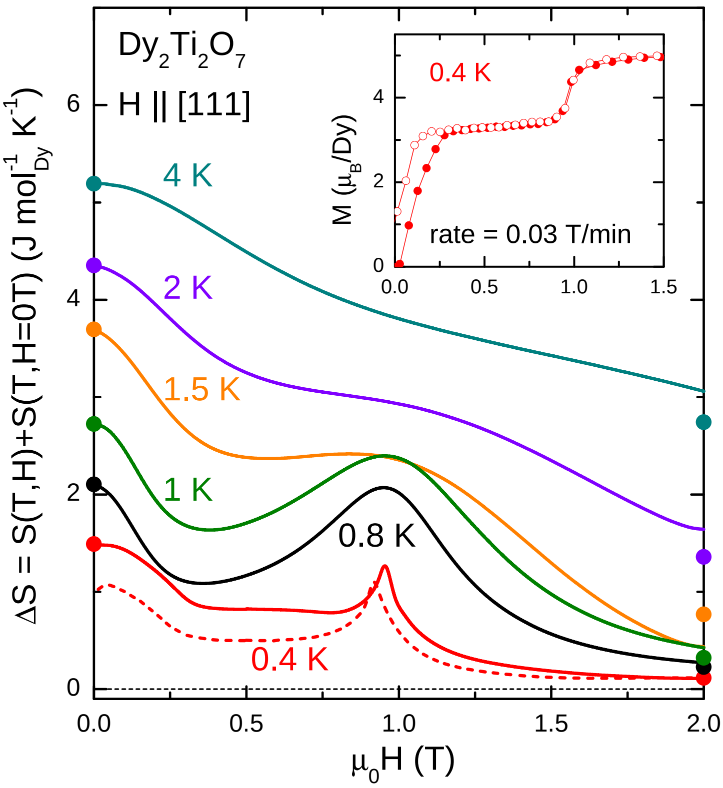

Figure 7.16: Entropy change ΔS of $Dy_2Ti_2O_7$ as a function of the magnetic field applied along [111] at temperatures between 0.4 K and 4 K. The closed symbols represent results from $\Delta S(T)$. The inset shows the magnetization $M(H)$ at 0.4 K.

state, the 3-fold degeneracy arises from the Kagomé planes in which 1 out of the 3 spins of every single tetrahedron has a component opposite to the applied field $\vec{H}\,||\,[111]$. The entropy within this Kagomé-ice phase is experimentally obtained to be 0.4–0.8 J/mol$_{\mathrm{Dy}}$K [91, 117, 118, 155, 158] and calculated for the nearest-neighbor spin-ice model to be 0.672 J/mol$_{\mathrm{Dy}}$K [159]. At 0.4 K, the experimentally obtained curve $\Delta S_{\uparrow}(H)$ yields an entropy of about 0.82 J/mol$_{\mathrm{Dy}}$K and $\Delta S_{\downarrow}(H)$ of about 0.50 J/mol$_{\mathrm{Dy}}$K. Both values are found to be in the right order of magnitude but uncertainties remain because of the present hysteresis. In general, it is found that $\Delta S(H)$ essentially reproduces $\Delta S(T, H = \text{const.})$ in the whole temperature range. The curves for $x = 0.75$ exhibit the best agreement. This is related to the fact that the corresponding $M(H)$ curves are non-hysteretic and additionally the slow relaxation has vanished. The suppression of the entropy with increasing magnetic field was observed for both systems $(Dy_{1-x}Y_x)_2Ti_2O_7$ with $x = 0$ and 0.75 as well as the Kagomé-ice plateau and the first-oder transition for $\vec{H}\,||\,[111]$. Thus, it can be concluded that this approach is a reliable and fast tool to determine the change of entropy as a function of the magnetic field. The accuracy is clearly enhanced if the field-dependent process is reversible and, thus, the magnetization is non-hysteretic. Moreover, the absence of slow relaxation processes improve the data quality.

7.2.3 Conclusion

In conclusion, it is found that the ultra-slow thermal equilibration in pure spin ice $Dy_2Ti_2O_7$ is rapidly suppressed upon dilution with non-magnetic yttrium and vanishes completely for $x \geq 0.2$ down to lowest accessible temperatures (≈ 0.3 K). In general, the low-temperature entropy of $(Dy_{1-x}Y_x)_2Ti_2O_7$, considerably decreases with increasing x, whereas its temperature dependence drastically increases. Thus, there is no experimental evidence for a finite zero-temperature entropy in $(Dy_{1-x}Y_x)_2Ti_2O_7$ above $x \simeq 0.2$, in clear contrast to the finite residual entropy $S_P(x)$ expected from a generalized Pauling approximation [19]. A similar discrepancy is also present between $S_P(x)$ and the low-temperature entropy obtained by Monte Carlo simulations [21], which reproduce the experimental data down to 0.7 K. The specific heat data suggest a rapid crossover from spin-ice physics in $Dy_2Ti_2O_7$ towards weakly interacting single-ion physics in $(Dy_{1-x}Y_x)_2Ti_2O_7$ at intermediate dilution. The change of entropy as a function of the magnetic field $\Delta S(H)$ obtained by magnetocaloric effect data agrees with the temperature-dependent $\Delta S(T, H = \text{const.})$ with a high degree of accuracy whereas small deviations occur in the low-temperature regime of $Dy_2Ti_2O_7$ where the change of entropy is irreversible (hysteresis in $M(H)$) and slow relaxation processes arise. The field-dependence of $\Delta S(H)$ coincides with the magnetization $M(H)$ and the suppression of the ground state degeneracy of $(Dy_{1-x}Y_x)_2Ti_2O_7$ is observed as well as the transition into the fully-polarized phase for $\vec{H} \,||\, [111]$. The hysteresis in $M(H)$ roughly agrees with an irreversible entropy $\Delta S(H)$. Thus, it can be concluded that measurements of the magnetocaloric effect are a reliable and rapid method to obtain $\Delta S(H)$ with a high point density but without great experimental effort. The accuracy is strongly enhanced for crystals whose magnetic system exhibits reversible properties in the measured temperature and field range.

7.3 Heat transport

7.3.1 Literature results

As already briefly introduced in Sec. 4.8, recently Sun *et al.* published heat transport data of $Dy_2Ti_2O_7$ [13] for a magnetic field applied along [001], [110] and [111]. It is found that the temperature dependence $\kappa(T)$ of $Dy_2Ti_2O_7$ in zero field follows a power-law behavior $\propto T^{2.5}$, see Fig. 7.17 (a). This value is smaller than the standard T^3 behavior of phonon thermal conductivity at the boundary scattering limit. Note that even the non-magnetic iso-structural reference compound $Y_2Ti_2O_7$, in which the thermal conductivity is purely phononic, exhibits a power-law behavior

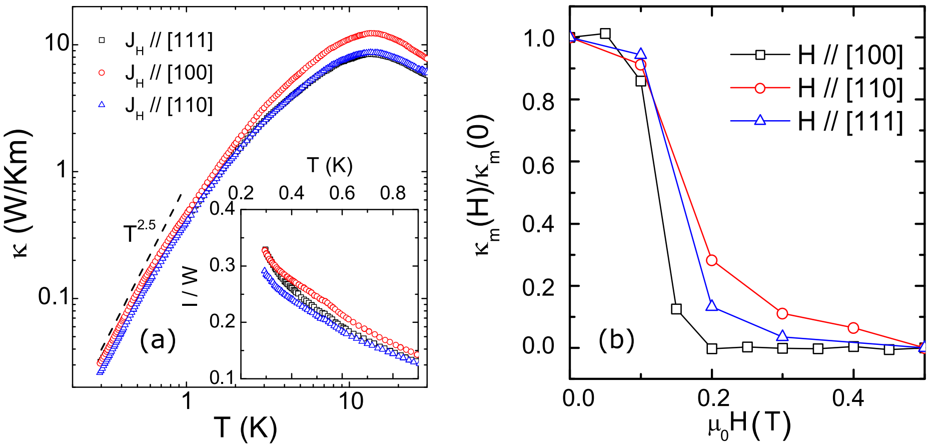

Figure 7.17: Literature result of the termal conductivity of $Dy_2Ti_2O_7$. Panel (a): $\kappa(T)$ in zero field for heat current along [100], [110] and [111]. The inset shows phonon mean free path divided by sample width. Panel (b): κ_{mag} at 0.36 K for $\vec{H}$ || [001], [110] and [111] assuming that the low-field decrease of $\kappa(H)$ from 0 to 0.5 T is just a decrease of κ_{mag}. Taken from Ref. 13.

with $T^{2.4}$ below about 4 K [14]. Via the kinetic formula, a ratio of the sample width and the phonon mean free path l/W is determined, see inset. It is claimed that a large magnetic monopole contribution to κ would lead to a smaller mean free path. This result is in contrast to the $\kappa(T, 0\text{ T})$ of $Dy_2Ti_2O_7$ shown below which reveal no power-law behavior in the low-temperature regime but a distinct shoulder compared to $\kappa(T, 0.5\text{ T})$. Furthermore, Sun *et al.* make the assumption that the low-field decrease of $\kappa(H)$ from 0 T up to 0.5 T for magnetic field along [100], [110] and [111] is purely a suppression of κ_{mag} at 0.36 K. The corresponding data are shown in Fig. 7.17 (b). By applying the Debye-Hückel theory to the extracted κ_{mag}, the monopole velocity v_{m} is determined to be of the order 10^4 m/s. It is concluded that v_{m} is unreasonably too large since monopoles are known to be dispersionless. Firstly, it is absolutely not reasonable to consider the low-field decrease of $\kappa(H)$ up to 0.5 T for $\vec{H}$ || [111] as the full suppression of κ_{mag}. Because for this particular field direction, $Dy_2Ti_2O_7$ enters the Kagomé-ice phase between 0 T and 1 T where the monopole density is increased in total and additionally the magnetization $M(H)$ only saturates for fields larger than 1 T, see Fig. 7.6 on page 91. Secondly, the Debye-Hückel theory is applied to calculate the monopole velocity v_{m} at 0.36 K which clearly fails to describe the enhanced specific heat of $Dy_2Ti_2O_7$ below about 0.6 K obtained by Pomaranski *et al.* [20]. Thus, the applicability of the theory is unreasonable. As will be discussed below, the interpretation is not supported by the study presented within this thesis.

Tokiwa *et al.* introduce a simple model for the monopole density in spin ice [123]

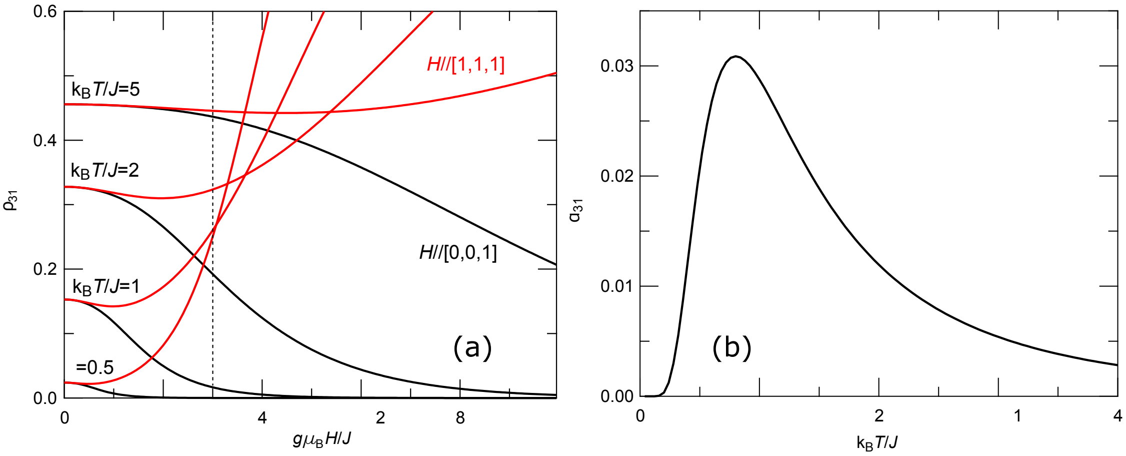

Figure 7.18: Panel (a): literature model of the monopole density $\rho_{31}(h)$ as a function of magnetic field $h = g\mu_\text{B}H$ calculated from the nearest-neighbor spin-ice model. Panel (b): h^2 coefficient α_{31} plotted against the normalized temperature $k_\text{B}T/J$; see text. Taken from Ref. 123

with a magnetic field along [001] and [111]. Within this model, the field dependence of the monopole density $\rho_{31}(h)$ with $h = g\mu_\text{B}H$ is obtained from considerations of the energy of all spin configurations in the effective nearest-neighbor spin-ice model, see Eq. (4.7) on page 38. The resulting field dependencies at different temperatures $k_\text{B}T/J$ are shown in Fig. 7.18 (a). Here, J denotes the nearest-neighbor exchange coupling. For $\vec{H} \,||\, [001]$, the energy of one 2in-2out configuration decreases most which simply originates from the Zeeman effect. This leads to the non-degenerate 2in-2out ground state and the monotonic decrease of the monopole density $\rho_{31}(h)$ for this field direction. For $\vec{H} \,||\, [111]$, the energy for one of the 3in-1out configurations decreases the most and crosses the lowest energy of a 2in-2out configuration at $g\mu_\text{B}H/J = 3$ indicated by the black vertical dashed line. Because of this crossing, $\rho_{31}(h)$ strongly increases with the magnetic field for this particular direction. But in the low-field region, $\rho_{31}(h)$ reveals a slight decrease as a function of h. In the model ρ_{31} is expanded around $h = 0$. For both field directions, h-linear term vanishes and the h^2 is identical. Then, the isotropic field dependence of $\rho_{31}(h)$ at zero-field limit is given by

$$\rho_{31}(h) = \rho_{31}(0) - \alpha_{31}h^2. \tag{7.3}$$

The coefficient α_{31} is plotted against $k_\text{B}T/J$ in Fig. 7.18 (b). It exhibits a maximum at $k_\text{B}T_{\text{max},\alpha_{31}}/J = 0.8$. For the relation between $T_{\text{max},\alpha_{31}}$ and the energy to create a monopole-antimonopole pair $\Delta_{31} = 2J$ follows $\Delta_{31} = 2J = 2.5k_\text{B}T_{\text{max},\alpha_{31}}$. This model will be applied to the low-field $\kappa(H)$ data of the pure spin ice $Dy_2Ti_2O_7$ and the dilute systems.

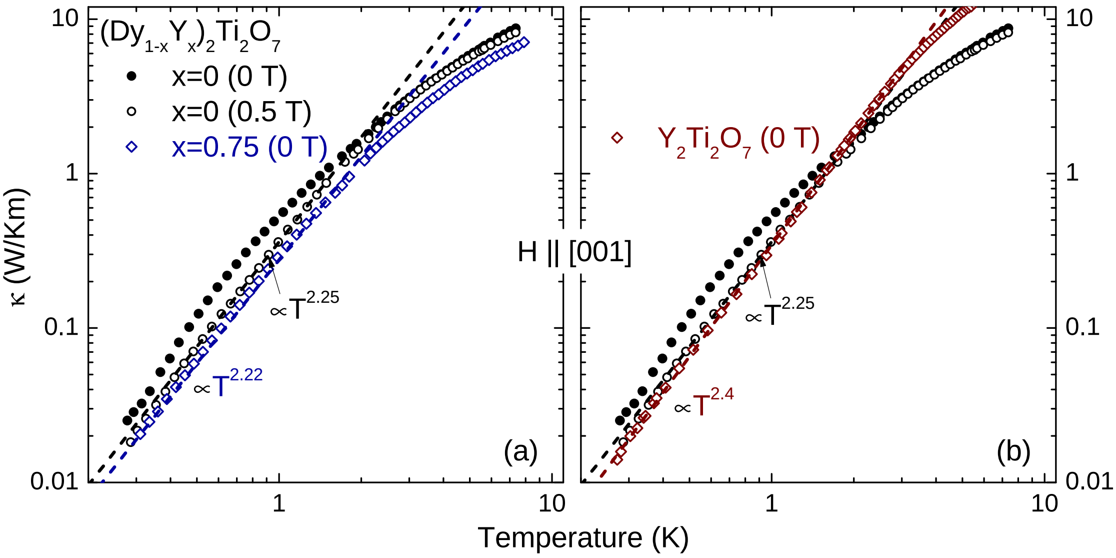

Figure 7.19: Panel (a): temperature-dependent $\kappa(T)$ of $(\mathrm{Dy}_{1-x}\mathrm{Y}_x)_2\mathrm{Ti}_2\mathrm{O}_7$ ($\vec{H} \,||\, [001]$) with $x = 0$ in zero field and 0.5 T (closed and open black circles) and with $x = 0.75$ in zero field (blue circles). Panel (b): $\kappa(T)$ of $\mathrm{Y}_2\mathrm{Ti}_2\mathrm{O}_7$ at 0 T in comparison with $\mathrm{Dy}_2\mathrm{Ti}_2\mathrm{O}_7$ in zero field and at 0.5 T.

7.3.2 Experimental results

Magnetic field || [001]

In order to get an insight into the magnetic contribution κ_{mag} to the heat transport of $\mathrm{Dy}_2\mathrm{Ti}_2\mathrm{O}_7$, the system is doped with non-magnetic yttrium. An increasing Y content leads to a successive dilution of the magnetic system. As a consequence, these materials were named dilute spin ice.

Fig. 7.19 (a) shows the temperature dependence of the thermal conductivity of $(\mathrm{Dy}_{1-x}\mathrm{Y}_x)_2\mathrm{Ti}_2\mathrm{O}_7$ with $x = 0$ in zero field and at 0.5 T in comparison with the highly dilute system with $x = 0.75$ in zero field. The magnetic field and the heat current are applied along [001]. It turns out that the $\kappa(T)$ for $x = 0$ reveals a distinct field dependence below about 4 K. Here, $\kappa(T)$ at 0.5 T is clearly reduced compared to the zero-field curve. Furthermore, the curve for $x = 0.75$ in zero field resembles the $x = 0$ curve at 0.5 T. Both curves exhibit a power-law behavior in a large temperature range below about 2 K with very similar exponents whereas the zero field curve for $x = 0$ reveals an additional shoulder within this temperature range and does not follow a power law. These data reveal a further signature of a magnetic contribution κ_{mag} to the heat transport of $\mathrm{Dy}_2\mathrm{Ti}_2\mathrm{O}_7$ in zero field on top of a phononic contribution κ_{ph}. Fig. 7.19 (b) shows a similar comparison between $\kappa(T)$ of $\mathrm{Dy}_2\mathrm{Ti}_2\mathrm{O}_7$ (0 T,0.5 T) and $\mathrm{Y}_2\mathrm{Ti}_2\mathrm{O}_7$ (0 T). The non-magnetic

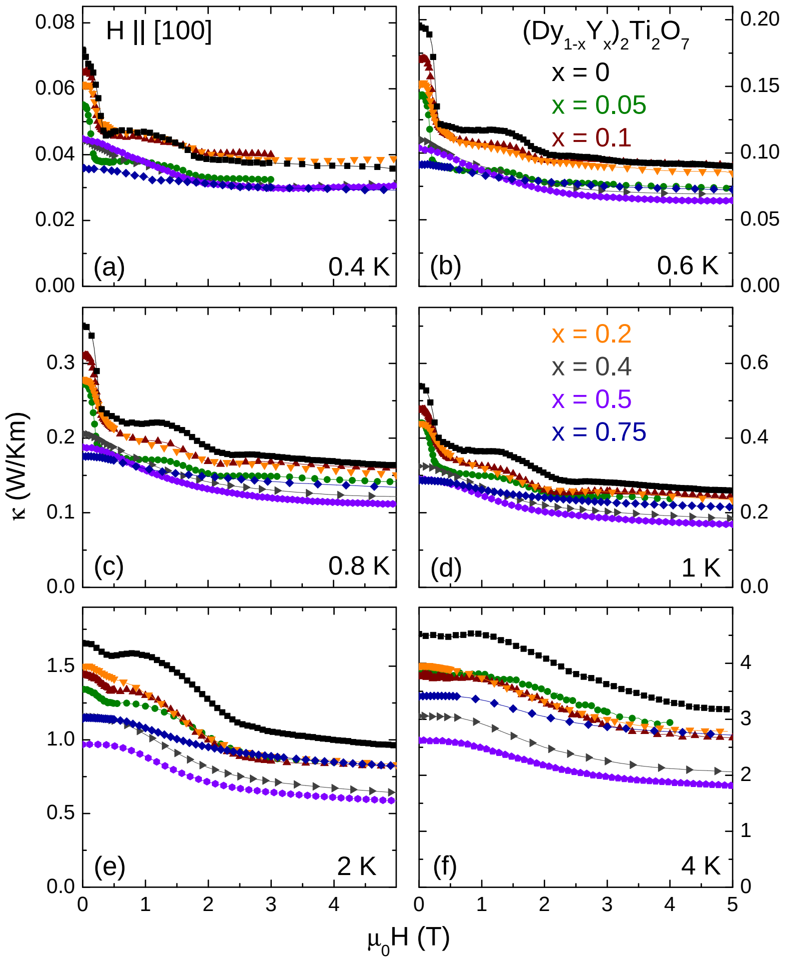

Figure 7.20: Thermal conductivity $\kappa(H)$ in absolute values of the dilution series $(Dy_{1-x}Y_x)_2Ti_2O_7$ for $\vec{H}\,||\,\vec{j}\,||\,[001]$ in a temperature range from 0.4 K to 4 K.

system $Y_2Ti_2O_7$ also reveals a power-law behavior in the low-temperature regime but the corresponding exponent is slightly enhanced compared to those of $x = 0$ at 0.5 T and $x = 0.75$ which suggests a phononic background with a finite x $\kappa_{\mathrm{ph}}(x > 0)$. At about 2 K, $\kappa(T)$ of $Y_2Ti_2O_7$ exceeds $\kappa(T)$ of $Dy_2Ti_2O_7$. This behavior is observed for $2\text{ K} < T < 110\text{ K}$ [14, 16] and it is related to the fact that κ_{ph} in $Dy_2Ti_2O_7$ is reduced due to phonon scattering via crystal-field excitations of the partly filled $4f$ shell of Dy^{3+}.

These above findings are supported by the field-dependent thermal conductivity $\kappa(H)$ of $(Dy_{1-x}Y_x)_2Ti_2O_7$ with $x = 0$–0.75 which is depicted in Fig. 7.20. The magnetic field $\vec{H}$ and the heat current $\vec{j}$ are again applied along [001] which is the longest dimension of all crystals. The data for $x = 0$ has already been discussed in Chap. 6. In summary, $\kappa(H, x = 0)$ reveals a strong low-field decrease by raising the external field from 0 T up to 0.5 T followed by a plateau-like feature in the intermediate field range. Around 1.5 T, an additional step-like decrease occurs. In the high-field range above 2 T, $\kappa(H)$ weakly decreases with increasing field. At

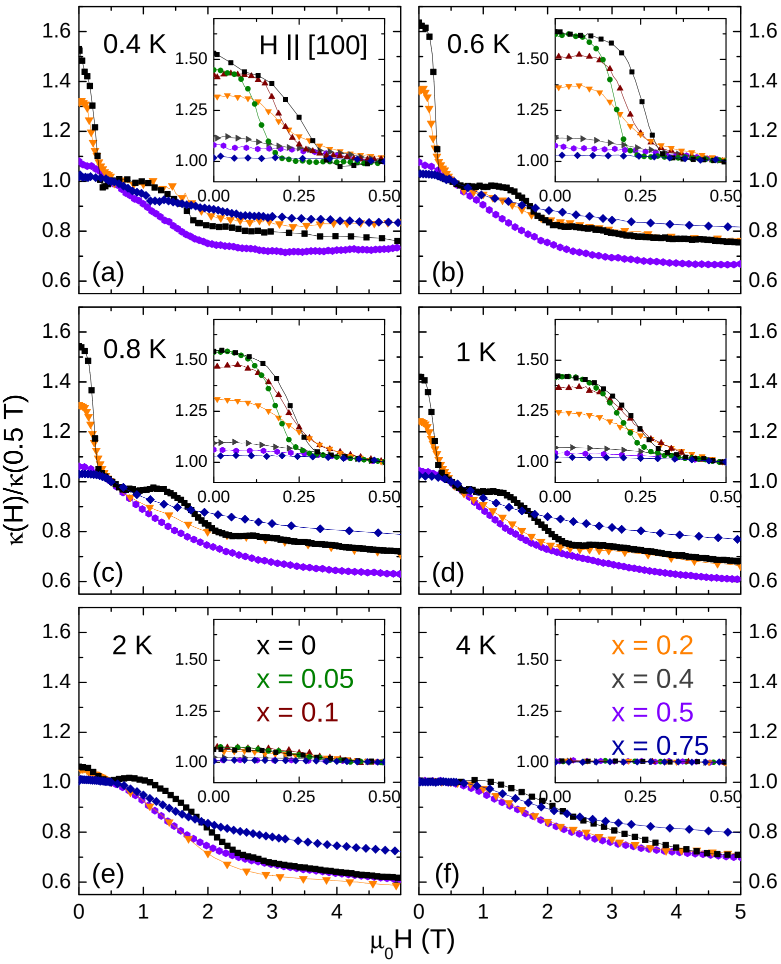

Figure 7.21: Normalized $\kappa(H)/\kappa(0.5\ \mathrm{T})$ of the dilution series $(\mathrm{Dy}_{1-x}\mathrm{Y}_x)_2\mathrm{Ti}_2\mathrm{O}_7$ with $\vec{H}\,||\,\vec{j}\,||\,[001]$. The insets show the low-field range up to 0.5 T.

4 K, the low-field decrease has vanished in contrast to the step-like decrease which is predominantly temperature-independent. For the weakly dilute systems with $x \leq 0.2$, similar field dependencies are observed whereas both the low-field drop and especially the step-like decrease around 1.5 T decrease with x. The higher dilutions $x \geq 0.4$ exhibit no distinct field-dependence. Here, a weak decrease of $\kappa(H)$ is observed with increasing field.

As can be seen in Fig. 7.20, the absolute values of $\kappa(H)$ vary for the different dilutions. This originates from experimental uncertainties and varying sample qualities. The experimental uncertainties originate from difficulties in determining the geometric factors of a sample and the field-dependent calibration of the RuO_2 thermometers. These uncertainties should not exceed 20%. Furthermore, the thermal conductivity is highly sensitive to the sample quality. Possible impurities strongly affect the absolute values of κ. As a consequence, the magnetic contributions of the dilution series $(\mathrm{Dy}_{1-x}\mathrm{Y}_x)_2\mathrm{Ti}_2\mathrm{O}_7$ can not calculated by simply subtracting a phononic background, *e.g.* the curves of $(\mathrm{Dy}_{0.5}\mathrm{Y}_{0.5})_2\mathrm{Ti}_2\mathrm{O}_7$, $(\mathrm{Dy}_{0.25}\mathrm{Y}_{0.75})_2\mathrm{Ti}_2\mathrm{O}_7$ or

$Y_2Ti_2O_7$. As already discussed in Chap. 6, the low-field decrease of $Dy_2Ti_2O_7$ is attributed to a suppression of κ_{mag} for $\vec{H}\,||\,[001]$ due to the anticorrelation with $M(H)$ resulting in a suppressed monopole mobility and density for this particular field direction. In order to compare this decrease for the different x, the $\kappa(H)$ curves of $(Dy_{1-x}Y_x)_2Ti_2O_7$ are depicted in the representation $\kappa(H)/\kappa(0.5\ \mathrm{T})$ in Fig. 7.21 (a)-(f). It is found that the low-field decrease correlates with the degree of dilution in the whole temperature range up to 4 K which is visualized in the insets of panels (a)-(f). Here, an expanded view of the low-field range below 0.5 T is depicted. In other words, the magnetic contribution to κ of $(Dy_{1-x}Y_x)_2Ti_2O_7$ reveals a systematic correlation with the dilution x. At 2 K, the magnetic contribution has almost vanished which also agrees with an increasing suppression of the spin-ice physics there and it is completely absent at 4 K. As already discussed, spin-ice physics is essentially suppressed within the highly dilute system with $x = 0.5$ and 0.75. But, both systems still exhibit a weak decrease of $\kappa(H)$ in the low-field regime, see insets panels (a)-(f). This suggests a phonon background which slightly depends on the dilution. An x-dependent κ_{ph} can be determined via

$$\kappa_{\mathrm{ph},[001]} = [\kappa(0\ \mathrm{T}, x = 0.75) - \kappa(0.5\ \mathrm{T}, x = 0.75)] \cdot 4(1-x). \tag{7.4}$$

The factor $4(1-x)$ accounts for the fact that $Dy_2Ti_2O_7$ contains four times more Dy^{3+} ions than $(Dy_{0.25}Y_{0.75})_2Ti_2O_7$. Then, $\kappa_{\mathrm{ph},[001]}$ is applied to obtain the magnetic contribution κ_{mag} for $\vec{H}\,||\,[001]$ via

$$\kappa_{\mathrm{mag},[001]} = [\kappa(0\ \mathrm{T}) - \kappa(0.5\ \mathrm{T})] - \kappa_{\mathrm{ph},[001]}(x) \tag{7.5}$$

in units of W/Km. The results for $\kappa_{\mathrm{mag},[001]}$ will be discussed in Sec. 7.3.2.

Furthermore, it is found that the low-field $\kappa(H)$ decreases as $\kappa(H) = \kappa(H = 0) - \alpha_{\mathrm{ex},001}H^2$ which is shown in Fig. 7.22 (a)-(e) for $(Dy_{1-x}Y_x)_2Ti_2O_7$ with $x = 0$–0.4. The insets show the data and the linear fits at 2 K and 4 K. Note that the data are presented in κ/T in order to enhance the visibility of the field dependence. As can be seen, the low-field decrease is well described the linear fit (solid lines) in this representation at almost all temperatures and for all dilutions x. At 4 K, the slope $\alpha_{\mathrm{ex},001}$ has almost vanished. It is reasonable that the thermal conductivity of monopoles is systematically determined by its number. Thus, $\alpha_{\mathrm{ex},001}$ is a measure of the suppression rate of the monopole thermal conductivity in the low-field regime according to the model of Tokiwa *et al.* [123], which was introduced in Sec. 7.3.1.

The temperature dependence of the obtained $\alpha_{\mathrm{ex},001}$ of $(Dy_{1-x}Y_x)_2Ti_2O_7$ with $x = 0$–0.4 is shown in Fig. 7.23. It turns out that $\alpha_{\mathrm{ex},001}$ decreases in the low- and high-temperature regime, but reveals a distinct maximum between approximately 1 K and 2 K. This temperature dependence of $\alpha_{\mathrm{ex},001}$ agrees well with the theoretically determined α_{31} in Fig. 7.18 on a qualitative level. In general, it is found that $\alpha_{\mathrm{ex},001}$ correlates with the degree of dilution and it has almost vanished for $x = 0.4$. For

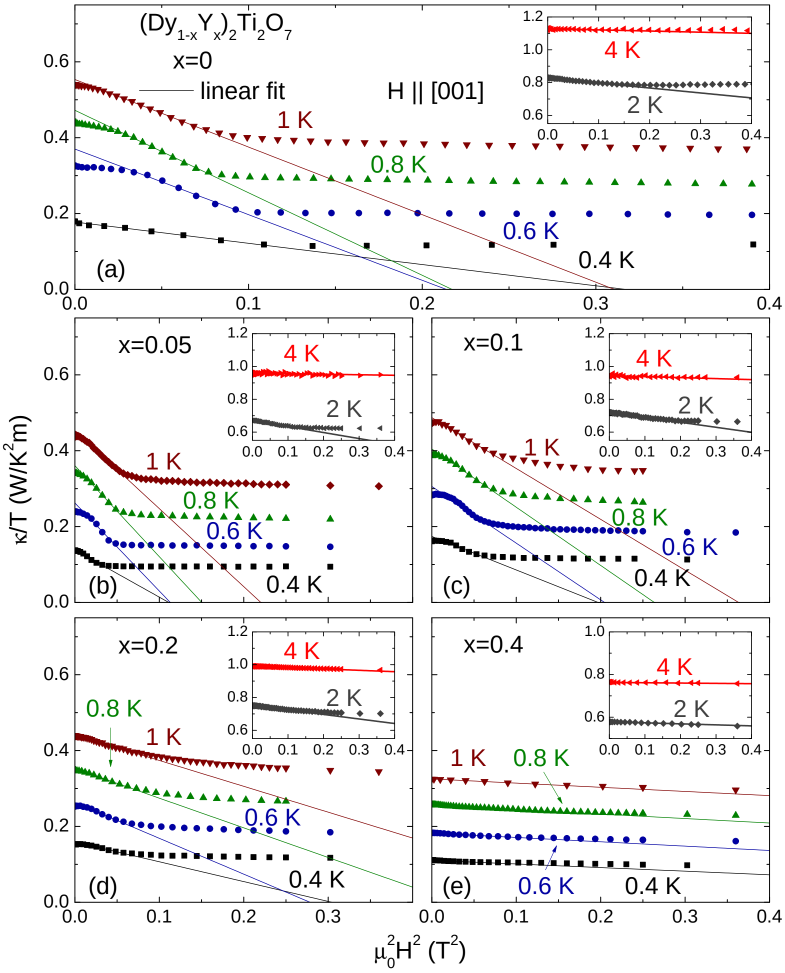

Figure 7.22: Linear fit of the low-field decrease of $\kappa(H)/T$ as a function of H^2 for $(\mathrm{Dy}_{1-x}\mathrm{Y}_x)_2\mathrm{Ti}_2\mathrm{O}_7$ with $x = 0$–0.4 at different temperatures. The insets show the corresponding curves at 2 K and 4 K.

$x = 0.05$ however, the experimentally obtained $\alpha_{\mathrm{ex},001}$ exceeds the corresponding results for $x = 0$. The origin of this deviation is unclear and might originate from experimental uncertainties. Note that the absolute value for $\alpha_{\mathrm{ex},001}$ is of minor importance. Because according to the model, the maximum in α_{31} is related to the cost for the creation of a monopole via $\Delta_{31} = 2J = 2.5k_\mathrm{B}T_{\mathrm{max},\alpha_{31}}$ [123]. In the case of $Dy_2Ti_2O_7$, the monopole cost is indicated to be $\Delta_{31} = 4.35$ K [10] which leads to a theoretical $T_{\mathrm{max},\alpha_{31}} \simeq 1.7$ K. The exact value of the experimentally obtained $T_{\mathrm{max},\alpha_{\mathrm{ex},001}}$ is difficult to determine because of the low density of points. But, a systematic agreement between the experiment and the model is found on a qualitative level. This finding further emphasizes the indication of a monopole heat transport in spin ice $Dy_2Ti_2O_7$ which is suppressed by an external magnetic field along [001].

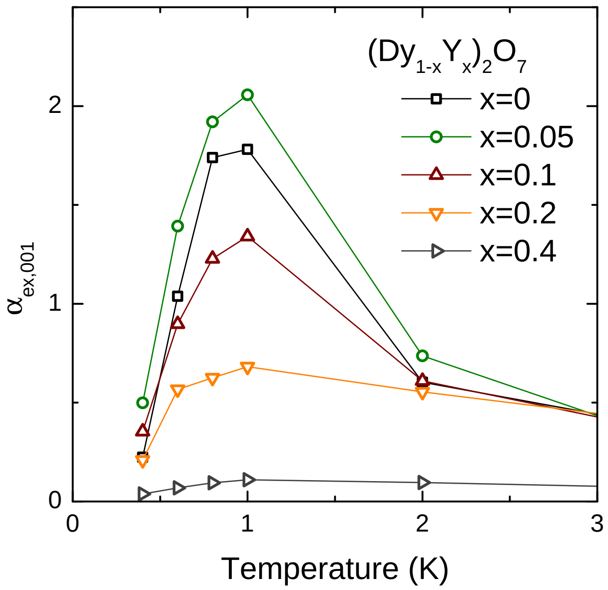

Figure 7.23: Temperature dependence of the initial slope of $\kappa(H)$ determined by fitting $\kappa(H) = \kappa(0) - \alpha_{ex,001}H^2$ of $(Dy_{1-x}Y_x)_2Ti_2O_7$ with $x = 0$–0.4 for $\vec{H} \,||\, [001]$.

Magnetic field || [111]

The field-dependent thermal conductivity of $(Dy_{1-x}Y_x)_2Ti_2O_7$ for $\vec{H} \,||\, \vec{j} \,||\, [111]$ at different temperatures has already been discussed concerning the influence of non-magnetic dilution on the hysteresis of $\kappa(H)$ within the Kagomé-ice phase, see Fig. 7.6 on page 91. Although the determination of κ_{mag} is more instructive for $\vec{H} \,||\, [001]$, these data can also be investigated to obtain an estimate of κ_{mag} to the heat transport in zero field which is, however, more difficult due to the complex field characteristics which do not correlate with $M(H)$ below 1 T. But, it is observed that the high-field dependence of $\kappa(H)$ is similar for all x, see Fig. 7.6 on page 91. Furthermore, $M(H)$ is essentially saturated above about 1.5 T (except van-Vleck susceptibility). In general, the phononic background contribution in zero magnetic field should be isotropic and, thus, the same κ_{ph} should be applied like for the data from the previous section with $\vec{H} \,||\, \vec{j} \,||\, [001]$. But as discussed before, the absolute values of κ and consequently also of κ_{ph} slightly vary because of the different crystal qualities and experimental uncertainties. Hence in order to get only a rough estimate of κ_{mag}, Fig. 7.24 shows $\kappa(H) - \kappa(1.5\text{ T})$ for $\vec{H} \,||\, [111]$ at different temperatures. For clarity only the curves with decreasing field are depicted which are closer to equilibrium than the data obtained with increasing field, see discussion in Sec. 7.1. It turns out that the low-field decrease (up to 1.5 T) again correlates with the degree of dilution x and the high-field regime reveals similar dependencies for all x. For $x = 0.05$, the high-field $\kappa(H) - \kappa(1.5\text{ T})$ is slightly enhanced for $T > 0.4$ K. This most likely originates from the field-dependent calibration of the thermometers. An x-dependent κ_{ph} is determined for this field direction analogue

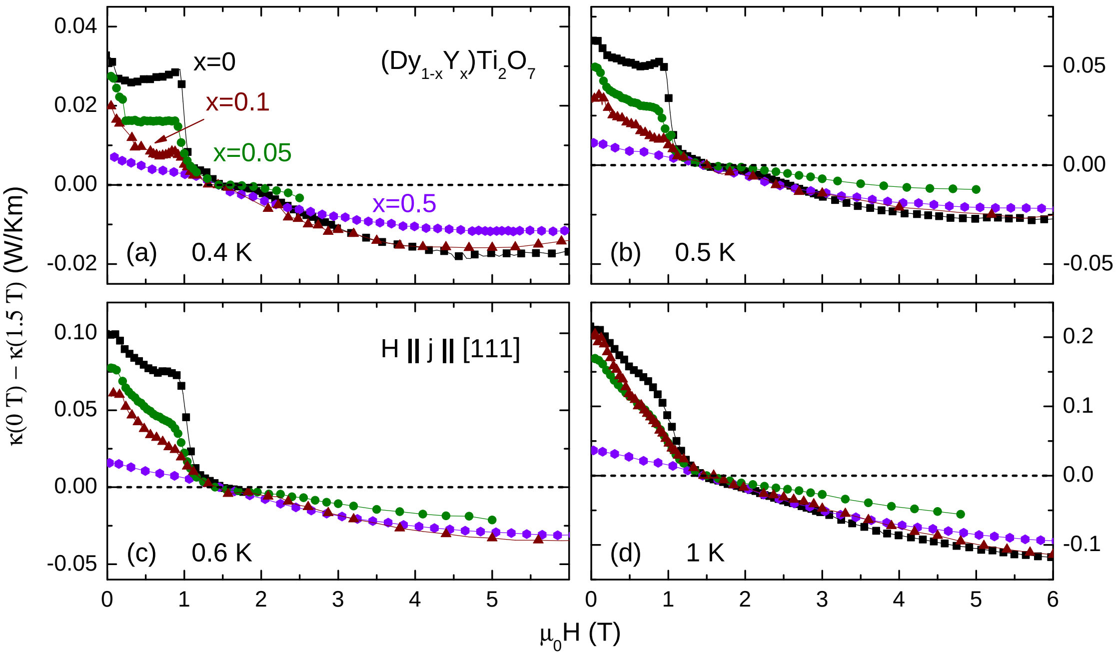

Figure 7.24: Thermal conductivity $\kappa(H) - \kappa(1.5\ \mathrm{T})$ of the dilution series $(\mathrm{Dy}_{1-x}\mathrm{Y}_x)_2\mathrm{Ti}_2\mathrm{O}_7$ with $\vec{H}\,||\,\vec{j}\,||\,[111]$ at different temperatures.

to $\vec{H}\,||\,[001]$ via

$$\kappa_{\mathrm{ph},[111]} = [\kappa(0\ \mathrm{T}, x = 0.5) - \kappa(1.5\ \mathrm{T}, x = 0.5)] \cdot 2(1-x). \tag{7.6}$$

Because $\kappa_{\mathrm{ph},[001]}(x = 0.5) = 2 \cdot \kappa_{\mathrm{ph},[001]}(x = 0.75)$ for $\vec{H}\,||\,[001]$, $\kappa(H)$ for $x = 0.75$ is not required to determine the x-dependent phonon background for $\vec{H}\,||\,[111]$ via Eq. (7.6). Then, $\kappa_{\mathrm{ph},[111]}$ is applied to calculate κ_{mag} in zero magnetic field from the $\kappa(H)$ data via

$$\kappa_{\mathrm{mag},[111]} = [\kappa(0\ \mathrm{T}) - \kappa(1.5\ \mathrm{T})] - \kappa_{\mathrm{ph},[111]}(x) \tag{7.7}$$

in units of W/Km. The results for $\kappa_{\mathrm{mag},[001]}$ from the previous section and for $\kappa_{\mathrm{mag},[111]}$ will be discussed in the following Sec. 7.3.2.

As studied in the previous section for $\vec{H}\,||\,[001]$, it is observed that $\kappa(H)$ for $\vec{H}\,||\,[111]$ also decreases with $\kappa(H) = \kappa(H = 0) - \alpha_{\mathrm{ex},111}H^2$ in the low-field regime. The corresponding data are shown in Fig. 7.25 (a)-(c) for $(\mathrm{Dy}_{1-x}\mathrm{Y}_x)_2\mathrm{Ti}_2\mathrm{O}_7$ with $x = 0$–0.2. Note that the data are presented in κ/T in order to enhance the visibility for different temperatures. The low-field decrease is well described by the linear fits (solid lines) in the representation $\kappa(H^2)/T$ at all temperatures and for all x. Panel (d) depicts the experimentally obtained $\alpha_{ex,111}$ as a function of temperature. The results for $\alpha_{ex,111}$ are represented by the closed symbol and $\alpha_{ex,001}$ is additionally shown by

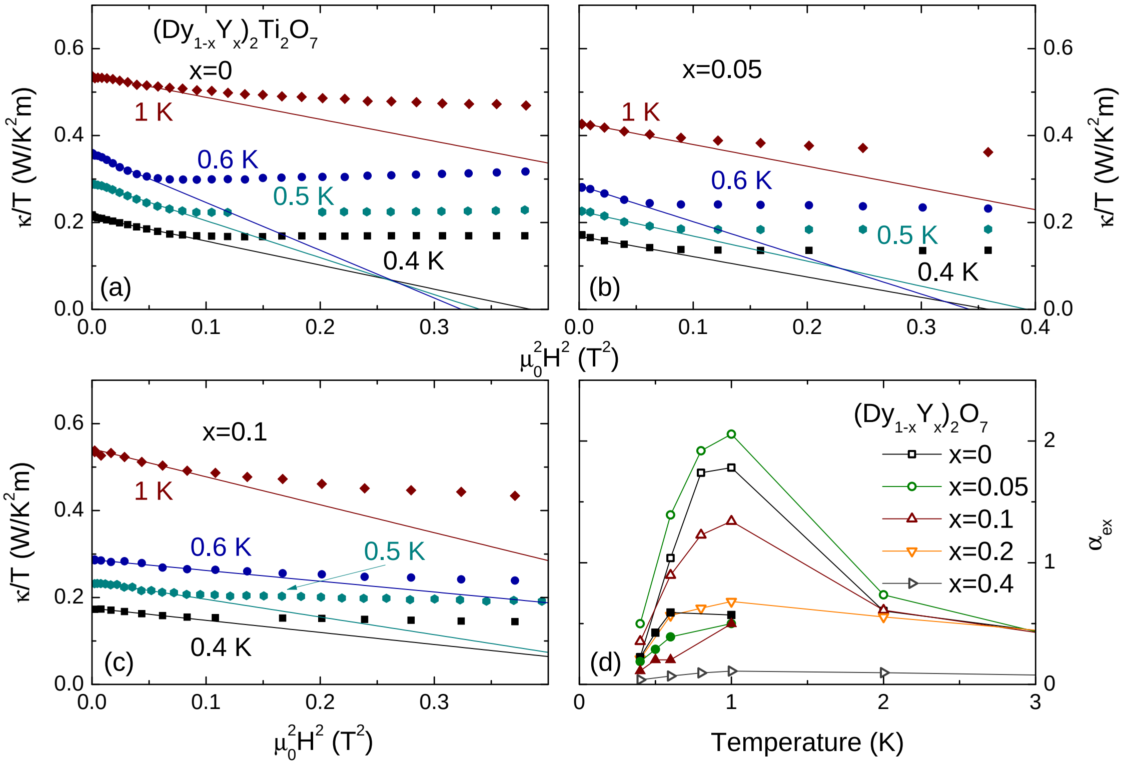

Figure 7.25: Panels (a)-(c): linear fit of the low-field decrease of $\kappa(H)/T$ as a function of H^2 for $(\mathrm{Dy}_{1-x}\mathrm{Y}_x)_2\mathrm{Ti}_2\mathrm{O}_7$ with $x = 0$–0.2 at different temperatures for $\vec{H} \,||\, [111]$. Panel (d): temperature dependence of the initial slope of $\kappa(H)$ determined by fitting $\kappa(H) = \kappa(0) - \alpha_{ex,111}H^2$ of $(\mathrm{Dy}_{1-x}\mathrm{Y}_x)_2\mathrm{Ti}_2\mathrm{O}_7$ with $x = 0$–0.4. The closed symbols are results for $\alpha_{ex,111}$ and the open symbols represent $\alpha_{ex,001}$.

the open symbols. It can be seen that $\alpha_{ex,111}$ is clearly reduced compared to $\alpha_{ex,001}$ which is consistent with the qualitative model of Tokiwa *et al.* [123]. According to the model, α_{ex} is a measure for the monopole heat transport due to the correlation to the monopole density ρ_{31} whose decrease is much more pronounced for $\vec{H} \,||\, [001]$ than for $\vec{H} \,||\, [111]$, see Fig. 7.18 (a). The maximum of $\alpha_{ex,111}$ cannot be determined from the $\kappa(H)$ data due to the restriction of the data to $T \leq 1$ K.

Magnetic contribution

As discussed above, a zero-field magnetic contribution of the dilute spin-ice systems $(\mathrm{Dy}_{1-x}\mathrm{Y}_x)_2\mathrm{Ti}_2\mathrm{O}_7$ are extracted from the heat transport data for a magnetic field parallel [001] and [111]. Under additional considerations of κ_{ph}, this is accomplished

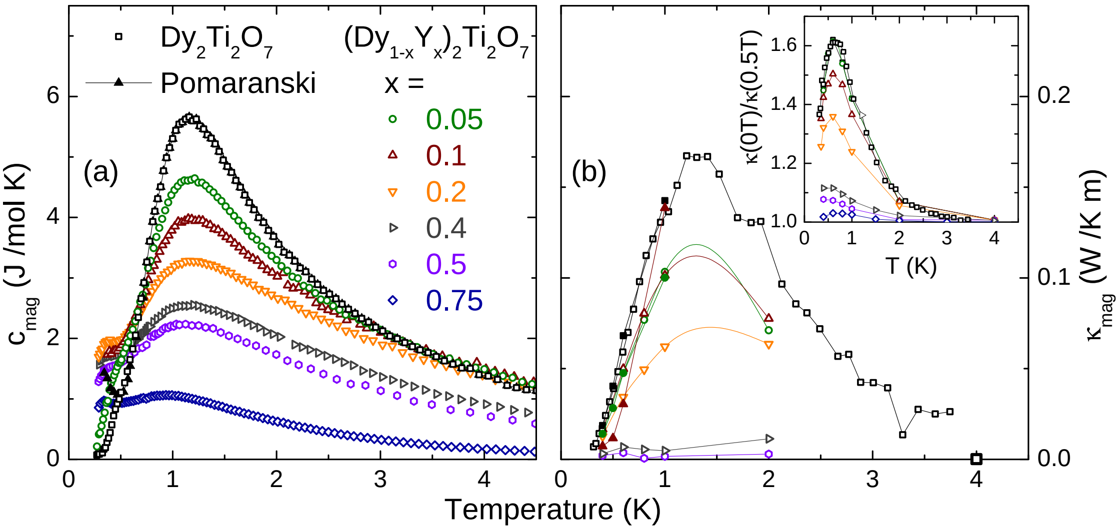

Figure 7.26: Panel (a): c_{mag} of the dilution series $(\text{Dy}_{1-x}\text{Y}_x)_2\text{Ti}_2\text{O}_7$ with $x = 0$–0.75. The low-temperature data from Ref. 20 are included. Panel (b): absolute values of κ_{mag} as a function of temperature. The open symbols represent results for κ_{mag} from $\vec{H} \,||\, [001]$ and the closed symbols from $\vec{H} \,||\, [111]$. The inset depicts the $\kappa(0\text{ T})/\kappa(0.5\text{ T})$ for $\vec{H} \,||\, [001]$. The lines connecting the data points are guides to the eye.

for both field directions via Eq. (7.5) and (7.7). The corresponding data of κ_{mag} are shown in Fig. 7.26 (b). The relative decrease $\kappa(0\text{ T})/\kappa(0.5\text{ T})$ for $\vec{H} \,||\, [001]$ is depicted in the inset. The open symbols represent $\kappa_{\text{mag},[001]}$ and the closed symbols $\kappa_{\text{mag},[111]}$ for the different dilutions x, respectively. For $x = 0$, $\kappa_{\text{mag},[001]}$ was determined from the temperature-dependent data shown in Fig. 7.19 which leads to the enhanced density of points. For $x > 0$, the corresponding data are extracted from the field-dependent curves depicted in Fig. 7.20 for which an interpolation from 2 K up to 4 K bares too large uncertainties. As can be seen from Fig. 7.26 (b), a vanishing κ_{mag} is found for $x = 0.5$ and a small contribution is conserved for $x = 0.4$. For $x \geq 0.2$, there is a finite monopole contribution in zero magnetic field which is maximum at about 1.3 K. A correlation is found between the degree of dilution x and the corresponding magnetic contribution whereas $\kappa_{\text{mag},001}(x = 0.05)$ and $\kappa_{\text{mag},001}(x = 0.1)$ almost coincide. At 4 K, κ_{mag} has vanished. Furthermore, it is found that $\kappa_{\text{mag},[001]}$ with $\vec{j} \,||\, [001]$ and the rough estimate of $\kappa_{\text{mag},[111]}$ with $\vec{j} \,||\, [111]$ nearly agree for $x = 0$ and 0.05 which signals an almost isotropic monopole mobility in zero field whereas the determination of $\kappa_{\text{mag},[111]}$ bares uncertainties which prevents a definite conclusion. The deviation for $x = 0.1$ is up to now unclear.

In Refs. 11, 12, the zero field $\kappa(T)$ of $\text{Dy}_2\text{Ti}_2\text{O}_7$ was interpreted to be purely phononic and its field dependence has been attributed to phonon scattering by magnetic excitations. The data shown in this thesis do not yield the same interpretation. There are several reasons why the heat transport cannot be purely phononic but also has a finite magnetic contribution below about 4 K. The phonon heat conductivity $\kappa(T)$ of the highly dilute system with $x = 0.75$ shows a very similar power-law behavior like the thermal conductivity of $Dy_2Ti_2O_7$ in a field of 0.5 T for $\vec{H} \,||\, [001]$, see Fig. 7.19. In contrast, the zero-field $\kappa(T)$ of $Dy_2Ti_2O_7$ exhibits a distinct shoulder below about 4 K. Because of this qualitative difference, it can be concluded that $\kappa(T, 0.5\text{ T})$ of $Dy_2Ti_2O_7$ essentially yields the phononic background to the thermal conductivity whereas in zero field an additional magnetic contribution is present on top of κ_{ph}. This interpretation is supported by the field-dependent $\kappa(H)$ data in Fig. 7.21 at constant temperatures where $\kappa(H)$ is strongly suppressed in the low-field range up to 0.5 T. This low-field drop systematically correlates with the degree of dilution and anticorrelates with the magnetization for $\vec{H} \,||\, [001]$. In addition, a hysteresis is found in both quantities below 0.6 K for $x \gtrsim 0.2$ and the anticorrelation of $\kappa(H)$ and $M(H)$ is explained straightforwardly by the monopole confinement due to an external magnetic field along [001] introduced in Sec. 4.8. Furthermore, the low-field decrease is compared to the theoretical predictions of the field dependence of the monopole density which is a measure for the monopoles contributing to κ. The experimentally obtained temperature dependence of α_{ex} agrees well with the theoretically calculated α_{31} for $Dy_2Ti_2O_7$ [123]. The maxima in κ_{mag} and c_{mag} are both located around 1.3 K, see Fig. 7.26 (a) and (b). Furthermore as discussed in Chap. 6, the field dependent $\kappa(H)$ data of the isostructural spin ice $Ho_2Ti_2O_7$ reveal an obvious low-field decrease which is similar to that of $Dy_2Ti_2O_7$. The phononic contributions of $Dy_2Ti_2O_7$ and $Ho_2Ti_2O_7$ are found to be of opposite sign by a comparative study with the highly dilute systems $(Dy_{0.5}Y_{0.5})_2Ti_2O_7$ and $(Ho_{0.5}Y_{0.5})_2Ti_2O_7$ which, however, do not exhibit a distinct low-field $\kappa(H)$ dependence. In summary, all the data give evidence for a finite magnetic contribution κ_{mag} in zero magnetic field in $Dy_2Ti_2O_7$ and in $Ho_2Ti_2O_7$ originating from the magnetic excitations (monopoles).

Diffusion coefficient

The magnetic contributions to the specific heat c_{mag} and to the heat transport κ_{mag} of $(Dy_{1-x}Y_x)_2Ti_2O_7$ have been extracted, see Fig. 7.26 (a) and (b). The diffusion coefficient of these systems is calculated via

$$D_{\text{mag}} = \frac{\kappa_{\text{mag}}}{c_{\text{mag}}} \cdot V_{\text{mol}}. \tag{7.8}$$

The corresponding data are shown in Fig. 7.27 together with D_{mag} determined by applying c_{mag} from Pomaranski *et al.* [20] below about 0.5 K (closed black triangles)

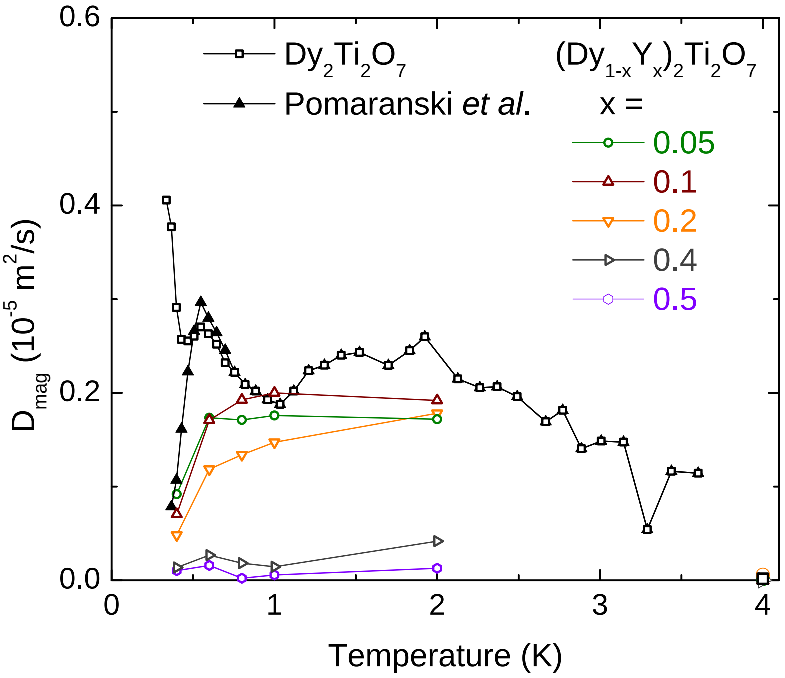

Figure 7.27: Diffusion coefficient $D_{\mathrm{mag}} = \kappa_{\mathrm{mag}}/c_{\mathrm{mag}} \cdot V_{\mathrm{mol}}$ of $(\mathrm{Dy}_{1-x}\mathrm{Y}_x)_2\mathrm{Ti}_2\mathrm{O}_7$ together with D_{mag} calculated with c_{mag} from Ref. 20. The lines are guides to the eye.

and κ_{mag} from this thesis. In general, it is observed that D_{mag} basically decreases with increasing yttrium dilution. Slight deviations are found for $x = 0.05$ and 0.1 above $T \geq 0.8$ K. For $x = 0.5$, D_{mag} is essentially suppressed which is correlated to the absence of spin-ice physics. For $x = 0.4$, the mobility is clearly suppressed which might originate from an enhanced defect scattering on non-magnetic yttrium ions as the monopoles can only propagate via spin flips of the magnetic ions. For $0.05 \leq x \leq 0.2$, an interpretation of D_{mag} is difficult for $T > 1$ K due to the weak point density. But in the low-temperature regime below about 0.8 K, D_{mag} systematically vanishes for all three systems. For $x = 0$, a weakly-pronounced maximum is found at about 1.6 K. Here, the monopoles are highly mobile and propagate via single spin flips. In this regime, the temperature seems to be high enough to create a sufficient number of monopole excitations but their mean-free path is still large enough resulting in a large D_{mag}. In the low-temperature regime for $x = 0$, D_{mag} reveals a distinct maximum at about 0.7 K which is observed in both data sets. By further lowering the temperature, D_{mag} is suppressed if the data from Pomaranski *et al.* [20] are applied. The origin of this additional maximum is unclear but it signals an evident increase of the monopole density and/or the mean-free path there. It has vanished for $x \geq 0.05$. Thus, D_{mag} seems to be highly sensitive to dilution there. The suppression of D_{mag} at lowest temperatures originates from the increase of c_{mag} and, hence, from the non-degenerate ground state which is established in the long-time limit [20]. At 4 K, D_{mag} has essentially vanished for all x because $\kappa_{\mathrm{mag}} \simeq 0$ which correlates with the suppression of spin-ice physics.

Due to the Ising-like magnetic moments in classical spin ice, the dynamics of the monopoles are predicted to be diffusive [10, 92] and described by an effective theory of quasiparticles, in this case a Coulomb gas of magnetic charges [4, 103, 160]. The dynamics can be considered as purely stochastic and the properties are almost identical to those of its electronic equivalent. Thus, the kinetic gas theory can be applied in which the diffusion coefficient D_{mag} is related via

$$D_{\mathrm{mag}} = v_{\mathrm{mag}} \ell / 3 \tag{7.9}$$

with the mean velocity v_{mag} and the mean-free path ℓ of the monopole particles. However, this relation has to be treated with caution due to the following reasons. The number of monopoles is not conserved and their interaction with each other or with phonon excitations is not well understood. However, a rough estimate of the monopole velocity and the mean-free path can be given. Assuming the monopole velocity to be $v_{\mathrm{mag}} = t_{\mathrm{eff}}/(\hbar\pi/a_d) \approx 20$ m/s [14] with $a_d = 4.34$ Å as the distance between neighboring tetrahedra and the effective bandwidth for monopole hopping t_{eff} which is of the order of 1 K. Then, the mean-free path is determined via $\ell = 3D_{\mathrm{mag}}/v_{\mathrm{mag}}$. According to the results in Fig. 7.27, a mean-free path of $\ell \approx 0.3$ μm is obtained for $\mathrm{Dy_2Ti_2O_7}$ at about 1 K. It turns out that D_{mag} only slightly decreases for $0 \leq x \leq 0.2$. This finding might be explained by an insensitive mean-free path to weak dilutions whereas the scattering in the highly dilute system $x = 0.4$ is strongly enhanced and D_{mag} has almost vanished.

7.3.3 Conclusion

An experimental evidence for a magnetic contribution κ_{mag} to the heat transport of $\mathrm{Dy_2Ti_2O_7}$ was found which reveals a maximum around 1.3 K and also scales with the degree of dilution with non-magnetic yttrium. It is observed that spin-ice physics has completely vanished for $x \geq 0.5$. The maximum of the relative decrease $\kappa(0\ \mathrm{T})/\kappa(0.5\ \mathrm{T})$ is located at about 0.8 K for $\vec{H}\,||\,[001]$. Furthermore, the $\kappa(H)$ data qualitatively agree with a microscopic model developed by Kolland *et al.* [14, 16], see also Sec. 4.8, which supports the interpretation in terms of a magnetic monopole contribution on top of κ_{ph} below about 4 K. A model from Tokiwa *et al.* [123] is found to be applicable in the low field range for $\vec{H}\,||\,[001]$ and [111]. From the experimental data, it was calculated that the energy of a monopole excitation is related to the decrease of $\kappa(H)$ as predicted in the model and the density of monopoles is suppressed by an external field in the low-field regime.

By means of c_{mag} and κ_{mag}, the diffusion coefficient D_{mag} of the monopole excitations is obtained whose dynamics are predicted to be diffusive [10]. D_{mag} reaches a maximum at about 1.5 K originating from an increased κ_{mag} in this intermediate temperature regime. A suppression of D_{mag} at low temperatures signals a non-degenerate ground state for the whole dilution series and even for the pure spin ice $Dy_2Ti_2O_7$ which has already been predicted experimentally and theoretically [20, 122]. However, the data for $x = 0$ reveal an additional distinct shoulder in D_{mag} at about 0.7 K which is not observed for $x \geq 0.05$. The origin of this additional contribution is up to now unclear but it is highly sensitive to the dilution x. At 4 K, spin-ice physics has vanished. Applying the kinetic gas theory to describe D_{mag} and with the assumption of the monopole velocity $v_{\mathrm{mag}} \approx 20$ m/s, a mean-free path is estimated to be in the order of about 100 unit cells which equals $\ell \approx 0.3$ µm for $Dy_2Ti_2O_7$ at about 1 K. Above 0.7 K, D_{mag} is insensitive to weak dilutions x, but for $x = 0.4$ it has almost vanished.

8 Summary

In this thesis the low-temperature magnetism of the spin-ice systems $Dy_2Ti_2O_7$ and $Ho_2Ti_2O_7$ was investigated. A detailed comparative study of the heat transport of both compounds and of the dilute reference systems was performed to distinguish the magnetic and the phononic contributions. Due to the more instructive characteristics in $Dy_2Ti_2O_7$, a special focus was put on the dilution series $(Dy_{1-x}Y_x)_2Ti_2O_7$ whose thermodynamic properties are studied in detail with respect to spin-ice physics.

$Dy_2Ti_2O_7$ and $Ho_2Ti_2O_7$ are prototype spin-ice materials where the geometric constraints prevent long-range magnetic order down to lowest temperatures. The low-temperature magnetism is described by non-collinear $S = 1/2$ Ising spins that form a network of corner-sharing tetrahedra. Due to the remarkable Ising character, which originates from a strong crystal electric field, an easy-axis anisotropy arises that leads to quantization axis along the local $\{111\}$ directions. An effective nearest-neighbor ferromagnetic coupling favors a six-fold degenerate ground state with 2in-2out arrangement. Pauling's ice rule describing the hydrogen displacement in water ice is equivalent to this 2in-2out configuration and predicts a residual zero-temperature entropy of $S_\mathrm{P} = (N_\mathrm{A} k_\mathrm{B}/2)\ln(3/2)$ for $T \to 0$. This model was even expanded to a generalized Pauling approximation $S_\mathrm{P}(x)$ for dilute spin ice [19]. Anomalous excitations are realized via single spin-flips which can fractionalize into pairs of monopoles and antimonopoles. In literature, the presence of Pauling's residual entropy was reported for $Dy_2Ti_2O_7$ [19, 90] whereas a recent long-time study of the thermal equilibration (10^4 s) confirmed an absence of S_P. Additionally, it is argued whether these monopole excitations contribute to the heat transport in spin ice or not [11–15, 18]. In this thesis, the prediction of the generalized Pauling approximation and a monopole contribution to the heat transport are studied by different thermodynamic properties. The measurements were performed applying custom home-built setups in a temperature range from 0.3 to 30 K and in magnetic fields up to 7 T.

A study of the two most prominent spin-ice materials $Ho_2Ti_2O_7$ and $Dy_2Ti_2O_7$ revealed that both systems exhibit equal characteristics, but also offer remarkable differences in the thermodynamic properties. In general, a clear experimental evidence for a sizable magnetic contribution κ_mag to the zero-field heat transport of both spin-ice materials $Ho_2Ti_2O_7$ and $Dy_2Ti_2O_7$ is determined below 4 K. This κ_{mag} of both system is of comparable magnitude whereas it is more pronounced for $Dy_2Ti_2O_7$. It can be attributed to the magnetic monopole excitations, which are highly mobile in zero field. Their mobility is effectively suppressed in external magnetic fields causing a drop of κ_{mag} in the low-field range according to a qualitative microscopic model [14, 16] which supports the interpretation in terms of a magnetic monopole contribution on top of κ_{ph} for $\vec{H} \,||\, [001]$. Towards high magnetic fields (> 4 T), significant field dependencies of the phononic heat conductivities $\kappa_{\mathrm{ph}}(H)$ of $Ho_2Ti_2O_7$ and $Dy_2Ti_2O_7$ are found, which are, however, of opposite signs. This was confirmed by studies of the highly dilute reference materials $(Ho_{0.5}Y_{0.5})_2Ti_2O_7$ and $(Dy_{0.5}Y_{0.5})_2Ti_2O_7$ in which spin-ice physics is essentially suppressed. The decreasing $\kappa_{\mathrm{ph}}(H)$ in the Dy-based materials most likely arises from field-induced lattice distortions, which can be clearly seen in magnetostriction data. It turned out that this effect is less important in the Ho-based materials, which show a significantly smaller magnetostriction. Here, the scattering of phonons by spin flips appears to be more dominant than in the Dy-based materials. Consequently, both κ_{mag} and κ_{ph} in zero field are smaller in $Ho_2Ti_2O_7$ than they are in $Dy_2Ti_2O_7$, and the field dependent κ_{ph} increases with field while the magnetization is identical. In addition, a comparative study of the thermal conductivity of the pure spin-ice systems with the zirconium-doped compounds $R_2(Ti_{1-x}Zr_x)_2O_7$, where the non-magnetic Ti^{4+} ions are partly replaced by Zr^{4+}, was performed. The dominant magnetic energy scale J_{eff} of spin ice systematically increases with the Zr content which can be explained straightforwardly by the Grüneisen ratio [53]. The magnitude and field dependence of κ_{mag} and κ_{ph} are clearly reduced compared to the pure systems which most likely originates from the enhanced defect scattering of the monopoles and phonons due to local lattice distortions.

The heat transport κ of $Dy_2Ti_2O_7$ within the low-temperature and low-field regime has also been investigated concerning strong hysteresis effects and slow-relaxation processes towards equilibrium states. It turned out that κ in the hysteretic regions slowly relaxes towards larger values which suggests that there is an additional suppression of the heat transport by disorder in the non-equilibrium states. The size and degree of the hysteresis do not only depend on the temperature and the magnetic-field direction, but also on the rate of the magnetic-field change. The equilibration can even be governed by the heat current for particular configurations. Thus, it can be concluded that the equilibration can also be controlled by the heat current which most likely yields important information about the dynamics of monopole excitations and their interaction with phonons. In addition, the hysteresis of the thermal conductivity within the Kagomé-ice phase was studied for the dilute spin-ice materials $(Dy_{1-x}Y_x)_2Ti_2O_7$ with $x \leq 0.5$ and for the pure compound $Dy_2Ti_2O_7$ at different angles θ of the applied field from the [111] direction within the [111]-[$1\bar{1}0$] plane. An increasing dilution x leads to a rapid suppression of the hysteresis whereas the initial $\kappa(0\ \mathrm{T})$ is recovered for all x for the configuration $\vec{H}\,||\,\vec{j}\,||\,[111]$. The degree of the hysteresis did not reveal any angle-dependence for small θ. These findings strongly suggest that the hysteresis within the Kagomé-ice phase originates from disorder and is not related to a misalignment of the applied magnetic field which would lift the 3-fold ground-state degeneracy there.

The specific heat study of $(\mathrm{Dy}_{1-x}\mathrm{Y}_x)_2\mathrm{Ti}_2\mathrm{O}_7$ revealed that the ultra-slow thermal equilibration in pure spin ice $\mathrm{Dy}_2\mathrm{Ti}_2\mathrm{O}_7$ is rapidly suppressed upon dilution with non-magnetic yttrium and has vanished completely for $x \geq 0.2$ down to the lowest accessible temperatures. A phononic background was estimated by measurements of the non-magnetic $\mathrm{Y}_2\mathrm{Ti}_2\mathrm{O}_7$ which yields a much better description than the Debye model or a simple power-law. As a consequence, the low-temperature entropy of $(\mathrm{Dy}_{1-x}\mathrm{Y}_x)_2\mathrm{Ti}_2\mathrm{O}_7$ is obtained which systematically decreases with increasing x, whereas its temperature dependence strongly increases. Thus, it can be concluded that there is no experimental evidence for a finite zero-temperature entropy in $(\mathrm{Dy}_{1-x}\mathrm{Y}_x)_2\mathrm{Ti}_2\mathrm{O}_7$ above $x \simeq 0.2$, in clear contrast to the finite residual entropy $S_\mathrm{P}(x)$ expected from the generalized Pauling approximation $S_\mathrm{P}(x)$ [19]. A similar discrepancy is also present between $S_\mathrm{P}(x)$ and the low-temperature entropy determined by Monte Carlo data [21]. The simulations reproduce the experimental data from 25 K down to 0.7 K, whereas the entropy at 0.4 K is overestimated. Thus, the classical spin-ice model is applicable to the intermediate temperature range, but a fundamental model including quantum effects would be highly desirable to unravel the true ground state of $(\mathrm{Dy}_{1-x}\mathrm{Y}_x)_2\mathrm{Ti}_2\mathrm{O}_7$. Generally, it turned out that spin-ice physics in $\mathrm{Dy}_2\mathrm{Ti}_2\mathrm{O}_7$ changes towards weakly interacting single-ion physics in $(\mathrm{Dy}_{1-x}\mathrm{Y}_x)_2\mathrm{Ti}_2\mathrm{O}_7$ at intermediate dilution. The change of entropy has also been obtained by means of the magnetocaloric effect. The suppression of S in $(\mathrm{Dy}_{1-x}\mathrm{Y}_x)_2\mathrm{Ti}_2\mathrm{O}_7$ with increasing magnetic field was systematically observed as well as the Kagomé-ice phase for the pure compound with $\vec{H}\,||\,[111]$. A good agreement was found between the temperature- and field-dependent entropy.

Because of the more instructive field dependence of $\kappa(H)$ in $\mathrm{Dy}_2\mathrm{Ti}_2\mathrm{O}_7$, a special focus was additionally put on the thermal conductivity of the dilution series $(\mathrm{Dy}_{1-x}\mathrm{Y}_x)_2\mathrm{Ti}_2\mathrm{O}_7$ which was measured for various $x < 1$. It was found that the magnetic contribution κ_mag of the whole dilution series systematically scales with the degree of dilution and exhibits a maximum around 1.3 K. Hereby, an x-dependent phononic background κ_ph was applied which results in a vanishing κ_mag for $x \leq 0.5$. Additionally, a model from Tokiwa *et al.* [123] is found to be applicable in the low field range of $\kappa(H)$ for $\vec{H}\,||\,[001]$ and [111]. The suppression of the monopole density correlates with $\kappa(H)$ in the low-field range which is a further signature of monopole heat transport. Moreover, it was calculated from the experimental data that the energy of a monopole excitation is related to the decrease of $\kappa(H)$ as predicted in the model. The diffusion coefficient D_mag of the monopole excitations was calculated by means of c_{mag} and κ_{mag}. It also correlates with the degree of dilution x and reveals a broad maximum around 1.5 K. Below about $T \leq 0.5$ K and in the high-temperature range for $T \geq 4$ K, D_{mag} vanishes for all x. This is related to the fact that the even the pure system $Dy_2Ti_2O_7$ enters a defined ground state at very low-temperatures in the long-time limit and at 4 K, the spin-ice physics has essentially vanished. Via the kinetic gas theory, a mean-free path of $Dy_2Ti_2O_7$ was estimated to be $\ell \approx 0.3$ µm at about 1 K. Furthermore, it turned out that D_{mag} is hardly sensitive to weak dilutions $x \lesssim 0.2$ whereas it has almost vanished for $x = 0.4$. However, some questions remain open and an applicable model to describe the monopole dynamics in spin ice is strongly required.

A 1D Ising-chain system $CoNb_2O_6$

Quantum phase transitions are exclusively driven by quantum fluctuations and appear at absolute zero temperature. Hence they may seem like an abstract theoretical idea which is of little interest for experimental work, however the influence of the quantum critical point extends over a wide regime even at finite temperature and is one of the most exciting subjects in condensed-matter physics [161–166]. The prime example for a quantum phase transition and the corresponding quantum criticality is the ferromagnetic Ising chain in transverse magnetic field. Experimentally it can be realized exemplary by $LiHoF_4$ where the transverse field case has already been studied in detail [167–169]. However, since some single-crystal neutron scattering experiments performed by Coldea *et al.* [170] and further studies [171–176], an emphasis is put on the columbite $CoNb_2O_6$. The system is the closest realization of a transverse 1D Ising-chain system found to date. In addition, it exhibits 3D magnetic order below about 3 K due to a small antiferromagnetic inter-chain coupling. Coldea *et al.* discovered the first experimental evidence for the long predicted E_8 symmetry in the excitation spectra of an Ising chain with small inter-chain coupling near its quantum critical point. Within this chapter, the study on the 1D Ising-chain system $CoNb_2O_6$ from the diploma thesis [54] is continued by measurements of the magnetization. The phase diagram of the 3D order regime is derived including additional specific heat data taken from Ref. 54. The 3D order exhibits an interplay with the quantum criticality and vice versa. Furthermore, the analytical results of the 1D Ising chain in transverse field are compared to both thermodynamic properties.

A.1 Introduction

A.1.1 Crystal structure

The columbite $CoNb_2O_6$ is an electric insulator and crystallizes in the orthorhombic space group *Pbcn* with lattice parameters: $a = 14.1337$ Å, $b = 5.7019$ Å, $c = 5.0382$ Å [177]. The crystal structure is shown in Fig. A.1. The system contains layers of CoO_6 octahedra separated by two non-magnetic NbO_6 layers (not shown) in a direction. The edge-sharing oxygen octahedra link the Co^{2+} spins

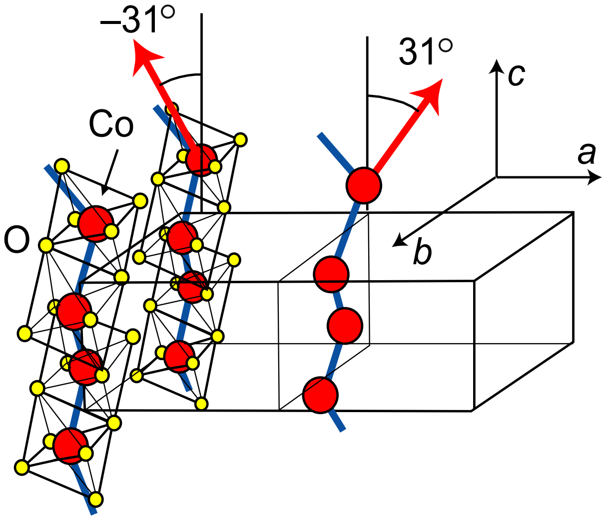

Figure A.1: Crystal structure of $CoNb_2O_6$. The easy axis is located within the ac plane and is alternating by ±31° with respect to the c axis for neighboring chains. Taken from Ref. 176.

through Co-O-Co super-exchange and form 1D ferromagnetic zigzag chains along the orthorhombic c axis. A strong crystal electric field compresses the CoO_6 octahedra which leads to an easy-axis anisotropy of the Co^{2+} moments. These easy axes of the ferromagnetic chains lie within the ac plane and are alternately tilted by $\pm 31^\circ$ with respect to the c axis for neighboring chains in a direction [178]. The strong easy-axis anisotropy leads the system to be considered as an effective spin-1/2-system described by the Ising model. Additionally, $CoNb_2O_6$ reveals long-range antiferromagnetic (AF) order due to a small coupling between the chains with $J \approx 0.01 \cdot J_1, J_2$ [179] where J denotes the intra-chain coupling and J_1, J_2 are the inter-chain couplings. Below $T_{\mathrm{N1}} = 2.95$ K, an incommensurate order sets in which becomes commensurate at $T_{\mathrm{N2}} = 1.97$ K [180]. A magnetic field parallel to the b axis is normal to the easy axis of both types of chains. It allows to study the quantum phase transition of an Ising-spin chain in a transverse field. The system is driven through its quantum critical point from a quasi 1D ferromagnet to a quantum paramagnet.

A.1.2 Sample growth

The single crystal of $CoNb_2O_6$ was grown by the floating-zone technique during the diploma thesis of J. Frielingsdorf [181]. The crystal was oriented in a X-ray backscattering Laue camera and bar-shaped samples were cut which had dimensions $1.5 \times 1.7 \times 3$ mm^3. The intermediate dimension was the b axis along which the magnetic field was applied. The magnetization was measured in a capacitance Faraday magnetometer whose experimental details were introduced in Sec. 3.2.

Considering initial results, it was found that an exact orientation of the sample with respect to the applied magnetic field is absolutely necessary to obtain data which captures all features connected with the 1D magnetism. This was accomplished in the diploma thesis [54] by building a bracket which allows to mount the calorimeter into the X-ray backscattering Laue camera to orient the sample in-situ on the sapphire platform for measuring the specific heat. The crystal for the magnetization measurement was carefully aligned under a microscope.

A.1.3 Literature results

In literature the transverse field case of the 1D system $\mathrm{CoNb_2O_6}$ is studied applying various methods. From neutron scattering data of Wheeler *et al.*, an effective g factor of $g = 3.55$ and an intra-chain coupling $J/k_\mathrm{B} \approx 23.2$ K are obtained [182]. Kinross *et al.* performed nuclear magnetic resonance (NMR) measurements with a transverse field and determine a critical field of 5.25 ± 0.15 T. From the temperature dependence of the ^{93}Nb longitudinal relaxation rate $1/T_1$, a power-law behavior $1/T_1 \propto T^{-3/4}$ is observed at the critical field of the NMR data, which is predicted by quantum critical scaling. Furthermore, the intra-chain coupling is calculated by exponential fits $1/T_1 \propto \exp(\Delta/T)$ to be $J/k_\mathrm{B} = 17.5^{+2.5}_{-1.5}$ K. Liang *et al.* measured the specific heat of $\mathrm{CoNb_2O_6}$ in transverse field [176]. The critical field is estimated to be $H_\mathrm{C}^\mathrm{3D} = 5.24$ T taken from the peak position of c/T at 0.45 K, which is indicated to be the closest approximation to the critical peak profile for $T \to 0$. The obtained phase diagram from the specific heat of Liang *et al.* will be directly compared to the phase diagram of this thesis, see Sec. A.2.3.

A.2 Experimental results

A.2.1 Magnetization

Fig. A.2 (a) displays zero-field cooled $M(H)$ curves in a temperature range from 0.5 K up to 4 K (symbols). In addition, the calculations of the 1D Ising model are shown which will be introduced and discussed in Sec. A.3. The curves are shifted by an offset of 0.5 with respect to each other. Considering the experimental data, the 0.5 K curve starts in the commensurate AF phase [178] and shows a first plateau at ≈ 2.7 T. On further raising the magnetic field the curve exhibits a kink at ≈ 5.2 T. In the high-field regime, the finite slope in $M(H)$ originates from a van Vleck susceptibility due to a mixing of higher crystal field levels to the ground state $|\pm 1/2\rangle$. The curve on lowering the magnetic field reveals no hysteresis at ≈ 5.2 T, however, a broad hysteresis occurs at the lower plateau-like feature. This

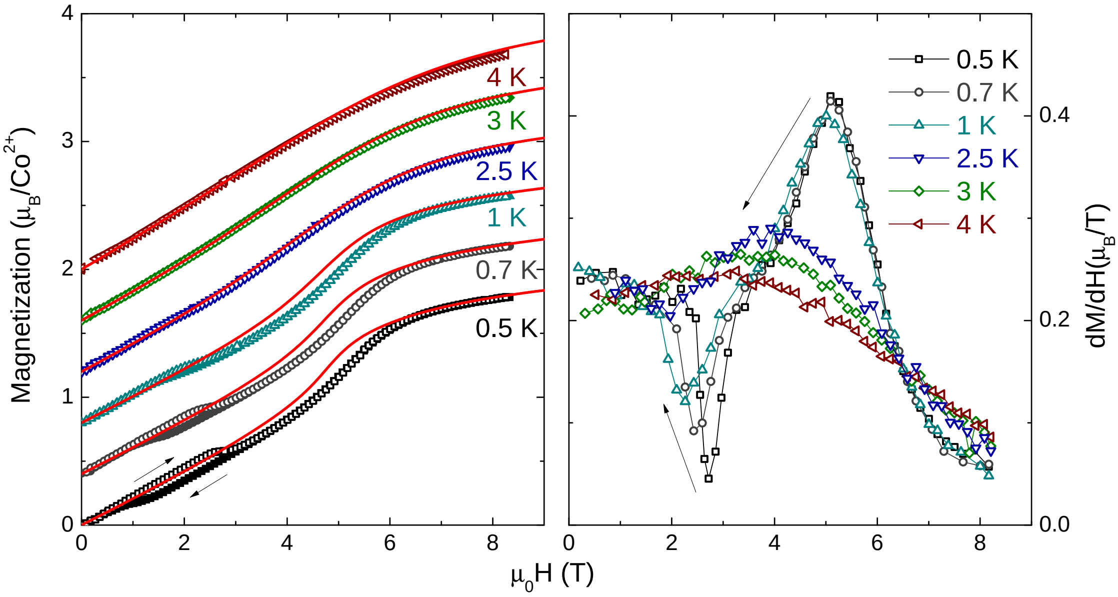

Figure A.2: Panel (a): zero-field cooled $M(H)$ data of $CoNb_2O_6$ (symbols). The red lines are calculation within the 1D Ising model, see text. The arrows indicate the field-sweep direction. Curves are offset with respect to each other. Panel (b): dM/dH at different temperatures. The arrows indicate the shift of the peaks with increasing temperature.

hysteresis reduces and shifts to smaller magnetic fields with increasing temperature. At 2 K $> T_{N2}$, the hysteresis has completely vanished. The 3 K- and 4 K-curves are located in the paramagnetic regime above $T_{N1} = 2.95$ K and possess Brillouin-like shape without any transition features. As can be seen in panel (b), the kinks in $M(H)$ measured with increasing magnetic field appear as sharp peaks in dM/dH. The arrows indicate the shift of the peak with increasing temperature.

The corresponding temperature-dependent $M(T)$ curves at various fixed magnetic fields are shown in Fig. A.3 (a) and (b). The curves are measured with decreasing temperature. Taking a look at the experimental data, it is found that the 7 T curve does not show any anomalies, see panel (a). It is located in the paramagnetic regime above the critical field and, thus, $M(T)$ continuously increases with decreasing temperature. At 4 T, the curve exhibits a kink at ≈ 2 K indicated by the arrow. The 2 T- and 1 T-curves in panel (b) also show kinks which shift to higher temperatures with decreasing magnetic field. However, the curve at 1 T exhibits an additional feature at ≈ 1.9 K.

Fig. A.4 (a) shows $M(H)$ data (symbols) of $CoNb_2O_6$ which were measured on a different single crystal grown during the diploma thesis of V. Cho [136] in comparison with $M(H)$ data (solid lines) with increasing field of this thesis. Curves

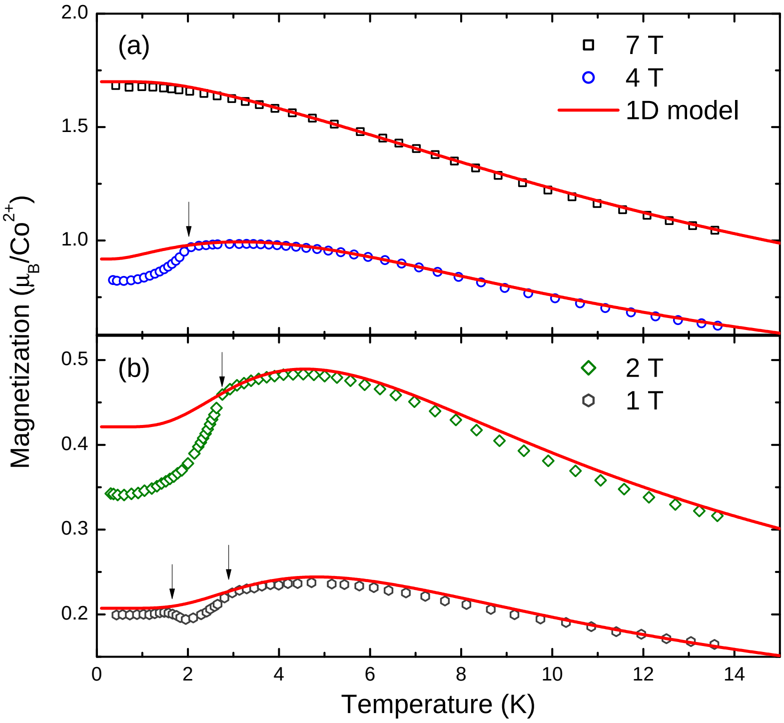

Figure A.3: Experimental $M(T)$ data for various magnetic fields measured with decreasing temperature (symbols). The kinks are highlighted by arrows. The solid red lines are calculations within the 1D Ising model.

are offset with respect to each other. It turns out that the field- and temperature-dependencies of both data sets are similar, but the data also reveal differences. Firstly, the low-field plateau-like feature occurs at different magnetic field and is systematically less pronounced in the data from Ref. 136. At 1 K, it has already completely vanished which is not observed in Fig. A.2 (a). This low-field hysteresis is related to a metastable phase which will be briefly introduced in the discussion of the phase diagram in Sec. A.2.3 and has been studied in detail in the diploma thesis [54]. This phase is found to be highly sensitive to the sample quality and its size strongly varies for different $CoNb_2O_6$ crystals [48, 136, 183]. Secondly, the high-field kink seems to be sharper in the data from this thesis which results in slightly enhanced values of $M(H)$ around the anomaly. This can be better seen in panel (b) where the corresponding $\mathrm{d}M/\mathrm{d}H$ data are depicted. For reasons of clarity, only the curve at 0.5 K (solid line) of this thesis is shown. The position of the high-field kinks coincides but it is clearly more pronounced for the data from this thesis which most likely originates from a more precise orientation of the external field with respect to the b axis of the samples. As can be also seen in panel (b), the low-field kink occurs at slightly different magnetic field as discussed before.

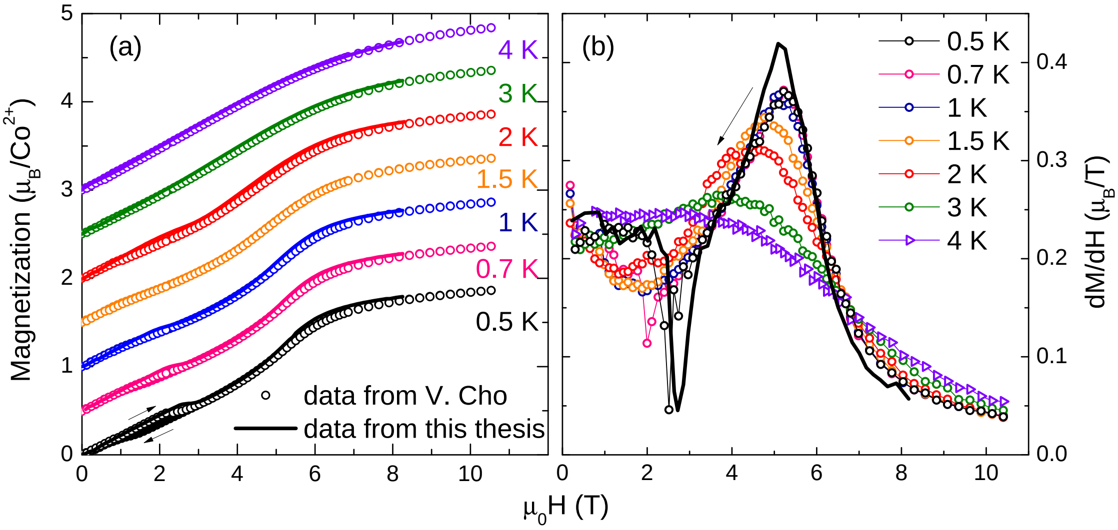

Figure A.4: Panel (a): field-dependent $M(H)$ data (symbols) of $CoNb_2O_6$ taken from V. Cho [136] in comparison with the results of $M(H)$ (solid lines) obtained in this thesis. Curves are offset with respect to each other. Panel (b): corresponding dM/dH curves determined from $M(H)$ measured with increasing field. For reasons of clarity, here only the curve at 0.5 K from this thesis is shown.

A.2.2 Specific heat

Zero-field cooled measurements of the specific heat $c(T)/T$ at magnetic fields between 0 T and 9.6 T are shown in Fig. A.5 (a) and (b) which are taken from the diploma thesis [54]. In addition, the calculations of the 1D Ising model are shown, see Sec. A.3. On raising the temperature in zero magnetic field, $c(T)/T$ exhibits a first step-like feature at ≈ 1.97 K, see panel (a). With increasing temperature, a sharp peak is observed at ≈ 3 K. Both features are marked by arrows. The plateau-like anomaly signals the commensurate-incommensurate (C-IC) transition whereas the sharp peak occurs at the transition into the paramagnetic regime. Both transition temperatures are in very good agreement with literature [170, 176, 179, 180]. Above 1 T, the plateau-like feature cannot be exactly resolved in the $c(T)/T$ data. The sharp peak of the order transition strongly broadens with increasing magnetic field and can be localized up to 3.8 T. The curve at 5.3 T does not exhibit any transition features. In general, $c(T)/T$ is systematically suppressed with further increasing magnetic field which can be seen in panel (b) where no anomalies are observed.

Experimental $c(H)/T$ from the diploma thesis [54] obtained after cooling in zero field are shown in Fig. A.6 (a)-(i). The data exhibit three anomalies for $T < 2$ K.

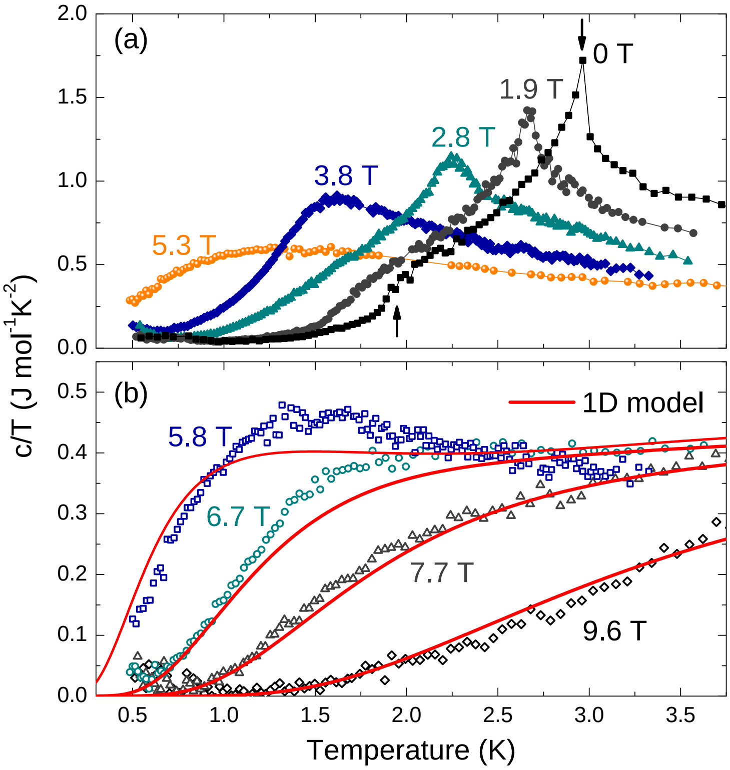

Figure A.5: Zero-field cooled $c(T)/T$ of $CoNb_2O_6$ in a magnetic field range from 0 T up to 9.6 T. The anomalies in zero field are marked by arrows. The solid red lines are calculations within the 1D Ising model.

In the low-field regime, a shoulder occurs at small fields for $T < 1.4$ K and below 1 K even a sharp jump is observed in $c(H)/T$ (marked by arrows). The $c(T)/T$ data contain a similar shoulder in zero field, see Fig. A.5 (a). Thus, this feature most likely signals the C-IC transition and it has vanished for $T > 2$ K. The two other anomalies can clearly be seen in $c(H)/T$ in form of two separated maxima, of which the lower one is much more pronounced. With decreasing temperature, both maxima start to merge and can hardly be resolved at 0.9 K. Above the magnetic ordering temperature ($T_{N1} = 2.95$ K), the data only exhibit one maximum. Here, $c(H)/T$ continuously decreases, except showing a shoulder, *e.g.* at ≈ 7 T in the 4 K curve. It is observed that this high-field maximum shifts to higher magnetic fields with increasing temperature. The existence of those high-field features in $c(H)/T$ in the vicinity of a quantum critical point is expected from the model of the 1D Ising chain in transverse magnetic field [163, 170].

Fig. A.7 (a) and (b) also depict field- and temperature dependent specific heat data c/T at different temperatures obtained by Liang *et al.* [176]. The maximum of the curve measured at the lowest temperature (0.45 K) is highlighted by the dark blue solid line and H_c marks the corresponding magnetic field, see panel (a). The data were measured using the *ac* calorimetry [184] which results in the high density of data points compared to the relaxation method, see Sec. 3.5.1. Within the field-dependent curves in panel (a), two maxima are resolved above about 0.8 K.

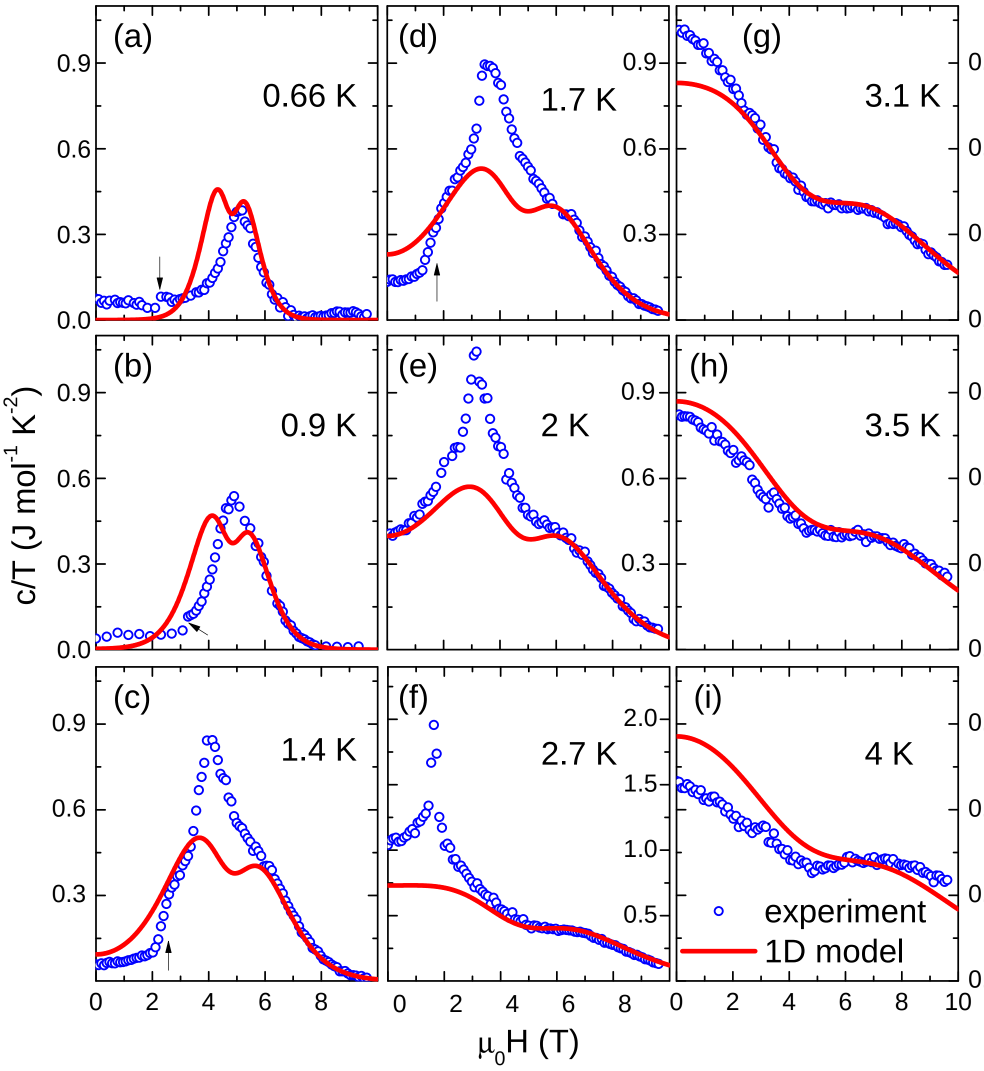

Figure A.6: Zero-field cooled specific heat $c(H)/T$ at fixed temperatures. The data is compared to the 1D Ising model which was fitted to the curves beyond the 3D order (solid red lines). An additional maximum is found for $H > H_C^{3D}$ that is also predicted by the 1D model. A shoulder occurs at small fields for $T < 1.4$ K and below 1 K even a sharp jump is resolved in $c(H)/T$ (marked by arrows).

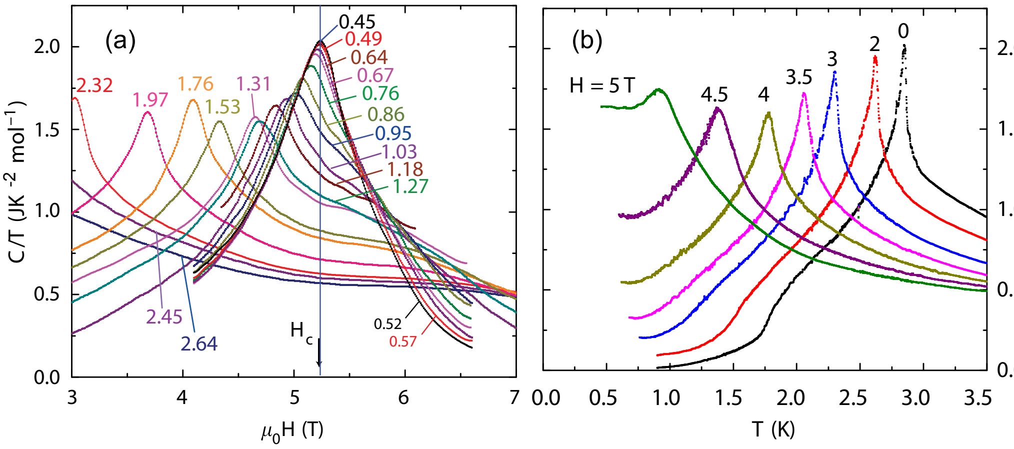

Figure A.7: Panel (a): field-dependent specific heat data of $CoNb_2O_6$ at different temperatures. H_c denotes the location of the maximum at the lowest temperature $T = 0.45$ K. Panel (b): temperature-dependent curves at different magnetic fields with $H < H_c$. Taken from Ref. 176.

The occurrence of these maxima is consistent with the data from this thesis in Fig. A.6 where they can only roughly resolved at 0.9 K. In Fig. A.7 (a), the low-temperature curves ($T < 1.18$ K) are not shown below 4 T which cuts out the low-field shoulder. The temperature-dependent c/T curves in panel (b) exhibit a pronounced peak which can be resolved up to 5 T. This is in contrast to the data in Fig. A.5 where the peak can only be exactly resolved up to about 2.8 T. The low-temperature shoulder is also more pronounced. These deviations can originate from the different measurements techniques that were applied or from the orientation of the external magnetic field with respect to the b axis. In the latter case, Liang *et al.* accomplished to orient the magnetic field more accurate than an in-situ installation in the X-ray backscattering Laue camera. The transition temperatures obtained from Liang *et al.* will also be compared to the results of this thesis within the phase diagram of $CoNb_2O_6$ in the following section.

A.2.3 Phase diagram

Panel (a) and (b) of Fig. A.8 compare $c(H)/T$ data to $\mathrm{d}M/\mathrm{d}H(H)$ at ≈ 0.7 K and 1.5 K. The anomalies in both properties are marked by arrows. The $c(H)/T$ data in panel (a) contain a low-field shoulder at about ≈ 2.5 T which signals the first-order C-IC transition followed by a broad maximum at ≈ 5 T. The positions of the shoulder and of the maximum match the peaks in $\mathrm{d}M/\mathrm{d}H$. At 1.5 K, the low-field shoulder in $c(H)/T$ still matches the $\mathrm{d}M/\mathrm{d}H$ data, however, it is found that the broad maximum in $c(H)/T$ does not match the peak position in

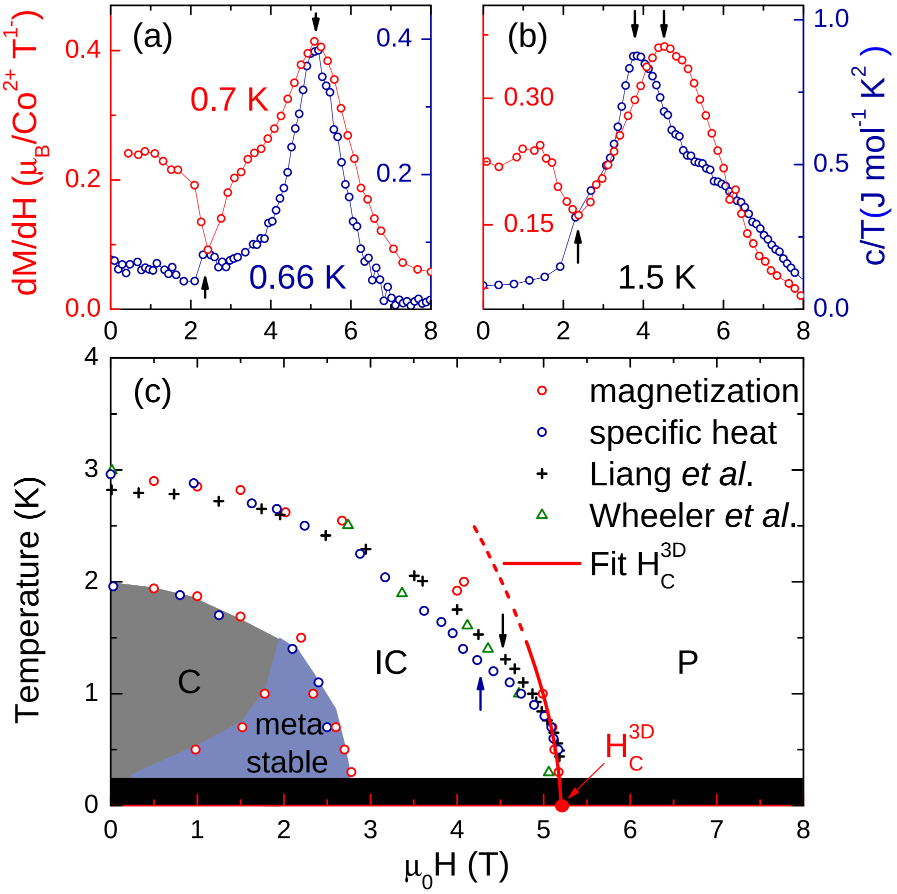

Figure A.8: Panels (a) and (b) compare $dM/dH(H)$ to $c(H)/T$ at 0.7 K and 1.5 K. Panel (c) shows the phase diagram obtained from $M(H,T)$ and $c(H,T)/T$. The black crosses are obtained from specific heat data from Liang *et al.* [176] and the green triangles originate from neutron scattering data by Wheeler *et al.* [182]. The red line is the power-law fit for H_C^{3D}.

dM/dH, see panel (b). There is a discrepancy of about 0.8 T between both features. Furthermore, the $c(H)/T$ data at 1.5 K exhibit another maximum which is located within the paramagnetic (P) phase. This additional maximum is much smaller than the low-field one and belongs to the 1D magnetism of the system. There is no corresponding feature found in the $M(H)$ which is consistent with the 1D model [163, 185].

Fig. A.8 (c) presents the phase diagram of $CoNb_2O_6$ which is obtained from the magnetization measurements $M(T,H)$ and the specific heat $c(H,T)/T$ data. The red circles represent the peaks in dM/dH, see Fig. A.2, and the kinks in $M(T)$, compare Fig. A.3. The transition features in $c(H,T)/T$ are depicted by the blue circles. The black crosses are transition temperatures into the paramagnetic regime from

Liang *et al.* [176] obtained by specific heat data and the green triangles originate from neutron scattering experiments data by Wheeler *et al.* [182]. The transition features from V. Cho [136] are not included because the data yield similar results at the transition into the P phase on which the emphasis is put. Within the 3D ordered phase and below about 1.95 K in zero magnetic field, the commensurate (C) phase sets in. It is confirmed by the magnetization and specific heat data which are consistent here. In Ref. 54, the C phase including a metastable regime is studied in detail. The C phase is suppressed at an external field of about 3 T. Considering the results for the C phase from V. Cho [136], it is found that the transition temperatures do not agree. However, especially the metastable phase exhibits clear sample-dependence, is highly sensitive to the orientation the b axis with respect to the applied field and additionally to its history in the phase diagram [54, 136, 183]. Thus, these deviations are not unexpected.

Concerning the transition into the P phase, the interpretation of the phase diagram is more difficult. The transition features from $c(H,T)/T$ only match the corresponding features from $M(H,T)$ in the low-field regime (0 T-2 T) and close to the critical field H_C^3D which is obtained by an exponential fit (solid red line) to be $H_\mathrm{C}^\mathrm{3D} \cong 5.2$ T. The critical field is in very good agreement with literature [176, 182, 186]. But, it is clearly smaller than the previously reported critical field of 5.5 T by Coldea *et al.* [170]. The transition into the P phase is second-order type. The magnetization $M(T,H)$ is an order parameter of a ferromagnet and the susceptibility $\mathrm{d}M/\mathrm{d}H$ diverges at the transition whereas the staggered magnetization is the order parameter of an antiferromagnet [187]. In this case, it is dealt with an incommensurate antiferromagnetic order in a transverse field whose order parameter in the magnetization cannot be captured in a simple model. Thus, the maxima in $\mathrm{d}M/\mathrm{d}H$ do not automatically occur at the exact phase transition [187]. In zero field, it is found that the transition from Ref. 176 obtained by specific heat data yield a smaller $T_\mathrm{N1} = 2.82$ K. In the intermediate field range, the transitions are located in-between the experimentally data of $M(H,T)$ and $C(H,T)/T$. A detailed look reveals that the transition temperatures from Ref. 176 exhibit a small shoulder at about 4.6 T (black arrow) which is also observed in the data from this thesis at a slightly smaller field of about 4.2 K (blue arrow). This shoulder originates from the fact that the two maxima of $c(H)/T$ start to merge here and, thus, a distinction of the exact position is prevented. This results in the determination of higher transition temperatures. The neutron scattering data by Wheeler *et al.* [182] provide the same zero-field T_N1. The data are rather noisy but support the interpretation that the specific heat yields the phase transition into the P phase. As mentioned above, the order parameter of an incommensurate antiferromagnet in transverse field of the magnetization is difficult to determine and by considering all the results from this thesis and literature [176, 182], it is most likely that $M(H,T)$ does not signal the order transition.

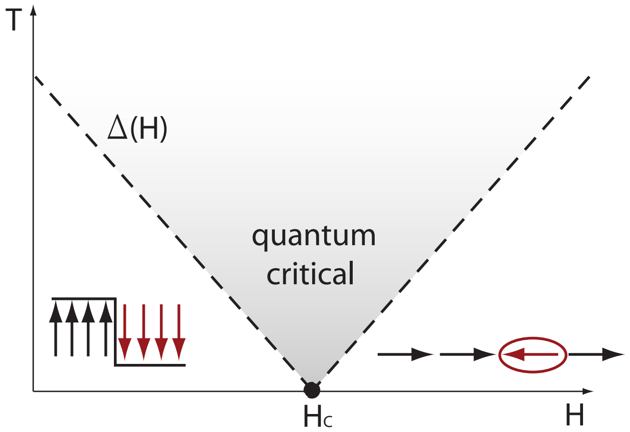

Figure A.9: Phase diagram of a single 1D Ising chain in transverse magnetic field. The gap $\Delta(H)$ denotes the energy to the first excited state from the ground state. Adapted from Ref. 170.

In general, all obtained transition features from the magnetization and the specific heat together with the literature results reveal that the creation of an exact phase diagram for CoNb$_2$O$_6$ bares several uncertainties. The transition temperatures are highly sensitive to an exact orientation of the applied field and the interplay of the 1D physics with the magnetic order prevents a definite conclusion.

A.3 Comparison to 1D Ising model in transverse magnetic field

The most prominent example of a quantum phase transition is the model of the ferromagnetic Ising chain in a transverse magnetic field which is exactly solvable. The corresponding phase diagram is shown in Fig. A.9. In the ground state at $T = 0$, all the spins of an isolated chain are pointing parallel with ferromagnetic coupling (upwards or downwards). The gap $\Delta(H)$ denotes the energy of the first excited state above the ground state realized by a domain-wall at which one ferromagnetic coupling between two neighboring spins is broken. By increasing the transverse external field $H \to H_C$, the gap $\Delta(H)$ linearly decreases and finally vanishes at the quantum critical point H_C. For $H > H_C$, the system is driven into the quantum paramagnetic regime where $\Delta(H)$ linearly opens and excitations appear in form of single spin-flips.

The Ising chain is one of the most studied models in theoretical physics and its Hamiltonian in transverse field is given by [163]

$$\mathcal{H} = \sum_i J\hat{S}_i^z \cdot \hat{S}_{i+1}^z + H\hat{S}_i^x \tag{A.1}$$

where J is the intra-chain coupling constant and H is the magnetic field in terms of energy. The essential tool in the solution of the Hamiltonian is the Jordan-Wigner transformation [188, 189]. This is a powerful mapping between models with spin-1/2 degrees of freedom and spinless fermions. The Hilbert space of a system with spin-1/2 degree of freedom per site is mapped onto spinless fermions hopping between sites with single orbitals. The Jordan-Wigner transformation is followed by the Bogoliubov transformation [190] in order to solve the Hamiltonian. Then, the dispersion relation is given by [163]

$$\epsilon_k = \sqrt{(J/2\cos(k) + H)^2 + (J/2\sin(k))^2}. \tag{A.2}$$

From Eq. (A.2), the specific heat $c(T, H)$ and the magnetization $M(T, H)$ can be derived which was accomplished by E. Sela [185]. The free energy $f(T, H)$ is related to $c(T, H)$ and $M(T, H)$ via

$$\frac{c}{T} = -\frac{\mathrm{d}^2 f}{\mathrm{d}T^2}, \quad M = \frac{\mathrm{d}f}{\mathrm{d}H}. \tag{A.3}$$

For the Ising chain in transverse field, the free energy is obtained from the excitation energies ϵ_k and is given by [163, 185]

$$f(T, H) = -T\int_0^\pi \frac{\mathrm{d}k}{\pi}\log\left[2\cosh\left(\frac{\epsilon_k}{T}\right)\right] - \int_0^\pi \frac{\mathrm{d}k}{2\pi}\epsilon_k. \tag{A.4}$$

The second term defines a magnetic-field-dependent zero-temperature ground-state energy. The result for the specific heat follows to be [185]

$$c_{\text{Ising}} = \frac{1}{\pi}\int_0^\pi \mathrm{d}k\left(\frac{\epsilon_k}{T}\right)^2 \frac{\mathrm{e}^{\epsilon_k/T}}{\left(\mathrm{e}^{\epsilon_k/T}+1\right)^2}. \tag{A.5}$$

The magnetization is given by [185]

$$M_{\text{Ising}} = \frac{1}{2\pi}\int_0^\pi \mathrm{d}k\frac{\frac{J}{2}\cos(k) + \tilde{H}}{\epsilon_k}\left(1 - 2f\left(\epsilon_k\right)\right) \tag{A.6}$$

with $f(E) = \left(1 + \mathrm{e}^{E/T}\right)^{-1}$ as the Fermi function.

First, the model of the 1D Ising chain was found to be applicable for the compound $\mathrm{LiHoF_4}$ [167]. However, the one-dimensional magnetism of $\mathrm{CoNb_2O_6}$ can also be compared to the transverse field case of this model. As a result, the intra-chain coupling J and the g factor of the system can be determined.

The specific heat c_{Ising} given by Eq. (A.5) and the magnetization M_{Ising} calculated by Eq. (A.6) of the 1D Ising chain in transverse field were fitted to the experimental data of $M(T, H)$ and $c(H, T)/T$ in a regime starting 10% above the 3D transition

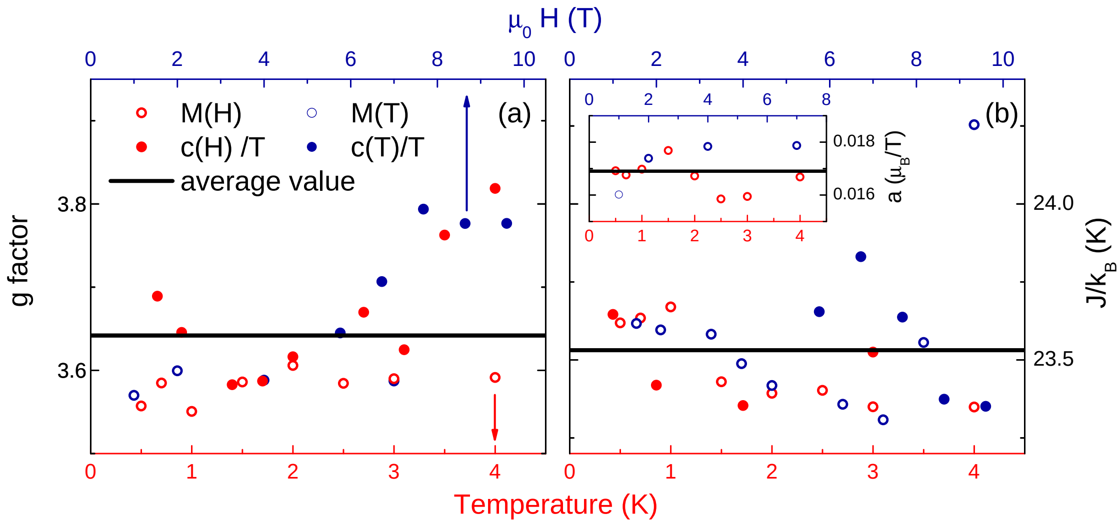

Figure A.10: Single fit parameters obtained from the temperature and field-dependent $M(H,T)$ and $c(H,T)/T$ data. The red symbols represent field-dependent measurements $M(H)$ and $c(H)/T$ at constant temperature. The blue circles stem from temperature-dependent data $M(T)$, and $c(T)/T$ at constant magnetic field. The average values are represented by the black solid lines. Panel (a): fit parameters of the g factor. Panel (b): fit parameters intra-chain coupling J/k_{B}. The inset depicts the corresponding results for the van-Vleck term a determined from $M(H,T)$.

features. Note that M_{Ising} has to be extended to $M_{\mathrm{Ising,exp}} = a \cdot \mu_0 H + g \cdot M_{\mathrm{Ising}}$. The first term accounts for the finite slope in the experimental $M(H)$ data (> 5 T) which originates from the mixing of higher crystal field levels to the $|\pm 1/2\rangle$ ground state (van-Vleck susceptibility) and, additionally, the g factor is included because $M_{\mathrm{Ising}}(H \to \infty) = 1/2$. For the specific heat, the experimental data is fitted by $c_{\mathrm{Ising,exp}} = N_{\mathrm{A}} k_{\mathrm{B}} \cdot c_{\mathrm{Ising}}$. Fig. A.10 (a)-(b) present the fit parameters of J/k_{B} and the g factor which were obtained by fitting the single experimental curves $M(H,T)$ and $c(H,T)/T$ curves. Note that the red symbols represent field-dependent curves at constant temperature and the blue symbols depict temperature-dependent measurements at constant field. The inset of panel (b) shows the van-Vleck parameter a determined from $M(H,T)$. The solid black lines highlight the average value of the parameters. As can be seen in Fig. A.10 (a)-(b), the results for the single parameters only slightly vary for the fits of the different curves and, in general, it is found that both quantities yield very similar results for J/k_{B} and the g factor. Thus, it appears reasonable to describe the experimental data of both quantities with theoretical curves based on the same temperature-independent parameters. The average values for the g factor, the intra-chain coupling J/k_{B} and the parameter a represented by the black lines in Fig. A.10 (a)-(b) and are additionally displayed in Tab. A.1.

The theoretically obtained curves $M_{\mathrm{Ising,exp}}(H,T)$ and $c(H,T)/T_{\mathrm{Ising,exp}}$ of the 1D model calculated with the parameters from Tab. A.1 are shown in Fig. A.2, A.3, A.5 and A.6 by the red solid lines in comparison with the corresponding experimental data. The phononic contribution to the specific heat data is smaller than 1% in the whole measured regime [179] and is neglected. Considering the fits to the experimental $M(H,T)$ and $c(H,T)/T$ curves, it is found that the data can be well described by the 1D model above the 3D order for both physical properties. Note that the fits for both magnetization and specific heat are based on the same parameters. The g factor $g = 3.64$ determined from the experimental results from this thesis is in good agreement with a g factor $g = 3.55$ obtained for the transverse field case from neutron scattering data by Wheeler *et al.* [182]. As already discussed above, the results for the intra-chain coupling J/k_{B} vary between 17.5 K and 23.2 K in literature. The analysis of the experimental data within this thesis yields a slightly larger value of $J/k_{\mathrm{B}} = 23.53$ K. Furthermore, the determination of J/k_{B} and the g factor yields the quantum critical point of the 1D Ising chain of $\mathrm{CoNb_2O_6}$ via Eq. (A.2). A critical field of $H_{\mathrm{C}}^{\mathrm{1D}} = 4.81$ T is determined. It is located within the 3D ordered regime according to the phase diagram in Fig. A.8. This originates most likely from the fact that the 1D model does not account for the inter-chain couplings which are, however, present in $\mathrm{CoNb_2O_6}$ and result in the 3D magnetic order below about 3 K. Thus, it appears reasonable that the 1D model predicts smaller values for the critical field of the system.

A.4 Quantum criticality

Fig. A.11 shows a density plot of c/T as a function of magnetic field and temperature. The maxima in $\mathrm{d}M/\mathrm{d}H$ are also displayed by the red circles. This representation resembles the predictions of a typical phase diagram of an Ising chain in transverse magnetic field [166]. Above the 3D order, the linear field dependence of the excitation gap is observed. The transition into the P phase is clearly seen in this representation whereas the C/IC transition can only be resolved for small fields

Parameters:		
g factor	J/k_{B}	a
3.64	23.53 K	0.0169 $\mu_{\mathrm{B}}/\mathrm{T}$

Table A.1: Parameters of the 1D Ising model in transverse field obtained from fits to the experimental data.

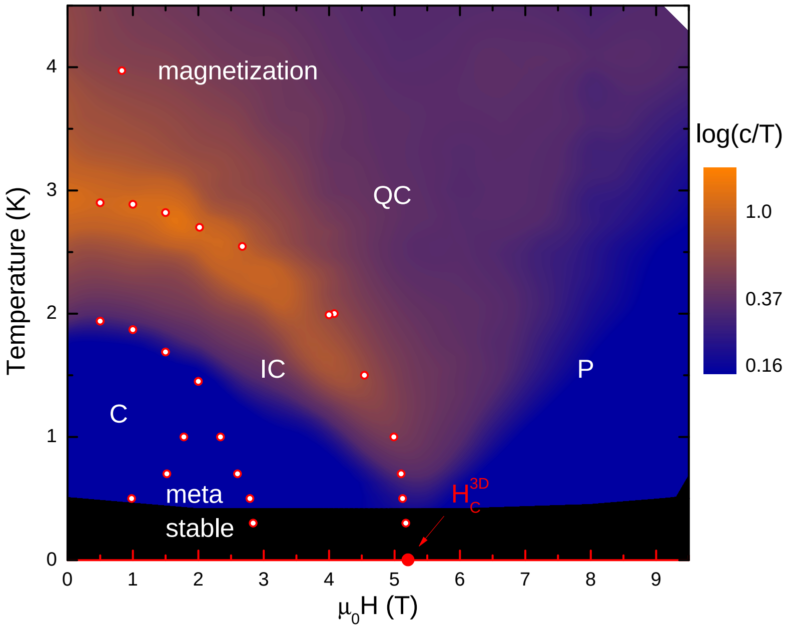

Figure A.11: Density plot of c/T as a function of the magnetic field and the temperature. The maxima in $\mathrm{d}M/\mathrm{d}H$ are also displayed by the red circles.

$H < 0.5$ T represented by a distinct increase in c/T. This density plot depicts the interplay of 3D magnetic order and quantum criticality at finite temperatures in $CoNb_2O_6$.

A.5 Conclusion

Magnetization measurements of $CoNb_2O_6$ were performed and with additional specific heat data from the diploma thesis [54], the phase diagram was derived. It contains the critical point $H_C^{3D} \cong 5.2$ T, determined by a power-law fit, where the 3D order is suppressed by an external field applied along the b axis. This result is in very good agreement with recent literature [176, 182, 186]. A meta-stable phase is confirmed within the 3D order which has already been studied in detail in Ref. 54. In general, it has to be noticed that the transition temperatures of the 3D order in $CoNb_2O_6$ exhibit a noticeable sample dependence which is much more pronounced for the metastable phase.

In addition, the 1D magnetism of $CoNb_2O_6$ is compared to the exactly solvable model of the Ising chain in transverse field. Fits to the experimental data of the magnetization and the specific heat yield values for the intra-chain coupling constant $J/k_B = 25.53$ K and the g factor of $g = 3.64$. Furthermore, the 1D critical field $H_C^{1D} = 4.81$ T is found to be located within the 3D ordered regime slightly below H_C^{3D}. Signatures of quantum criticality are observed and it is found that a zero-temperature feature like the quantum critical point clearly influences the physics at finite temperature.

Bibliography

[1] J. F. Sadoc and R. Mosseri, *Geometrical frustration* (Cambridge University Press, 1999).

[2] H. T. Diep, *Frustrated spin systems* (World Scientific, 2004).

[3] R. Moessner and A. P. Ramirez, Physics Today **59(2)**, 24 (2006).

[4] C. Castelnovo, R. Moessner, and S. L. Sondhi, Nature **451**, 42 (2008).

[5] L. Pauling, Journal of the American Chemical Society **57**, 2680 (1935).

[6] J. Nagle, Journal of Mathematical Physics **7**, 1484 (1966).

[7] P. A. M. Dirac, Proceedings of the Royal Society of London. Series A **133**, 60 (1931).

[8] S. T. Bramwell, S. R. Giblin, S. Calder, R. Aldus, D. Prabhakaran, and T. Fennell, Nature **461**, 956 (2009).

[9] S. R. Giblin, S. T. Bramwell, P. C. W. Holdsworth, D. Prabhakaran, and I. Terry, Nature Physics **7**, 252 (2011).

[10] C. Castelnovo, R. Moessner, and S. L. Sondhi, Physical Review B **84**, 144435 (2011).

[11] B. Klemke, M. Meissner, P. Strehlow, K. Kiefer, S. A. Grigera, and D. A. Tennant, Journal of Low Temperature Physics **163**, 345 (2011).

[12] C. Fan, Z. Y. Zhao, H. D. Zhou, X. M. Wang, Q. J. Li, F. B. Zhang, X. Zhao, and X. F. Sun, Physical Review B **87**, 144404 (2013).

[13] S. J. Li, Z. Y. Zhao, C. Fan, B. Tong, F. B. Zhang, J. Shi, J. C. Wu, X. G. Liu, H. D. Zhou, X. Zhao, and X. F. Sun, Physical Review B **92**, 094408 (2015).

[14] G. Kolland, O. Breunig, M. Valldor, M. Hiertz, J. Frielingsdorf, and T. Lorenz, Physical Review B **86**, 060402(R) (2012).

[15] G. Kolland, M. Valldor, M. Hiertz, J. Frielingsdorf, and T. Lorenz, Physical Review B **88**, 054406 (2013).

[16] G. Kolland, PhD thesis (Universität zu Köln, 2013).

[17] C. Grams, PhD thesis (Universität zu Köln, 2015).

[18] W. H. Toews, S. S. Zhang, K. A. Ross, H. A. Dabkowska, B. D. Gaulin, and R. W. Hill, Physical Review Letters **110**, 217209 (2013).

[19] X. Ke, R. S. Freitas, B. G. Ueland, G. C. Lau, M. L. Dahlberg, R. J. Cava, R. Moessner, and P. Schiffer, Physical Review Letters **99**, 137203 (2007).

[20] D. Pomaranski, L. R. Yaraskavitch, S. Meng, K. A. Ross, H. M. L. Noad, H. A. Dabkowska, B. D. Gaulin, and J. B. Kycia, Nature Physics **9**, 353 (2013).

[21] T. Lin, X. Ke, M. Thesberg, P. Schiffer, R. G. Melko, and M. J. P. Gingras, Physical Review B **90**, 214433 (2014).

[22] R. Barnard, *Thermoelectricity in Metals and Alloys* (Taylor and Francis Ltd, London, 1972).

[23] C. Hess, PhD thesis (Universität zu Köln, 2002).

[24] C. Kittel, *Einführung in die Festkörperphysik* (Oldenburgverlag, München, Wien, 2005).

[25] N. Ashcroft and N. Mermin, *Solid State Physics* (Saunders College Publishing, 1976).

[26] R. Berman, *Thermal Conduction in Solids* (Clarendon Press, Oxford, 1976).

[27] N. Johannsen, PhD thesis (Universität zu Köln, 2008).

[28] J. Ziman, *Principles of the Theory of Solids*, 2nd ed. (Cambridge University Press, 1972).

[29] C. Weissmantel and C. Hamann, *Grundlagen der Festkörperphysik* (Springer, Berlin, 1979).

[30] J. Parrott and A. Stuckes, *Thermal Conductivity of Solids* (Pion Limited, London, 1975).

[31] P. Klemens, *Thermal Conductivity and Lattice Vibrational Modes in Solid State Physics (Vol. 7)* (Academic, New York, 1958).

[32] K. Berggold, PhD thesis (Universität zu Köln, 2006).

[33] S. Niesen, PhD thesis (Universität zu Köln, 2015).

[34] K. Kordonis, PhD thesis (Universität zu Köln, 2006).

[35] J. Callaway, Physical Review **113**, 1046 (1959).

[36] J. Callaway, Physical Review **122**, 787 (1961).

[37] H. Ibach and H. Lüth, *Festkörperphysik* (Springer-Verlag Berlin, Heidelberg, 2009).

[38] M. Kriener, PhD thesis (Universität zu Köln, 2005).

[39] H. Stern, Journal of Physics and Chemistry of Solids **26**, 153 (1965).

[40] K. Kawasaki, Progress of Theoretical Physics **29**, 801 (1963).

[41] H. Fröhlich and W. Heitler, Proceedings of the Royal Society of London A **155**, 640 (1936).

[42] B. Lüthi, Journal of Physics and Chemistry of Solids **23**, 35 (1962).

[43] H. N. De Lang, H. van Kempen, and P. Wyder, Physical Review Letters **39**, 467 (1977).

[44] A. Sologubenko, T. Lorenz, H. Ott, and A. Freimuth, Journal of Low Temperature Physics **147**, 387 (2007).

[45] C. Hess, B. Büchner, U. Ammerahl, L. Colonescu, F. Heidrich-Meisner, W. Brenig, and A. Revcolevschi, Physical Review Letters **90**, 197002 (2003).

[46] N. Prasai, A. Rebello, A. B. Christian, J. J. Neumeier, and J. L. Cohn, Physical Review B **91**, 054403 (2015).

[47] C. Hess, The European Physical Journal Special Topics **151**, 73 (2007).

[48] S. Scharffe, G. Kolland, M. Hiertz, M. Valldor, and T. Lorenz, Journal of the Physical Society of Japan Conference Proceeding **3**, 014030 (2014).

[49] C. Grams, M. Valldor, M. Garst, and J. Hemberger, Nature Communications **4**, 4853 (2013).

[50] T. Lorenz, *Vorlesung Magnetism* (Universität zu Köln, 2014).

[51] http://www.oxford-instruments.com/.

[52] D. Loewen, Diploma thesis (Universität zu Köln, 2011).

[53] M. Hiertz, Diploma thesis (Universität zu Köln, 2013).

[54] S. Scharffe, Diploma thesis (Universität zu Köln, 2012).

[55] http://www.qdusa.com/.

[56] http://www.arepoc.sk/.

[57] B. H. Vos, Applied Scientific Research **5**, 425 (1956).

[58] D. J. Sanders and D. Walton, Physical Review B **15**, 1489 (1977).

[59] T. M. Tritt, *Thermal Conductivity* (Springer, 2005).

[60] M. Otter, G. Athanasopoulos, N. Hlubek, M. Montagnese, M. Labois, D. A. Fishman, F. de Haan, S. Singh, D. Lakehal, J. Giapintzakis, C. Hess, A. Revcolevschi, and P. H. M. van Loosdrecht, International Journal of Heat and Mass Transfer **55**, 2531 (2012).

[61] P. Zhang, B. Shi, Y. Xuan, and Q. Li, Measurement Science and Technology **24**, 095004 (2013).

[62] http://www.heraeus.de/.

[63] http://www.plano-em.de/.

[64] http://www.kunstpark-shop.de/.

[65] http://www.lakeshore.com/.

[66] M. Hofmann, PhD thesis (Universität zu Köln, 2002).

[67] http://www.keithley.com/.

[68] O. Heyer, Diploma thesis (Universität zu Köln, 2005).

[69] G. Brändli and R. Griessen, Cryogenics **13**, 299 (1973).

[70] S. Orbe, Diploma thesis (Universität zu Köln, 2011).

[71] J. J. Neumeier, R. K. Bollinger, G. E. Timmins, C. R. Lane, R. D. Krogstad, and J. Macaluso, Review of Scientific Instruments **79**, 033903 (2008).

[72] O. Breunig, Diploma thesis (Universität zu Köln, 2012).

[73] O. Breunig, PhD thesis (Universität zu Köln, 2015).

[74] C. A. Swenson, Review of Scientific Instruments **70**, 2728 (1999).

[75] W. Schnelle, J. Engelhardt, and E. Gmelin, Cryogenics **39**, 271 (1999).

[76] H. Tsujii, B. Andraka, K. Muttalib, and Y. Takano, Physica B: Condensed Matter **329–333**, 1552 (2003).

[77] X. Moya, S. Kar-Narayan, and N. D. Mathur, Nature Materials **13**, 439 (2014).

[78] V. K. Pecharsky and K. A. Gschneidner Jr, Journal of Magnetism and Magnetic Materials **200**, 44 (1999).

[79] S. T. Bramwell and M. J. Gingras, Science **294**, 1495 (2001).

[80] B. C. den Hertog and M. J. P. Gingras, Physical Review Letters **84**, 3430 (2000).

[81] G. H. Wannier, Physical Review **79**, 357 (1950).

[82] W. F. Giauque and M. F. Ashley, Physical Review **43**, 81 (1933).

[83] W. F. Giauque and J. W. Stout, Journal of the American Chemical Society **58**, 1144 (1936).

[84] H. R. von Gaertner, Neues Jahrbuch der Mineralogie **61**, 1 (1930).

[85] M. J. Harris, S. T. Bramwell, D. F. McMorrow, T. Zeiske, and K. W. Godfrey, Physical Review Letters **79**, 2554 (1997).

[86] T. Fennell, O. A. Petrenko, B. Fåk, S. T. Bramwell, M. Enjalran, T. Yavors'kii, M. J. P. Gingras, R. G. Melko, and G. Balakrishnan, Physical Review B **70**, 134408 (2004).

[87] J. Lian, J. Chen, L. M. Wang, R. C. Ewing, J. M. Farmer, L. A. Boatner, and K. B. Helean, Physical Review B **68**, 134107 (2003).

[88] M. Harris, S. T. Bramwell, T. Zeiske, D. F. Mcmorrow, and P. J. C. King, Journal of Magnetism and Magnetic Materials **177**, 757 (1998).

[89] H. Fukazawa, R. Melko, R. Higashinaka, Y. Maeno, and M. Gingras, Physical Review B **65**, 054410 (2002).

[90] A. P. Ramirez, A. Hayashi, R. J. Cava, R. Siddharthan, and B. S. Shastry, Nature **399**, 333 (1999).

[91] Z. Hiroi, K. Matsuhira, S. Takagi, T. Tayama, and T. Sakakibara, Journal of the Physical Society of Japan **72**, 411 (2003).

[92] D. J. P. Morris, D. A. Tennant, S. A. Grigera, B. Klemke, C. Castelnovo, R. Moessner, C. Czternasty, M. Meissner, K. C. Rule, J.-U. Hoffmann, K. Kiefer, S. Gerischer, D. Slobinsky, and R. S. Perry, Science (New York) **326**, 411 (2009).

[93] R. Siddharthan, B. S. Shastry, a. P. Ramirez, A. Hayashi, R. J. Cava, and S. Rosenkranz, Physical Review Letters **83**, 1854 (1999).

[94] T. Yavors'kii, T. Fennell, M. J. P. Gingras, and S. T. Bramwell, Physical Review Letters **101**, 037204 (2008).

[95] J. P. C. Ruff, R. G. Melko, and M. J. P. Gingras, Physical Review Letters **95**, 097202 (2005).

[96] R. G. Melko and M. J. P. Gingras, Journal of Physics: Condensed Matter **16**, R1277 (2004).

[97] S. T. Bramwell and M. J. Harris, Journal of Physics: Condensed Matter **10**, L215 (1998).

[98] S. Rosenkranz, A. P. Ramirez, A. Hayashi, R. J. Cava, R. Siddhartan, and B. S. Shastry, Journal of Applied Physics **87**, 5914 (2000).

[99] S. T. Bramwell, M. J. Harris, B. C. den Hertog, M. J. P. Gingras, J. S. Gardner, D. F. Mcmorrow, A. R. Wildes, A. L. Cornelius, J. D. M. Champion, R. G. Melko, and T. Fennell, Physical Review Letters **87**, 047205 (2001).

[100] K. Kitagawa, R. Higashinaka, K. Ishida, Y. Maeno, and M. Takigawa, Physical Review B **77**, 214403 (2008).

[101] B. Z. Malkin, T. T. A. Lummen, P. H. M. van Loosdrecht, G. Dhalenne, and A. R. Zakirov, Journal of Physics: Condensed Matter **22**, 276003 (2010).

[102] Y. M. Jana, A. Sengupta, and D. Ghosh, Journal of Magnetism and Magnetic Materials **248**, 7 (2002).

[103] L. D. C. Jaubert and P. C. W. Holdsworth, Journal of Physics: Condensed Matter **23**, 164222 (2011).

[104] B. Tomasello, C. Castelnovo, R. Moessner, and J. Quintanilla, Physical Review B **92**, 155120 (2015).

[105] M. Maczka, M. L. Sanjuán, A. F. Fuentes, L. Macalik, J. Hanuza, K. Matsuhira, and Z. Hiroi, Physical Review B **79**, 214437 (2009).

[106] A. Bertin, Y. Chapuis, P. Dalmas de Réotier, and A. Yaouanc, Journal of Physics: Condensed Matter **24**, 256003 (2012).

[107] Y. M. Jana and D. Ghosh, Physical Review B **61**, 9657 (2000).

[108] J. G. Rau and M. J. P. Gingras, Physical Review B **92**, 144417 (2015).

[109] M. J. P. Gingras and P. A. McClarty, Reports on Progress in Physics **77**, 056501 (2014).

[110] J. Carrasquilla, Z. Hao, and R. G. Melko, Nature Communications **6**, 7421 (2015).

[111] K. Matsuhira, C. Paulsen, E. Lhotel, C. Sekine, Z. Hiroi, and S. Takagi, Journal of the Physical Society of Japan **80**, 123711 (2011).

[112] H. M. Revell, L. R. Yaraskavitch, J. D. Mason, K. A. Ross, H. M. L. Noad, H. Dabkowska, B. D. Gaulin, P. Henelius, and J. B. Kycia, Nature Physics **9**, 34 (2012).

[113] L. R. Yaraskavitch, H. M. Revell, S. Meng, K. A. Ross, H. M. L. Noad, H. A. Dabkowska, B. D. Gaulin, and J. B. Kycia, Physical Review B **85**, 020410 (2012).

[114] J. A. Quilliam, L. R. Yaraskavitch, H. A. Dabkowska, B. D. Gaulin, and J. B. Kycia, Physical Review B **83**, 094424 (2011).

[115] S. Erfanifam, S. Zherlitsyn, S. Yasin, Y. Skourski, J. Wosnitza, A. A. Zvyagin, P. McClarty, R. Moessner, G. Balakrishnan, and O. A. Petrenko, Physical Review B **90**, 064409 (2014).

[116] S. Erfanifam, PhD thesis (Technische Universität Dresden, 2013).

[117] K. Matsuhira, Z. Hiroi, T. Tayama, S. Takagi, and T. Sakakibara, Journal of Physics: Condensed Matter **14**, L559 (2002).

[118] R. Higashinaka, H. Fukazawa, and Y. Maeno, Physical Review B **68**, 014415 (2003).

[119] P. Henelius, T. Lin, M. Enjalran, Z. Hao, J. G. Rau, J. Altosaar, F. Flicker, T. Yavors'kii, and M. J. P. Gingras, Physical Review B **93**, 024402 (2016).

[120] H. D. Zhou, C. R. Wiebe, Y. J. Jo, L. Balicas, Y. Qiu, J. R. D. Copley, G. Ehlers, P. Fouquet, and J. S. Gardner, Journal of Physics: Condensed Matter **19**, 342201 (2007).

[121] N. Shannon, Nature Physics **9**, 326 (2013).

[122] P. A. McClarty, O. Sikora, R. Moessner, K. Penc, F. Pollmann, and N. Shannon, Physical Review B **92**, 094418 (2015).

[123] Y. Tokiwa, T. Yamashita, M. Udagawa, S. Kittaka, T. Sakakibara, D. Terazawa, Y. Shimoyama, T. Terashima, Y. Yasui, T. Shibauchi, and Y. Matsuda, Nature Communications **7**, 10807 (2016).

[124] I. A. Ryzhkin, Journal of Experimental and Theoretical Physics **101**, 481 (2005).

[125] L. D. C. Jaubert and P. C. W. Holdsworth, Nature Physics **5**, 258 (2009).

[126] H. Kadowaki, N. Doi, Y. Aoki, Y. Tabata, T. J. Sato, J. W. Lynn, K. Matsuhira, and Z. Hiroi, Journal of the Physical Society of Japan **78**, 103706 (2009).

[127] D. Slobinsky, C. Castelnovo, R. Borzi, A. Gibbs, A. Mackenzie, R. Moessner, and S. Grigera, Physical Review Letters **105**, 267205 (2010).

[128] S. J. Blundell, Physical Review Letters **108**, 147601 (2012).

[129] S. Scharffe, G. Kolland, M. Valldor, V. Cho, F. Welter, and T. Lorenz, Journal of Magnetism and Magnetic Materials **383**, 83 (2015).

[130] K. A. Ross, L. Savary, B. D. Gaulin, and L. Balents, Physical Review X **1**, 021002 (2011).

[131] J. S. Gardner, J. P. Gingras, and J. E. Greedan, Reviews of Modern Physics **82**, 53 (2010).

[132] R. Applegate, N. R. Hayre, R. R. P. Singh, T. Lin, a. G. R. Day, and M. J. P. Gingras, Physical Review Letters **109**, 097205 (2012).

[133] M. Hirschberger, J. W. Krizan, R. J. Cava, and N. P. Ong, Science **348**, 106 (2015).

[134] C. Castelnovo, R. Moessner, and S. Sondhi, Physical Review Letters **104**, 107201 (2010).

[135] M. Valldor, *Private Communication* (2013).

[136] V. Cho, Diploma thesis (Universität zu Köln, 2014).

[137] P. Laschitzky, Diploma thesis (Universität zu Köln, 2013).

[138] J. F. Welter, Diploma thesis (Universität zu Köln, 2015).

[139] G. Sala, M. J. Gutmann, D. Prabhakaran, D. Pomaranski, C. Mitchelitis, J. B. Kycia, D. G. Porter, C. Castelnovo, and J. P. Goff, Nature Materials **13**, 488 (2014).

[140] D. Prabhakaran and A. T. Boothroyd, Journal of Crystal Growth **318**, 1053 (2011).

[141] D. J. Flood, Journal of Applied Physics **45**, 4041 (1974).

[142] E. Riedel and C. Janiak, *Anorganische Chemie* (de Gruyter, Berlin, New York, 2007).

[143] H. D. Zhou, J. G. Cheng, A. M. Hallas, C. R. Wiebe, G. Li, L. Balicas, J. S. Zhou, J. B. Goodenough, J. S. Gardner, and E. S. Choi, Physical Review Letters **108**, 207206 (2012).

[144] I. Mirebeau and I. Goncharenko, Journal of Physics: Condensed Matter **16**, S653 (2004).

[145] O. A. Petrenko, M. R. Lees, and G. Balakrishnan, Physical Review B **68**, 012406 (2003).

[146] A. Cornelius and J. Gardner, Physical Review B **64**, 060406 (2001).

[147] C. Krey, S. Legl, S. R. Dunsiger, M. Meven, J. S. Gardner, J. M. Roper, and C. Pfleiderer, Physical Review Letters **108**, 257204 (2012).

[148] L. Benito, J. I. Arnaudas, M. Ciria, C. de la Fuente, and A. del Moral, Journal of Physics: Condensed Matter **16**, 7151 (2004).

[149] S. Scharffe, O. Breunig, V. Cho, P. Laschitzky, M. Valldor, J. F. Welter, and T. Lorenz, Physical Review B **92**, 180405(R) (2015).

[150] J. Snyder, B. G. Ueland, J. S. Slusky, H. Karunadasa, R. J. Cava, and P. Schiffer, Physical Review B **69**, 064414 (2004).

[151] C. Paulsen, M. J. Jackson, E. Lhotel, B. Canals, D. Prabhakaran, K. Matsuhira, S. R. Giblin, and S. T. Bramwell, Nature Physics **10**, 135 (2014).

[152] A. Sen and R. Moessner, Physical Review Letters **114**, 247207 (2015).

[153] B. Klemke, PhD thesis (Technische Universität Berlin, 2011).

[154] R. Higashinaka, H. Fukazawa, D. Yanagishima, and Y. Maeno, Journal of Physics and Chemistry of Solids **63**, 1043 (2002).

[155] R. Higashinaka, H. Fukazawa, K. Deguchi, and Y. Maeno, Journal of Physics: Condensed Matter **16**, S679 (2004).

[156] P. C. Guruciaga, S. A. Grigera, and R. A. Borzi, Physical Review B **90**, 184423 (2014).

[157] T. Fennell, M. Kenzelmann, B. Roessli, H. Mutka, J. Ollivier, M. Ruminy, U. Stuhr, O. Zaharko, L. Bovo, A. Cervellino, M. K. Haas, and R. J. Cava, Physical Review Letters **112**, 017203 (2014).

[158] H. Aoki, T. Sakakibara, K. Matsuhira, and Z. Hiroi, Journal of the Physical Society Japan **73**, 2851 (2004).

[159] M. Udagawa, M. Ogata, and Z. Hiroi, Journal of the Physical Society Japan **71**, 2365 (2002).

[160] G. Ehlers, A. L. Cornelius, M. Orenda, M. Kajnakova, T. Fennell, S. T. Bramwell, and J. S. Gardner, Journal of Physics: Condensed Matter **15**, L9 (2003).

[161] J. A. Hertz, Physical Review B **14**, 1165 (1976).

[162] S. Chakravarty, B. I. Halperin, and D. R. Nelson, Physical Review B **39**, 2344 (1989).

[163] S. Sachdev, *Quantum Phase Transitions* (Cambridge University Press, 1999).

[164] P. Gegenwart, Q. Si, and F. Steglich, Nature Physics **4**, 186 (2008).

[165] C. Rüegg, B. Normand, M. Matsumoto, A. Furrer, D. F. McMorrow, K. W. Krämer, H. U. Güdel, S. N. Gvasaliya, H. Mutka, and M. Boehm, Physical Review Letters **100**, 205701 (2008).

[166] S. Sachdev and B. Keimer, Physics Today **64(2)**, 29 (2011).

[167] D. Bitko, T. F. Rosenbaum, and G. Aeppli, Physical Review Letters **77**, 940 (1996).

[168] H. M. Rønnow, R. Parthasarathy, J. Jensen, G. Aeppli, T. F. Rosenbaum, and D. F. McMorrow, Science **308**, 389 (2005).

[169] S. M. A. Tabei, M. J. P. Gingras, Y.-J. Kao, and T. Yavors'kii, Physical Review B **78**, 184408 (2008).

[170] R. Coldea, D. A. Tennant, E. M. Wheeler, E. Wawrzynska, D. Prabhakaran, M. Telling, K. Habicht, P. Smeibidl, and K. Kiefer, Science **177**, 327 (2010).

[171] S. Lee, R. K. Kaul, and L. Balents, Nature Physics **6**, 702 (2010).

[172] J. A. Kjäll, F. Pollmann, and J. E. Moore, Physical Review B **83**, 020407 (2011).

[173] C. Morris, R. Valdés Aguilar, A. Ghosh, S. Koohpayeh, J. Krizan, R. Cava, O. Tchernyshyov, T. McQueen, and N. Armitage, Physical Review Letters **112**, 137403 (2014).

[174] S. Kobayashi, S. Hosaka, H. Tamatsukuri, T. Nakajima, S. Mitsuda, K. Prokeš, and K. Kiefer, Physical Review B **90**, 060412 (2014).

[175] N. J. Robinson, F. H. L. Essler, I. Cabrera, and R. Coldea, Physical Review B **90**, 174406 (2014).

[176] T. Liang, S. M. Koohpayeh, J. W. Krizan, T. M. Mcqueen, R. J. Cava, and N. P. Ong, Nature Communications **6**, 7611 (2015).

[177] H. Weitzel, Zeitschrift für Kristallographie **144**, 238 (1976).

[178] W. Scharf, H. Weitzel, I. Yaeger, I. Maartense, and B. Wanklyn, Journal of Magnetism and Magnetic Materials **13**, 121 (1979).

[179] T. Hanawa, K. Shinkawa, M. Ishikawa, K. Miyatani, K. Saito, and K. Kohn, Journal of the Physical Society of Japan **63**, 2706 (1994).

[180] H. Weitzel, H. Ehrenberg, C. Heid, H. Fuess, and P. Burlet, Physical Review B **62**, 12146 (2000).

[181] J. Frielingsdorf, Diploma thesis (Universität zu Köln, 2011).

[182] E. M. Wheeler, PhD thesis (Oxford University, 2007).

[183] D. Bruening, Master thesis (Universität zu Köln, 2016).

[184] P. F. Sullivan and G. Seidel, Physical Review **173**, 679 (1968).

[185] E. Sela, *Private Communication* (2012).

[186] A. W. Kinross, M. Fu, T. J. Munsie, H. A. Dabkowska, G. M. Luke, S. Sachdev, and T. Imai, Physical Review X **4**, 031008 (2014).

[187] D. I. Khomskii, *Basic aspects of the quantum theory of solids: order and elementary excitations* (Cambridge University Press, 2010).

[188] P. Jordan and E. Wigner, Zeitschrift für Physik **47**, 631 (1928).

[189] E. Lieb, T. Schultz, and D. Mattis, Annals of Physics **16**, 406 (1961).

[190] N. Bogoliubov, Journal of Physics **11**, 23 (1947).

List of Figures

List of Tables

Publikationsliste

Teilpublikationen dieser Arbeit

- **Hysteresis and Relaxation Effects in the Spin-Ice Compound $\mathbf{Dy_2Ti_2O_7}$ studied by Heat Transport**
  S. Scharffe, G. Kolland, M. Valldor, M. Hiertz, and T. Lorenz
  Journal Physical Society Japan Conference Proceeding **3**, 014030 (2014)
- **Heat Transport of the Spin-Ice Materials $\mathbf{Ho_2Ti_2O_7}$ and $\mathbf{Dy_2Ti_2O_7}$**
  S. Scharffe, G. Kolland, M. Valldor, V Cho, J. F. Welter and T. Lorenz
  Journal of Magnetism and Magnetic Materials **383**, 83 (2015)
- **Suppression of Pauling's residual entropy in dilute spin ice $\mathbf{(Dy_{1-x}Y_x)_2Ti_2O_7}$**
  S. Scharffe, O. Breunig, V Cho, P. Laschitzky, M. Valldor, J. F. Welter and T. Lorenz
  Physical Review B **92**, 180405(R) (2015)

Danksagung

In diesem Abschnitt möchte ich mich bei allen bedanken, die mich während der Anfertigung dieser Arbeit begleitet haben.

Zu allererst möchte ich mich natürlich bei meinem Doktorvater Prof. Dr. Thomas Lorenz bedanken, der mir während der ganzen Zeit zur Seite gestanden hat und immer mit einer Idee oder Erklärung aufwarten konnte, egal zu welcher Tages- oder auch Nachtzeit. Diese Diskussionen haben diese Arbeit eindeutig voran getrieben. Zusätzlich ist die Teilnahme an mehreren nationalen aber auch internationalen Tagungen während einer Doktorarbeit denke ich nicht selbstverständlich. Darüber hinaus gilt mein Dank den übrigen Mitgliedern der Prüfungskommission. Prof. Dr. Markus Braden danke ich für die Anfertigugng des Zweitgutachtens, Prof. Dr. Simon Trebst für die Übernahme der Prüfungsvorsitzes und Dr. Oliver Breunig für die Bereitschaft das Protokoll anzufertigen.

Darüber hinaus muss hier auch noch erwähnt werden, dass Oliver Breunig nicht nur das Protokoll anfertigt, sondern mir auch bei diversen anderen Problemen mit Rat und Tat bei Seite stand. Ob es sich dabei um das Korrekturlesen oder IT-Probleme handelte, zeigte er immer wieder eine bemerkenswerte Hilfsbereitschaft. Mittlerweile sieht man sich sogar mal mehr und mal weniger im Fitnessstudio.

Darüber hinaus möchte ich mich natürlich auch bei meinem Vorgänger Gerhard bedanken, der mir zu Beginn meiner Tätigkeit bei diversen Labview-Problemen und bei dem Umgang mit den zahlreichen Messapparaturen geholfen hat. Seine Messungen an den Spin-Ice Verbindungen lieferten zudem eine super Basis für die Ergebnisse dieser Arbeit.

Grundlage für die Anfertigung dieser Arbeit sind natürlich die diversen Kristalle, die angefertigt wurden um diese Arbeit berhaupt zu ermglichen. Deshalb möchte ich mich bei Francois Welter, Victoria Cho und Peter Laschitzky bedanken, die eben diese Kristalle unter extremsten Bedingungen gezüchtet haben. An die diversen Gespräche über Fussball oder Apple Produkte werde ich mich natürlich auch gerne zurück erinnern. Ebenso bedanke ich mich bei den weiteren Mitgliedern der Gruppe Lorenz Johannes Engelmayer, Lionel Andersen und Daniel Brüning mit denen ich immer eine gute Zeit hatte. Besonders im Gedächtnis geblieben ist mir auch die Heavy Metal Musik, die von Martin Valldor als ehemaligem direkten Sitznachbar während der Arbeitszeit gehört wurde. Diverse Fragen ob ich die jeweiligen Lieder kenne, musste ich alle verneinen!

Auch wenn sie mittlweile nicht mehr im Institut ist möchte ich mich noch bei Sandra Niessen bedanken, die 3 Jahre mit mir ein Büro geteilt hat und sich als Gruppenmama immer gut um uns gekümmert hat. Hierbei haben auch immer besonders die Besuche von Emma zu einem noch besseren Arbeitsklima bei getragen.

Ralph Müller gilt meine Dank für die starke Unterstützung bei dem Betrieb der Kaffeekasse und natürlich auch für die nahezu unerschöpfliche Versorgung mit flüssig Nahrung. Desweiteren muss Carmen Handels erwähnt werden, die mir bei allen verwaltungstechnischen Angelegenheiten geholfen hat.

Zum Schluss gilt mein besonderer Dank natürlich meiner Freundin Carolin, die mich im gesamten Zeitraum dieser Arbeit begleitet hat und mich in dieser nicht immer nur einfachen Zeit immer liebevoll unterstützt hat. Ferner möchte ich mich natürlich bei meinen Eltern bedanken, ohne die dies alles nicht möglich gewesen wäre.

Zusammenfassung

Die vorliegende Arbeit beinhaltet eine detailierte Analyse der thermodynamischen Eigenschaften der Spin-Eis Verbindungen $Ho_2Ti_2O_7$ und $Dy_2Ti_2O_7$. Aus dem direkten Verlgeich der Wärmeleitfähigkeiten in Verbindung mit Referenzmessungen an korrespondierenden magnetisch verdünnten Systemen konnte für beide Materialien ein eindeutiger Tieftemperaturbeitrag von magnetischen Monopolen κ_{mag} im Nullfeld, wo diese höchst mobil sind, nachgewiesen werden. Ihre Mobilität wird mit ansteigendem Magnetfeld sukzessive unterdrückt. Im Hochfeldbereich zeigen die phononischen Wärmeleitfähigkeiten der isostrukturellen Verbindungen $Dy_2Ti_2O_7$ und $Ho_2Ti_2O_7$ unterschiedliche Vorzeichen auf. Dies resultiert aus einer erhöhten Streuung der Phononen durch Spin Flips in $Ho_2Ti_2O_7$, die mit ansteigendem Magnetfeld unterdrückt wird, wohingegen in $Dy_2Ti_2O_7$ ausgeprägte Magnetostriktion beobachtet wurde, welche zu einer Abhnahme von $\kappa_{\mathrm{ph}}(H)$ führt. Ferner wurden die Relaxations- und Hystereseneffekte in $Dy_2Ti_2O_7$ im Detail untersucht. Es konnte gezeigt werden, dass die Wärmeleitfähighkeit durch Unordnung unterdrückt wird und dass die Hystereseneigenschaften durch die Magnetfeldrate und teilweise sogar durch den Wärmestrom gesteuert werden können. Ebenfalls stellte sich heraus, dass die Hysterese in der Kagomé-Ice Phase durch Unordnung entsteht und nicht durch eine Fehlorientierung des angelegten Magnetfeldes. Ein besonderer Fokus wurde desweiteren auf die verdünnten Spin-Ice Systeme $(Dy_{1-x}Y_x)_2Ti_2O_7$ gelegt. Die extrem langsamen Equilibrationsprozesse bei tiefsten Temperaturen in $Dy_2Ti_2O_7$ werden schnell unterdrückt, wenn das System mit nicht-magnetischem Yttrium verdünnt wird. Für $x \geq 0.2$ konnten die Prozesse nicht mehr nachgewiesen werden. Hinsichtlich der Entropie wurde aus den gemessenen Daten deutlich, dass die Temperaturabhängigkeit im Tieftemperaturbereich mit erhöhtem x stark ansteigt. Es gibt somit keinen Hinweis auf eine Restentropie in $(Dy_{1-x}Y_x)_2Ti_2O_7$ für $x \gtrsim 0.2$, was im Kontrast zur generalisierten Pauling Abschätzung steht. Die gemessenen Werte der spezifischen Wärme konnten bis zu einer Temperatur von 0.7 K quantitativ mit Monte Carlo Simulationen beschrieben werden, wobei es für tiefere Temperaturen zu Abweichungen vom Model kommt. Für die verdünnten Spin-Ice Systeme $(Dy_{1-x}Y_x)_2Ti_2O_7$ konnte ebenfalls ein eindeutiger Monopol-Beitrag extrahiert werden, welcher ein Maximum bei circa 1.3 K aufweist. Er skaliert mit dem Grad der Verdünnung und lässt sich durch qualitiative Modelle erklären. Die Monopol-Anregungsenergie korreliert mit dem Abfall von $\kappa(H)$ für $H < 0.5$ T. Darüber hinaus wurde der Diffusionskoeffizient D_{mag} aus den extrahierten Grössen κ_{mag}

und c_{mag} berechnet. D_{mag} weist bei 1.6 K ein breites Maximum auf und wird für $T < 0.5$ K und für $T \geq 4$ K komplett unterdrückt. Dies lässt sich auf einen eindeutigen Grundzustand für $T \to 0$ K und einen Zusammenbruch der Spin-Ice Physik über 4 K zurückführen. Die mittlere freie Weglänge $\ell \approx 0.3$ µm der Monopole wurde für $Dy_2Ti_2O_7$ bei 1 K bestimmt.

Abstract

In this thesis the low-temperature magnetism of the spin-ice systems $Dy_2Ti_2O_7$ and $Ho_2Ti_2O_7$ is investigated in detail. In general, a clear experimental evidence for a sizable magnetic contribution κ_{mag} to the low-temperature, zero-field heat transport of both spin-ice materials is observed. This κ_{mag} can be attributed to the magnetic monopole excitations, which are highly mobile in zero field and are suppressed by a rather small external field resulting in a drop of $\kappa(H)$. Towards higher magnetic fields, significant field dependencies of the phononic heat conductivities $\kappa_{\mathrm{ph}}(H)$ of $Ho_2Ti_2O_7$ and $Dy_2Ti_2O_7$ are found, which are, however, of opposite signs, as it is also found for the highly dilute reference materials $(Ho_{0.5}Y_{0.5})_2Ti_2O_7$ and $(Dy_{0.5}Y_{0.5})_2Ti_2O_7$. The dominant effect in the Ho-based materials is the scattering of phonons by spin flips which appears to be significantly stronger than in the Dy-based materials. Here the thermal conductivity is suppressed due to enhanced lattice distortions observed in the magnetostriction. Furthermore the thermal conductivity of $Dy_2Ti_2O_7$ has been investigated concerning strong hysteresis effects and slow-relaxation processes towards equilibrium states in the low-temperature and low-field regime. The thermal conductivity in the hysteretic regions slowly relaxes towards larger values suggesting that there is an additional suppression of the heat transport by disorder in the non-equilibrium states. The equilibration can even be governed by the heat current for particular configurations. A special focus was put on the dilution series $(Dy_{1-x}Y_x)_2Ti_2O_7$. From specific heat measurements, it was found that the ultra-slow thermal equilibration in pure spin ice $Dy_2Ti_2O_7$ is rapidly suppressed upon dilution with non-magnetic yttrium and vanishes completely for $x \geq 0.2$ down to the lowest accessible temperatures. In general, the low-temperature entropy of $(Dy_{1-x}Y_x)_2Ti_2O_7$ considerably decreases with increasing x, whereas its temperature-dependence drastically increases. Thus it could be clarified that there is no experimental evidence for a finite zero-temperature entropy in $(Dy_{1-x}Y_x)_2Ti_2O_7$ above $x \simeq 0.2$, in clear contrast to the finite residual entropy $S_{\mathrm{P}}(x)$ expected from a generalized Pauling approximation. A similar discrepancy is also present between $S_{\mathrm{P}}(x)$ and the low-temperature entropy obtained by Monte Carlo simulations, which reproduce the experimental data down to 0.7 K, whereas the data are overestimated at 0.4 K. A straightforward description of the field-dependence $\kappa(H)$ of the dilution series with qualitative models justifies the extraction of κ_{mag}. It was observed that κ_{mag} systematically scales with the degree of dilution and its low-field decrease is related to the monopole excitation energy.

The diffusion coefficient D_{mag} for the monopole excitations was calculated by means of c_{mag} and κ_{mag}. It exhibits a broad maximum around 1.6 K and is suppressed for $T \leq 0.5$ K, indicating a non-degenerate ground state in the long-time limit, and in the high-temperature range for $T \geq 4$ K where spin-ice physics is eliminated. A mean-free path of $\ell \approx 0.3$ µm is obtained for $Dy_2Ti_2O_7$ at about 1 K within the kinetic gas theory.

Offizielle Erklärung

Ich versichere, dass ich die von mir vorgelegte Dissertation selbständig angefertigt, die benutzten Quellen und Hilfsmittel vollständig anegeben und die Stellen der Arbeit – einschließlich Tabellen, Karten und Abbildungen –, die anderen Werken im Wortlaut oder dem Sinn nach entnommen sind, in jedem Einzelfall als Entlehnung kenntlich gemacht habe; dass diese Dissertation noch keiner anderen Fakultät oder Universität zur Prüfung vorgelegen hat; dass sie – abgesehen von unten angegebenen Teilpublikationen – noch nicht veröffentlicht worden ist sowie, dass ich eine solche Veröffentlichung vor Abschluss des Promotionsverfahrens nicht vornehmen werde. Die Bestimmungen der Promotionsordnung sind mir bekannt. Die von mir vorgelegte Dissertation ist von Prof. Dr. T. Lorenz betreut worden.

Köln, den 22. Februar 2016

Simon Scharffe